GAS TURBINE LABORATORY
DEPARTMENT OF AERONAUTICS AND ASTRONAUTICS
MASSACHUSETTS INSTITUTE OF TECHNOLOGY
CAMBRIDGE, MA 02139

A FINAL REPORT ON

NASA GRANT NGL-22-009-383

entitled

UNSTEADY DESIGN-POINT FLOW PHENOMENA
IN TRANSONIC COMPRESSORS

by

J.B. Gertz and A.H. Epstein

prepared for

NASA Lewis Research Center
Cleveland, OH 44135

August 1986

UNSTEADY DESIGN-POINT FLOW PHENOMENA
IN TRANSONIC COMPRESSORS

by

J.B. Gertz and A.H. Epstein

ABSTRACT

High-frequency response probes which had previously been used exclusively in the MIT Blowdown Facility were successfully employed in two conventional steady state axial flow compressor facilities to investigate the unsteady flowfields of highly loaded transonic compressors at design point operation. Laser anemometry measurements taken simultaneously with the high response data were also analysed. The time averaged high response data of static and total pressure agreed quite well with the conventional steady state instrumentation except for flow angle which showed a large spread in values at all radii regardless of the type of instrumentation used. In addition, the time resolved measurements confirmed earlier test results obtained in the MIT Blowdown Facility for the same compressor.

The results of these tests have further revealed that the flowfields of highly loaded transonic compressors are heavily influenced by unsteady flow phenomena. The high response measurements exhibited large variations in the blade to blade flow and in the blade passage flow. In particular, total pressure defects in the rotor wakes were found to vary by a factor of two or more in the time span of a rotor revolution and fluctuations in the rotor exit relative flow angle of ±10 to 20 degrees were observed in nearly every blade wake. Static pressure fluctuations as high as 50 percent of the dynamic pressure were also observed in the blade wakes.

The observed unsteadiness in the blade wakes is explained in terms of the rotor blades' shed vorticity in periodic vortex streets. The wakes were modeled as two-dimensional vortex streets with finite size cores. The model fit the data quite well as it was able to reproduce the average wake shape and bi-modal probability density distributions seen in the laser anemometry data. The presence of vortex streets in the blade wakes also explains the large blade to blade fluctuations seen by the high response probes which is simply due to the intermittent sampling of the vortex street as it is swept past a stationary probe.

TABLE OF CONTENTS

LIST OF TABLES

LIST OF FIGURES

CHAPTER I

INTRODUCTION

The flow through an axial compressor blade row is by its very nature unsteady. Ideally, energy is transferred from moving blade rows to the fluid in a series of unsteady though perodic compressions. Understanding the resulting flow field in the convenient reference frame of a stationary coordinate system is a difficult task at best and thus, it is not surprising that the analysis of the performance of such blade rows has proceeded for the most part by assuming the flow in the frame relative to the blades is both steady and uniform from blade to blade.

Over the past decade, however, it has been found, using a variety of high frequency response instrumentation, that even in the frame relative to the moving blade rows, the flow field of a transonic compressor is highly unsteady in nature. A transonic compressor is defined here as an axial flow compressor in which the inlet flow relative to the rotating blades varies from subsonic at the hub to fully supersonic at the tip. The term "unsteady" is used in the sense that the detailed flow field in the rotor blade passages is significantly influenced by unsteady aerodynamic phenomena. In addition, it should be emphasized that the unsteadiness, while occurring over a wide range of operating conditions in particular, is observed to occur at the maximum performance and/or design point operating condition. The unsteady flow fields of axial flow transonic compressors operating at or near their design point is thus the subject of this thesis.

In the past, flow measurements in high-speed turbomachinery have generally been confined to obtaining the mean flow properties with conventional pneumatic pitot-static type probes which are incapable of resolving the blade to blade flow field. The mean quantities have tradi-

tionally been the focus of interest by the designer since the technology did not exist for quantitative time-resolved measurements. Hot-wire techniques, while having the capability of providing high response time-resolved measurements of either velocity or temperature, are somewhat impractical in the highly compressible flowfield of a transonic compressor, due to the enormous difficulty in assembling the necessary array of wires in order to make it possible to separate variations of density and temperature from variations of velocity. More recently, laser anemometry techniques have been used to map the blade passage velocity field, and while these techniques provide excellent spatial resolution they cannot resolve the time-dependent flow field. Instead, they rely on averaging data acquired over many rotor revolutions. It is not surprising then, that the design and development of transonic compressors has proceeded over the years based, primarily, on axisymmetric analysis which presumes steady and uniform blade to blade flow and accounts for blade row losses by using banks of empirical data which have been correlated into various loss factor coefficients.

The task of this study has been to explore the actual unsteady flow fields of a number of transonic compressors using high frequency response instrumentation designed specifically for this purpose. The time-resolved flow field in a typical transonic rotor requires instrumentation with a frequency response well above the 5 to 6 kHZ of blade passing. Using miniature strain gage pressure transducers with natural frequencies in excess of 200 KHz, probes have been constructed at the MIT Gas Turbine Laboratory which are capable of measuring the time resolved total and static pressures as well as the tangential and radial flow angles (see Refs. [1.1], [1.2], and [1.3]). This type of instrumentation was

initially used in the MIT Blowdown Compressor Facility [1.4] where an operating point can be maintained for approximately 30 m-sec (approximately five rotor revs). Two of the compressors investigated here have been tested previously in this facility. They are the first stage of the NASA Low-Aspect Ratio Two-Stage Axial Flow Fan [1.5] and the Air Force Aero-Propulsion Laboratory's (AFAPL) High Through Flow Compressor [1.6]. The results of these tests can be found in [1.2] and [1.3].

In this study the high response instrumentation was used for the first time in conventional steady state test facilities at both the NASA Lewis Research Center in Cleveland, OH and at Pratt and Whitney Aircraft (PWA) in Hartford, CT. In addition, laser anemometry and conventional steady state aero data were obtained simultaneously with the high response data downstream of the rotor blade rows. Also, a comparison of the high response probe data from the blowdown facility and the high response data from a steady state facility was made possible by testing the same NASA low aspect ratio compressor, which had previously been tested in the MIT Blowdown Facility, in the NASA Lewis facility. A third rotor, typical of a commercial split-flow fan, was tested at the PWA facility.

The environment of the steady state facilities required the ability to calibrate the sensors during the test time with the rotor operating at design speeds. Traversing mechanisms were designed to allow this. The ability to acquire data in these "steady-state" facilities allowed greater test times than could be achieved in the MIT Blowdown Facility. Typically probes were immersed in the flow for time periods on the order of 50 to 100 rotor revolutions. This aided in the analysis of the unsteady blade to blade flow field since stationary probes can only sample each blade passage once every rotor revolution.

In general, high response measurements taken in the rotor exit flow of a transonic rotor operating at its design point, show that not only are there large variations in the flow from one blade to the next, but that even the flow within the blade passages, themselves, is highly unsteady. While physical differences among blade passages can be seen, they are generally small and play a relatively insignificant role in the development of the unsteady flow field. For example, near the rotor tip, it has been observed that the total pressure defect in the same blade wake may vary by as much as a factor of two in the time span of a rotor revolution. Fluctuations in the rotor exit relative flow angle of between ±10 to 20 degrees have been observed in nearly every blade wake as well. Even in the longer time frame of rotor rotation, the time-averaged total pressure at the exit of a rotor operating at "design" conditions can vary as much a two to three percent.

One explanation of the unsteadiness observed in the rotor exit flow fields ,and in particular, the blade wakes, is that the rotor blades shed vorticity in periodic vortex streets. This is a well known phenomena for the flow over cylinders or bodies with blunt trailing edges, however, studies of shedding from airfoils with sharp trailing edges typical of fan and compressor blading are somewhat ambiguous, some showing shedding some not. Several investigators have observed vortex shedding in various cascade flows representing both turbine and compressor blade profiles. In an earlier work by Ng [1.3], this type of vortex shedding was proposed as a mechanism for inducing unsteadiness in the motion of the blade passage shock which results in total pressure and total temperature non-uniformities in the blade to blade flow.

In this thesis, experimental evidence will be presented which supports

the existence of a vortex street structure in the rotor blade wakes of a transonic compressor along with a model of the wake structure which fits the data. Implications of this structure to compressor performance and analysis will also be discussed.

CHAPTER II

TEST FACILITIES AND COMPRESSORS

The data presented in this report were obtained in three seperate axial flow compressor facilities: the MIT Blowdown Facility, the NASA Lewis Single Stage Test Facility, and P&WA Wilgoos Compressor Test Facility. The latter two facilities were operated in a conventional "steady-state" mode while the MIT facility was operated in a blowdown mode. Three highly loaded transonic rotors have been investigated in these facilities. The NASA Lewis Low-Aspect Ratio Fan and the Air Force Aero-Propulsion Laboratory (AFAPL) High Through Flow Compressor were both tested in the MIT Blowdown Facility. The NASA Lewis rotor was also tested in the Lewis steady state facility, while the PWA split-flow fan was tested exclusively at the Wilgoos Facility. A complete set of high response measurements was obtained for the rotor exit flow in the Blowdown facility and at NASA Lewis, however, only total pressure measurements will be presented for PWA rotor. A brief description of each facility will be presented along with the basic performance characteristics and flow paths of the three rotors.

2.1 MIT Blowdown Compressor Facility

The MIT Blowdown Compressor Facility consists of a supply tank, a test section, and a dump tank as shown in Fig. 2.1. A full description of its design and operation can be found in Ref. [1.4]. The results obtained for the NASA Low Aspect Ratio Rotor and the AFAPL High Through Flow Stage can be found in Refs. [1.2] and [1.3] respectively.

The facility operates in the following manner. The rotor is brought to speed in vacuum, a diaphragm is ruptured ,and the test gas is passed through the test section from the supply tank to the dump tank. During this time the rotor is driven by its own inertia. By proper matching of

the rotor's moment of inertia and the initial supply tank pressure, the rotor's inlet tangential Mach number can be held nearly constant for a test time of 50 to 100 msec depending on the particular rotor being tested. A discharge orifice maintains constant axial Mach number by remaining choked over the desired test time.

2.2 NASA Lewis Single-Stage Compressor Test Facility

The single stage test facility at NASA Lewis is a conventional steady state operating rig. A complete description of the facility is given in [1.5] and a brief description will be given here. Atmospheric air enters the test facility at an inlet located on the roof of the building and flows into a plenum chamber upstream of the test compressor. The air then passes through the test fan into the collector and is exhausted to the atmosphere. The mass flow is controlled with a sleeve valve collector and is determined by means of calibrated thin plate orifice located far upstream of the compressor test section.

Typical operation of the facility involves bringing the rotor up to the desired corrected speed with the sleeve valve wide open to avoid the compressor stall line. The desired mass flow is then set by slowly closing the valve while maintaining the desired speed setting. Depending on the skill of the operator this process can take anywhere from ten to fifteen minutes. Once at design speed, re-setting the operating point is a relatively simple matter and typically takes less than five minutes to accomplish.

2.3 Pratt and Whitney Single Stage Test Facility

Proprietary considerations do not permit a full description of the facility, however, it is similar in many respects to the NASA Lewis facility except that air enters the facility at below atmospheric pressure and two separate exhaust systems control the fan duct and "core" mass flows.

Also, setting the operating point in this facility involved a somewhat more complicated flow control system requiring at least twenty to thirty minutes to set a desired flow point.

2.4 Test Compressors: Flow Paths and Design Performance

The flow paths of the three facilities can be seen in Fig. 2.2. Table 2.1 lists the actual physical dimensions of the rotors and the location of the instrumentation ports. The relevant parameters which describe the performance of the three compressors at their respective design point operating conditions can be seen in Table 2.2.

The NASA Lewis compressor is the first stage of a two-stage axial flow fan in which a low-aspect ratio was incorporated to eliminate the need for part span dampers which were present in an earlier design (see Ref. [1.5]). The NASA rotor has a design pressure ratio of 1.63 at a massflow of 33.25 kg/sec. The inlet relative Mach number at the rotor tip is 1.38 and the design tip speed is 429 m/sec at a rotational speed of 16000 RPM. The first-stage rotor has 22 blades, an inlet tip diameter of 51.3 cm, and an inlet hub/tip radius ratio of 0.375. The rotor tip clearance at design speed is 0.5 mm. The rotor was tested with a 34 blade multiple-circular-arc designed stator row.

The AFAPL High Through Flow compressor is described in Ref. [1.6]. This stage was also designed with relatively low-aspect ratio blading. The AFAPL rotor has a design pressure ratio of 2.10 at a massflow of 28.41 kg/sec. The inlet relative Mach number at the rotor tip is 1.65 and the design tip speed is 456 m/sec. The rotor has 20 blades, an inlet tip diameter of 43.2 cm, and an inlet hub/tip radius ratio of 0.312. The rotor was tested with a 31 blade stator row.

The Pratt & Whitney Aircraft fan was designed under the NASA E3

program, and is typical of a commercial split flow fan. The fan has a design pressure ratio of 1.60 at a massflow of 88.84 kg/sec. The inlet relative Mach number at the fan tip is 1.35 and the design tip speed is 449 m/sec. The fan has 26 blades, an inlet tip diameter of 79.1 cm, and an inlet hub/tip radius ratio of 0.316. The flow is split at about one-half a chord downstream of the fan trailing edge into a core and duct flow. At design conditions approximately 14% of the flow is passes through a core-compressor duct and the remaining 86% of the flow passes through the fan duct. For the tests presented here, the core compressor was represented solely by its inlet stator blade row.

2.5 Summary

High-response measurements were obtained in two conventional steady-state axial-flow compressor test facilties and compared to earlier tests results obtained in the MIT blowdown compressor facility. Three axial flow compressors were tested: the NASA Low-Aspect Ratio Fan, the Air Force High Through Flow Compressor, and the PWA Split-Flow Fan. The performance of these machines are similar in the sense that they are are all highly efficient, highly loaded, and transonic. Significant differences exist, however. In particular, the AFAPL rotor has a significantly higher mass flow capacity and pressure ratio than the other two rotors. Also, while the geometry of the NASA and Air Force rotors is similar in that they both have relatively low aspect ratios (1.6 and 1.3 respectively), the PWA rotor has a relatively high aspect ratio of 2.8. In addition, the size of the rotor-stator gaps in these machines varies significantly from less than one-sixth of a rotor chord in the AFAPL compressor to over one and one-half times a rotor chord in the PWA fan.

CHAPTER III

INSTRUMENTATION AND DATA ACQUISITION

The steady state facilities were all instrumented with conventional pneumatic probes to determine averaged values of total and static pressure and flow angle. A detailed comparison of these measurements with the time-averaged high response data acquired at the Lewis test facility is presented in Chapter IV. In the following sections a brief description of the high-response probes will be presented followed by a description of the data acquisition systems and processing techniques. Also a short description of the NASA Lewis Anemometer system will be given as these measurements were found to be useful in the analysis of the rotor blade wakes (see Chapter VII).

3.1 High Frequency Response Aerodynamic Probes

High frequency response silicon diaphragms have been used in various probe configurations to measure total and static pressure and flow angle. The diaphragms, themselves, typically have natural frequencies of over 200 kHz, however, their incorporation into high response pressure probes results in instruments with frequency responses ranging from 20 to 40 kHz. The rated accuaracy of the transducers, themselves, is generally better than 0.5% over a temperature range of 100°F.

3.1.1 High Response Total Pressure Probes

Over the past decade the MIT Gas Turbine Laboratory has designed and built a number of high frequency response total pressure probes. They are basicially covential impact type probes with high-response silicon dia-phragms mounted one-diaphragm diameter downstream of a sharp edged inlet to minimize sensitivity to changes in flow angle. Tests have shown these types of probes to be relatively insensitive to variations in flow direction

of up to ±20 degrees. The total pressure data presented here was obtained from two probes both of which use high response Kulite transducers.

The first probe consists of a single sensor impact tube mounted "piggy-back" on the MIT aspirating probe as shown in Fig. 3.1. The pressure transducer is an 0.093" diameter XCQ-093 Kulite transducer. A more complete description of this probe can be found in Ref. [1.3]. The second probe is a rake consisting of four impact tubes separated by 1.13" in which four separate 0.062" diameter XCQ-062 Kulite transducers are mounted as shown in Fig. 3.2.

Shocktube tests have shown that the transducers themselves, have natural frequencies above 200 kHz [3.1], however, the frequency response of these probes is limited by the acoustic resonance of the cavity formed by mounting the transducer one-diameter downstream of the probe inlet. This resonance can be estimated as the quarter wave frequency of the passage (c/4L), where c is the speed of sound and L is the length of the duct. For air at 270°K, c is equal to 330 m/sec and for L=0.24 cm (.093") the resonance frequency is calculated to be approximately 35 kHz. In order to determine the useful frequency range for a probe of this type its damping ratio must be known. Assuming the cavity behaves as a second order system, a damping ratio of between 0.5 and 0.7 would be required to give a fairly flat response up to about 30 kHz. The value of this damping ratio is not known at this time and additional shocktube testing will be required to estimate its magnitude.

3.1.2 High Response Four-Way Cylinder Probe

Time-resolved blade-to-blade measurements of total and static pressure and radial and tangential flow angle were obtained using a 4-way cylinder probe developed at MIT (see Ref. [1.3]). The probe actually has an

elliptical cross-section with a 3.3 mm face which is shown in Fig. 3.3. Four high-response silicon pressure transducers are flush mounted on flats on the surface of the probe and covered with a thin (.050 mm) layer of silcon rubber. This reduces the thermal sensitivity of the probe as well as aiding in protecting the transducers from external damage. The thermal sensitivity of the probe is further reduced by supplying cooling water through the base of the probe.

The transducers, themselves, have natural frequencies of greater than 200 kHz, however, in practice, the actual frequency response of the probe is limited by its overall physical size. Since the information extracted from the probe measurements must involve an integration of the instantaneous pressure distribution over the entire sensing area of the four diaphragm configuration, the minimum wavelength that can be resolved with a reasonable degree of accuracy is approximately four times the probe's diameter, d, (3.3 mm). This corresponds to a frequency of U/(4d), where U is the speed at which a disturbance is swept over the probe face. In this case, U, represents the rotor wheel speed which for the rotors considered here ranges from 400 to 500 m/sec at the rotor tips. The maximum frequency that can be resolved then is approximately 40 kHz. In practice,however, the actual output of the probe has very little useful content above 20 kHz, which is still three to four times the blade passing frequency of any of the rotors tested.

Dynamic effects of an unsteady flow around the probe head can also be important although they have not been accounted for in the present data reduction scheme. Kovasznay [3.2] has shown that for a sphere probe the ratio of the unsteady surface pressure fluctuations to the instantaneous dynamic pressure can be expressed as,

$$(2\pi fdu)/U^2 \qquad\qquad (3.0a)$$

where d is the diameter of the sphere, f is the frequency of the disturbance, and,

$$V(t) = U + ucos(2\pi ft) \qquad\qquad (3.0b)$$

is the form of the unsteady velocity disturbance. For the rotor wakes encountered in the transonic compressors of the present investigation, this ratio can be as high as 0.15 and thus unsteady effects should be considered in the probe calibration and subsequent data reduction. Unfortunately, this has not been done at this time, although an estimate of the errors associated with the unsteady flow could be made by considering a similar unsteady flow over the surface of a cylinder.

Another measure of the probe's resolution is simply its size relative to the phenomena being investigated. The ratio of the probe's diameter, d, to the blade spacing, s, at the rotor tips is approximately 5 percent for the NASA and AFAPL rotors and 3.5 percent for the P&WA rotor. At the rotor hubs this ratio rises to about 10 percent for all three rotors. Hence while there is adequate resolution to map the blade to blade flow, the resolution of the rotor wakes, which typically occupy 20 to 30 percent of the blade passage flow, is marginal especially near the hub where the probe may be one-third to one-half the size of the wake, itself. This will be of particular importance if an accurate determination of the wake's internal structure is desired (see Chapter VII).

In order to retrieve the flow quantities of interest, a method must be devised which can extract this information from the four pressures which are measured by each sensor. This was accomplished by calibrating a pneumatic model of the probe in a one-inch free jet. The probe's aerodynamic behavior was determined for a range of Mach numbers from 0.35 to 0.85 and a

range of radial and tangential flow angles of ±20 degrees from the probe's axis [3.3]. From this data a series of calibration curves was obtained following a procedure similar to the one originally described by Figueiredo [3.4] for a 5-way sphere probe. The four time-resolved quantities of total and static pressures and radial and tangential flow angle are determined from the four measured pressures, P1-P4 by the procedure which is described below.

The calibration data was reduced to the following six non-dimensional coefficients:

$$F23 = (P2-P3)/[(P2-P1)+(P3-P1)] \tag{3.1}$$

$$H23 = (Pt-Ps)/[(P2-P1)+(P3-P1)] \tag{3.2}$$

$$CP1 = (P1-Ps)/(Pt-Ps) \tag{3.3}$$

$$CP4 = (P4-Ps)/(Pt-Ps) \tag{3.4}$$

$$KPn = (Pn-Ps)/[(P2-P1)+(P3-P1)] \tag{3.5}$$

$$(n = 2 \text{ or } 3)$$

where Pt and Ps are the total and static pressures respectively. F23 was found to depend principally on the tangential angle, θ and very weakly on the radial angle, ϕ. Since F23 is antisymmetric in θ, only positive values of θ need be considered. The behavior of F23 versus θ is shown in Fig. 3.4a for a radial angle, ϕ of 0.0 degrees and for Mach numbers of 0.35, 0.50, 0.60, and 0.85. A small correction can be applied for radial angles other than zero degrees and is shown in Fig. 3.4b. The corresponding value of F23 for ϕ = 0.0 degrees, $(F23)_o$, can then be found for non-zero values of ϕ by the following relation,

$$(F23)_o = |F23| - (F23)_{cor} \tag{3.6}$$

Since F23 is known immediately from the output of sensors P1-P3, then given ϕ and the Mach number, the correction factor, $(F23)_{cor}$, can be found from

Fig. 3.4b. Using Eq. (3.6), the value of $(F23)_O$ can then be calculated and the value of $|\theta|$ can be found from Fig. 3.4a. The sign of θ is then set to the sign of F23.

The radial angle, ϕ, can be determined in a similar manner from the coefficient CP4 since it depends primarily on ϕ and to a much lesser extent on θ. Figure 3.4c shows the variation of CP4 with ϕ for $\theta = 0.0$. The correction for non-zero values of θ is shown in Fig. 3.4d. Since CP4 should be symmetrical about $\theta = 0.0$, only positive values of θ are shown for the correction factor. Given the static and total pressure and the pressure P4, the value of CP4 can be calculated. Given $|\theta|$, the correction factor $(CP4)_{cor}$ can be found from Fig. 3.4d. The corresponding value of CP4 for $\theta = 0.0$, $(CP4)_O$, can then be found from the calculated value and the correction factor as follows,

$$(CP4)_O = CP4 - (CP4)_{cor} \tag{3.7}$$

Given the Mach number, the value of ϕ can then be found from Fig. 3.4c.

The static pressure can best be determined from the coefficient KPn. By symmetry, $KP2(\theta) = KP3(-\theta)$ so that only values for $|\theta|$ need be considered. KPn depends primarily on θ and to a lesser extent on ϕ. Figure 3.4e shows the variation of KPn for positive values of θ and Fig. 3.4f shows a correction factor for non-zero values of ϕ. Given $|\theta|$ and ϕ, both $(KPn)_O$ and $(KPn)_{cor}$ can be found from the above figures. The value of KPn can then be calculated as follows,

$$KPn = (KPn)_O + (KPn)_{cor} \tag{3.8}$$

The static pressure can then be determined by using the lesser of P2 or P3.

$$Ps = (P2,3)_{min} - [(P2-P1)+(P3-P1)]KPn \tag{3.9}$$

The total pressure is determined from the coefficients H23 and CP1. Since both are even functions of θ, only the absolute value need be considered.

Figures 3.5a-d show the variation of H23 and CP1 versus θ for $\phi = 0.0$ and

the corresponding correction factors versus ϕ. The values of H23 and CP1

can then be calculated for arbitrary values of θ and ϕ as follows,

$$H23 = (H23)_o + (H23)_{cor} \qquad (3.10)$$

$$CP1 = (CP1)_o + (CP1)_{cor} \qquad (3.11)$$

The total pressure can then be calculated from the following relation.

$$Pt = P1 + H23(1-CP1)[(P2-P1)+(P3-P1)] \qquad (3.12)$$

The full data reduction procedure is thus an iterative procedure and can be

summarized as follows:

Input: P1,P2,P3,P4
        1) Calculate F23
        2) First guess: Pt = P1, Ps = $(P2,P3)_{min}$ (or previous values
                             from last converged iteration)
        3) Calculate Mach number from Pt and Ps
        4) Calculate CP4 (Eq. 3.4)
        5) Find θ and ϕ from $(CP4)_o$ and $(F23)_o$ (Figs. 3.4a and 3.4c)
        6) Find KPn from θ and ϕ (Eq. 3.8)
        7) Calculate Ps from KPn (Eq. 3.9)
        8) Find H23 and CP1 from θ and ϕ (Figs. 3.5a-d)
        9) Calculate Pt from Eq. 3.12
      10) Check convergence of Ps; if not converged re-estimate Ps and
           go to step (3)

Once the four flow quantities (Pt, Ps, θ, ϕ) have been determined by

the above iterative process, the Euler turbine equation can be used to

solve for the total temperature which in turn makes it possible to

calculate the static temperature and a variety of relative flow quantities

(such as relative Mach number and relative total pressure). An adiabatic

efficiency can also be computed. In practice, for data records larger than

10,000 points it is much less demanding to calculate these quantities after

processing the complete set of data for the basic four quantities of

pressure and flow angle, rather than calculating them all simultaneously.

The actual calibration data, as presented by Holt [3.3], show some

asymmetries which to date have not been explained. In particular, nearly all the even functions of θ exhibited some asymmetries about $\theta = 0.0$. These asymmetries were averaged out for the calibration curves that were used in the data reduction scheme resulting in maximum uncetainties in the coefficients CP1 and H23 of approximately $\pm 0.8\%$ and 1.3% respectively for $\theta = 10.0$ degrees. This can result in uncertainties in total pressure of up to $\pm 2.0\%$ of the dynamic pressure. Similar uncertainties in the values of KP2 and KP3 result in errors in static pressure measurements of ± 0.5 percent of the dynamic pressure. These types of uncertainties, of course, diminish as one approaches the symmetry point of $\theta = 0.0$ degrees.

For values of θ between 6 and 9 degrees, the coefficient F23 was found to be dependent on the angle ϕ as well as the Mach number. This dependence on ϕ was not included in the curves for F23 used in the data reduction scheme (see Fig. 3.4a) and has been estimated to result in an uncertainty of the measured flow angle of ± 1.0 degree for values of θ between 6 and 9 degrees and Mach numbers less than 0.5. For higher Mach numbers the dependence on ϕ becomes quite small and results in errors of the measured flow angle of less than ± 0.5 degrees.

For the calculation of static pressure, the extrapolation for values of KPn for Mach numbers greater than 0.85 led to serious convergence problems in the iterative scheme. In order to avoid these difficulties values of KPn for Mach numbers greater than 0.85 were held constant. The magnitude of the error in the calculated value of static pressure for Mach numbers greater than 0.85 due to this procedure is not known at this time.

Finally, since the probe is calibrated in a uniform flow, errors in

static pressure and flow angle will occur whenever the probe encounters a shear flow. The magnitude of these errors for a simple cylindrical type probe have been estimated in Appendix A. For the shear flows typical of the transonic rotor wakes in the present investigation, (shear stress parameter of approximately 0.2 [see Appendix]) errors in flow angle can be as high as 4 or 5 degrees depending on the value of the mean flow angle. The value of static pressure calculated in the rotor wakes may be ±5 percent of the dynamic pressure for off-axis flow angles of ±10 degrees.

3.2 Laser Anemometer System

The NASA Lewis laser anemometer system was used in the present experimental investigation simultaneously with the high response instrumentation described above at the NASA Lewis Test Facility with the NASA Low-Aspect Ratio Fan. The system is a single channel, dual beam, fringe anemometer with on-axis backscatter collection optics, and has been previously described in detail in Refs. [3.5], [3.6]. Optical access to the compressor flowfield is provided through a 3mm thick glass window which closely conforms to the rotor flowpath contour in both the circumferential and streamwise directions, thus minimizing the disturbance of the tip region flow. As this is a single channel laser anemometer, rotation of the fringe orientation is necessary for measuring each component of velocity.

Flourescent liquid seed particles, nominally 1-1.4 microns in diameter, are introduced into the flowfield through a 6mm diameter tube located 35 mm upstream of the rotor. The seeder tube is installed in a radial and circumferential actuator to provide capability for positioning the seeder to optimize the data rate each time the laser probe volume location is changed.

Each time an LA velocity measurement is acquired, it is tagged with

the rotor rotational position at which it occurred. This position information is used to assign the velocity measurement to the proper circumferential location relative to the rotor blade. Measurements are acquired across 17 of the 22 rotor blade passages, but are averaged into one representative blade passage containing 50 equally spaced blade-to-blade measurement locations. The individual velocity measurements which occur at each blade-to-blade measurement location are sorted into "velocity bins" which are 5 ft/sec wide. This process yields a probability density distribution (p.d.d.) for the measured velocity at each of the 50 blade-to-blade measurement locations.

It is important to point out that if the distributions of velocities were not retained at each measurement location, then the average velocity measurement may be misleading, since the distributions may not be not singly peaked. Analysis of the velocity p.d.d.'s will be useful for analysis of rotor blade vortex shedding as will be shown later in Chapter VII.

3.3 Test Procedures

In the NASA tests the probes were generally held at fixed radial positions for periods of between 500 and 1000 millisec. The P&WA test data was obtained on a traverse from the casing to a point 4.0" from the rotor tip where the probe was held for another 300 millisec. The blowdown data obtained at MIT was acquired over much shorter times of between 50 to 100 millisec during which the probes were traversed from tip to hub.

3.4 Probe Test Calibration Procedures

Calibration of the pressure transducers in the blowdown tests was carried out before and after each test. Due to the relatively short test times and similarities in the post test conditions of temperature and

pressure, the calibrations were easily repeatable and accurate to less than 1.0% of the absolute pressure. Calibration of the sensors on the steady state rigs required the ability to calibrate the sensors with the rig operating at design speed. In order to do this a high-speed pneumatic translator was built with a special calibration chamber which could be connected to an external pressure reference system. This is shown in Fig. 3.6. Calibration of the sensors was achieved by withdrawing the probe through the compressor casing into the calibration chamber which was outside the casing wall. The chamber was then sealed off by a quick opening (20 m/s) gate valve so that the desired reference pressure could be attained. The reference pressures were measured directly with an external pressure gauge while the entire traverser assembly was mounted on the rig before and after each set of tests and were repeatable to the accuracy of the gauge markings (±0.01 psi).

Before each test, the pressure tranducers were calibrated at three reference pressures corresponding to atmospheric pressure, atmospheric + 5 psi, and atmospheric + 10 psi. These pressures represent fairly well the full range of static and total pressures encountered both upstream and downstream of the rotor. Although only two reference pressures are required with this particular set-up to obtain a scale and zero for each sensor, the third pressure provided an additional check on the accuracy of the calibrations.

3.5 Data Acquisition

The MIT Blowdown data was digitized directly using an MIT nine channel 10 bit A/D system with a sampling rate of 100 kHZ per channel. This results in about 25 data points sampled per blade passing. The signal to noise performance for this system exceeds 1000:1.

The data obtained in the steady state facilities was initially recorded on a 14-track analog FM tape recorder and later played back and digitized using a NASA Lewis 12 bit A/D system. Equivalent real-time sampling rates of between 190 and 200 kHz per channel were chosen, resulting in 30 to 40 data points sampled per blade passing. The FM recorder was set up with Wideband Group I electronics, and a tape speed of 120 ips was chosen. This results in a bandwidth of DC to 80 kHz and a signal to noise ratio of over 300:1. On playback at 7-1/2 ips the signal to noise ratio drops to 200:1, however, the in-situ calibration of the transducers, provides a more direct measure of the fidelity of the complete data aquisition process including the calibration technique itself.

The noise in the calibration data was generally quite small on the order of two to three thousandths of an atmosphere for the 4-way probe and the 093 total pressure probe. The noise level for the total pressure rake was somewhat larger but was generally less than one-hundredth of an atmosphere. Occaisionally irregularities in the output voltages of some of the sensors corresponding to five or six-hundredths of an atmosphere resulted in unusable data. In general, however, the sensors were quite stable and errors of this type were similar to the errors associated with the overall noise level (±0.003 atm). Uncertainties in the computed scale values (atm/volt) generally resulted in uncertainties in the DC levels of pressure of less than ±0.005 atm. A comparison between the time-averaged high response data and the steady state aero data is detailed in Chapter IV and provides some additional insight into the accuracy of the DC levels of the measurements obtained in steady state rigs.

3.6 Summary

Several high frequency response probes originally developed for use in the MIT Blowdown Facility were employed in conventional steady state facilities. The total pressure probes are believed to have a fairly flat frequency response from DC to 30 kHz. A 4-way cylinder probe capable of measuring total and static pressure and tangential and radial flow angle has a somewhat lower frequency response. Calibrations of this probe in a uniform steady flow demonstrated good angular sensistivity (±0.5 degrees) and total and static pressure measurements accurate to less than 1 percent of the dynamic head. However, this type of probe is subject to errors when in the presence of shear flows typical of transonic rotor blade wakes. Errors in static pressure of up to ±5 percent of the dynamic pressure and in flow angle of ±4 degrees have been predicted for a simple linear velocity gradient across the face of the probe. Also, an estimate of the dynamic or unsteady effects which are inherent in this type of flow revealed that this might be another source of measurement error. Calculations of the unsteady flow over a simple cylindrical probe would be useful companion to the shear stress calculations, however they have not been carried out at this time and thus were not accounted for in the data reduction scheme. The results of the 4-way probe should then be carefully considered in the highly unsteady and highly sheared flows encountered in the rotor wakes.

A single channel dual beam fringe anemometer was also employed in the NASA Lewis steady state tests. This system had the capability of providing probability density distributions of the rotor exit velocity at the 50 blade-to-blade measurement locations in 17 of the 22 rotor blade passages. These distributions have been found to be useful in the analysis of rotor blade vortex shedding as explained in Chapter VII.

CHAPTER IV

COMPARISON OF TIME-AVERAGED HIGH-RESPONSE DATA
WITH CONVENTIONAL STEADY STATE AERO DATA

A direct comparison between data obtained with conventional aero probes and data obtained with high-response probes was made possible at the NASA Lewis Facility for a series of fixed immersion tests. For these tests both types of probes were positioned simultaneously at the same axial and radial locations in the rotor exit flow at Station 2 of the NASA Low Aspect Ratio Fan. The high response probes were held in the flow for 300 to 500 millisec, which is equivalent to 80 to 130 rotor revolutions. This data was then time-averaged in order to compare to the conventional aero data.

The "steady-state" aero measurements were made with either a combination probe which measured values of total pressure and flow angle or a wedge-static probe which measured values of static pressure and flow angle. These probes were automatically aligned to the direction of flow with a null balancing control system, while the high response probes were fixed at an angle of 45 degrees from the axial direction, which is approximately the mean rotor exit flow angle over most of the span.

The comparisons presented in this chapter are for the same near design 100% speed operating point in which the mass flow rate was nominally set to a value of 72.8 lbm/sec (33.0 kg/sec). A summary of the test conditions can be seen in Table 4.1. The total pressure ratio listed in the table is the spanwise average obtained from a conventional rake probe downstream of the stator at station 4.

Time-averaged high response total pressure at various spanwise locations were obtained with the total pressure rake, the piggy-backed 0.093" total pressure probe (ASP), and the 4-way cylinder probe. Before comparing

these measurements to the steady state data, it is instructive to examine
the variations of the once-per-rev averaged total pressure ratio versus
time. Figure 4.1 shows the once-per-rev averaged 093 total pressure probe
data at three radii for elasped times corresponding to 100 rotor revolutions.
The scaling for the time axis was chosen such that each division represents
20 rotor revolutions. The fluctuations of total pressure even after being
averaged over an entire rotor revolution are still substantial, especially
near the tip where they can be as high as 2 percent of the mean level.
This is significant since at these flow conditions, a one percent error in
total pressure ratio results in an error of two points in efficiency.

If the total pressure measurements are then time averaged over the
entire immersion time, a comparison can then be made with the conventional
aero data. This can be seen in Fig. 4.2 where measurements of the
averaged total pressure ratio has been plotted versus a non-dimensional
radius, r/r_{tip}. There is very good agreement between the aero data and the
time-averaged 4-way data, however both high response total pressure probes
measured values which are about 4 percent higher at all four radii at which
the measurements were taken. Slightly differing test conditions cannot
explain these differences, especially since several of the tests employed
both the 4-way and the 0.093" total pressure probe simultaneously. One
possible explanantion for the discrepancy may be due to thermal drift
stability problems with the total pressure probes which, unlike the 4-way
probe, are not water cooled. Even though the probes may come to thermal
equilibrium in the calibration chamber on the translator, the probe head
may be adversely affected by convective cooling of the rotor outflow.
Tests conducted in a one-inch open jet with a single head 0.060" total
pressure probe showed that although the output from the probe could be

stabilized under a no flow condition, convective cooling of the jet over the probe body resulted in DC shifts in output corresponding to as high as one-tenth of an atmosphere.

Static pressure comparisons can be made with the time-averaged 4-way data and are shown in Table 4.2 for three separate radii. The agreement is quite remarkable and is better than 0.1 per cent except at the near tip radii where the agreement is less than 1.5 percent. It is also instructive to examine the once-per-rev averaged variations in the high response static pressure measurements. Figures 4.3a-c show the once-per-rev averaged 4-way probe static pressure data at three radii for elasped times corresponding to 100 rotor revolutions. The fluctuations are again significant and can be as high as two percent of the mean level.

A Mach number measurement by conventional techniques was not obtained simultaneously with the 4-way measurements because during this series of tests the conventional combination probe which measures the total and static pressure used to calculate the Mach number had to be removed in order to mount the 4-way probe on the compressor casing. The wedge-static probe was used instead to obtain measurements of static pressure and flow angle. The Mach numbers presented in Table 4.2 were thus acquired from interpolation between earlier results obtained at mass flows of 67.2 and 74.7 lbm/sec. Also shown are the arithmetic averages of Mach numbers computed from the laser anemometer data taken simultaneously at the same radial and axial positions. Again the agreement is quite good at the lower radius, but is 3 to 4 percent lower than both the aero and high response measuremnts at the other two radii.

Although the Mach number and static pressure levels measured by the three techniques are in fairly good agreement, the average flow angle

measurements are not. Figures 4.3d-f show the variations in the once-per-rev averaged tangential flow angle measured by the 4-way probe versus time. The fluctuations are two to three degrees at the two lower radii and approach five degrees near the tip. Figure 4.4 shows a comparison between the time-averaged 4-way probe measurements and the tangential flow angles measured by the aero probes, and the laser anemometer. There is about a five degree spread in the angles measured at any particular radius even among the aero probe measurements, themselves. The 4-way data, however, is always higher than the conventional aero data while the laser anemometry measurements are generally lower. Even so, the trends observed with all three techniques as one proceeds from hub to tip are all quite similar in that there is little change from r/r_t = 0.95 to 0.80 and about a five degree rise from r/r_t = 0.80 to 0.70. The discrepancies in the DC levels with the LA and 4-way data may simply be due to alignment problems. Although alignment with respect to the translator was probably within one or two degrees, there was no direct check made on the actual angular position of the 4-way probe with respect to the rotor axis once it was mounted on the compressor casing.

In summary, time-averaged high response measurements from the 4-way probe of total and static pressure agreed quite well with conventional aero measurements. Time-averaged values of Mach number were also in good agreement with laser anemometry measurements. However, the rev-averaged high-response total pressure measurements showed that the mean level, itself, can fluctuate as much as 2 percent over a time period of the order of 10 to 20 rotor revolutions. In addition, the high-response total pressure probes, which unlike the 4-way probe are not water cooled, seemed to have problems with thermal drift which resulted in a 4 percent upward

bias in the measured level of total pressure.

Measurements of flow angle were not in very good agreement. There was about a five degree spread in the angles measured at any particular radius even among the aero probe measurements, themselves. Alignment errors resulted in 4-way measurements which were consistently higher than the aero measurements and in LA measurements which were consistently lower.

CHAPTER V

COMPARISON OF HIGH RESPONSE DATA IN THE MIT BLOWDOWN FACILITY WITH HIGH RESPONSE DATA IN THE NASA STEADY STATE FACILITY

The high response probes described in Chapter III had previously been used exclusively in the MIT Blowdown Facility. It was desirable to confirm the results with measurements taken in a conventional steady state facility. This was accomplished at the NASA Lewis Single Stage Compressor facility for the same first stage of the NASA Lewis Low-Aspect Ratio Fan that had been tested previously in the MIT Blowdown Facility [1.2]. This chapter will begin with a discussion of the differences in operation of the two facilities and the effect these differences have on the performance of the high response instrumentation. This will be followed by a comparison of data obtained in both facilities.

5.1 Blowdown vs. Steady State

The motivation behind the development of the MIT Blowdown Facility came about through the desire to provide an inexpensive method of studying compressor aerodynamics without the attendant problems of mechanical stress and high power requirements. The use of a high molecular weight gas allowed testing at the high Mach numbers required without serious stress problems. This also reduced the actual blade passing frequency which had the added benefit of improving the resolution of the high response probes. However, the facility was built with the expressed interest in studying "aerodynamic phenomena...[which] occur on the time scales of the order of or much less than the rotational period of the compressor" [1.4]. Thus the facility was scaled to provide a test time of only a few rotational periods. At the time the nature and extent of the unsteadiness exhibited in these types of flows was not well known.

Unsteady flow phenomena occuring on the time scale of the order of rotor rotation will require more than a few rotational periods to analyze their effects. Unsteady phenomena occurring on the order of blade passing will also require many rotational periods since the high response probes will not obtain an "instantaneous" snap-shot of the blade to blade flow field. In this case, the probes will act as sampling devices at a particular point in space relative to the blades. In order to examine the unsteady flow field of a particular blade passage many rotor rotations will be required since a passage can only be sampled once every rotor rotation. This problem, of course, could have been alleviated by the rather costly alternative of instrumenting the rotor at more than one circumferential location. Also a test time of a few rotational periods is not endemic to blowdown facilities in the sense that this time is only limited by the size of the supply and dump tanks.

One particular advantage of the Blowdown Facility, however, is that the flow conditions are very repeatable. This is because the initial conditions of rotor speed and supply tank pressure can be set quite precisely since at least initially they do not influence each other. This is unlike the operation of a steady state rig where both the rotor speed setting and the mass flow directly influence one another and must be constantly monitored to maintain the desired operating point.

The operating point of a steady state rig is basically set by the corrected mass flow and rotor speed. Estimates of the errors in these measurments for the NASA Lewis facilty are quite small: ±0.7 lbm/sec for mass flow and ±0.2% for rotor speed. During the tests at NASA Lewis it was possible to maintain a particular operating point to this precision as is shown below in Table 5.1, where values of the corrected mass flow and

percent corrected speed (N) have been tabulated for two typical near-design
operating points at different times during the rig operation.

TABLE 5.1: STEADY STATE RIG FLOW CONDITIONS - NASA LEWIS

Test #	ṁ (lbm/sec)	N(%)	<PR>	Time(EST)
223	74.54	99.93	1.632	12:47:59
	74.81	100.03	1.632	12:49:44
	74.94	99.99	-	12:50:11
	74.68	99.92	1.622	12:50:33
225	72.80	99.96	1.643	12:58:48
	72.63	99.94	1.634	12:59:14
	72.84	100.10	1.633	12:59:56
	73.76	100.14	1.637	00:06:19

The accuracy to which flow conditions can be re-set in the steady-
state facilities is also of importance for the fixed immersion tests since
resetting the immersion point of the probes with the high speed translators
could only be done manually. This required bringing the compressor down to
about a 50% speed point in order to be allowed into the test cell to physi-
cally re-set the immersion point. The compressor then had to be brought
back up to the desired operating point. The variability in operating
conditions due to this procedure, nevertheless, seemed to be no greater
than the variability due to the uncertainties in maintaining a particular
operating point. The difficulty with this procedure, however, was that it
was cumbersome and overly time consuming.

5.2 Blowdown Versus Steady State High Response Measurements

Several high response measurements were obtained in both the MIT
facility and the NASA Lewis facility. In order to compare the results, the
mass flow of the steady state tests was set nominally to the same value

which was calculated for the Blowdown tests (33.0 kg/sec [72.8 lbm/sec]).
This is slightly lower than the maximum performance operating point
determined by the conventional instrumentation in the Lewis facility of
33.9 kg/sec (74.7 lbm/sec). At the MIT facility the probes were traversed
from tip to hub in approximately 25 millisec, while at NASA Lewis facility
the probes were traversed to a fixed radial location where data was
obtained for 500 to 1000 millisec.

5.2.1 High Response Total Pressure Measurements

Total pressure measurements were taken at NASA Lewis and at MIT using
similar 093 high response total pressure probes. In addition, the high
response total pressure rake was used for the first time as it was
incorporated into the NASA steady state tests.

Figure 5.1a shows the total pressure ratio in a blowdown test for the
complete traverse from tip to hub. Note that the total pressure defects in
the rotor wakes are more pronounced near the hub than at the tip, while the
overall level of total pressure is nearly constant. In fact, near the tip
it is very difficult to pick out any recognizable structure which might
correspond to blade passing. Data for complete traverses in the steady
state facility was not available for the single head 093 probe, since these
tests were conducted for fixed immersions. However, time traces during the
immersion of the rake probe were available and shows similar trends as seen
in the Blowdown measurements. One such trace is shown in Fig. 5.1b for the
outer most sensor of the rake as it is traversed from the tip casing to a
fixed immersion point (r/r_t = 0.60) similar to the Blowdown test. The
corresponding immersion point for the Blowdown traverse has been noted in
Fig. 5.1a. The actual traverse time for the NASA tests is about a factor of
two times longer than the MIT tests. This coupled with the lower

rotational speed in the Blowdown tests (same corrected speed, higher molecular weight gas) accounts for the differences in the scaling of the time axes. Figure 5.1c shows the time trace for all four sensors of the rake as it emerges from the casing. It is interesting to note the similarities in the time traces of each sensor as they pass through certain characteristic regions of the flow field. In particular, the trend toward the gradual decline of the total pressure excesses near the tip to the rather substantial total pressure defects near the hub, can be seen in all four traces.

A direct comparison of the single head 093 probes can be made by comparing short time segments of the Lewis data to short time segments of the blowdown data that correspond to the fixed radial immersions of the Lewis tests. These comparisons can be seen in Figs. 5.2-5.5. In each figure the time scaling of the two upper traces is set such that six blade passings are shown. The third trace is for the Lewis test and is over a time which corresponds to approximately 68 blade passings or about 3 rotor rotations. As can be seen, the comparisons are made difficult by the fact that the rotor exit flow as seen by Lewis data has an unsteadiness which occurs over a time of many blade passings depending on the particular radial location. In each case a time segment of the Lewis data was chosen which best matches the blowdown data in terms of the magnitude of the wake defects or excesses.

In general, the DC levels of the Lewis data are about 3 to 4 percent higher than the MIT blowdown data. This is believed to be due to thermal drift problems associated with the pressure transducers in the steady state facility (see Chapter IV). The profiles of total pressure at each radial station, however, are quite similar. Near the tip, the flow seems to have

very little recognizable structure. From the longer time segement of the Lewis data, most of the wakes in the very near tip region ($R/R_t > 0.95$) seem to have an excess of total pressure which is not surprising for a rotor of this type and is due primarily to the acceleration of the wake fluid by the rotor blades to velocities higher than those of blade passage fluid. This effect is accentuated by the higher wheel speeds and relative flow angles experienced as one proceeds towards the rotor tips (see Ref. [5.1]). Thus, defects in the relative total pressure may appear as excesses of absolute total pressure, especially at higher radii. Towards the hub the defects in total pressure become more pronounced and more regular in both sets of data. High frequency fluctuations in the regions between the rotor wakes are also seen in both sets of data. These fluctuations were shown by Ng, as a result of the MIT Blowdown tests, to be due to the unsteady motion of the blade passage shock [1.3].

Power spectral densities (psd) for the four fixed immersion tests at NASA Lewis are shown in Fig. 5.6. It should be pointed out that the amplitude scaling for the psd's at the two higher radii (Figs. 5.6a and 5.6b) is ten times less than the scaling for the lower radii (Figs. 5.6c and 5.6d). In general, the psd's are dominated by the blade passing frequency (5.9 kHz) and its higher harmonics. This is especially true as one moves towards the hub. Near the tip a 8.3 kHz peak can be found along with several other minor peaks. The magnitude of these peaks, however, varies considerably depending on the particular time segment which is sampled. The 8.3 kHz peak in Fig. 5.6a has been shown at approximately its maximum amplitude. The origin of this peak is unknown at this time.

5.2.2 **Total Pressure Rake Measurements**

The results of the total pressure rake measurements at the NASA Lewis

facility will now be discussed. The rake measurements are unique in that

data was obtained simultaneously at four radial stations in the rotor exit

flow. The results are somewhat complicated in that the probe is not

traversed in the direction of the backward sweep of the rotor trailing

edge. At full immersion, the upper sensor was approximately one-half of a

rotor chord downstream of the trailing edge while the bottom sensor was

only slightly over one-quarter of a chord downstream of the trailing edge.

A short time trace of approximately 18 blade passings is shown in Fig. 5.7.

Here, similar features in the blade passage signatures can be seen at each

radius as was seen in single head probe data, however in this case the

measurements are obtained simultaneously. Figure 5.8 shows a longer

sampling of the rake data for a time of approximately 10 rotor revolutions.

No significant radial correlations on this time scale have been established

to date. Power spectral densities at the four radial locations can be seen

in Fig. 5.9. Again blade passing and its harmonics are the predominant

frequencies. There is also a large contribution of the fifth harmonic at

the 67% span location. This is seen in the time trace (see Fig. 5.7) as

the rather high-frequency jitter in the blade passage core flow and might

be due to the blade passage shock motion described earlier.

Contour plots of total pressure ratio can be formed using the rake

probe measurements and can be seen in Figs. 5.10 and 5.11 for two

successive rotor revolutions. These plots represent a spiral in time and

space as the rotor sweeps over the rake. The asterisks denote the radial

positions of each sensor. The structure is rather complex, however the 22

blade passings are easily identified by the relatively low regions of total

pressure which occur in the wakes at the lower radii near the hub. It

should be pointed out that plots of this type had heretofore required some

sort of ensemble averaging of the data in order to piece together sets of data which occurred at different times. For comparison, a rotor averaged ensemble of the total pressure ratio was calculated by averaging the profiles of each blade passage separately over 30 rotor revolutions. The results of these calculations can be seen in Fig. 5.12. Note that the immense complexity of the flow structure is almost completely lost and only small blade to blade variations remain. The plot is instructive, however, in that it shows more clearly the general structure of the flow field in particular the change in character of the wakes from distinct regions of low total pressure near the hub to relatively indistinct regions of high total pressure near the tip.

5.2.3 Flow Angle and Static Pressure Measurements

Measurements of static pressure and flow angle in the two facilities can also be compared. The 5-way sphere probe was used in the Blowdown facility while the 4-way cylindrical probe was used in the Lewis facility. Although the mean values of static pressure agree quite well, the mean flow angles do not. This is perhaps due to probe alignment errors in the Lewis tests (see Chapter IV).

Figure 5.13 shows the static pressure ratio for the complete traverse from tip to hub in the blowdown test. The static pressure variations in the rotor wakes are significant at all radii and are quite large near the hub where they are regularly 10 to 15 percent above and below the mean level and are occaisionally as low as 25 percent below the mean level. Some of these variations are undoubtedly due to probe error resulting from the presence of large transverse velocity gradients (shear flows) in the rotor wakes (see Appendix A). However, errors of this type can only account for about a 10 percent drop in the measured static pressure.

A comparison of short time segments of the blowdown data that correspond to the fixed radial immersions of the Lewis tests are shown in Figs. 5.14-5.16. As before, the upper two traces show six blade passings while the third trace shows approximately 68 blade passings of the Lewis data. Again, the comparisons are made difficult by the unsteady nature of the flow, which is observed in both sets of data. Unfortunately, the 4-way data for the immersion nearest the hub ($r/r_t = 0.58$), where the large variations of static pressure were observed in the Blowdown data, could not be reduced due to transient problems with the output of two of the sensors on the 4-way probe during that test at NASA Lewis.

Similar comparisons of the rotor exit flow angle can be seen in Figs. 5.17-5.20. Again the blade to blade features of the flow field are quite similar with deviations in the wakes which vary from 10 to 15 degrees at all radii.

The ability to sample over many rotor revolutions in the steady state facility allows for a more quantitative presentation of the fluctuations seen in the high response data. Probability density distributions (p.d.d.) can be formed by considering each data point in a given revolution to represent a particular shaft position of the rotor. The first shaft position then corresponds to the occurrence of a once-per-rev timing signal which was recorded along with the probe data. The location of the blade wakes in terms of the rotor shaft position can be found by examining a 90 revolution rotor-averaged time trace. The results of these calculations can be seen in Figs. 5.21-5.23 for measurements of total pressure, static pressure, and tangential flow angle in blade passage #1. The average wake profiles can clearly be seen in the data taken at the two lower radii. However, the data taken near the tip show no distinctive wake profile.

Probability density distributions for the lower two radii for blade passage #1 are presented in Figs. 5.24-5.32. Shaft positions corresponding to the free-stream core flow, the suction surface wake, the wake centerline, and the pressure surface wake are shown respectively. At the near tip radius, p.d.d's are presented for shaft positions corresponding to equally spaced points in blade passage #1 since no recognizable wake structure could be identified. There is very little distinction in the p.d.d's of the wakes for both measurements of pressure and flow angle. At the two lower radii the free-stream is clearly recognizable by a much narrower peaked p.d.d. representative of a more uniform flow field as opposed to the near tip radii where there is no distinctive free-stream signature in the p.d.d.

5.3 Summary

The time-resolved high response data obtained previously in the MIT Blowdown facility was confirmed by employing the same high frequency response instrumentation in a conventional steady state facility with the same compressor stage. Similar trends in total and static pressure and flow angle were observed in both sets of measurements. In particular, both sets of data exhibited the trend towards a gradual decline in the total pressure excesses seen in the rotor wakes near the tip regions to the rather substantial total pressure defects observed near the hub. The fixed immersion tests conducted in the steady state facility further confirmed the complex and unsteady nature of the rotor exit flow.

CHAPTER VI

TIME-RESOLVED TOTAL PRESSURE MEASUREMENTS
IN THREE TRANSONIC COMPRESSORS

Using the 093 high-response total pressure probe, measurements were obtained in the rotor exit flow of the three axial flow compressors operating near their respective design points. The measurements were obtained separately in each of the three facilities which have been described in Chapter II. The measurements presented for the NASA Fan and the P&WA compressor were obtained in their respective steady state facilities, while the AFAPL measurements were obtained from previous tests conducted at the MIT Blowdown Facility. There are remarkable similarities in the flow fields considering the differences in flow path, rotor performance and test operating mode. The emphasis in this work is, of course, on the unsteady nature of the flow fields.

The flow paths of the three facilities can be seen in Fig. 2.2 and Tables 2.1 and 2.2 show the relevant geometric and performance characteristics of the three compressors. The flow path of the NASA rotor has a slightly decreasing tip radius and increasing hub radius while the Air-Force-High-Through-Flow-Stage has a constant tip radius and a sharply increasing radius contour at the hub. The Pratt & Whitney rotor has a splitter plate approximately one-half of a rotor chord downstream of the rotor trailing edge. During design point operations approximately 86% of the total fan mass-flow was passed through the fan duct. As with the AFAPL stage, the tip radius is nearly constant with the change in flow area being taken up by an increasing hub radius.

One important difference among the stages is the larger overall absolute dimensions of the P&WA fan and its higher aspect ratio. The P&WA

rotor has a tip radius which is more than 50% larger than either of the other two rotors. This results in improved spatial resolution relative to the high-response probes. All three stages have similar hub to tip ratios.

Two important factors should also be noted concerning the stage geometries. They are the relative position of the stators and instrumentation ports. In the AFAPL stage, the leading edge of the stator is less than one-third of a rotor chord downstream of the trailing edge of the rotor. In fact, the instrumentation port for this stage is actually in the stator passage. On the other extreme, the stator row in the P&WA stage is more than two rotor chords downstream of the rotor trailing edge with the instrumentation port approximately one-chord upstream of the stator.

Both the NASA and P&WA rotors have design pressure ratios of about 1.6 while the AFAPL rotor has a pressure ratio of over 2.0. Most of the other flow parameters are quite similar and all three stages report efficiencies of over 90%. The AFAPL rotor has a slightly higher inlet relative Mach number at the tip and a larger fraction of the inlet relative flow is supersonic as can be seen by the lower r/r_t of the inlet sonic line. The loading distribution of the NASA rotor is nearly constant across the entire span with a slight increase towards the tip. The loading of the other two rotors ,however, changes more dramatically towards the tip region, increasing by about 10 percent for the AFAPL rotor and decreasing by about 20 percent for the P&WA rotor.

In the NASA tests the probe was held at a fixed radius for a period of about 500 millisec. In the P&WA tests the probe was traversed from the casing to a point 4.0" from the rotor tip where it was held for another 300 millisec before being withdrawn into the casing. In the MIT Blowdown tests the probe was traversed from the tip to an r/r_t of about 0.65 in about 130

millisec. The time history of the two traverses can be seen in Fig. 6.1.

The comparison of the test results was made for streamlines which coincide with similar inlet/leading edge relative Mach numbers. The location of the streamlines have been obtained from the results of conventional streamline curvature analyses. Table 6.1 shows the relative position in the three rotors at the four inlet relative Mach numbers corresponding to the fixed immersion tests conducted at NASA Lewis and at an additional Mach number of 1.14. Figures 6.2-6.6 show the instantaneous time traces of the total pressure ratios for these comparisons. The time scales have been adjusted so that approximately six blade passings are shown for each rotor. Also, some of the fine structure observed in the blade passage flow (as opposed to the wake flow) in the NASA and P&WA data does not appear as sharply defined in the AFAPL data due primarily to the lower sampling rate (100 kHZ). In general, the comparisons are similar at the lower radii in that large variations exist from blade to blade in the total pressure defect for all three rotors. These defects presumably occur in the blade wakes. Near the tip regions, however, for the streamlines coresponding to an inlet relative Mach number of 1.34, the blade to blade total pressure ratio of the NASA rotor has significant, excesses of total pressure in what appears to be the blade wakes, while the other two rotors have total pressure defects similar to the lower radii.

A simple wake model which assumes uniform static pressure and relative flow angle across the wake [5.1], predicts that the wakes may have an excess or a deficiency of total pressure, depending on the relative flow angle and the velocity defect in the following manner,

$$\sin\beta_{rel} - \left(\frac{v_{rel}}{2\omega r}\right)\left(1 + \frac{v_{wake}}{v_{rel}}\right) \tag{6.1}$$

where,

β_{rel} = rotor exit relative flow angle

ω = rotor angular speed

r = radius

v_{rel} = blade passage velocity relative to the rotor

v_{wake} = wake velocity relative to the rotor

Using the mean circumferentially averaged flow angles and velocities, the model predicts total pressure excesses in the wakes for all three rotors regardless of the size of the velocity defect which is contrary to the measurements taken in both the AFAPL and P&WA rotors. As will be shown in Chapter VII, a much more complex structure is needed to explain the measurements obtained in the rotor blade wakes.

Figures 6.7-6.11 show the power spectral densities for the corresponding inlet relative Mach numbers. The dominant frequency in all cases is blade passing which ranges from 5.69 kHz for the NASA rotor to 4.69 kHz for the AFAPL rotor.

A comparison of the total pressure ratios over a longer time period can be seen in Fig. 6.12 for the NASA rotor at the streamline corresponding to an inlet Mach number of 1.03 and the P&WA rotor at an inlet Mach number of 1.14. These time traces correspond to a time period of approximately 5 rotor rotations. Except for the DC levels the two time traces are nearly indistinguishable. The power spectral density for these traces can be seen in Fig. 6.13 which shows that the frequency content of both signals occurs almost entirely around blade passing and its harmonics.

Summary

Total pressure measurements were obtained in the rotor exit flows of three high-speed compressors. The compressors are similar in that they are all highly loaded, highly efficient, and transonic. The NASA fan was designed for high efficiency with low-aspect ratio blading as was the AFAPL rotor, although it was designed primarily for high through flow. On the other hand, the P&WA fan was designed as a highly efficient first stage rotor of a more conventional split-flow commercial fan with relatively high-aspect ratio blading. The measurements showed that all three rotors exhibited a high degree of unsteadiness especially in the rotor wakes where defects and/or excesses in total pressure may vary from 5 to 15 percent of the mean level from blade to blade.

CHAPTER VII

ROTOR BLADE VORTEX SHEDDING

7.1 Background: Vortex Shedding In Wake Flows

It is well known that bodies with blunt trailing edges can shed a
regular array of vortices due to intermittent separation of the surface
boundary layers at the trailing edge. Vortex streets have also been
documented in the wakes behind flat plates and airfoils with blunt trailing
edges, both isolated and in cascade. They have been observed through the
transonic region and at Reynolds numbers typical of gas turbine operation.
Techniques include high speed flow visualization, spectral analysis of hot
wire signals, and probabililty density measurements from laser anemometers.
Studies of the shedding from airfoils with sharp trailing edges typical of
fan and compressor blading are somewhat ambiguous, some showing shedding,
some not.

Vortex shedding downstream of the trailing edge of a flat plate has
been reported by several investigators. Heinemann, Lawaczeck,and Butefisch
[7.1] were able to photograph vortex streets in the wake flow behind
isolated flat plates using a high-speed Schlieren system for Mach numbers
up to 0.84. A flow visualization study by Greenway and Wood [7.4] showed
vortex shedding in the wake of a flat plate with both blunt and sharply
bevelled trailing edges. More recently, while attempting to simulate the
trailing edge flow field of an axial compressor, Paterson and Weingold
[7.2] observed vortex shedding from the trailing edge of a flat plate which
was 3.36 meters long and 2.54 cm thick at a free stream velocity of 33
m/sec. Vortex shedding was indicated by spectral analysis of hot wire
measurements and by bimodal probability density distributions of laser
anemometer measurements obtained in the wake at a point three plate

thicknesses downstream of the trailing edge. In a recent report by Xing and Marenbach [7.3], regular arrays of vortex streets downstream of an isolated flat plate were observed in Mach-Zender interferograms at Mach numbers of up to 2.2.

Other investigators have observed vortex shedding in various cascade flows representing both turbine and compressor blade profiles. Schlieren photographs taken by Heinemann and Butefisch [7.5] of the flow through various transonic and supersonic turbine cascades, clearly show the presence of vortex streets in the blade wakes. Trailing edge thicknesses of the cascade blades varied from 0.8 to 5 percent chord and Reynolds numbers based on the trailing edge diameter varied from 0.3×10^4 to 1.6×10^5 Strouhal numbers were found to lie within a range of 0.2 to 0.4. In another report, Bryanston-Cross [7.6] were able to visualize vortex streets downstream of a supersonic cascade using holographic interferometry. Young, et al. [7.7] found a vortex street downstream of a subsonic airfoil operating at high angle of attack. Vortex shedding has also been observed by Dunker [7.8] in the rotor wakes of an actual transonic compressor operating at design speed. Using a laser velocimeter, Dunker was able to distinguish vortex-like structures from measurements taken in the rotor wakes for three different mass flow rates.

The parameters which have been used in the above investigations to determine the likelihood of vortex shedding, are presented in Table 7.1 along with the corresponding parameters for the fan and compressor rotor blades tested in the present investigation. The blade Reynolds numbers are based on the mean relative velocity at the trailing edge plane and the Strouhal numbers for the plates and cascades are based on the geometric trailing edge thickness as reported by each investigator. A boundary layer

displacement or momentum thickness is not included.

Two parameters which might be important in determining whether or not vortex shedding will occur are the Reynolds number based on the airfoil or flat plate chord and the trailing edge thickness as a percentage of chord. These parameters act jointly in affecting what would seem to be the significant flow parameter, which is the relationship between the size and spacing of the separating shear layers as represented by the ratio of the trailing edge thickness to the boundary layer thickness. To the degree that the boundary layer thickness is proportional to the blade chord, the relevant parameter might be the trailing edge thickness-to-chord ratio. One might think then that as this ratio approaches zero, the blade wake would be formed by the mixing of the two surface shear layers into an uncorrelated turbulent wake with no vortex shedding. The flow visualization study of Greenway and Wood [7.4] demonstrated that this is not necessarily the case.

Greenway and Wood conducted a series of experiments using a wind tunnel and a flow visualization technique in a towing tank to investigate reducing vortex induced vibrations by means of bevelled trailing edges. While Reynolds numbers of comparable magnitude to the current investigation were achieved, Mach numbers were quite low (<0.1). However, several important conclusions were obtained. First, the use of microphones in the wind tunnel experiments to record the resonant vibrations induced by the shedding resulted in the false conclusion that the trailing edge bevel reduced the intensity of the vortex shedding. As the trailing edge angle was reduced, there was an apparent progressive reduction of intensity until, for trailing edge angles below 30 degrees there was no significant resonance remaining. The reason for this was that as the trailing edge

angle was reduced the shedding became more and more intermittent. This was clearly seen in the flow visualization experiments.

> "A sequence of five or six vortices could often be seen in an apparently normal array, but these periods of regular shedding were increasingly interspersed with intervals of uncorrelated flow in which no distinct vortices were seen....Unfortunately, the intervals of regular shedding were not sufficiently long for reliable frequency measurements to be made." [7.4]

This result may also explain why Hobbs, et al. [7.9] were unable to detect vortex shedding in a cascade of conventional multiple circular arc airfoils with a trailing edge thickness-to-chord ratio of 0.0056.

The second conclusion from the Greenway and Wood experiments was that the trailing edge bevel produced no measureable reduction in strength of the vortex shedding, only growing intermittency. This has important consequences for high speed measurements in turbomachinery in the sense that while vortex shedding may be an important component of the wake flow, it may appear only intermittantly separated in time by periods of uncorrelated turbulent flow.

From Table 7.1 it appears that vortex shedding frequencies generally correspond to a Strouhal number in the range of 0.2-0.3. If the Strouhal number is based on the blade trailing-edge thickness, then, for the current rotor blades, the shedding frequencies corresponding to a Strouhal number of 0.2 would be greater than 50 kHz, which is nearly ten times the blade passing frequency. In the previous investigations, the flow-fields consisted of favorable or in the case of the flat plates, neutral pressure gradients. The present work, however, deals with the unfavorable pressure gradient of a compressor blade row. It seems more likely that the proper Strouhal number to be used in this case should include a measure of the blade's boundary layer thickness, an estimate which can be made by following

the approach of Koch and Smith [7.10]. A momentum thickness-to-chord ratio of 0.02 would result in shedding frequencies in the range of 15 kHz to 25 kHz which is only three or four times the blade passing frequency.

7.2 Experimental Observations

Previous analyses of LA measurements of the NASA rotor presented in [7.11] and [7.12] indicate that the presence of moving vortices is clearly manifested in LA measurements by the existence of a bi-modal velocity probability distribution (p.d.d.). In order to further investigate the possibility of vortex shedding in the rotor blade wake, LA measurements were therefore acquired simultaneously with the 4-way probe experiments at NASA Lewis.

At each radius investigated, an LA run was made at the pitchwise-averaged flow angle, β_{av}, determined from earlier LA measurements. Figure 7.1 is the mean velocity distribution measured during an LA run made at aero-survey station 2 at 60% span and 140% chord at an angle, β_{av}, of 42 degrees. The mean velocity distribution is obtained by averaging together the velocity distributions in each of the 17 measured blade passages. The probability density distributions of the measurements at points labelled A-F in Fig. 7.1 are shown in Fig. 7.2. In each case the abscissa is the number of velocity measurements which occurred within a velocity "bin" which is 5 ft/sec wide. The ordinate is the center velocity of each "bin". The mean velocities determined from these p.d.d.'s form the time-averaged velocity distribution of Fig. 7.1. In the region outside of the wake (points A and F), the p.d.d. is single-valued. The most probable velocity always occurs in the bin centered at 770 ft/sec. In the edges of the wake (points B and E), the probability of velocities in the range of 600-650 ft/sec begins to rise. At the center of the wake (points C and D), the

probability of velocities centered at these low levels reaches a maximum. However, a significant number of velocity measurements still occur at the free stream level of 770 ft/sec.

Analysis of the 4-way probe measurements also indicate the presence of a vortex street in the blade wakes. While it is clear that the presence of a vortex street could be verified by measurements from a probe of sufficiently high frequency response which is rotating with the rotor, the probes used in the present investigation are all stationary in space. The detection of a vortex street by a stationary probe requires some careful consideration. The wake width measured by the 4-way probe and LA varies between 20 and 50% of blade pitch depending on the compressor operating condition. One would therefore expect that at least one or two vortices would be shed in the time corresponding to the rotor wake moving circumferentially over a stationary probe. However, it is the probe's trajectory relative to the vortex street which determines the ease at which the structure can be resolved. The more skewed the trajectory, in either direction, the greater the number of vortices passing over the probe. Fortunately, for the case considered here, the probe trajectory is nearly normal to the mean relative flow direction, which is the direction at which the street is convected downstream. The probe will then see a thin slice of the street, all of which is at the same relative position in the street each time the wake passes over the probe. The relative positions which are actually sampled will then depend on the phasing of the shedding from blade to blade.

Before actual time traces of the flow quantities measured by the 4-way probe are presented, it is instructive to examine what might be expected from such measurements. The conventional approach [5.1] has been to

represent the rotor wakes as regions of uniform static pressure with a velocity defect relative to an inviscid blade passage flow in the same direction as the blade passage flow. This can be seen in Fig. 7.3a. The velocity triangle shows that the flow angle measured in the absolute (laboratory) frame will be larger in the wake while the absolute velocity in the wake can be either larger or smaller depending on the geometry of the flow and the magnitude of the velocity defect. On the other hand, if the wake flow is structured as a vortex street, then both the relative flow angle and static pressure will vary through the wake region. A schematic of this flow is shown in Fig. 7.3b. As can be seen, changes in the relative flow angle do not necessarily appear as changes in the absolute flow angle and instead may appear as changes in the absolute velocity.

Time traces of various quantities measured by the 4-way probe at the same axial station and spanwise location as the LA measurements presented above, can be seen in Figs. 7.4-7.6 for an elapsed time corresponding to slightly more than one rotor revolution (time for one rev = 3.87 ms). In each figure, the upper trace is the "instantaneous" measurement and the lower trace is a 90 rotor revolution blade by blade ensemble average. The ensemble averaged component of velocity corresponding to the LA velocity measurements is in fact quite similar to the LA data in that both sets of data show relatively small blade to blade variations probably attributable to geometric differences. The "instantaneous" measurements, however, show enormous fluctuations, especially in the blade wakes which vary considerably from one blade passage to the next. Three distinctive features of the blade wakes can be noted. First, the level of the measured velocity component within the wakes is sometimes above the mean level. Second, the static pressure is not only highly variable in the blade wakes but in most

instances is considerably below the mean, and third, there are enormous variations of the relative flow angle in the regions which correspond to the blade wakes. Deviations of up to ±20 degrees from the mean can be seen from one blade passage to another. Such variations in the wake signature are likely to result from the probe sampling the passage of the periodic vortex street in the wake as it is convected past the stationary probe.

The probe data has also been analyzed to derive the velocity distributions corresponding to those from the LA measurements and shows similar trends. The location of the blade wakes can be obtained by examining the time trace of the component of velocity which lies 42 degrees from the axial direction (i.e., the velocity component measured by the LA). This can be seen in Fig. 7.7 for a time period of slightly more than one-blade passing. The upper trace is the instantaneous velocity distribution across blade passage #1, which is defined as the first blade passage which occurs after the passage of a once-per-rev timing mark on the rotor disk. The lower trace is the rotor-averaged velocity distribution across blade passage #1 which has been calculated by averaging the instantaneous distributions of each blade passage measured over 90 consecutive rotor revolutions. The points labeled A-F correspond to similarly labeled points in the LA data of Fig. 7.1. These points have been located on the probe data by setting point C at the bottom of the wake and locating the remaining points at the proper pitch-wise locations relative to point C.

Probability density distributions can be formed for the probe data by considering the digitized data which occurs at points A-F for each rotor revolution. Performing this process on the data acquired during 90 consecutive rotor revolutions yields the p.d.d.'s shown in Figs. 7.8 and 7.9 for the component of absolute velocity measured by the 4-way probe

which corresponds to the component measured by the LA. Figure 7.8 represents the p.d.d. for the corresponding points A-F in all 22 blade passages, while Fig. 7.9 represents the p.d.d. for only blade passage #1. Due to the lower spatial resolution of the 4-way probe the bi-modal p.d.d. at the wake centerline is not as pronounced as the LA p.d.d., yet there is clearly a wider range of velocities which occur in the wake than in the blade passage flow. The p.d.d.'s at additional pitchwise locations within the wake show a gradual increase in the width of the p.d.d. as one moves from the wake edges toward the center of the wake. More importantly, both the LA and 4-way p.d.d.'s at points C and D indicate that the flow at points near the wake centerline actually spend little time at the time-averaged velocity level.

7.3 Rotor-Blade Wake Model

It is proposed that the rotor blade wakes be modeled as modified ideal Karman vortex streets consisting of two staggered rectilinear rows of Rankine vortices of opposite sign in a uniform free stream. The addition of finite-size vortex cores to the classical potential flow analysis of point vortices is considered a more realistic assumption, since it avoids infinite velocities at the vortex centers and also allows for smoothly varying averaged wake profiles as seen in the experimental data. From this model it will be possible to obtain a simplified picture of the unsteady flow field. Of particular interest will be the predictions of flow angle deviations, static pressure defects, and velocity distributions within the street. By performing the analysis in the reference frame moving with the vortex cores, the use of the unsteady Bernoulli equation is avoided, thus greatly simplifying the calculations of the pressure field. A simple coordinate transformation is then all that is necessary to compute the flow

field as would be seen by a stationary probe.

In order to determine the relevant parameters for this flow model, it is useful to examine the flow field of an isolated Rankine vortex. The flow field of an isolated vortex can be divided into two regions: an inner region consisting of a forced vortex flow and an outer region consisting of free-vortex potential flow. The boundary between these two regions is denoted as the core radius, r_o. In the vortex core the tangential velocity varies linearly with distance from the center of the vortex as follows,

$$r < r_o \quad : \quad v = r\omega_o \tag{7.1}$$

where, ω_o, is the angular velocity at the vortex core, $r = r_o$,

$$\omega_o = k/(2\pi r_o^2) \tag{7.2}$$

and, k, is the vortex strength. In the outer region the tangential velocity is then,

$$r > r_o \quad : \quad v = (\omega_o r_o^2)/r \tag{7.3}$$

The pressure in the outer region of an isolated vortex can be found by using the Bernoulli equation in the frame of reference moving with the vortex. In this frame the free-stream velocity is exactly zero and so the static pressure is then simply,

$$P = P_\infty - \tfrac{1}{2}\rho q^2 \tag{7.4}$$

The pressure drop from the free stream to the edge of the vortex core is then related to the velocity at the edge of the core, q_o, which from Eq. (7.1) or (7.3) is equal to $\omega_o r_o$. This velocity will be denoted as the pressure-defect-velocity, U_p, and will be used to non-dimensionalize the equations which describe flow field of the full vortex street.

$$U_p = \omega_o r_o$$

The velocities in the inner and outer regions can then be written as follows:

$$r > r_o \quad : \quad v = U_p(r/r_o) \tag{7.5}$$

$$r < r_o \quad : \quad v = U_p(r_o/r) \tag{7.6}$$

The pressure-defect-velocity can also be expressed in terms of the vortex strength, k, from Eq. (7.2),

$$U_p = k/(2\pi r_o) \tag{7.7}$$

The ratio of the pressure-defect velocity to the free-stream velocity is also a useful input parameter to the model to set the strength of the vortex street.

The flow field of the full vortex street is modeled by summing the contributions of two staggered rows of Rankine vortices of opposite sign of the type described above. Following Lamb [7.1], the complex velocity of a single infinite row of equally spaced vortices of strength, k, and spaced apart by a distance, a, can be written as,

$$w(z) = \frac{-ik}{2a} \cot \frac{\pi z}{a} \tag{7.8}$$

where

$$w(z) = u'' - iv''$$

and,

$$z = x'' + iy''$$

as shown in Fig. 7.10. Here the (x'',y'') frame moves with the vortex cores and is fixed to the center of a vortex in either the upper or lower row. In this frame the velocity components parallel and perpendicular to the direction of motion of the vortices are u'' and v'' respectively. The (x',y') frame also moves with the vortex cores but is positioned at the centerline between the two rows of vortices. A third reference frame, (x,y), is fixed to the rotor blade trailing edge. The velocity components in the (x',y') and (x,y) frames are (u',v') and (u,v) respectively.

These components are then non-dimensionalized with respect to the

pressure-defect velocity, U_p, and all lengths are expressed with respect to the vortex spacing, a. The equations describing the velocity components of a single isolated row in the (x'', y'') frame are then,

$$\bar{u}'' = -\bar{k} \frac{\sinh(2\pi \bar{y}'')}{\cosh(2\pi \bar{y}'') - \cos(2\pi \bar{x}'')} \tag{7.9a}$$

$$\bar{v}'' = \bar{k} \frac{\sin(2\pi \bar{x}'')}{\cosh(2\pi \bar{y}'') - \cos(2\pi \bar{x}'')} \tag{7.9b}$$

where,

$$\bar{u}'' = u''/U_p \qquad\qquad \bar{v}'' = v''/U_p$$

$$\bar{x}'' = x''/a \qquad\qquad \bar{y}'' = y''/a$$

and,

$$\bar{k} = k/(2aU_p)$$

In order to ensure that the velocity decays smoothly from the edge of the vortex core to the center, the velocity in the core is obtained by subtracting the contributions of an isolated potential vortex from the velocity field of the row of vortices and adding the contributions of an isolated viscous core. The velocity components in a vortex core of positive circulation are then,

$$\bar{u}'' = [\bar{u}_{row} - \bar{u}_{pot}] + \bar{u}_{core} \tag{7.10a}$$

$$\bar{v}'' = [\bar{v}_{row} - \bar{v}_{pot}] + \bar{v}_{core} \tag{7.10b}$$

where,

$$\bar{u}_{pot} = -\left(\frac{\bar{r}_o}{\bar{r}}\right)\left(\frac{\bar{y}''}{\bar{r}}\right) \qquad\qquad \bar{u}_{core} = -\left(\frac{\bar{y}''}{\bar{r}_o}\right)$$

$$\overline{v}_{pot} = \left(\frac{\overline{r}_o}{\overline{r}}\right)\left(\frac{(\overline{x}'')_{min}}{\overline{r}}\right) \qquad \overline{v}_{core} = \left(\frac{(\overline{x}'')_{min}}{\overline{r}_o}\right)$$

Here $(x'')_{min}$ is the axial distance to the center of the nearest vortex core. For a vortex core of negative circulation the direction of the contributions due to the isolated vortex must be reversed.

The flow field of the complete vortex street is then found by summing the velocity components of two isolated rows spaced a distance, h, apart and staggered by a distance of one-half the vortex spacing, a/2. In this system the circulation of the upper row is defined to be negative (-k) and the circulation of the lower row is defined to be positive (+k).

Each row induces a motion in the opposite row which results in the motion of the entire vortex street. This motion is found by solving for the velocity induced at the center of a vortex by the opposing row and is called the induced velocity, U_i.

$$U_i = \frac{-k}{2a} \tanh\left(\pi \frac{h}{a}\right) \tag{7.11}$$

If the vortex street is formed in a free-stream of velocity, U_∞, then in the frame of reference fixed to the blades (x,y) the vortex-street moves with velocity, U_s, where,

$$U_s = U_\infty + U_i \tag{7.12}$$

In the frame moving with the vortex centers (x',y'), the free-stream velocity is simply $(-U_i)$. The velocity components in the primed frame are then,

$$u' = u_{upper} + u_{lower} - U_i \tag{7.13a}$$

$$v' = v_{upper} + v_{lower} \tag{7.13b}$$

Given a location in the (x',y') frame the upper and lower velocity components can be calculated by a simple coordinate transformation. For the upper row,

$$\bar{x}'' = \bar{x}' - 1/2$$

$$\bar{y}'' = \bar{y}' - h/2a$$

and for the lower row,

$$\bar{x}'' = \bar{x}'$$

$$\bar{y}'' = \bar{y}' + h/2a$$

The velocity, q', is then,

$$q' = \sqrt{(u')^2 + (v')^2} \qquad (7.14)$$

Since the vortex cores move at a velocity of $(U_\infty + U_i)$, the lateral and transverse velocity components in the frame relative to the rotor blades are then,

$$u_{rel} = u' + (U_\infty + U_i) \qquad (7.15a)$$

$$v_{rel} = v' \qquad (7.15b)$$

The relative velocity is simply,

$$q_{rel} = \sqrt{(u_{rel})^2 + (v_{rel})^2} \qquad (7.16)$$

(Note: $(q_{rel})_\infty = U_\infty$.)

To facilitate the fit of the model to the measurements, the velocity components predicted by the vortex model are translated from the blade relative frame to the stationary laboratory frame in a straightfoward coordinate transformation using the velocity triangle shown in Fig. 7.11 with the measured wheel speed (U) and the average exit angle $(\beta_{rel})_\infty$.

Pressure Coefficient

In the frame of reference moving with the vortices (x',y') the flow is

steady and the free-stream velocity is equal to $(-U_i)$. For the cases of interest considered here, it is sufficient to assume constant density, since the maximum Mach number in this frame of reference is approximately 0.10. Bernoulli's equation can then be written as follows,

$$P_\infty + \tfrac{1}{2}\rho_\infty U_i^2 = P(x',y') + \tfrac{1}{2}\rho_\infty (q')^2 \tag{7.17}$$

The pressure coefficient based on the pressure-defect velocity is then defined as follows,

$$\overline{C}_p \equiv \frac{P - P_\infty}{\rho_\infty U_p^2} \tag{7.18}$$

For those regions outside of a vortex core,

$$r > r_0$$

$$\overline{C}_p = -\tfrac{1}{2} (\overline{q}')^2 - \overline{U}_i^2 \tag{7.19}$$

To solve for the pressure in a vortex core, the radial momentum equation is integrated across the core. Assuming radial symmetry for the moment, the radial momentum equation can be expressed as follows,

$$\frac{\partial p}{\partial r} = \rho \left(\frac{q_0^2}{r_0}\right)\left(\frac{r}{r_0}\right) \tag{7.20}$$

which can be integrated to obtain,

$$P(r) = \tfrac{1}{2} \rho q_0^2 \left(\frac{r}{r_0}\right)^2 + P(0) \tag{7.21}$$

Here, q_0 is the velocity at the edge of the vortex core $(r = r_0)$. For an isolated vortex this would simply be equal to the pressure-defect-velocity, $Up = \omega_0 r_0$, but in the actual case of a double row of vortices, q_0 will vary around the circumference of the core. In order to account for this the expression in (7.21) will be modified by introducing the average of the

square of the velocity along the circumference, $\langle q_0^2 \rangle$, and rewriting (7.21) as follows:

$$r < r_o$$

$$P(r,\theta) = \frac{1}{2} \rho \left(\frac{r}{r_o}\right)^2 [2\langle q_0^2 \rangle - q_0^2(\theta)] + P(0) \tag{7.22}$$

If this expression is then averaged around the circumference at $r = r_o$, the pressure at the center of the vortex, $P(0)$ can be eliminated, by matching the values at $r = r_o$ from Eq. (7.21).

$$P(0) = P_\infty - \rho\langle q_0^2 \rangle + \frac{1}{2} \rho U_i^2 \tag{7.23}$$

By substituting Eq. (7.23) into the modified pressure equation (7.22), the expression for the pressure coefficient, C_p, can be obtained.

$$r < r_o$$

$$\bar{C}_p = -\frac{1}{2}\overline{q_0^2}\left[2 - \left(\frac{r}{r_o}\right)^2\left(2 - \frac{\overline{q_0^2}}{\langle \overline{q_0^2} \rangle}\right)\right] + \frac{\overline{U}_i^2}{2} \tag{7.24}$$

The average of the velocity squared at the vortex core, $r = r_o$, can be found numerically given the vortex street geometry. For a typical Von-Karman-like street ($h/a = 0.28$) with a core-radius ratio of 0.5, $\langle q_0^2 \rangle$ is nearly equal to unity (1.002). For values of $r < r_o$, q_0 is evaluated at a point on the circumference ($r = r_o$) where a ray from the center of the vortex through the point in question intersects the edge of the core at $r = r_o$.

Vortex-Street Temperature Distribution

As with the calculation of static pressure, the calculation of total temperature in the vortex street is greatly simplified by examining the flow in the frame of reference moving with the vortices (x',y'). In this

frame the flow is steady. For the fluid outside the vortex cores, the flow

is irrotational as well, and so it can be assumed that both the total

temperature, Tt_{vor}, and entropy are constant. The static temperature can

then be found from the velocity field as follows,

$$r > r_o$$

$$Ts = Tt_{vor} - (q')^2/(2CP) \tag{7.25}$$

where CP is the specific heat at constant pressure. Ttvor can be expressed

in terms of the total temperature in the frame fixed to the blade row,

Tt_{rel}, by equating the expressions for static temperature in the free-stream.

In the frame moving with the vortices the free-stream velocity is $(-U_i)$

while in the frame fixed to the blade row the free-stream velocity is equal

to U_∞, and thus,

$$Tt_{vor} = Tt_{rel} + (U_i^2 - U_\infty^2)/(2CP) \tag{7.26}$$

Since the vortex cores are modeled as having a solid-body velocity distri-

bution, there are no shear stresses in the core. Futhermore, since the

flow is steady in the frame moving with the vortices, the energy equation

is satisfied by a constant static temperature distribution. This assumption

is strictly valid only for a circular core in which their are no radial

velocities. The value of static temperature in the core is then set to

match the value at the edge of the core from the above calculations.

$$Ts(r_o) = Tt_{vor} - (q_o)^2/(2CP) \tag{7.27}$$

In order to account for the circumferential variations around the

circumference of the core, the averaged circumferential velocity, $\langle q_o^2 \rangle$,

is used in a similar manner to that employed for the calculation of static

pressure in the vortex cores. This results in the following expression for

the static temperature distribution in the vortex cores.

$$r < r_o$$

$$Ts = Tt_{vor} - \left[<q_o^2> + (r/r_o)\left\{(q')^2 - <q_o^2>\right\} \right]/(2CP) \qquad (7.28)$$

Once the static temperature has been calculated, it is a relatively simple matter to calculate the total temperature in the frame fixed to the rotor blades, including the vortex cores, since the velocity field is already known. The expression for "relative" total temperature is thus,

$$Tt_{rel} = Ts + q^2_{rel}/(2CP) \qquad (7.29)$$

The relative total pressure can now be formulated without the restriction of incompressibilty, and is expressed as follows,

$$Pt_{rel} = Ps\left[1-q^2_{rel}/(2CPTt_{rel})\right]^{[-\gamma/(\gamma-1)]} \qquad (7.30)$$

A relative total pressure coefficient can then be defined,

$$Cp_{t_{rel}} = (Pt_{rel}-P_\infty)/\left[\tfrac{1}{2}\,\rho U_\infty^2\right] \qquad (7.31)$$

7.4 Fitting the Wake Vortex Model to the Experimental Data

The wake model described above is quite general. In order to represent the wakes of actual rotor blades, it is necessary to specify or set the parameters which determine the geometry and strength of the vortex street. The resulting flow-field can then be compared to the experimental data of both the LA and 4-way probe. The geometry of the vortex street is specified by the lateral spacing ratio, h/a, and the core-radius ratio, r_o/h, while the strength of the vortices is related to the ratio of the pressure-defect velocity to the free-stream velocity, U_p/U_∞. Since these quantities were not measured directly they must be inferred from the experimental data.

Little in the way of quantitative data concerning the parameters which characterize the vortex street is available in the literature for geometries other than right circular cylinders. The extensive testing of turbine cascades by Heinemann and Butefisch [7.5] was concerned only with the determination of the vortex shedding frequency, which was correlated in terms of a Strouhal number based on the trailing edge thickness. Such a Strouhal number is not a useful parameter in determining the size and strength of the vortex street since small changes in Strouhal number result in a large changes in the vorticity for a given spacing ratio, h/a. Also it is not clear at this time if the blade trailing edge thickness is the proper length to use in computing the Strouhal number for the case of a highly loaded compressor blade.

A comprehensive overview of the available data for vortex shedding on circular cylinders has been presented by Chen [7.14]. A wide range of Reynolds numbers ,based on the cylinder diameter, is investigated up to 10^7. A "universal wake number" is introduced which seems to be valid over the entire range of Reynolds numbers and is presented here in the following form,

$$ C = \frac{\left(\frac{h}{a}\right)^2}{2} \left[\frac{1}{\pi \frac{h}{a} (r_o/h)(U_p/U_\infty)} - \tanh\pi \frac{h}{a} \right] \qquad (7.32) $$

Chen found the value of the constant, C, to be 0.172 for highly turbulent flows and 0.165 for flows with low free-stream turbulence. As will be shown a considerably larger value is obtained for the rotor blade wakes investigated here.

Without the "classical" experimental data as a guide, the following procedure was adopted to set the vortex street in the blade wake. A

core-radius ratio, r_o/h, and vortex strength, k, were chosen in order to match the shape and depth of average wake profile as measured by the LA. The spacing ratio was then chosen such that the probability density distribution of the velocity at the wake centerline approximates the bi-modal distribution measured by the LA. This was accomplished by matching both the upper and lower most-probable velocities.

The core-radius must be chosen so that the averaged velocity profile of the vortex street resembles a smooth wake-like profile of the type observed in both the LA and 4-way probe data. If the core-radius is considerably smaller than the spacing between the two rows of vortices ($r_o/h \ll 1$) then the averaged velocity profile across the wake will have a uniform defect. This is shown in Fig. 7.12a for a typical Von-Karman vortex street with $h/a = 0.2806$ and $r_o/h = 0.25$. The average of the transverse component of velocity is also shown which is exactly zero throughout the entire street. In order to match the averaged experimental velocity profiles, the core-radius, r_o, must be at least one-half the vortex spacing, h. For $r_o/h = 0.5$, the edge of the vortex cores on both the upper and lower rows of the street coincide with the wake centerline. Several investigations designed to measure the core size have shown that in the fully developed region of the street, the core-radius ratio may in some cases exceed 1.0. Griffin and Ramberg [7.15] reported core-radius ratios exceeding 1.0 in flows past vibrating cylinders. Schaefer and Eskinazi [7.16] reported core-radius ratios of between 0.50 and 0.86 in what is described as a stable region of "periodic regularity" behind the cylinder. The formation and extent of this region was found to be a function of the Reynolds number based on the cylinder diameter. For purposes of this study a core-radius ratio of 0.5 will be used. This will result in an averaged

wake profile of the type as shown in Fig. 7.12b.

Since the actual size of the wake, which will be denoted as W, is determined by the extent of the vortex cores, it can be expressed as a function of the vortex spacing, h, and the core radius, r_o.

$$W = h[1 + 2(r_o/h)] \tag{7.33}$$

For r_o/h equal to 0.5, h is exactly one-half the wake width.

The experimental data for the vortex spacing ratio, h/a, in flows behind circular cylinders, show a large spread with respect to Karman's stability critieria of 0.2806. Chen [7.14] was not able to find any sound correlations. Griffin and Ramberg [7.17] found the vortex spacing ratio for a stationary cylinder to be 0.180 for Reynolds numbers of 144 and 450, while Schaefer and Eskinazi[7.16] found values which ranged from 0.06 to 0.31 for Reynolds numbers from 62 to 118.

In order to choose the spacing and vortex strength by matching the LA velocity profiles and p.d.d.'s, the velocities predicted by the wake model must be corrected, since the LA measures only the component of the absolute velocity which is normal to its fringe orientation. Since the model of the vortex street is presented in the frame of reference relative to the rotating blade row, the velocity components must be transformed into the absolute frame where the "measured" component can be calculated. The relevant velocity triangle for this purpose can be seen in Fig. 7.11. Here the free-stream velocity of the vortex street, U_∞, is taken to be the mean relative velocity outside the blade wake, $\langle q_{rel} \rangle$, and the street is taken to be aligned with the free-stream relative flow angle, $(\beta_{rel})_\infty$. The relative velocity in the vortex street is found by adding the free-stream velocity to the velocity components induced by the street as described in Eqs. (4.15-4.16). The relative flow angle, β_{rel}, is found by adding the

flow angle deviations induced by the vortices to the free-stream flow angle, $(\beta_{rel})_\infty$, as follows,

$$\beta_{rel} = (\beta_{rel})_\infty + \arctan(v_{rel}/u_{rel}) \tag{7.34a}$$

The axial component of the absolute velocity, V_z, is found from the velocity triangle in Fig. 7.11,

$$V_z = q_{rel}\cos(\beta_{rel}) \tag{7.34b}$$

and given the rotor wheel speed, U, the absolute velocity can be calculated from the following relation,

$$q_{abs} = \sqrt{\left(v_z^2 + \left(U - q_{rel}\sin(\beta_{rel})\right)\right)} \tag{7.34c}$$

Finally, the actual velocity measured by the LA is,

$$V_{meas} = q_{abs}\cos(\beta_{abs} - \beta_{\ell fa}) \tag{7.35}$$

where,

$$\beta_{abs} = \arccos(V_z/q_{abs})$$

and $\beta_{\ell fa}$ is the angle normal to the orientation of the LA fringes.

For the test case being considered here, the mean measured velocity can be obtained from the LA's averaged absolute velocity profile (see Fig. 7.1), from which it is found that,

$$\langle V_{meas}\rangle = 770 \text{ ft/sec}$$

With a laser fringe orientation angle, $\beta_{\ell fa}$, of 42 degrees and an absolute free-stream flow angle, $(\beta_{abs})_\infty$, of 45 degrees, the mean absolute velocity, $\langle q_{abs}\rangle$, using Eq. (7.35), is then 771 ft/sec. The wheel speed, U, for this particular run was 922 ft/sec and therefore, the mean relative velocity, $\langle q_{rel}\rangle$, which is equal to the free-stream vortex street velocity, U_∞, can be calculated from the following relation,

$$\langle q_{rel}\rangle = \sqrt{\left[U^2 - 2U\langle q_{abs}\rangle\sin\left((\beta_{abs})_\infty\right) + \langle q_{abs}\rangle^2\right]} \tag{7.36}$$

with the following result,

$$\langle q_{rel} \rangle = U_\infty = 662.7 \text{ ft/sec.}$$

The free-stream relative flow angle, $(\beta_{rel})_\infty$, is now set by the velocity triangle as follows,

$$(\beta_{rel})_\infty = \arccos[\langle q_{abs} \rangle \cos((\beta_{abs})_\infty)/\langle q_{rel} \rangle] \qquad (7.37)$$

This results in a free-stream relative flow angle of 34.65 degrees.

The vortex strength as represented by the quantity, $k/(2\pi a U_\infty)$, will determine the depth of the averaged "measured" velocity profile. This can be seen in Fig. 7.13 where the variation of the ratio of the measured velocity at the wake centerline to the free-stream relative velocity, U_∞, has been plotted versus the non-dimensional vortex strength. A velocity profile calculated with a vortex strength of 0.07 can be seen in Fig. 7.14 where it can be compared to the experimentally measured profile. For this plot, the actual vortex spacing, h, has been chosen so that the width of the wake predicted by the model matches the measured wake width, which in this case is approximately 26 percent of the blade passage.

From the LA p.d.d. for the wake centerlines (see Fig. 7.2, point C) the two most-probable velocities in the bi-modal distribution can be seen to be,

$$(V_{meas})_{high} = 780 \text{ ft/sec}$$

$$(V_{meas})_{low} = 630 \text{ ft/sec}$$

These velocities can be calculated from the vortex wake model as a function of the vortex spacing ratio, h/a. This is shown in Fig. 7.15 for various values of the vortex strength, $k/(2\pi a U_\infty)$. A vortex spacing ratio of 0.635 results in a good match of both the upper and lower most-probable velocities for a vortex strength of 0.07.

Given the vortex strength, the core-radius ratio (r_o/h) and the spacing

ratio (h/a), the pressure velocity, U_p, can be found since,

$$U_p/U_\infty = [k/(2\pi a U_\infty)]/[(r_o/h)(h/a)] \tag{7.38}$$

This results in a value of 0.2205.

A summary of the parameters which determine the shape and strength of the rotor blade vortex street can be seen in Table 7.2 and a comparison of certain key measurements to the predictions of the model can be seen in Table 7.3. There is an excellent match of the values of the two most probable velocities even though the wake profile predicted by model is not quite as deep as the measured profile. An estimate of the uncertainty of the fit is presented in Appendix B.

Figure 7.16 shows the variation of the velocity components, u' and v', in the frame of reference relative to the rotor blade for various distances from the wake centerline, denoted by y/a = 0.0. The centerline of the upper row of vortices is at y/a = 0.3175 and the upper edge of the vortex cores lies along y/a = 0.635. The relative velocity and flow angle distributions are shown in Fig. 7.17. As expected, the average flow angle deviation at a given distance from the wake centerline is exactly zero with the result that the average relative flow angle at any point in the wake is exactly equal to the mean relative flow angle.

The velocity field in the frame of reference moving with the vortex centers and in the frame fixed to the blade trailing edge are shown in Figs. 7.18 and 7.19 respectively. Note that in addition to the regions of low velocity in the vortex cores there is a also a region of low velocity between the vortices in both the upper and lower rows. This results in a region of high static pressure as can be seen in the instantaneous static pressure contours shown in Fig. 7.20. The maximum overshoot of static pressure corresponds to a Cp = +0.461. The minimum static pressure, which occurs at the center of the vortex cores, corresponds to a Cp = -0.614.

In Fig. 7.21a the absolute velocity as predicted by the model is shown for various values of y/a. The component of velocity as would be seen by the LA is shown in Fig. 7.21b. Note that the sinusoidal-type distribution of velocity at the wake centerline (y/a = 0.0) will result in a bi-modal p.d.d. This is shown explicitly in Fig. 7.22 where two distinct peaks appear in the p.d.d. for the wake centerline (y/a = 0.0, point C) at the velocities listed in Table 7.3.

Figure 7.23 shows the absolute flow angles as predicted by the wake model for various values of y/a. Here it can be seen that the variation laterally along the wake is quite small compared to the variation transversely across the wake. In particular, a value of approximately 67 degrees is predicted along the wake centerline. The average value across the wake is shown in Fig. 7.24. Note that there is a sharp rise and fall of the flow angle in the wake which reaches a maximum at the wake centerline. This is similar to the behavior of the time traces of absolute flow angle measured by the 4-way probe (see Fig. 5.14).

Finally, the velocity field as seen in the absolute frame of reference is shown in Fig. 7.25. In this frame, which is, of course, the frame in which all the measurements are taken, the presence of the vortex street is well hidden, thus requiring the above analysis to infer its existence.

Once the geometry and kinematics of the vortex street have been set, it is possible to calculate the corresponding Strouhal number. The frequency used in the calculation of the Strouhal number is due to the periodic passage of the vortices in the frame fixed to the rotor blades. This is related to the velocity of the street ($U_\infty + U_i$) and the vortex spacing, a, as follows,

$$f = (U_\infty/a)(1+U_i/U_\infty) \qquad (7.39)$$

(note: $U_i < 0$)

If the Strouhal number is then expressed in terms of a distance, d, such that,

$$St = fd/U_\infty$$

then,

$$St = (d/a)(1+U_i/U_\infty) \qquad (7.40)$$

If d, in turn, is taken to be the measured wake width, W, then a wake-width Strouhal number, St_w, can be expressed solely as a function of the vortex street parameters (see Eq. (7.33)).

$$St_w = (h/a)[1+2(r_o/h)](1+U_i/U_\infty) \qquad (7.41)$$

For the case considered here, the value of St_w is nearly equal to unity (1.008). Given a wake-width to blade-passage ratio, (W/s), of 0.26, a blade gap of 0.161 ft, and a relative velocity of 662.7 ft/sec, the resulting frequency is 15.8 kHz or approximately 2.8 times blade passing.

A boundary layer thickness to chord ratio which would correspond to a conventional Strouhal number of 0.2 can be found from the wake-width Strouhal number, St_w, given the chord to spacing ratio, c/s.

$$\frac{\delta}{c} = \frac{\left(\dfrac{0.2}{St_w}\right)\left(\dfrac{w}{s}\right)}{\left(\dfrac{c}{s}\right)} \qquad (7.42)$$

For a c/s of 1.888, δ/c is equal to 0.027, which is in the range of values for a momentum thickness-to-chord ratio given by Koch and Smith [7.10].

7.5 Comparison of Vortex Model to the 4-way Probe Data

A further examination of the predictions of the vortex model can aid in the understanding of measurements obtained from the 4-way probe. In addition to the variations of static pressure and relative flow angle, the model can be used to calculate variations of relative and absolute total

pressure and total temperature which can be compared to the time-resolved measurements. The vortex street also contributes to fluctuations in the calculated adiabatic efficiency.

Many of these comparisons will tend to be qualitative in nature since the probe's diameter is approximately one-quarter the size of rotor wake or about one-half the size of a vortex core. Even if the traverse of the probe through the wake did not disturb the structure of the street itself, the probe's size would not allow for a very detailed resolution of the flow field due to gradients across the probe face which are not accounted for at the present time since the probe is calibrated in a uniform flow. The influence of a simple linear shear flow on measurements obtained from a probe of this type have been estimated in Appendix A. The flowfield of the vortex street, however, is considerably more complex with gradients in flow angle and static pressure as well as in velocity. Nevertheless, the comparisons that can be made can help explain the apparent random fluctuations in the measurements.

The comparisons of the measurements of the 4-way probe and the vortex model are made by sampling the flow-field predicted by the model in a manner which simulates the passage of the wake over the probe. The resulting time-trace takes into account the rotor wheel speed and the convection of the vortices in the mean relative flow angle direction. Each sampling through the street constitutes a blade passing and begins at a random value of (x'/a) between 0.0 and 1.0, and then proceeds through the street according to the probe's trajectory. The coordinates of the probe's position in the frame fixed to the vortices will then vary in time for each simulated blade passing. For the particular case considered here, the probe traces a path through the frame fixed to the vortices (x',y')

which is almost exactly parallel to the y' axis.

The total temperature in the absolute (laboratory) reference frame can be calculated given the static temperature field (see Eq. (7.28)) and the absolute velocity field, q_{abs} (see Eq. (7.34)).

$$Tt_{abs} = T_s + q^2_{abs}/(2CP) \tag{7.43}$$

Contours of the ratio of the wake total temperature to the free-stream absolute total temperature can be seen in Fig. 7.26 and contours of the absolute velocity, q_{abs}/U_p can be seen in Fig. 7.27. Contours of the relative total temperature and the relative velocity can be found from Eqs. (7.29) and (7.16) and are shown in Figs. 7.28 and 7.29. The effect of the coordinate transformations to both the relative and absolute frames are quite pronounced, obscuring even the location of the vortex centers. Note that both the relative and absolute total temperature variations follow the variations in velocity quite closely. This is due to small variations in static temperature. In particular, in the regions of high velocity both the absolute and relative total temperature in the vortex street are greater than their respective free-stream values.

The total pressure in the absolute frame can also be calculated from the following expression, once the total temperature is known,

$$Pt_{abs} = P[1-q^2_{abs}/(2CPTt_{abs})]^{[-\gamma/(\gamma-1)]} \tag{7.44}$$

and an absolute stagnation pressure coefficient can be defined as follows,

$$\left(C_{pt}\right)_{abs} = \left(P_{tabs}-P_\infty\right)/\left(\frac{1}{2}\rho(q_{abs})^2_\infty\right) \tag{7.45}$$

contours of which can be seen in Fig. 7.30.

In Figs. 7.31 and 7.36 time traces from various 4-way probe measurements are compared to the simulated time traces from the vortex model. The

only additional inputs to the model that are required to make these comparisons are those which are necessary to set the relative free-stream conditions for the model. These include the ratio of the free-stream static pressure to the upstream stagnation pressure, the free-stream absolute total temperature ratio, and the free-stream relative Mach number. For the case considered here, these values are respectively 1.20, 1.175, and 0.591.

The ensuing calculations then predict the variations from the free-stream conditions. The pressures and temperatures have all been scaled to the upstream stagnation conditions. The model predicts both total pressure defects and excesses in the blade wakes, as well as about the same amplitude of fluctuation. The predicted magnitude of the variations of static pressure, however, are five to six times smaller than those measured and the depth of the relative total pressure defects are somewhat larger in magnitude and more uniform than the measured values. Similar trends can be seen in the time traces of the absolute and relative flow angles, although the magnitudes of the deviations in the relative flow angle predicted by the model are not quite as large as the deviations measured by the 4-way probe (12 degrees vs. 20 degrees). The seemingly erratic variations in relative flow angle are seen then to be due simply to the fact that the probe only samples a particular portion of the street as each blade wake passes over it.

In general, the effect of the vortex structure is to add a psuedo-random component to what would otherwise be a periodic structure. The model predicts the nature of the pertubations about the mean but in most instances underpredicts the amplitude of the fluctuations. This is perhaps due to the probe size limitations and the calibration procedures discussed

previously.

7.6 Entropy and Efficiency in Rotor Blade Wake Vortex Streets

The adiabatic efficiency is often used to express the losses through a turbomachinery blade row. In this section the effects of an unsteady flow on the calculation of efficiency will be investigated coupled with the vortex flow structure in the rotor wakes. The overall results are fairly general and can be applied with and without vortex shedding.

The local adiabatic efficiency can be defined in the usual manner relating the total pressure and total temperature ratios in the absolute frame as follows,

$$\eta = \frac{\left(\dfrac{P_{t2}}{P_{t1}}\right)_{abs}^{\frac{\gamma-1}{\gamma}} - 1}{\left(\dfrac{T_{t2}}{T_{t1}}\right)_{abs} - 1} \qquad (7.46)$$

where the subscripts 1 and 2 denote stations upstream and downstream of the rotor blade. Station 1 is assumed to have uniform conditions of total temperature and pressure as would be the case with the first stage of a fan or compressor. Station 2 consists of a free-stream region with the blade wakes represented by vortex streets as modeled above. The change in entropy from station 1 to station 2 may be expressed as follows,

$$e^{-(S_2-S_1)/C_p} = \frac{\left(\dfrac{P_{t2}}{P_{t1}}\right)_{abs}^{\frac{\gamma-1}{\gamma}}}{\left(\dfrac{T_{t2}}{T_{t1}}\right)_{abs}} \qquad (7.47)$$

This can be seen in Fig. 7.37 for the vortex model with a free-stream stagnation temperature ratio of 1.175. As expected the entropy variation

is exactly zero in the regions outside the vortex cores with the only variation occurring in the vortex cores themselves.

Equation (7.46) for the efficiency may now be re-written by eliminating the stagnation pressure ratio using Eq. (7.47).

$$\eta = \frac{\left(\dfrac{T_{t2}}{T_{t1}}\right)_{abs} e^{-(S_2-S_1)/C_p} - 1}{\left(\dfrac{T_{t2}}{T_{t1}}\right)_{abs} - 1} \tag{7.48}$$

If there is no change in entropy from station 1 to station 2 then the efficiency is exactly 1.0 regardless of the variations in total temperature. However, if between stations 1 and 2 there is some loss mechanism (such as a normal shock) so that $S_2 > S_1$ in the free-stream region, then the efficiency will be less than 1.0 and, in fact, will vary through the vortex street as the total temperature varies. This will be the case even outside the vortex cores in the wake where the flow is modeled to be irrotational and inviscid. In these regions the entropy does not vary as shown in Fig. 7.37. This means that the value of entropy outside the vortex cores is constant and so the value of (S_2-S_1) is constant as well. Now since the flow in the absolute frame is unsteady (with or without vortex shedding!) and the gradient of entropy is zero outside the cores, the total temperature must vary according to Crocco's theorem which may be written as follows,

Crocco's Theorem

$$T\vec{\nabla}S = \vec{V}(C_p T_t) - \vec{q}(\nabla\times\vec{q}) + \frac{\partial\vec{q}}{\partial t} \tag{7.49}$$

In the regions outside the vortex cores this reduces to,

$$C_p\vec{\nabla}T_t = \frac{-\partial\vec{q}}{\partial t} \tag{7.50}$$

This implies that the total pressure will vary as well and in such a manner that (S_2-S_1) remains constant (see Eq. (7.47)). In any case, since (S_2-S_1) is constant and T_{t2}/T_{t1} varies throughout the vortex street, the efficiency will vary as well, even though the entropy is constant (see Eq. (7.47)). This can be seen in Fig. 7.38 for the case considered in the above analysis. Again as with the calculation of total temperature, there are regions in which the efficiency is greater than the free-stream value. It should be pointed out, however, that no matter how large the variations in total temperature, the efficiency will always be less than one, since by Eq. (7.47), S_2-S_1 is always greater than zero. The comparison of the variations predicted by the model compared to the calculated values from the 4-way probe measurements can be seen in Fig. 7.39. The agreement is not very good except in a qualitative sense in that the model predicts fluctuations above and below some free-stream value which are present in the measurements on a much larger scale.

7.7 Summary

The simple vortex street wake model fits the experimental data reasonably well. The vortex model reproduces the wake shape and bi-modal p.d.d.'s of the LA data, a feature otherwise difficult to explain. The vortex model also accounts for the nature of the blade to blade fluctuations observed in the high frequency response probe data, particularly in static pressure and relative flow angle. The high level of fluctuations, observed in several transonic rotors has always been puzzling and could not be explained by geometric blade to blade differences. The intermittent sampling of the vortex street by the fixed frame probe reproduces these features, although the model presented here generally underpredicts the level of the fluctuations.

CHAPTER VIII

8.1 Conclusions

High response probes which had previously been used exclusively in the MIT Blowdown Facility have been successfully employed in two conventional steady state rigs to investigate the unsteady flow fields of highly loaded transonic compressors at design point operation. The tests revealed that the high response probes were both durable and practical devices for measuring the time resolved quantities of total and static pressure and flow angle in a continuously operating facility. The time averaged high response data agreed quite well with the conventional steady state instrumentation except for flow angle which showed a large spread in values at all radii regardless of the type of instrumentation used.

In addition, the time resolved measurements obtained in a steady state facility agreed quite well with previous results for the same compressor in the Blowdown Facility. This in a sense confirms the results obtained earlier in this facility.

To date three highly loaded compressors have been investigated with the high frequency response probes. Two have been studied in steady state rigs while a third was tested in the MIT Blowdown Facility. The results of these tests have revealed that the flow field of a highly loaded transonic compressor is in general heavily influenced by unsteady flow phenomena. The rotor exit flow of all three rotors exhibited total pressure fluctuations outside the blade wakes presumably due to the motion of the blade passage shock system. Highly variable wake flows were also seen, which were found to be due to vortex shedding from the rotor blades.

The blade wakes were modeled as classical two-dimensional streets of Rankine vorticies with finite sized cores. This model fit the data quite

well although only one radial location has been studied to date. The model was able to reproduce the wake shape and bi-modal probability density distribution seen in the laser anemometry data and also explains the large blade to blade fluctuations seen by the high response probes due to the intermittent sampling of the street as it is swept past the stationary probes.

The presence of a vortex street in the rotor blade wakes has several implications concerning the interpretation of certain flow measurements, in particular, laser anemometry, as the time averaged wake profiles will not represent an actual physical state of the flow field. The arithmetic average of the velocity at some point in the flow may represent a very lowly populated state especially if a bi-modal p.d.d. is prevalent.

The existence of a vortex street introduces additional difficulties for numerical analysis schemes which require steady flow boundary conditions. This will be of particular importance in the calculation of the transport of rotor wakes through adjacent stator blade rows and even in the interpretation of the losses associated with rotor exit flow itself.

8.2 Recommendations

The vortex streets in the wakes of transonic compressors are undoubt-edly more complex than the relatively simple model presented. The evolution of the street in both time and space should be considered, particularly for the vortex cores. The spanwise distribution of the vortex strength and spacing ratio should also be investigated. If the vortex pattern has an appreciable spanwise coherence, radial transport through the vortex cores may be an important contribution to the spanwise redistribution of the wake fluid. In addition, the interblade phasing of the shedding should be addressed. Vortex shedding from cylinders has been shown to lock on in

frequency and phase to an external disturbance. This lock-on also has the effect of increasing the intensity of the shedding. External disturbances in turbomachinery, whether due to acoustic resonance phenomena or blade row interactions, may contribute to this effect.

The high response probes were originally designed for use in the MIT Blowdown tunnel. Tests in steady state facilities revealed that the probes are able to withstand the relatively harsh environment of a continuously operating facility, however, the probe translators should be re-designed for use in steady state facilities to allow for remote setting of the immersion point to avoid re-setting the operating point of the rig thus saving a considerable amount of time and effort. The apparent thermal drift of the high response total pressure probes in these facilties should also be investigated. Perhaps some sort of active cooling will be required to achieve acceptable DC stability as was done for the 4-way angle probe. Some sort of angular alignment for the 4-way probe should also be provided to mimimize errors in the overall level of the tangential flow angle.

The effect of a simple shear flow on the measurements obtained with the 4-way angle probe was simulated and revealed that significant errors in static pressure and flow angle may occur for flows encountered in the blade wakes of transonic rotors. This should be further investigated with the calibration model of the probe in an actual shear flow and the results should be incorporated into the data reduction scheme. Unsteady flow effects should also be explored particularly in light of Kovasznay's calculations for a sphere probe [3.2] which showed that these effects can be significant given the magnitude of the unsteadiness encountered in transonic compressors.

APPENDIX A
MEASUREMENT ERRORS FOR A CYLINDER PROBE
IN A SIMPLE SHEAR FLOW

Since the 4-way angle probe described in Chapter III is calibrated in a uniform flow, errors in the measurements of static pressure and flow angle may result if the probe is subjected to a shear flow such as those observed in wakes and vortex streets. To investigate the magnitudes of these errors, the effect of simple shear flow over an idealized cylindrical probe will be evaluated.

A simple cylindrical probe is modeled to consist of three sensors: P1, P2, P3 as shown in Fig. A.1. P2 and P3 are offset above and below the center sensor P1 by 45 degrees similar to the design of the 4-way probe. The angle, α, represents the orientation of the probe to the direction of the undisturbed shear flow which is of the following form.

$$u = u_o\left(1 + \frac{\omega_o}{u_o} y\right)$$

(A.1)

Here ω_o is a constant which determines the magnitude of the shear. The undisturbed flowfield is then one of constant static pressure with a linearly varying velocity gradient, and the subsequent variation in total pressure.

Following a procedure similar to the one used in the calibration of the 4-way probe, the calibration curves for the idealized cylindrical probe are simulated by calculating the pressure on the surface of the cylinder in a uniform flow ($\omega_o = 0.0$). For simplicity, a steady 2-D incompressible inviscid flowfield will be assumed. The pressure at any point on the cylinder in a uniform flow is simply,

Uniform Flow

$$P_n = P_\infty + \frac{\rho u_o^2}{2} (1 - 4\sin^2\theta_n) \qquad n = (1,2,3) \qquad (A.2)$$

where,

$\theta_1 = -\alpha$ $\qquad$ u_o = undisturbed velocity at y=0

$\theta_2 = -(\alpha+45°)$ $\qquad$ ρ = fluid density

$\theta_3 = 45°+\alpha$ $\qquad$ P_∞ = undisturbed static pressure

These pressures can be expressed in terms of a pressure coefficient of the following form.

Uniform Flow

$$Cp_n = \frac{P_n - P_\infty}{\left(\frac{\rho u_o^2}{2}\right)} = (1 - 4\sin^2\theta_n) \qquad n = (1,2,3) \qquad (A.3)$$

The effect of an upsteam shear flow on the surface pressures is evaluated following Batchelor [A.1]. The stream function for the shear flow over a cylinder of radius, a, is,

$$\psi = -\frac{1}{2} \omega_o r^2 \sin^2\theta - u_o r\sin\theta + \frac{u_o a^2 \sin\theta}{r} - \frac{\omega_o a^4 \cos 2\theta}{4r^2} \qquad (A.4)$$

In order to find the pressure at the surface of the cylinder (r=a), the position of the stagnation streamline far upstream (r=∞) must be found by matching the values of the stream function at these two locations.

$$\psi(r=a) = -\frac{1}{4} \omega_o a^2 \qquad (A.5a)$$

$$\psi(r=\infty) = -\frac{1}{2} \omega_o y^2 - u_o y \qquad (A.5b)$$

The value of y which satisfies these two conditions can then be found by

solving the quadratic relation formed by equating Eqs. (A.5a) and (A.5b).

$$\frac{y_o}{a} = \frac{-2\left(\frac{u_o}{a\omega_o}\right) + \sqrt{\left(2\frac{u_o}{a\omega_o}\right) + 2}}{2} \qquad (A.6)$$

The Bernoulli constant or total pressure along this streamline is then found by substituting the value of y_o/a into the following expression for the undisturbed stagnation pressure.

$$P_{t_o}(y=y_o) = P_\infty + \frac{\rho u_o^2}{2}\left[1 + \left(\frac{\omega_o u_o}{a}\right)\frac{y_o}{a}\right] \qquad (A.7)$$

The static pressure at any point on the surface of the cylinder is then found by first differentiating the stream function to obtain the tangential velocity on the surface of the cylinder.

$$u_\theta(r,\theta) = \frac{\partial \psi}{\partial r} = -\omega_o r\sin^2\theta - u_o\sin\theta - \frac{u_o a^2\sin\theta}{r^2} + \frac{\omega_o a^4\cos2\theta}{2r^3} \qquad (A.8a)$$

At the surface of the cylinder, $r=a$, the velocity is then,

$$u_\theta(a,\theta) = u_o\left[-2\sin\theta + \left(\frac{\omega_o a}{u_o}\right)\left(\frac{\cos2\theta}{2} - \sin^2\theta\right)\right] \qquad (A.8b)$$

and since total pressure is constant along the stagnation streamline, the static pressure on the surface of the cylinder is simply,

Shear Flow

$$P(\theta)_{r=a} = P_{t_o} - \frac{\rho u_\theta^2(a,\theta)}{2} \qquad (A.9)$$

The terms $\omega_o a/u_o$ now define a non-dimensional shear stress parameter.

The 4-way data reduction scheme can now be simulated for the idealized cylinder flow in a shear flow. First, the flow angle, α, is found by using

the coefficient F23 (see Eq. (3.1)). F23 can be expressed in terms of the non-dimensional pressure coefficients Cp_1, Cp_2, and Cp_3 as follows.

$$F23(\alpha) = (Cp_2-Cp_3)/[(Cp_2-Cp_1)+(Cp_3-Cp_1)] \qquad (A.10)$$

Following the procedure used in the 4-way data reduction scheme, the measured flow angle, α_m, for a given flow angle, α_o, is found by finding an angle, α, such that the value of F23 with the uniform flow pressure coefficients (Eq. (A.3)) matches the value of F23 with the shear flow pressure coefficients (from Eq. (A.9)) at the given angle, α_o. The error is then the difference between the two angles, α_m and α_o and is shown in Fig. A.2 for various values of flow angle α_o and shear stress parameter. The error is an odd function of both the shear stress parameter and the flow angle.

$$\varepsilon_{angle}(-\omega_o,-\alpha) = -\varepsilon_{angle}(\omega_o,\alpha) \qquad (A.11)$$

Following the 4-way data reduction scheme, the measured static pressure can now be found using the minimum of Cp_2 or Cp_3 and the value of Kp_n (see Eq. (3.9)) calculated with the uniform flow pressure coefficients at the measured angle, α_m.

$$(Kp_n)_o = (Cp_n)_{min}/[(Cp_3-Cp_1)+(Cp_2-Cp_1)] \quad n=(2 \text{ or } 3) \qquad (A.12)$$
$$(\text{no shear})$$

The measured pressure is then,

$$P_{meas} = (P_n)_{min} - [(P3-P1)+(P2-P1)](Kp_n)_o \qquad (A.13)$$

A pressure coefficient Cp_m is now defined to represent the error in the measured static pressure due to the influence of the shear flow.

$$Cp_m = \frac{P_{meas}-P_\infty}{\frac{1}{2}\rho u_o^2} \qquad (A.14)$$

Using Eqs. (A.12) and (A.13), the expression for Cp_m is then,

$$Cp_m = (Cp_n)_{min} - [(Cp_3-Cp_1)+(Cp_2-Cp_1)](Kp_n)_o \qquad (A.15)$$

$$\text{(shear)} \qquad\qquad \text{(shear)} \qquad\qquad \text{(no shear)}$$

Figure A.3 shows the variation of Cp_m with flow angle α_o for several values of the non-dimensional shear stress parameter. For a shear stress of 0.2, which might be encountered in a highly loaded compressor, the error can be as high as 6 percent of the dynamic head if the probe is aligned to within ±10 degrees of the instantaneous flow angle.

APPENDIX B
SENSITIVITY ANALYSIS OF VORTEX STREET FIT

The fit of the vortex model to the LDV wake data will be influenced by the uncertainties in the input parameters to the model. Namely, uncertainties in the free-stream flow conditions and the location of the peaks in the bi-modal velocity histograms will result in uncertainties in the lateral spacing of the vortices, h/a, and the vortex strength.

The geometry of the vortex street is set by the lateral spacing, h/a, and the core-radius ratio, r_o/h. The value of the core-radius ratio chosen will not affect the fit of the model to the measurements, as long as the vortex cores do not extend past the wake centerline ($r_o/h < 0.5$). As was shown, a value of exactly 0.5 will reproduce the smooth wake-like character of the averaged velocity profile which is seen in the experimental data. With the core-radius ratio set equal to 0.5, the vortex strength and the lateral spacing will set the location of the peaks in the bi-modal velocity distribution at the wake centerline. While the vortex strength will determine the magnitude of the velocity defect in the averaged velocity profile, it is chosen instead in such a manner that the peaks in the velocity distribution can be matched by varying the lateral spacing.

The relevant input parameters for the test case at 60% span and 140% chord are presented here along with an estimate of their uncertainties.

Free-Stream (Blade Passage)
$(\beta_{abs})_{fs}$ = 45 (±1) degrees
$(V_{meas})_{fs}$ = 770 (±5) fps

Bi-Modal Most Probable Velocities
$(V_{meas})_{high}$ = 780 (±2.5) fps
$(V_{meas})_{low}$ = 630 (±10.0) fps

Note that the upper peak in the velocity distribution is more sharply

defined than the lower peak resulting in a much lower uncertainty in its value.

Table B.1 shows the results of calculations to determine the effect of the uncertainty in the most probable velocities on the allowable values of the spacing ratio h/a for a given vortex strength. This is also shown graphically in Fig. B.1 for a non-dimensional vortex strength of 0.07. In general, the results show that the uncertainty in the most probable velocities can lead to uncertainties in the spacing ratio of 2 to 4 percent and in the vortex strength of about 9 percent. Table B.2 shows the results of calculations to determine the effect of the uncertainties in the free-stream velocity and flow angle. This leads to an additional uncertainty in the spacing ratio of 2 to 4 percent and in the vortex strength of 4 to 6 percent. The combination of both effects can lead to uncertainties in vortex strength as high as 15 percent and in the spacing ratio as high as 8 percent.

The effect of the uncertainty in the spacing ratio and the vortex strength on the calculated vortex shedding frequency is not as dramatic as the combination of the above uncertainties. The shedding frequency is a function of both quantities, as shown below.

$$f = 2(U_\infty/s)(h/a)/(w/s)[1-|U_i|/U_\infty] \quad (r_o/h = 0.5)$$

where,

$$U_i/U_\infty = -\pi(k)\tanh[\pi(h/a)]$$

Since lower values of the vortex strength tend to be associated with lower values of h/a (see Tables B.1 and B.2), the resulting uncertainty in shedding frequency is only 3 to 6 percent or approximately ±1 kHz. Additional uncertainties in the wake width and free-stream velocity,

however, also impact the uncertainty in the shedding frequency. Whereas the uncertainty in the free-stream velocity is quite small (<1.0%), the uncertainty in the wake width can be as high as 10 percent. This will lead to an additional ±1 kHz uncertainty in the calculated shedding frequency, for a total uncertainty of approximately ±2 kHz.

REFERENCES

Chapter I

1.1 Kerrebrock, J.L., Epstein, A.H., Thompkins, W.T., "A Miniature High Frequency Sphere Probe," Proc. ASME Symposium Measurement Methods in Rotating Components of Turbomachinery, 1980.

1.2 Ng, W.F., "Detatiled Time Resolved Measurements and Analysis of Unsteady Flow In a Transonic Compressor," MIT GTL Report. No. 150, 1980.

1.3 Ng, W.F., "Time-Resolved Stagnation Temperature Measurement in a Transonic Compressor Stage,"MIT GTL Rep. No. 177, 1983.

1.4 Kerrebrock, J.L., "The MIT Blowdown Compressor Facility," MIT GTL Report No. 108, 1975.

1.5 Urasek, D.C., Gorell, W.T., and Cunnan, W.S., "Performance of Two-Stage Fan Having Low-Aspect-Ratio, First-Stage Rotor Blading," NASA TP-1493, August 1979.

1.6 Wennerstrom, A.J. and Frost, G.R., "Design of a 1500 Ft/Sec, Transonic, High-Through-Flow, Single-Stage Axial-Flow Compressor with Low Hub/Tip Ratio," AFAPL-TR-76-59, 1976.

Chapter III

3.1 Unpublished shock tube tests conducted at the MIT Gas Turbine Laboratory by Jeffrey L. Holt, 1985.

3.2 Kovasznay, L.S.G. et. al., "Instantaneous Pressure Distribution Around a Sphere in Unsteady Flow", J. of Fluids Eng., Vol. 103, 1981.

3.3 Holt, J.L., "Time-Resolved Flowfield Measurements in a Turbine Stage," MIT S.M. Thesis, 1985.

3.4 Figueriedo, W.A., "Spherical Pressure Probe for Retrieving Freestream Pressure and Directional Data," MIT GTL Rep. No. 137, 1977.

3.5 Strazisar, A.J., Powell, J.A., "Laser Anemometer Measurements in a Transonic Axial Flow Compressor Rotor," ASME J. of Eng. for Power, Vol. 103, No. 2, April 1981, pp. 430-437.

3.6 Powell, J.A., Strazisar, A.J., and Seasholtz, R.G., "Efficient Laser Anemometer for Intra-Rotor Flow Mapping in Turbomachinery," ASME J. of Eng. for Power, Vol. 103, No. 2, April 1981, pp. 424-429.

Chapter V

5.1 Kerrebrock, J.L. and Mikolajczak, A.A., "Intra-Stator Transport of Rotor Wakes and Its Effect on Compressor Performance," ASME Paper 70-GT-39, 1970.

Chapter VII

7.1 Heinemann, H.J.,Lawaczeck, O., Butefisch, K.A., "V. Karman Vortices and Their Frequency Determination in the Wakes of Profiles in the Sub- and Transonic Regimes," IUTAM Symposium, 1976, pp.75-82.

7.2 Paterson, R.W. and Weingold, H.P., "Experimental Investigation of a Simulated Compressor Airfoil Trailing Edge Flowfield," AIAA-84-0101, 1984.

7.3 Xing, W.F. and Marenbach, G., "Periodic Vortex Shedding in the Super- sonic Wake of a Flat Plate", (German), A84-20842, 1983.

7.4 Greenway, M.E. and Wood, C.J., "The effect of a bevelled trailing edge on vortex shedding and vibration," JFM, Vol. 61, part 2, 1973.

7.5 Heinemann, H.J. and Butefisch, K.A., "Determination of the Vortex Shedding Frequency of Cascades With Different Trailing Edge Thick- nesses," AGARD CP-227, 1977, pp.35-1 to 35-10.

7.6 Camus, J.J. and Bryanston-Cross, P.J., "One MHz Bandwidth, Real Time Schlieren Techniques in a Linear Cascade," Proc. of Symposium Measurement Techniques in Transonic and Supersonic Flows in Cascades and Turbomachines, Lyon, 1981.

7.7 Young, W.H., Meyers, J.F., and Hepner, T.E., "Laser Velocimeter Systems Analysis Applied to a Flow Survey Above a Stalled Wing," NASA TN D-8408, 1977.

7.8 Dunker, R.J., "Flow Measurements in the Stator Row of a Single Stage Transonic Axial Compressor with Controlled Diffusion Stator Blades," AGARD CP-351, 1983.

7.9 Hobbs, D.E., et al., "Experimental Investigation of Compressor Cascade Wakes," ASME 82-GT-299, 1982.

7.10 Koch, C.C. and Smith, L.H., "Loss Sources and Magnitudes in Axial Flow Compressors," J. of Eng. for Power, Vol. 98, No. 3, 1976.

7.11 Strazisar, A.J., Powell, J.A., "Laser Anemometer Measurements in a Transonic Axial Flow Compressor Rotor," ASME J. of Eng. for Power, Vol. 103, No. 2, April 1981, pp. 430-437.

7.12 Powell, J.A., Strazisar, A.J., and Seasholtz, R.G., "Efficient Laser Anemometer for Intra-Rotor Flow Mapping in Turbomachinery," ASME <u>J. of Eng. for Power</u>, Vol. 103, No. 2, April 1981, pp. 424-429.

7.13 Lamb, H.L., "Hydrodynamics," Dover Publications, New York, 1945.

7.14 Chen, Y.F., "Fluctuating Lift Forces of the Karman Vortex Street on Single Circular Cylinders and in Tube Bundles - Part 1," <u>J. of Eng. for Industry</u>, May 1972.

7.15 Griffin, O. and Ramberg, S., "The vortex-street wakes of vibrating cylinders," <u>J. of Fluid Mechanics</u>, Vol. 66, 1974.

7.16 Shaefer, J. and Eskinazi, S., "An analysis of the vortex street generated in a viscous fluid," <u>J. of Fluid Mechanics</u>, Vol. 6, 1959.

7.17 Griffin, O. and Ramberg, S., "On vortex strength and drag in bluff-body wakes," <u>J. of Fluid Mechanics</u>, Vol. 69, 1975.

Appendix A

A.1 Batchelor, G.K., "An Introduction to Fluid Dynamics," Cambridge University Press, 1967.

TABLE 2.1: TRANSONIC ROTOR GEOMETRY AND INSTRUMENTATION PORTS
(dimensions in inches)

Rotor	Aspect Ratio	No. Blades	Chord
NASA	1.56	22	3.6
AFAPL	1.32	20	3.5-3.9
P&WA	2.80	26	4.2

Rotor	Leading Edge		
	R_{tip}	R_{hub}	R_{hub}/R_{tip}
NASA	10.05	3.77	0.375
AFAPL	8.50	2.65	0.312
P&WA	15.58	4.92	0.316

Rotor	Trailing Edge			
	R_{tip}	R_{hub}	R_{hub}/R_{tip}	Span
NASA	9.75	4.66	0.477	5.09
AFAPL	8.50	4.50	0.529	4.00
P&WA	15.16	6.38	0.420	8.77

Rotor	Instrumentation Port				
	R_{tip}	R_{hub}	Span	d(tip)	d(hub)
NASA	9.61	4.73	4.88	1.73	0.75
AFAPL	8.50	5.00	3.50	1.3	0.7
P&WA	14.92	8.86	6.07	3.60	2.97

(d = distance from blade trailing edge
to instrumentation port)

TABLE 2.2:   TRANSONIC ROTOR DESIGN PERFORMANCE

Rotor	Mass Flow	Tip Mach No.	$\langle Pt/Pt_1 \rangle$	$\langle eff \rangle$	L.E. Sonic Line R/R_{tip}
NASA	75.0	1.29	1.67	0.91	0.66
AFAPL	62.6	1.43	2.13	0.92	0.55
P&WA	196.0		1.61	0.92	0.57

Rotor	L.E. Relative Mach Number		Pt/Pt_1			Efficiency		
	Tip	Hub	Tip	Mid-Span	Hub	Tip	Mid-Span	Hub
NASA	1.35	0.75	1.74	1.68	1.63	0.80	0.94	0.90
AFAPL	1.65	0.67	2.22	2.05	1.99	0.82	0.99	0.99
P&WA	1.45	0.74	1.41	1.69	1.61	0.69	0.96	–

TABLE 4.1: NASA LEWIS ROTOR RUN CONDITIONS

Mass Flow = 72.8 lbm/sec
100% Corrected Speed

Date	Run	M_{dot}	N_{cor}	$<Pt_4/Pt_1>$
11/22/83	221	72.78	100.0	1.639
11/23/83	225	72.80	100.0	1.643
11/23/83	225	72.63	99.9	1.634
11/23/83	225	72.84	100.1	1.633
11/23/83	225	73.76	100.1	1.637
11/23/83	228	72.33	99.9	1.637
11/23/83	228	72.27	99.9	1.635
11/23/83	228	73.33	99.9	1.634
11/23/83	228	72.80	99.9	1.629
11/23/83	232	71.66	100.0	1.634
11/23/83	232	72.37	100.0	1.642
11/23/83	232	72.84	100.0	1.639
11/23/83	232	72.76	100.1	1.631
03/07/84	253	72.78	100.1	1.645
03/07/84	256	73.17	99.9	1.643
03/07/84	259	72.60	100.0	1.638
03/12/84	264	73.12	100.0	1.646
03/12/84	267	72.60	100.1	1.642
03/12/84	270	72.45	100.1	1.648
03/12/84	277	72.40	100.1	1.647
03/12/84	280B	72.11	100.1	1.640
03/13/84	283	72.90	100.0	1.646
03/13/84	286	72.81	100.0	1.647
03/13/84	289	72.87	100.0	1.647
03/13/84	293	72.65	100.1	1.649
03/13/84	296	72.87	100.0	1.647
03/13/84	299	72.76	99.9	1.646

TABLE 4.2: COMPARISON OF HIGH RESPONSE DATA TO LASER
ANEMOMETRY AND CONVENTIONAL AERO DATA

A) R/R_{tip} = 0.93

	Station 2	
	$\langle Ps/Pt_1 \rangle$	$\langle M_{abs} \rangle$
4-Way	1.255	0.669
LA	-	0.644
Aero(wedge)	1.271	0.664

B) R/R_{tip} = 0.82

	Station 2	
	$\langle Ps/Pt_1 \rangle$	$\langle M_{abs} \rangle$
4-Way	1.231	0.670
LA	-	0.643
Aero(wedge)	1.230	0.664

C) $R/Rtip$ = 0.70

	Station 2	
	$\langle Ps/Pt1 \rangle$	$\langle Mabs \rangle$
4-Way	1.198	0.683
LA	-	0.677
Aero(wedge)	1.198	0.680

TABLE 6.1: TRANSONIC ROTOR COMPARISON ALONG
            STREAMLINES OF PRESCRIBED INLET
            RELATIVE MACH NUMBER AT DESIGN
            SPEED AND MASS FLOW

Inlet Relative Mach No.	Rotor	R/R_{tip}	Span
1.34	NASA	0.95	82%
	AFAPL	0.82	55%
	PWA	0.90	82%
1.25	NASA	0.83	66%
	AFAPL	0.78	47%
	PWA	0.82	66%
1.14	AFAPL	0.73	34%
	PWA	0.74	54%
1.03	NASA	0.71	43%
	AFAPL	0.69	25%
0.89	NASA	0.59	20%
	AFAPL	0.64	13%

TABLE 7.1:   COMPARISON OF VORTEX SHEDDING PARAMETERS

A) Plates and Cascades

Investigator	Plate Length c (cm)	Plate Thickness t (cm)	t/c	Rec	Ret	Mach No.	St #	f (kHz)
Paterson [7.2] (flat plate)	365	2.54	0.007	8×10^6	5.6×10^4	0.1	0.18	0.25
Heinemann [7.1] (flat plate)	6-8	0.3-0.6	0.075 0.050	0.4×10^5 2.0×10^5	0.3×10^4 1.5×10^4	0.2-1.3	0.20	2.5-14.0
Greenway, Wood [7.4] (flat plate: bevelled t.e.)	46	3.8	0.083	1.3×10^6	1.1×10^5	0.1	0.24	0.25
Heinemann, Butefisch [7.5] (cascade)	6-8	0.45-0.6	0.008 0.05	3.7×10^5 3.2×10^6	0.3×10^4 1.6×10^5	0.2-0.9	0.2 -0.4	2.0-160.0
Xing [7.3] (flat plate)	21.6	0.6	0.028	-	-	0.4-2.2	0.2 -0.3	50.0

B) Compressors and Fans

Rotor	Aero Chord c (cm)	T.E. Thickness t (cm)	t/c	Rec	Ret	M_{rel}
NASA (Tip)	9.28	0.034	0.004	1.9×10^6	0.7×10^4	0.79
NASA (Hub)	9.45	0.095	0.010	1.1×10^6	1.1×10^4	0.50
AFAPL (Tip)	9.87	0.025	0.0025	3.8×10^6	0.9×10^4	0.82
AFAPL (Hub)	9.00	0.031	0.0035	1.3×10^6	0.5×10^4	0.57
PWA (Tip)	4.20	0.070	0.0026	1.9×10^6	0.5×10^4	0.99
PWA (Hub)	4.20	0.119	0.0044	1.2×10^6	0.5×10^4	0.72

TABLE 7.2:   ROTOR BLADE VORTEX STREET PARAMETERS

Spacing Ratio (h/a)	= 0.635
Core-Radius Ratio (r_o/h)	= 0.50
Pressure-Defect Velocity Ratio (U_p/U_∞)	= 0.2205
Vortex Strength $(k/[2\pi a U_\infty])$	= 0.07
Induced Velocity Ratio (U_i/U_∞)	=-0.212
Chen's Universal Wake #	= 0.722
Wake-Width Strouhal # (Stw)	= 1.008
Vortex Shedding Frequency	= 15.8 kHz

TABLE 7.3: COMPARISON OF VORTEX MODEL TO LA DATA

		LA Data	Vortex Model
Wake Depth	$1 - [(V_{meas})cl/U_\infty]$	0.1261	0.0878
Velocity Probability Density Distribution	$(V_{meas}/U_\infty)_{high}$	1.177	1.167
	$(V_{meas}/U_\infty)_{low}$	0.951	0.952

TABLE B.1:   EFFECT OF UNCERTAINTY IN MOST-PROBABLE VELOCITIES

$$\beta_{abs} = 45.0 \text{ degrees}$$
$$V_{meas} = 770 \text{ fps}$$
$$(V_{meas})_{high} = 780 \ (\pm 2.5) \text{ fps}$$
$$(V_{meas})_{low} = 630 \ (\pm 10.0) \text{ fps}$$

$\dfrac{k}{2\pi a(U_\infty)}$	h/a	f (kHz)
0.062	no match	
0.064	0.610-0.625	15.5-15.9
0.066	0.620-0.644	15.6-16.2
0.068	0.620-0.646	15.5-16.2
0.070	0.622-0.645	15.5-16.0
0.072	0.625-0.646	15.4-15.9
0.074	0.630-0.640	15.4-15.6
0.076	0.642-0.647	15.6-15.7
0.078	no match	
0.064-0.076	0.610-0.647	15.4-16.2

TABLE B.2:   EFFECT OF UNCERTAINTY IN FLOW ANGLE AND VELOCITY

$(V_{meas})_{high}$ = 780
$(V_{meas})_{low}$ = 630

β_{abs}	V_{meas} (fps)	$\dfrac{k}{2\pi a(U_\infty)}$	h/a	f (kHz)
44	765	0.066	0.620	15.6
44	775	0.072	0.647	15.9
45	770	0.070	0.635	15.8
46	765	0.067	0.610	15.3
46	775	0.073	0.636	15.6
		0.066-0.073	0.610-0.647	15.3-15.9
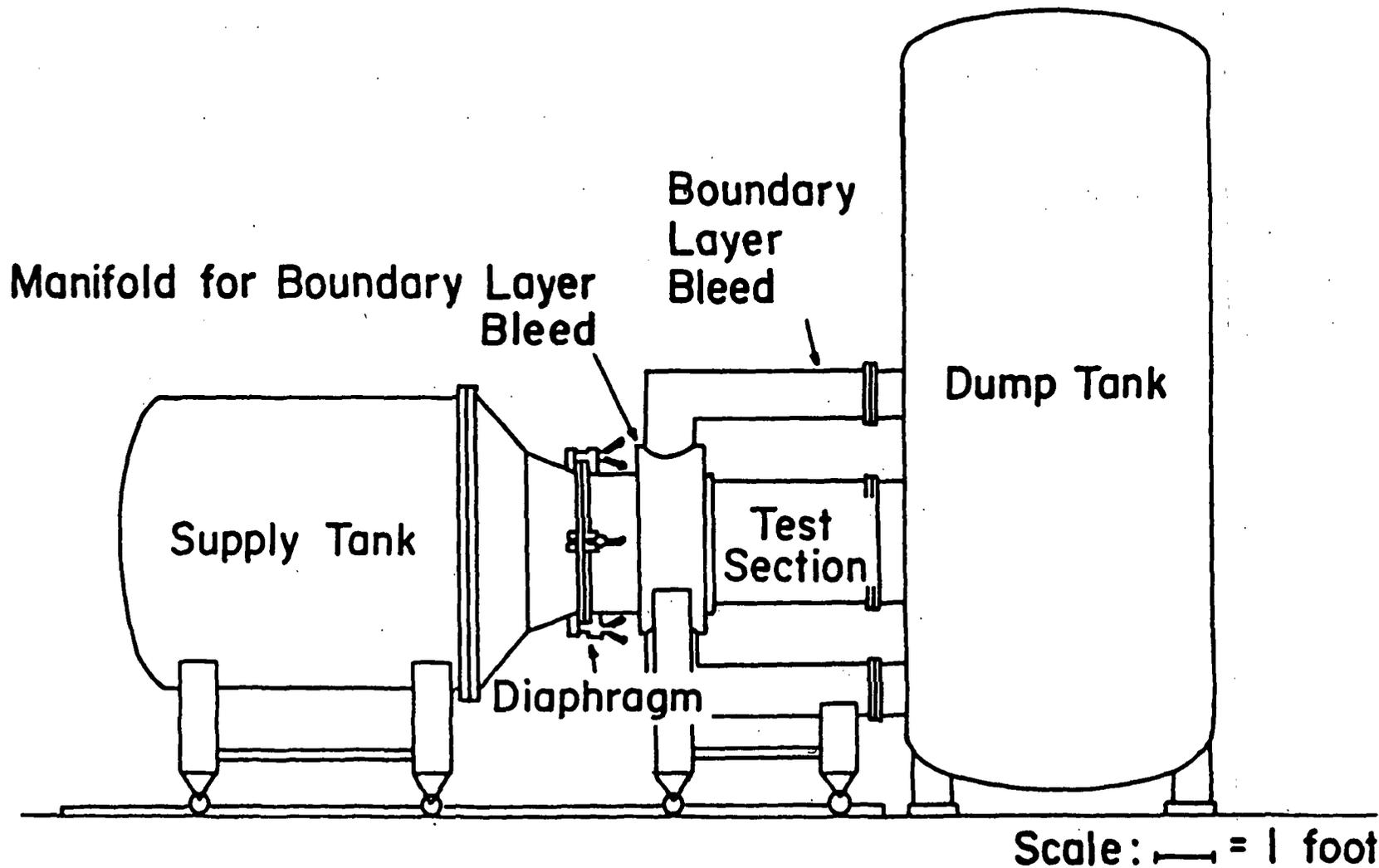
Figure 2.1   Scale Drawing of the MIT Blowdown Facility

Transducer
Diaphragm

3mm

Total Pressure
Probe
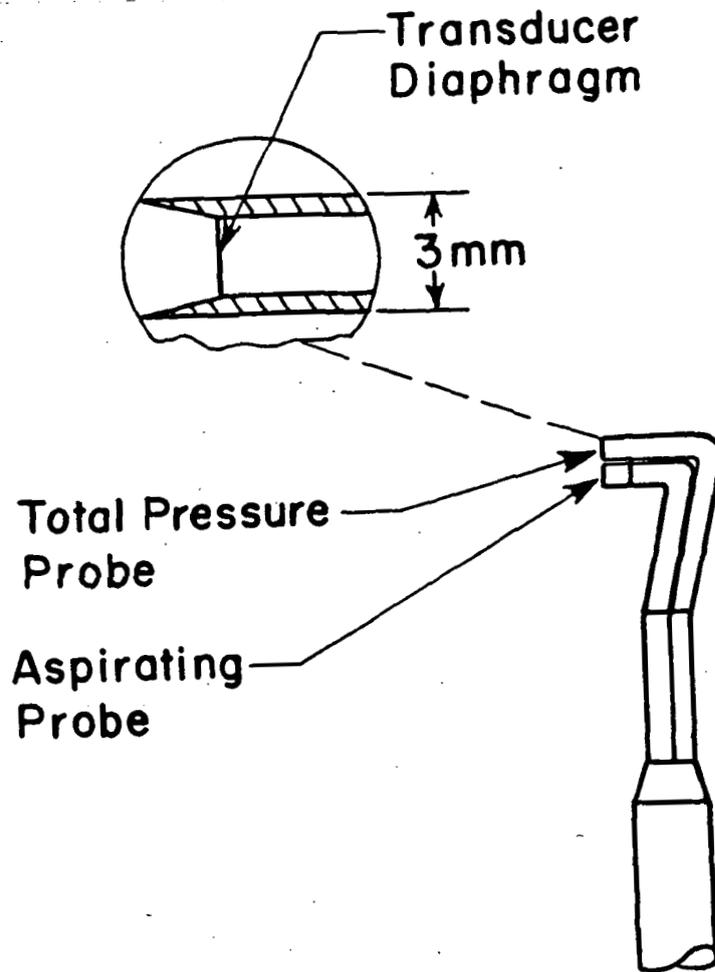
Aspirating
Probe

Figure 3.1   High frequency response total pressure probe
mounted piggyback with aspirating probe

TOTAL PRESSURE RAKE
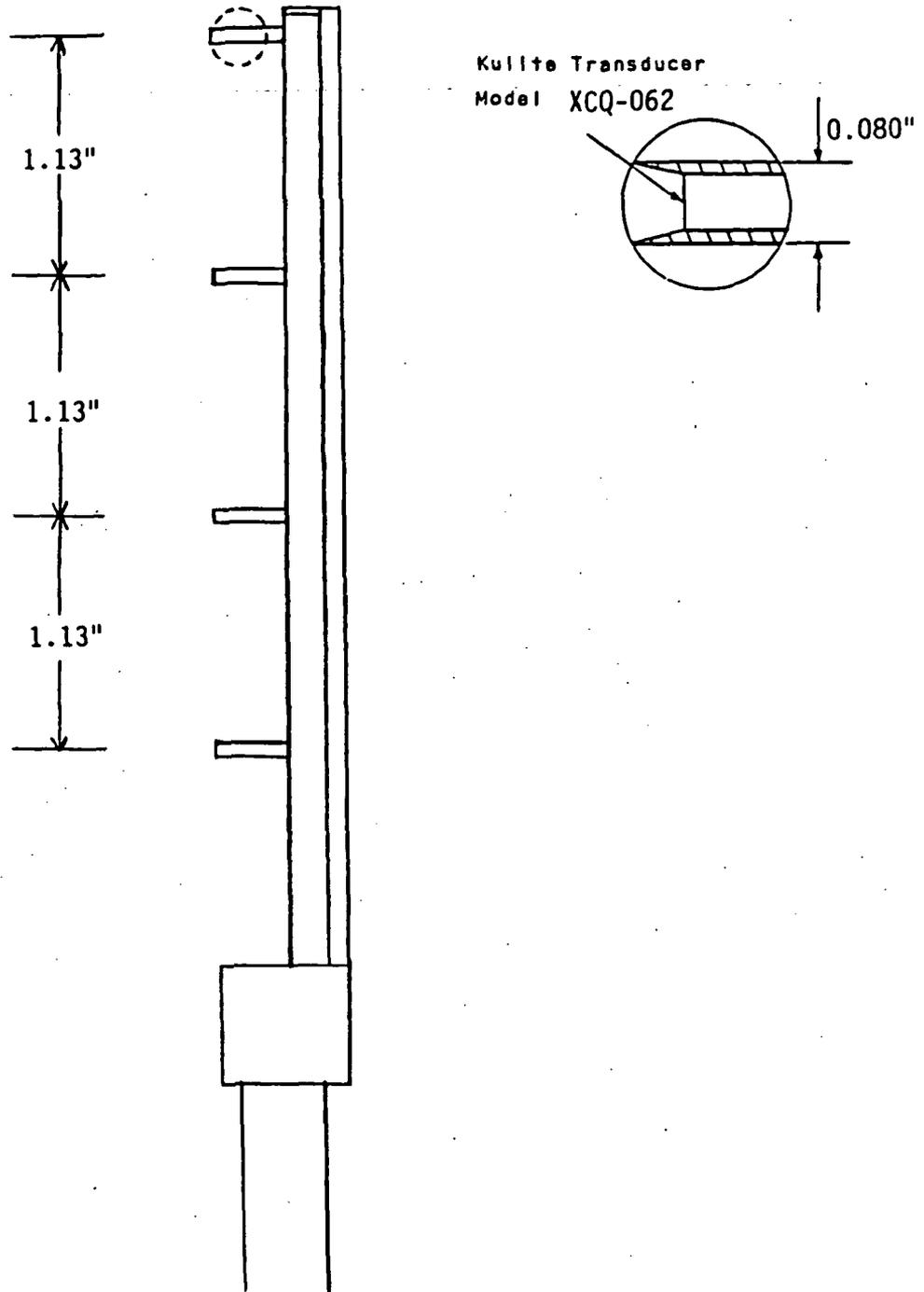
Figure 3.2   High frequency response Total Pressure Rake
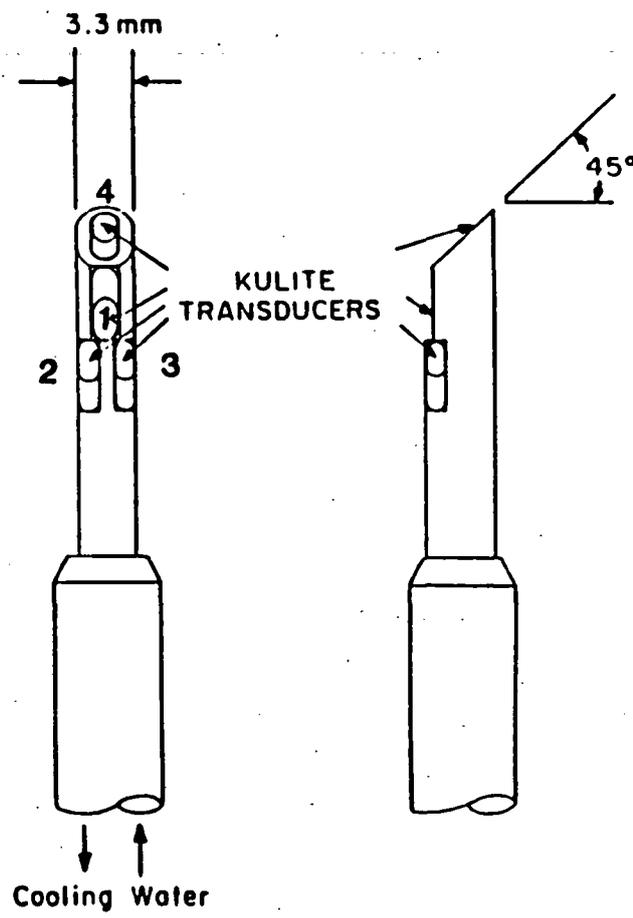
Figure 3.3   High frequency response 4-Way Angle Probe
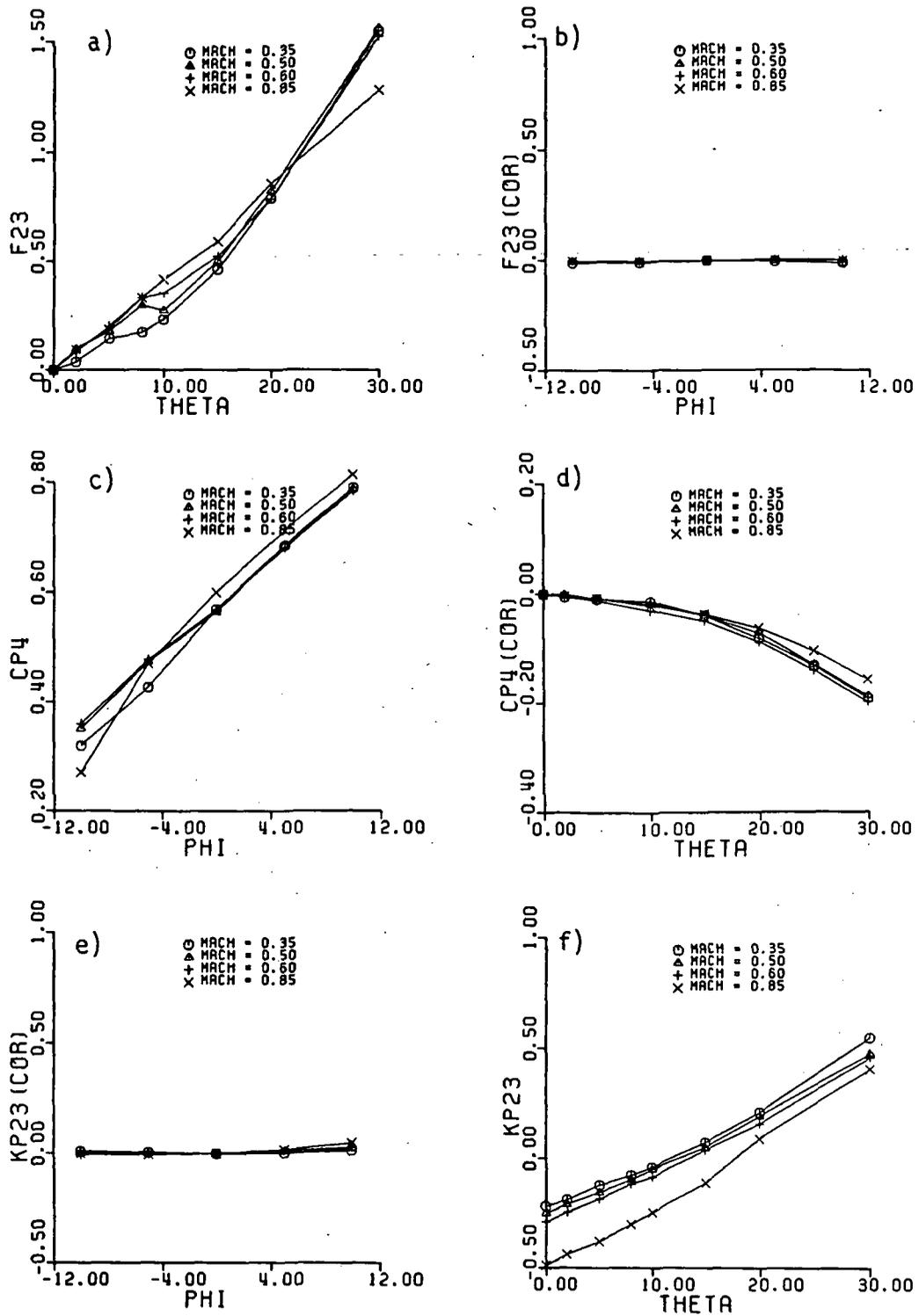
Figure 3.4   4-Way Probe calibration curves for
              tangential and radial flow angle and
              static pressure
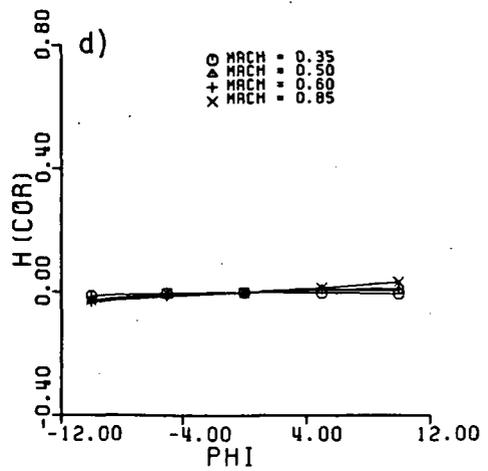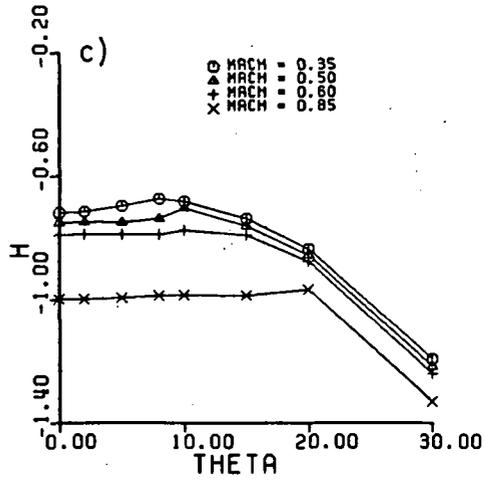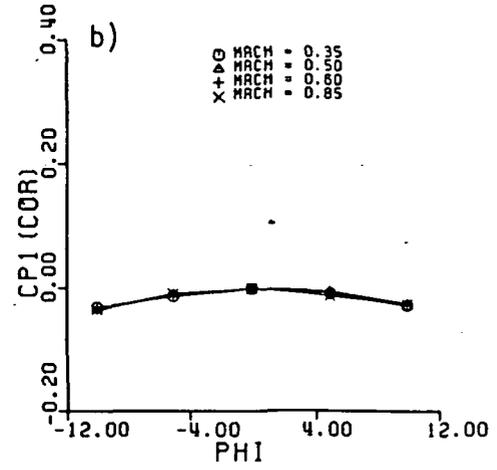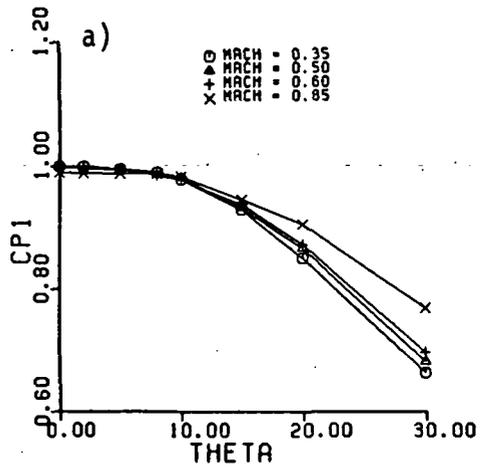
Figure 3.5 4-Way Probe calibration curves for total pressure

HIGH SPEED PROBE TRANSLATOR

WITH CALIBRATION CHAMBER:MOUNTED ON COMPRESSOR CASING
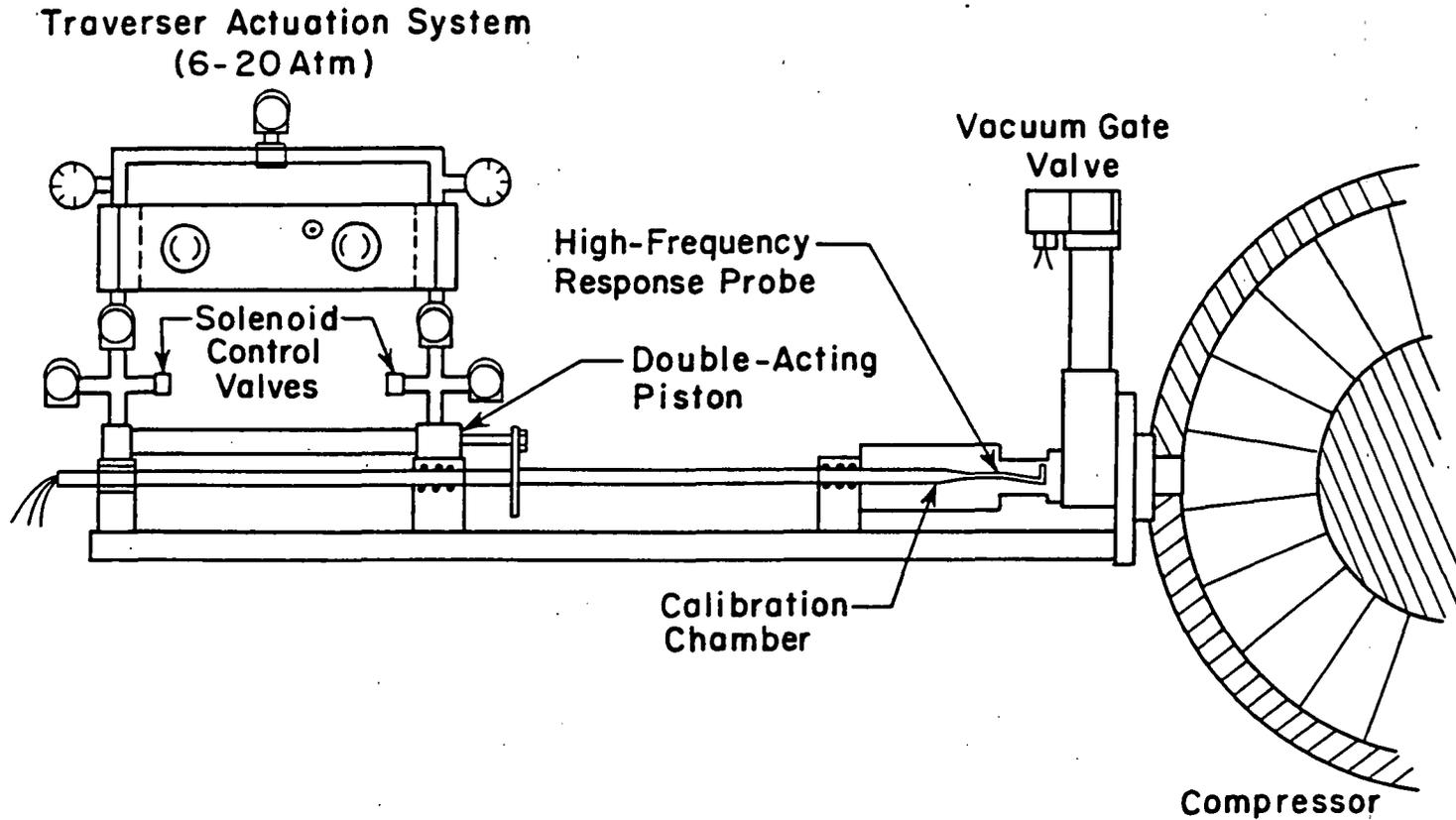
Figure 3.6   High speed probe translator and calibration
chamber mounted on compressor casing

TIME-AVERAGED
ROTOR EXIT TOTAL PRESSURE RATIO
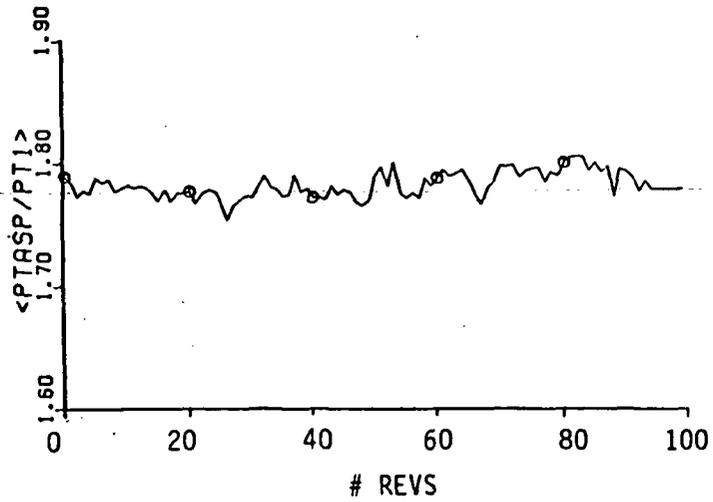
$R/R_T = .93$
89% SPAN
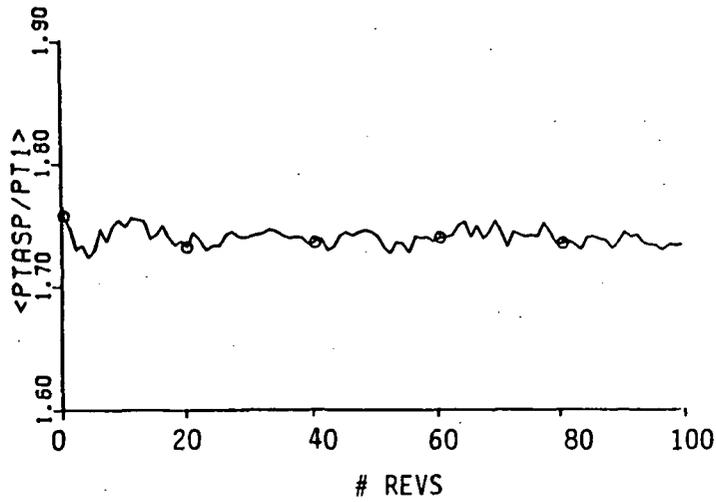
$R/R_T = .82$
66% SPAN
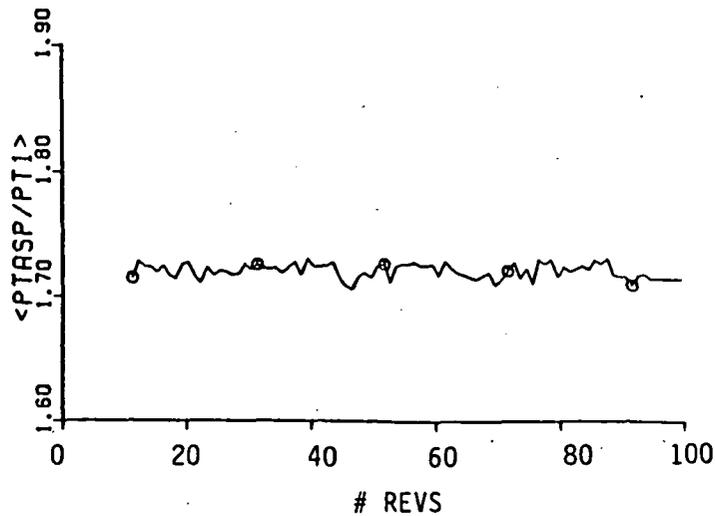
$R/R_T = .70$
43% SPAN

Figure 4.1   Once-per-rev time-averaged rotor exit total pressure ratio for the NASA Lewis Fan at three radial positions
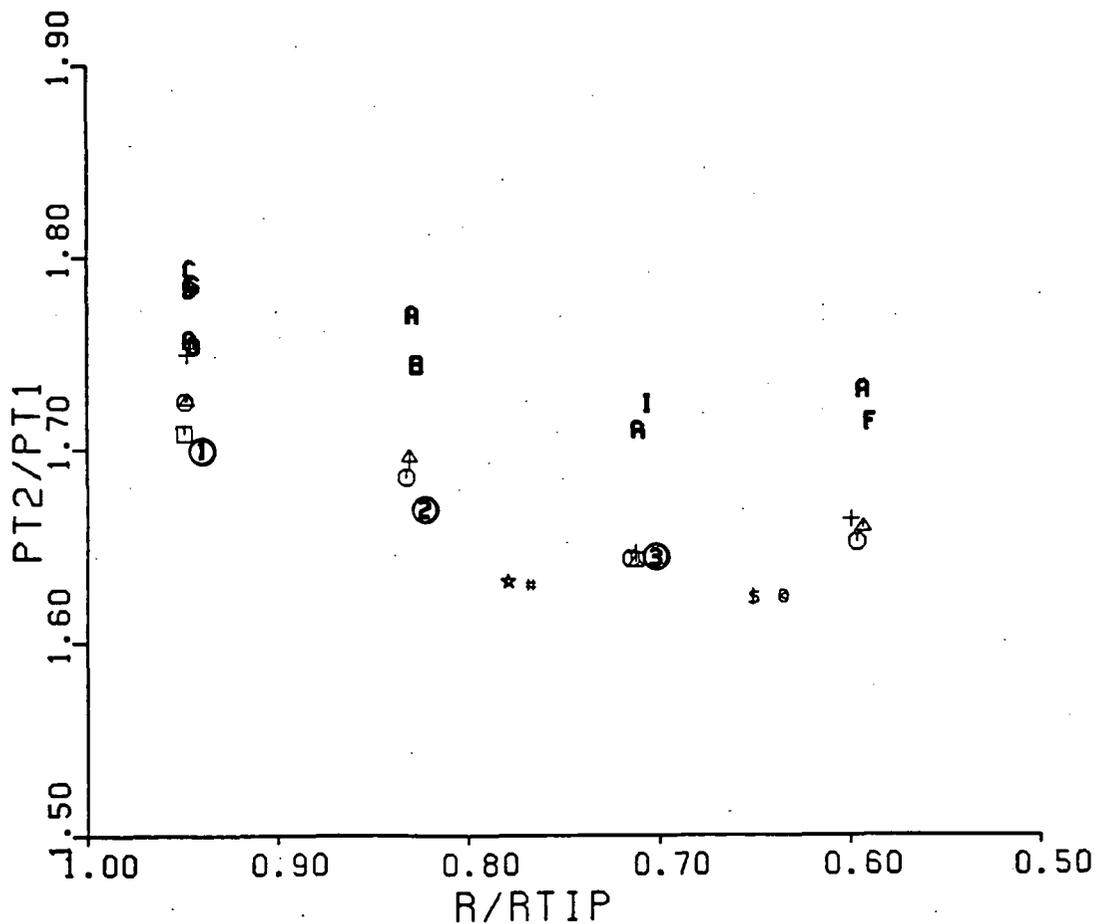
Figure 4.2   Comparison of time-averaged high response total
pressure measurements and conventional aero
measurements for the NASA Lewis Fan

TIME-AVERAGED
ROTOR EXIT STATIC PRESSURE

$R/R_T = .93$
89% SPAN

REVS

$R/R_T = .82$
66% SPAN

REVS

$R/R_T = .70$
43% SPAN

REVS
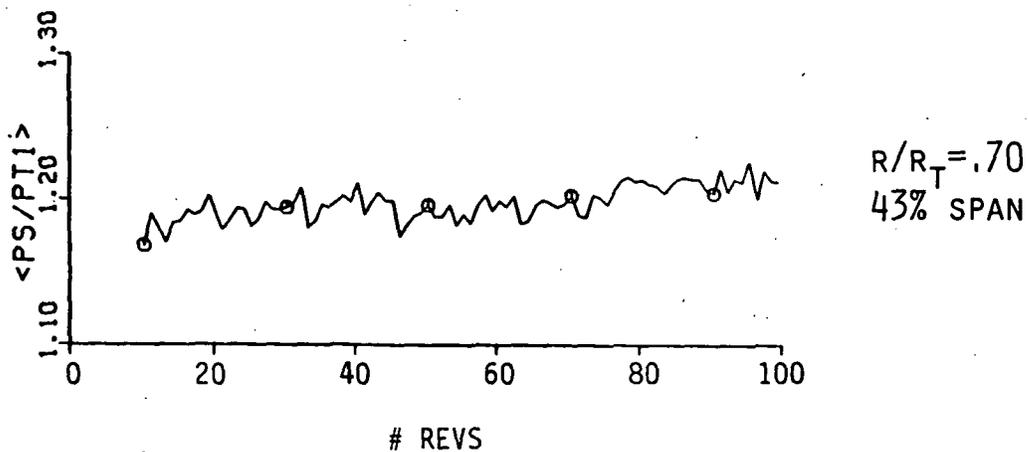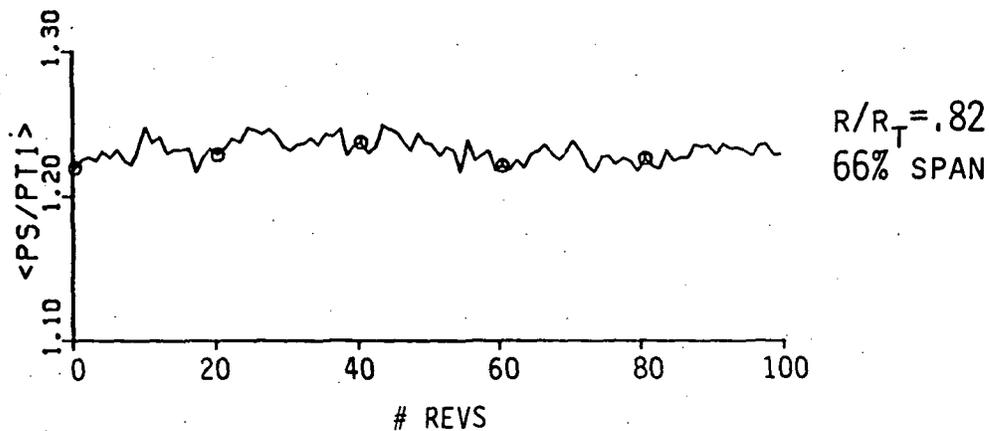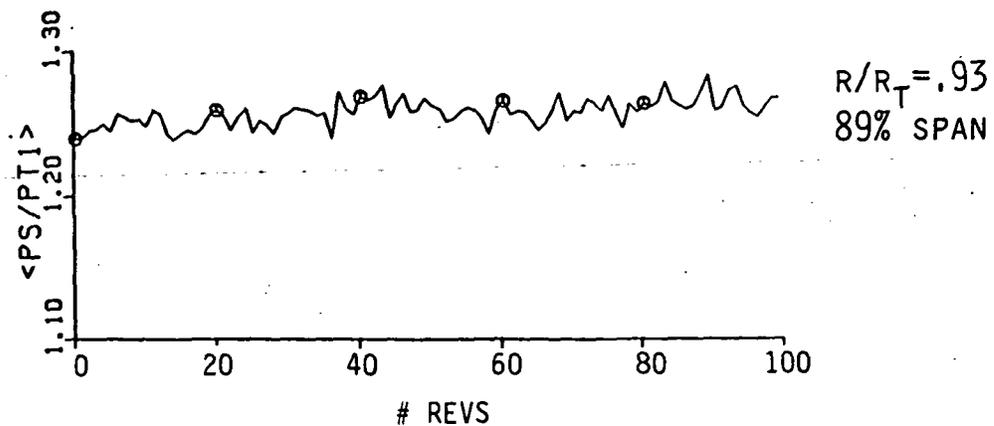
Figure 4.3 Once-per-rev time averaged ratio of the rotor exit
a-c   static pressure to the upstream stagnation pressure
for the NASA Lewis Fan at three radial positions

TIME-AVERAGED
ROTOR EXIT FLOW ANGLE

$R/R_T = .93$
89% SPAN

$R/R_T = .82$
66% SPAN

$R/R_T = .70$
43% SPAN
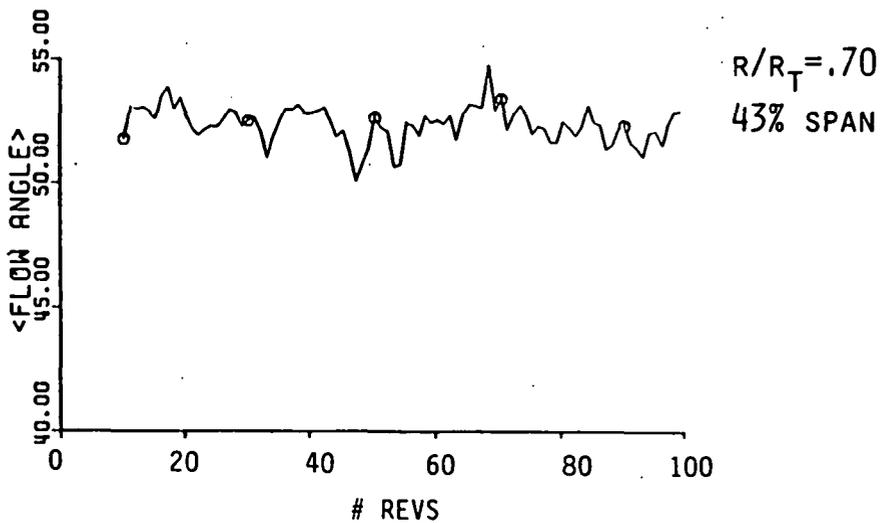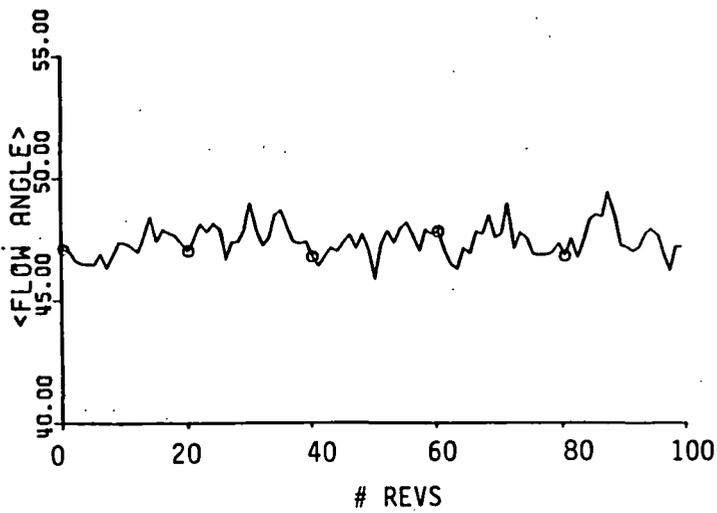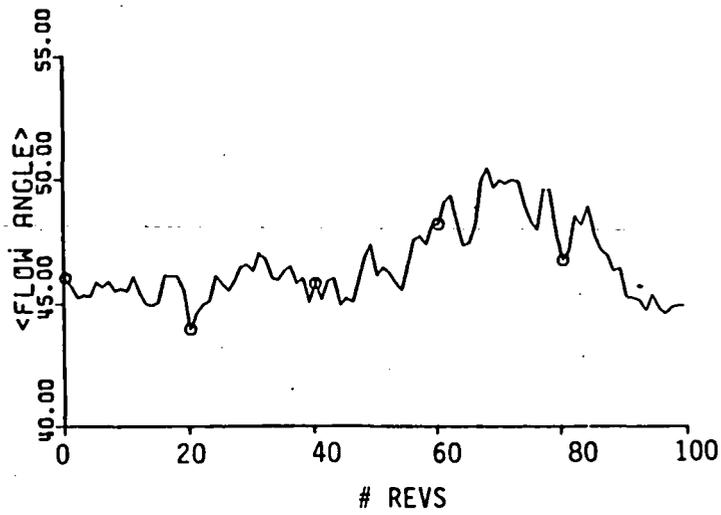
Figure 4.3   Once-per-rev time averaged rotor exit absolute
d-f   tangential flow angle for the NASA Lewis Fan at
             three radial positions

BETA   STN. # 2   MDOT=72.8 LBM/SEC

☉	N225 AERO	☒	N259 AERO	⊃	N283 AERO	①	**N264 4WAY**	
△	N228 AERO	Z	N264 AERO	★	N286 AERO	Ⓙ	N264 LA	
+	N232 AERO	Y	N267 AERO	⊕	N289 AERO	②	**N267 4WAY**	
X	N250 AERO	⋈	N270 AERO	v	N293 AERO	Ⓚ	N267 LA	
◇	N253 AERO	✳	N277 AERO	#	N296 AERO	③	**N270 4WAY**	
♈	N256 AERO	⊠	N280B AERO	$	N299 AERO	Ⓛ	N270 LA	
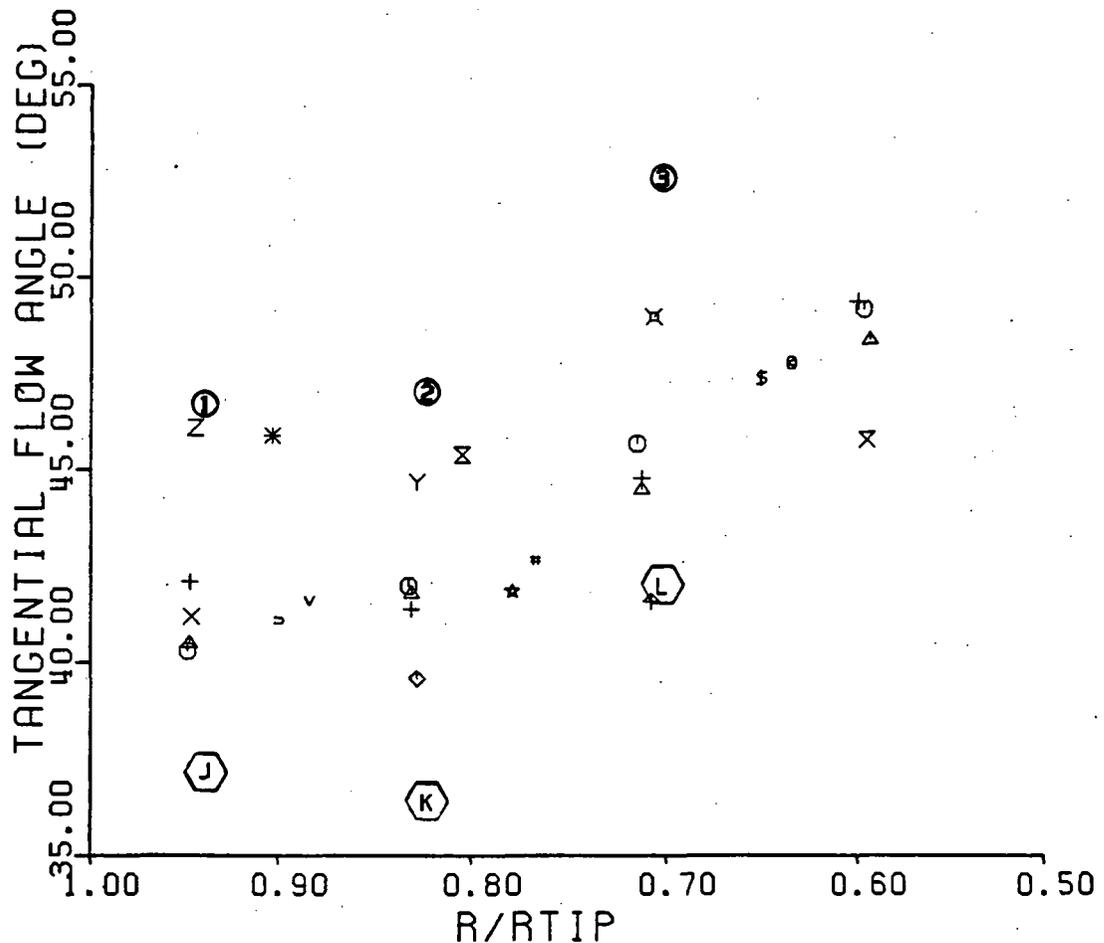
Figure 4.4   Comparison of rotor exit absolute tangential flow angle measurements with time-averaged high response probe data, pitchwise-averaged laser anemometry data, and conventional aero probe data for the NASA Lewis Fan

ROTOR EXIT TOTAL PRESSURE RATIO
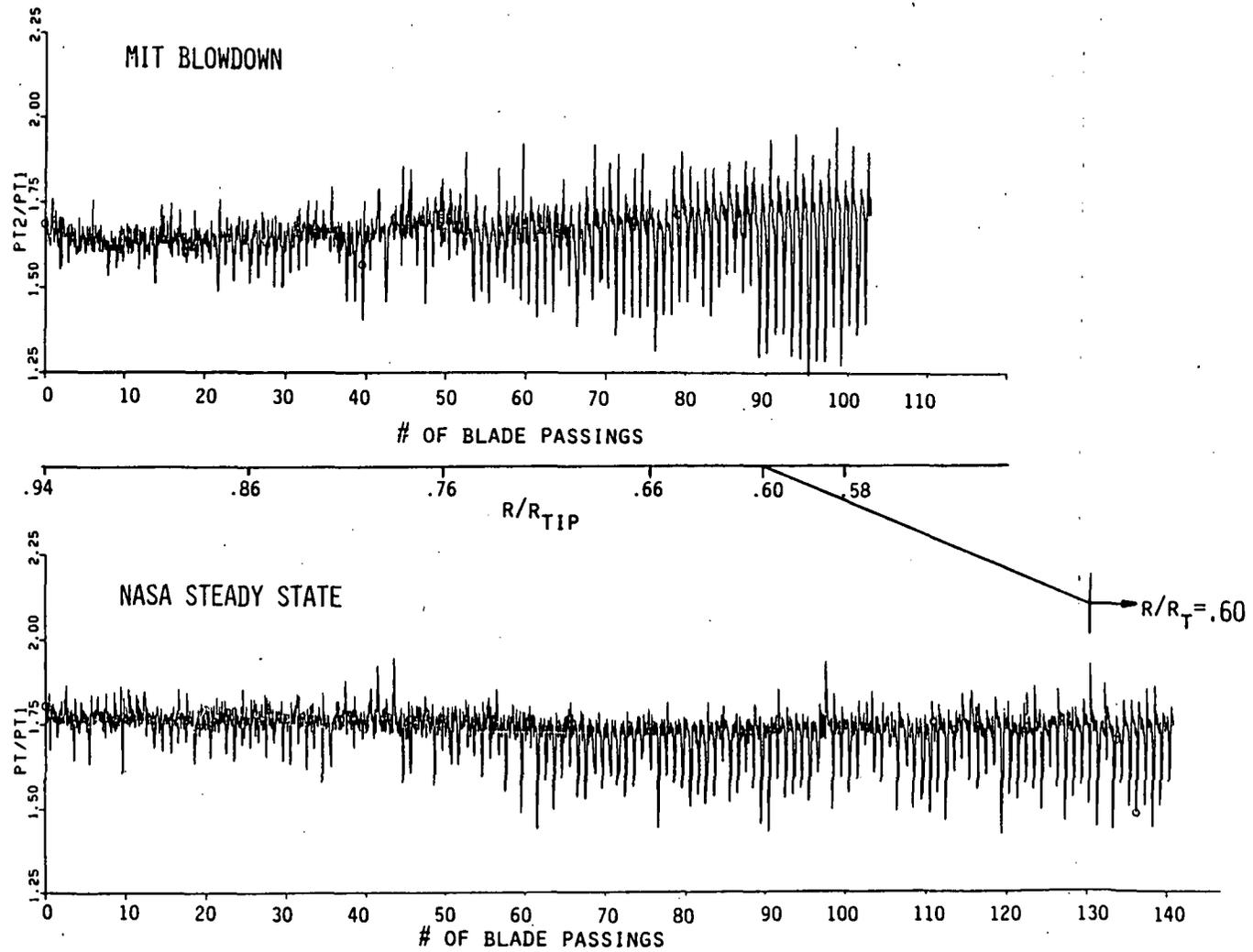
Figure 5.1   Rotor-exit total pressure ratio for a two probe traverses
a) MIT Blowdown test b) NASA Lewis test

ROTOR EXIT TOTAL PRESSURE RATIO
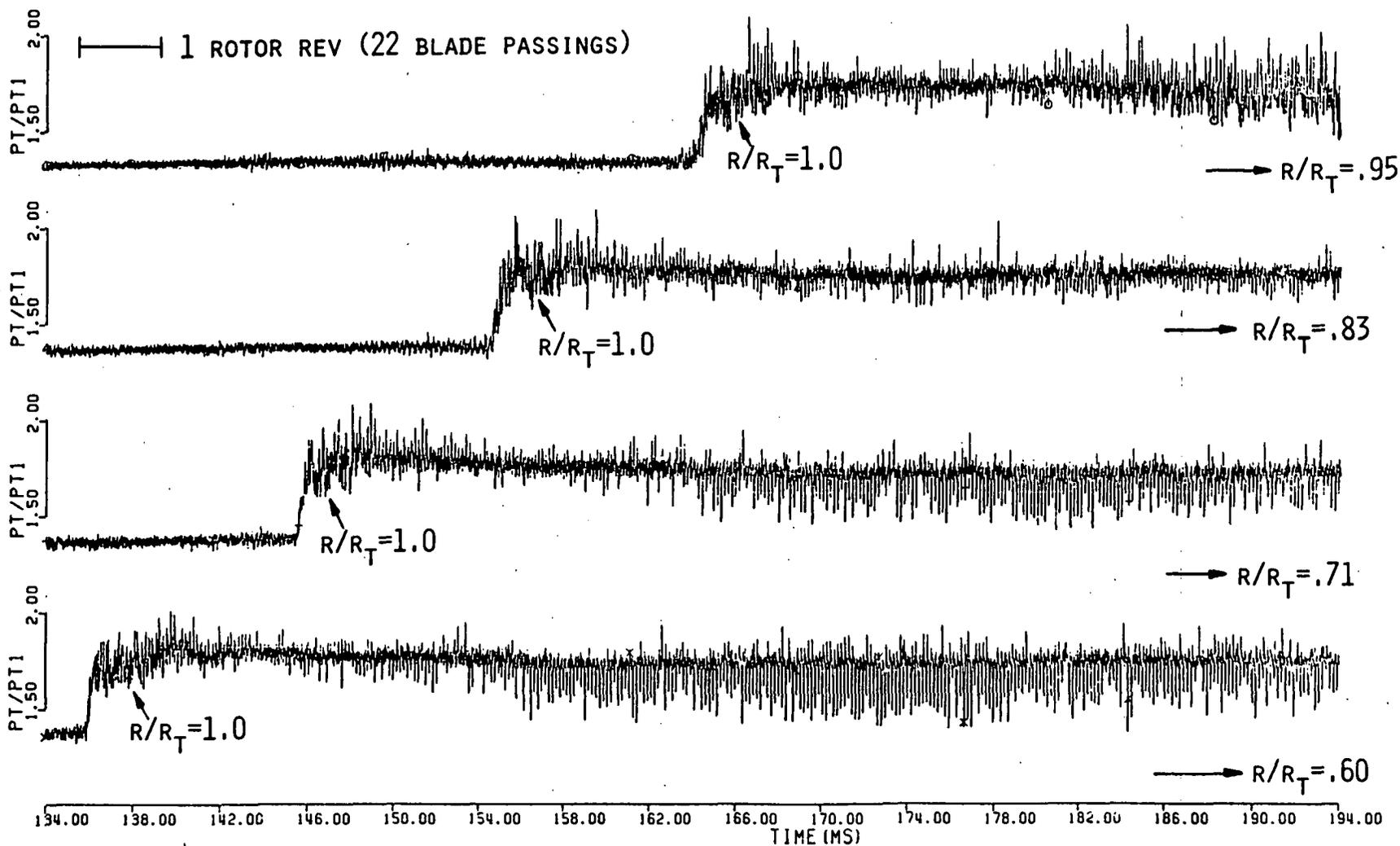
Figure 5.1c   Total pressure ratio measured by the high-response
total pressure rake as it is traversed to a fixed
immersion at the NASA Lewis Facility
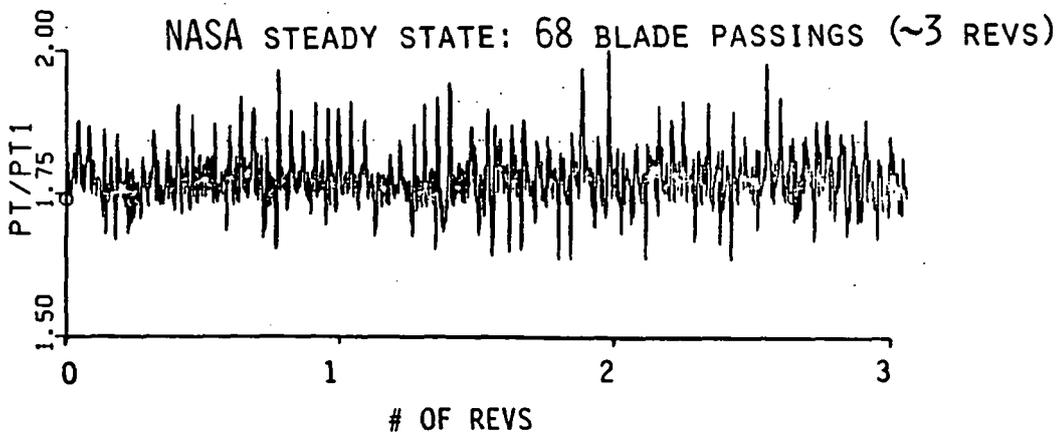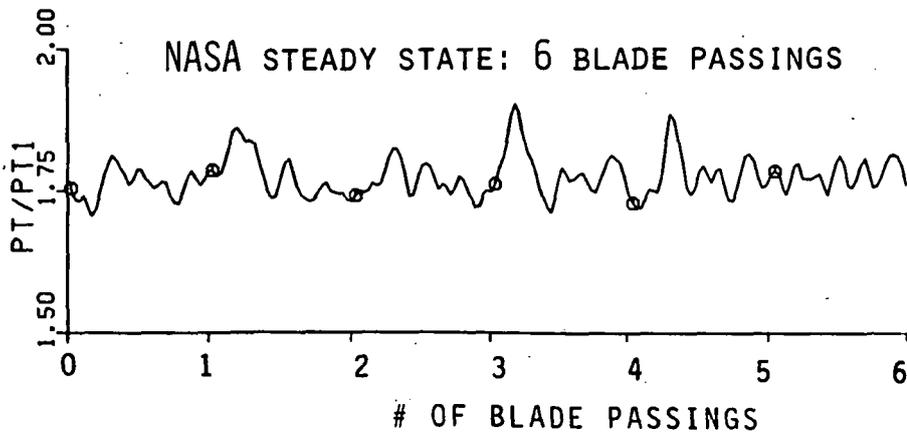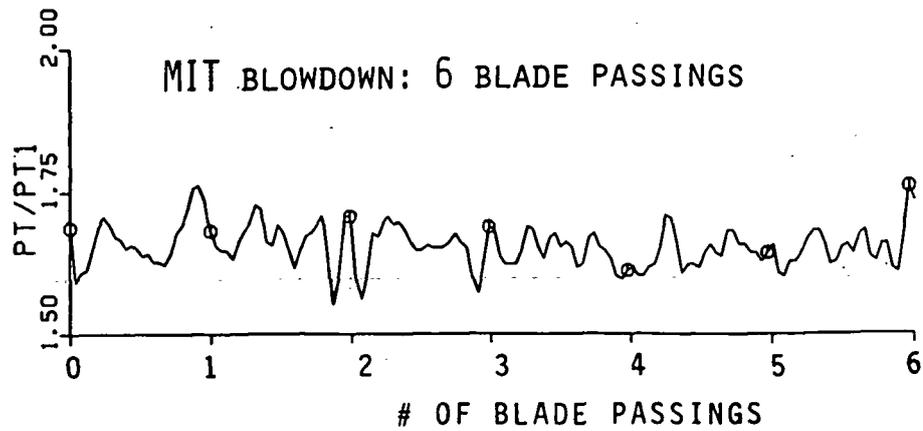
Figure 5.2   Comparison of rotor exit total pressure ratio
measurements in the MIT Blowdown Facility and
the NASA Lewis Steady State Facility at R/Rt=.93
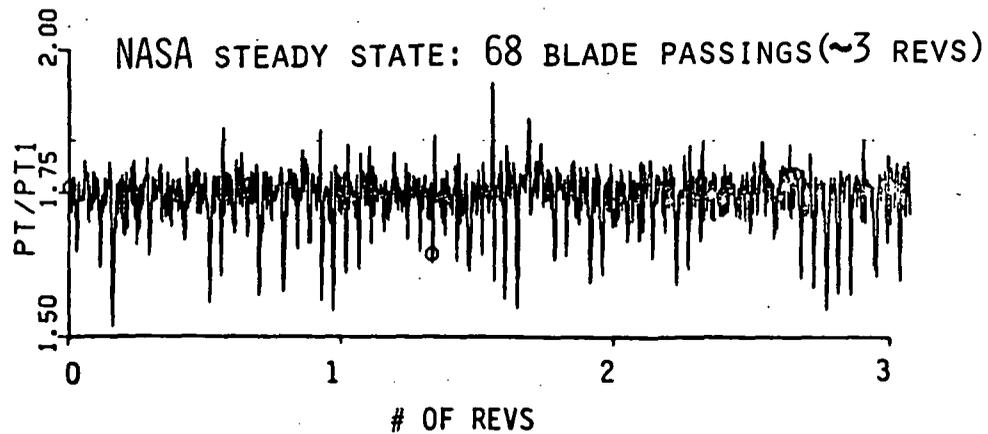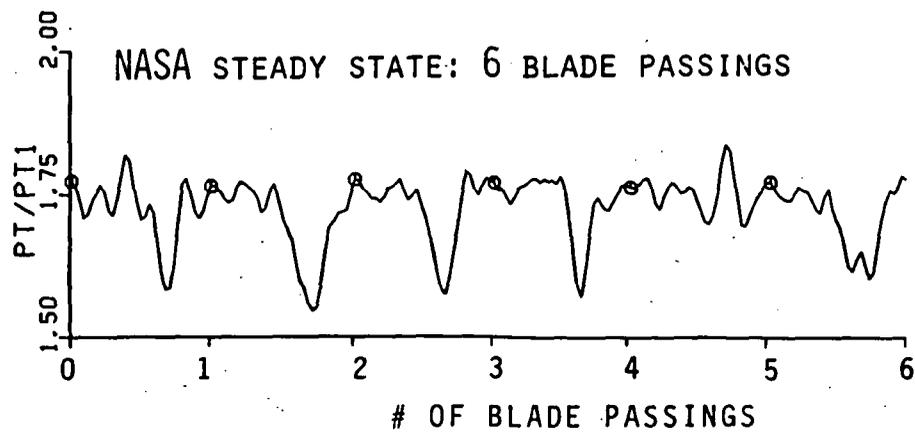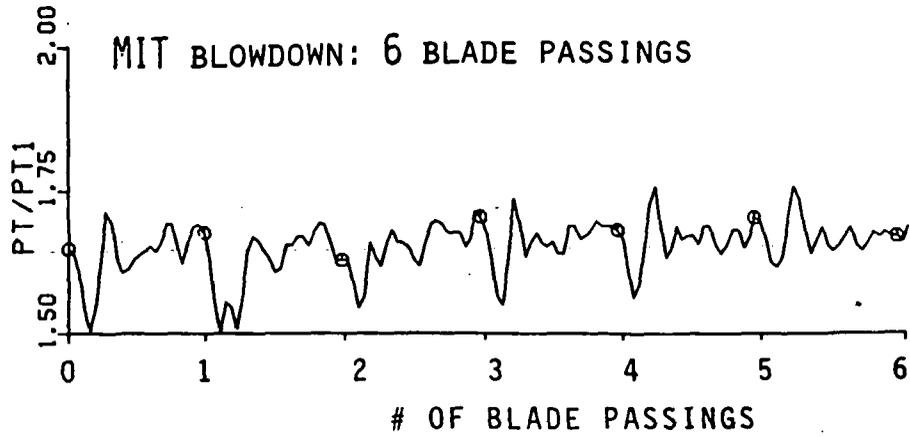
Figure 5.3   Comparison of rotor exit total pressure ratio
               measurements in the MIT Blowdown Facility and
               the NASA Lewis Steady State Facility at R/Rt=.82
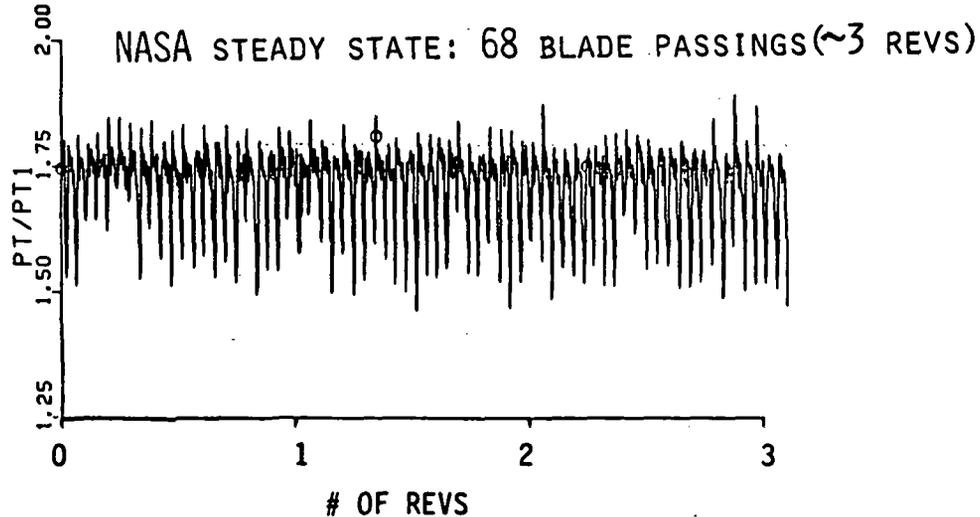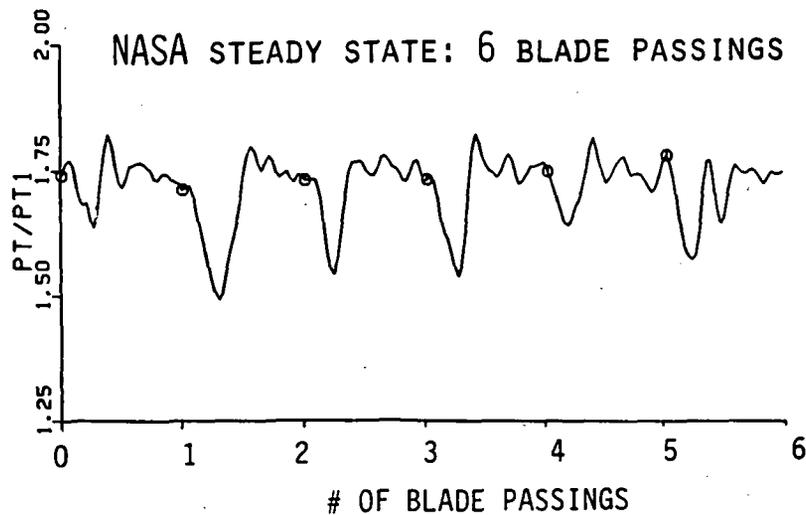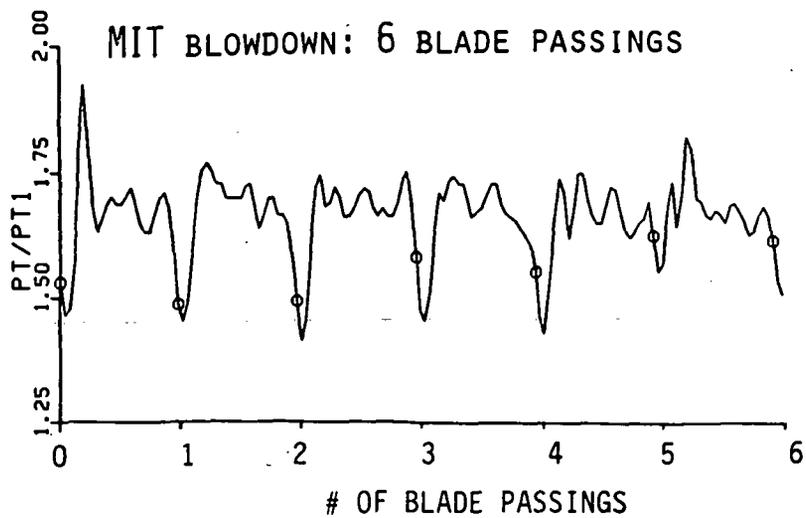
Figure 5.4   Comparison of rotor exit total pressure ratio
             measurements in the MIT Blowdown Facility and
             the NASA Lewis Steady State Facility at R/Rt=.70
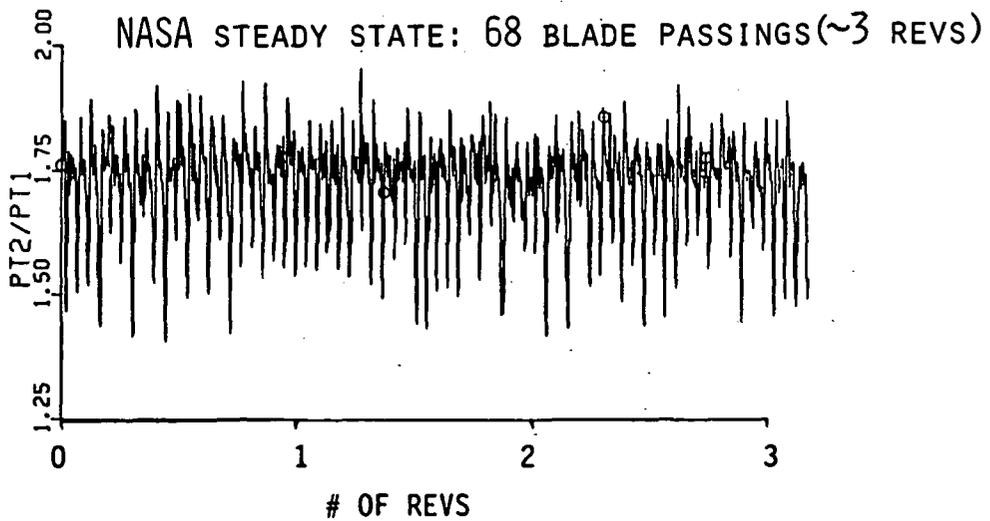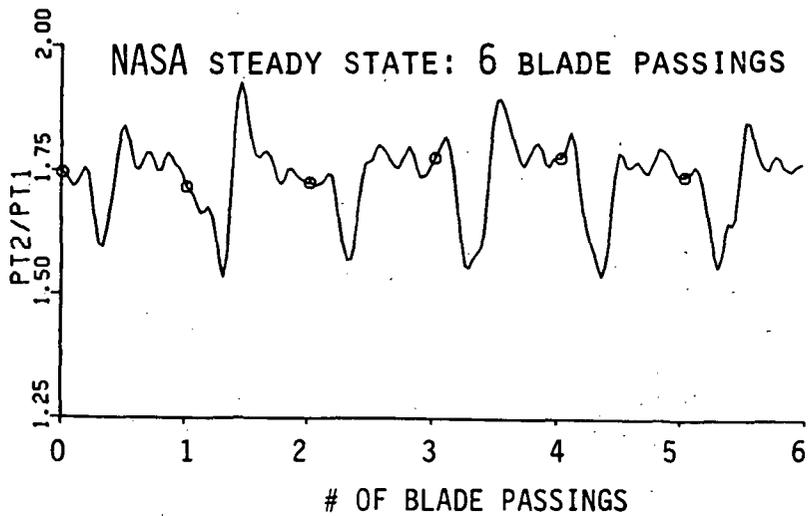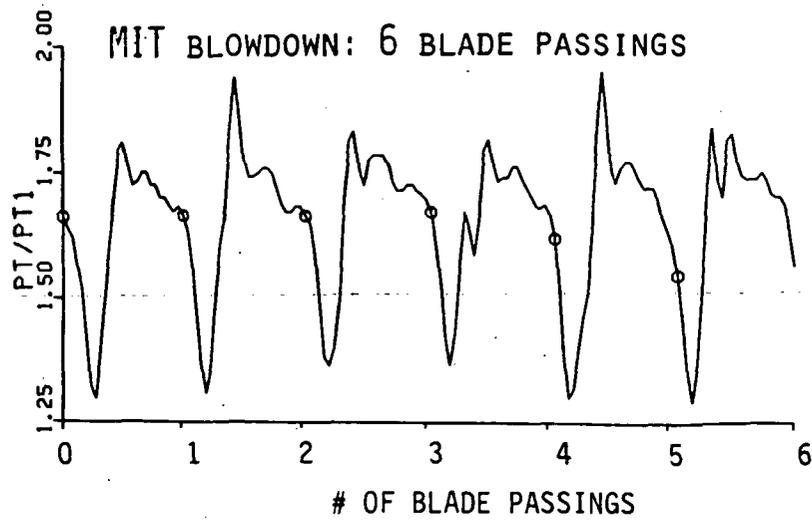
Figure 5.5   Comparison of rotor exit total pressure ratio
measurements in the MIT Blowdown Facility and
the NASA Lewis Steady State Facility at R/Rt=.58

TEST N264
POWER SPECTRAL DENSITY OF PTASP/PTI   (LEWIS)
FREQUENCY RANGE 0.05 KHZ TO 30.0 KHZ

$R/R_T = .93$

TEST N267
POWER SPECTRAL DENSITY OF PTASP/PTI   (LEWIS)
FREQUENCY RANGE 0.05 KHZ TO 30.0 KHZ

$R/R_T = .82$

TEST N270
POWER SPECTRAL DENSITY OF PTASP/PTI   (LEWIS)
FREQUENCY RANGE 0.05 KHZ TO 30.0 KHZ

$R/R_T = .70$

TEST N273
POWER SPECTRAL DENSITY OF PTASP/PTI   (LEWIS)
FREQUENCY RANGE 0.05 KHZ TO 30.0 KHZ

$R/R_T = .58$

Figure 5.6   Power spectral densities of total pressure
measurements for four fixed immersion tests at
the NASA Lewis facility

ROTOR EXIT TOTAL PRESSURE RATIO (RAKE)

$R/R_T = .95$

$R/R_T = .83$

$R/R_T = .71$

$R/R_T = .60$

OF BLADE PASSINGS
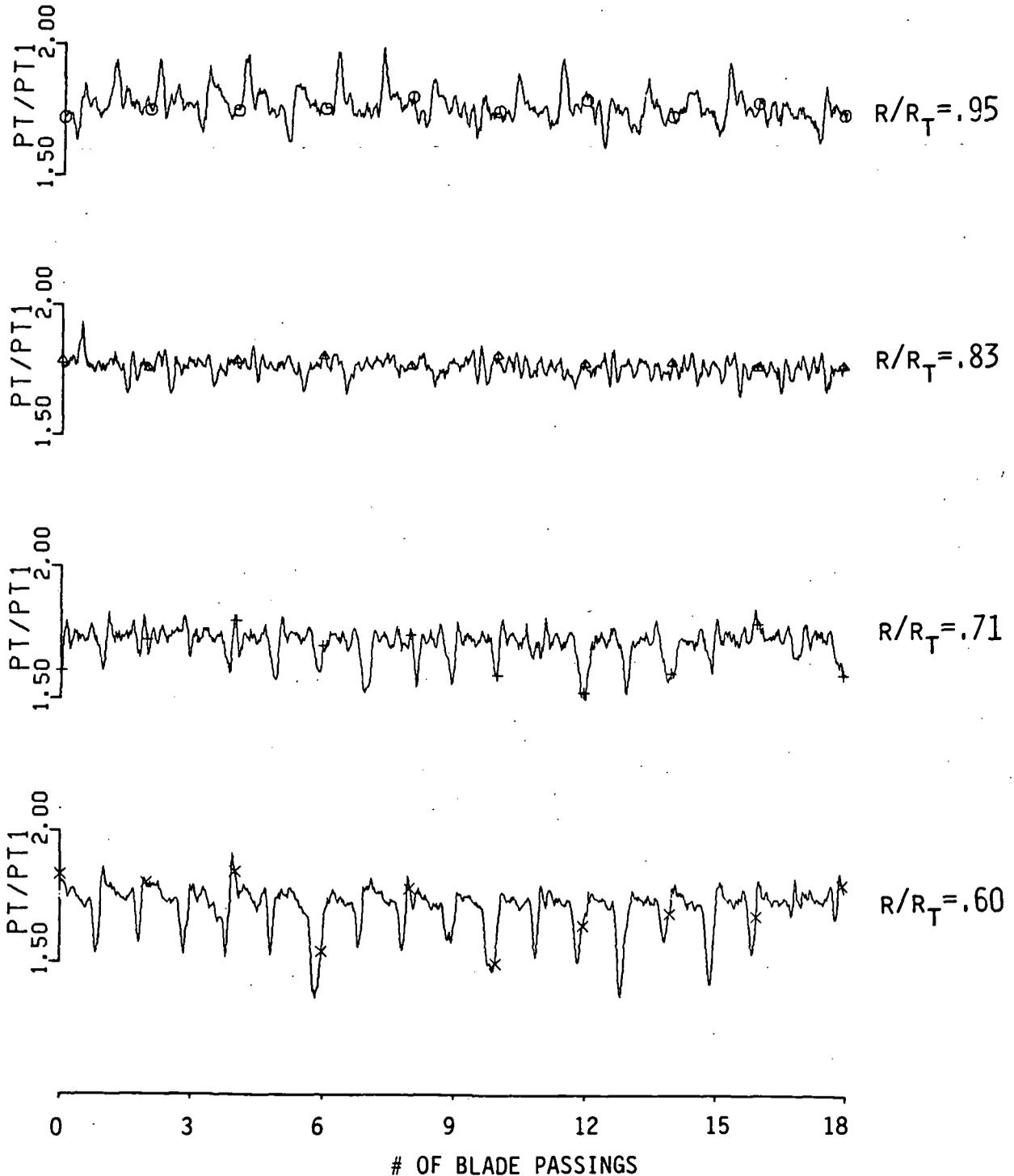
Figure 5.7   Instantaneous time traces of the rotor exit total
             pressure ratio at four spanwise locations taken
             simultaneously with the total pressure rake for a
             period of slightly less than one rotor revolution

ROTOR EXIT TOTAL PRESSURE RATIO (RAKE)

$R/R_T = .95$

$R/R_T = .83$

$R/R_T = .71$

$R/R_T = .60$

OF REVS
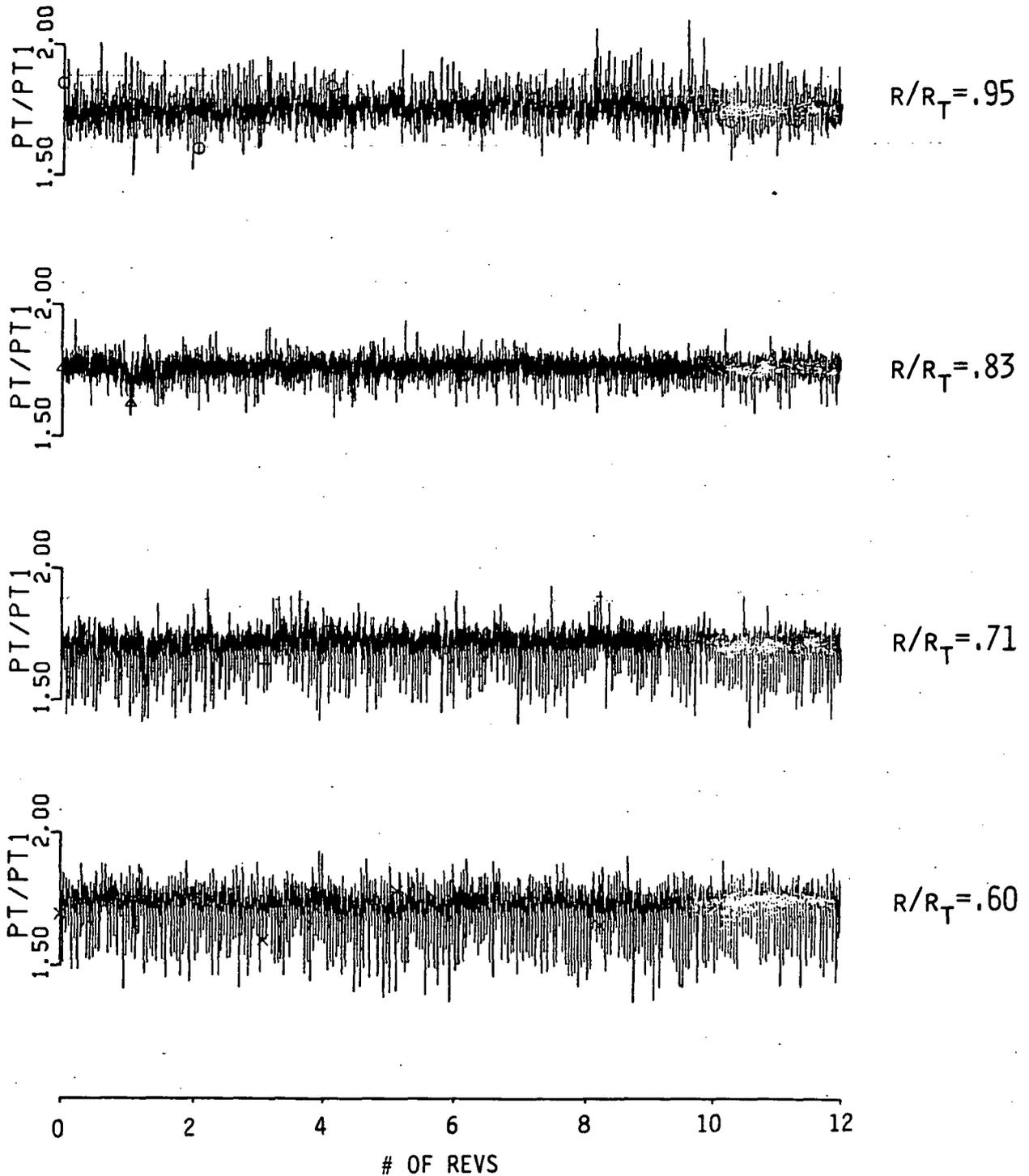
Figure 5.8   Instantaneous time traces of the rotor exit total pressure ratio at four spanwise locations taken simultaneously with the total pressure rake for a period of about ten rotor revolutions

TEST N221A

POWER SPECTRAL DENSITY OF RAKE   R/RT=.95   90%

TO=285.00 MS   TF=300.87 MS   4096 PTS
FREQUENCY RANGE 0.05 KHZ TO 30.0 KHZ
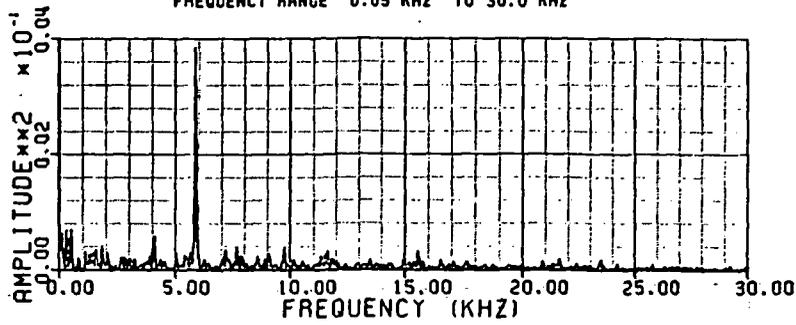
TEST N221A

POWER SPECTRAL DENSITY OF RAKE   R/RT=.83   67%

TO=285.00 MS   TF=300.87 MS   4096 PTS
FREQUENCY RANGE 0.05 KHZ TO 30.0 KHZ
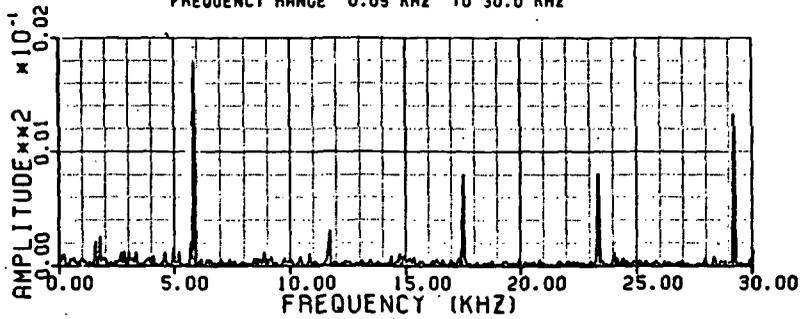
TEST N221A

POWER SPECTRAL DENSITY OF RAKE   R/RT=.71   44%

TO=285.00 MS   TF=300.87 MS   4096 PTS
FREQUENCY RANGE 0.05 KHZ TO 30.0 KHZ
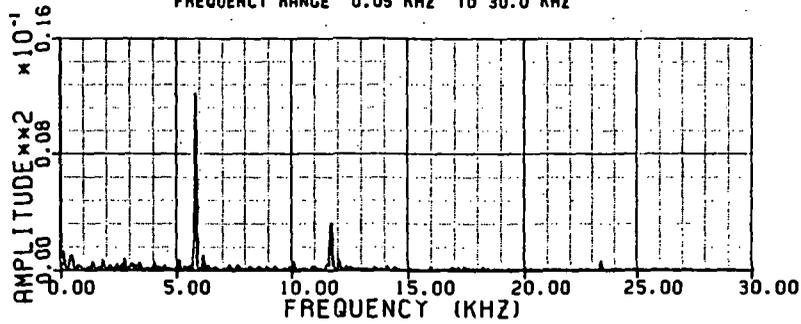
TEST N221A

POWER SPECTRAL DENSITY OF RAKE   R/RT=.60   20%

TO=285.00 MS   TF=300.87 MS   4096 PTS
FREQUENCY RANGE 0.05 KHZ TO 30.0 KHZ
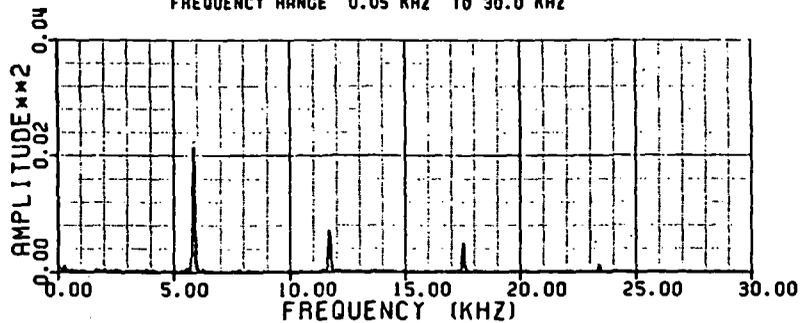
Figure 5.9   Power spectral densities of the rotor exit total
pressure ratio at four spanwise locations taken
simultaneously with the total pressure rake

ROTOR EXIT TOTAL PRESSURE RATIO
(INSTANTANEOUS)

REV #1
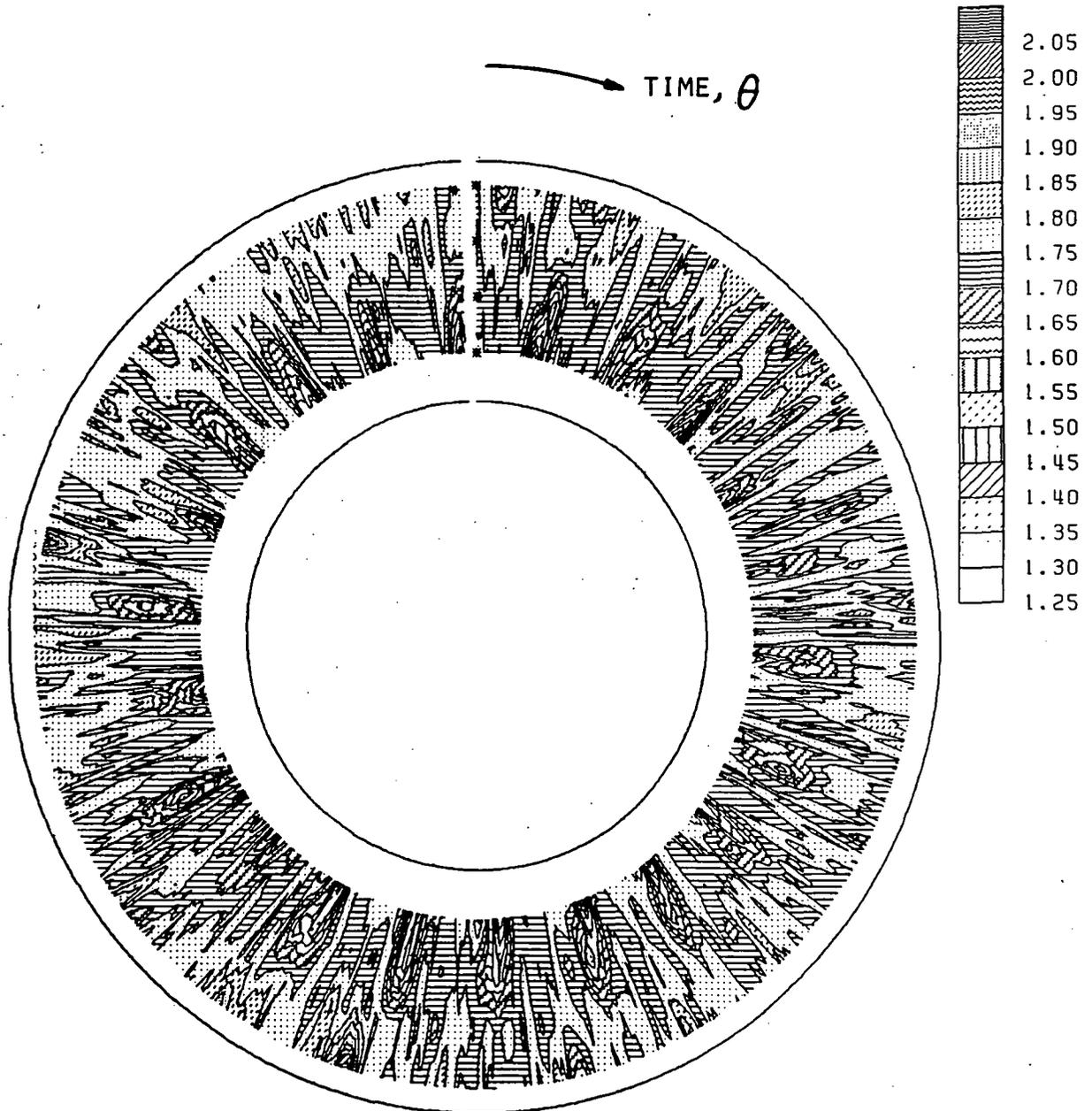
Figure 5.10   Contours of the instantaneous rotor exit total
pressure ratio from measurements obtained with
the total pressure rake for approximately one
rotor revolution

ROTOR EXIT TOTAL PRESSURE RATIO
(INSTANTANEOUS)
REV #2

	2.05
	2.00
	1.95
	1.90
	1.85
	1.80
	1.75
	1.70
	1.65
	1.60
	1.55
	1.50
	1.45
	1.40
	1.35
	1.30
	1.25
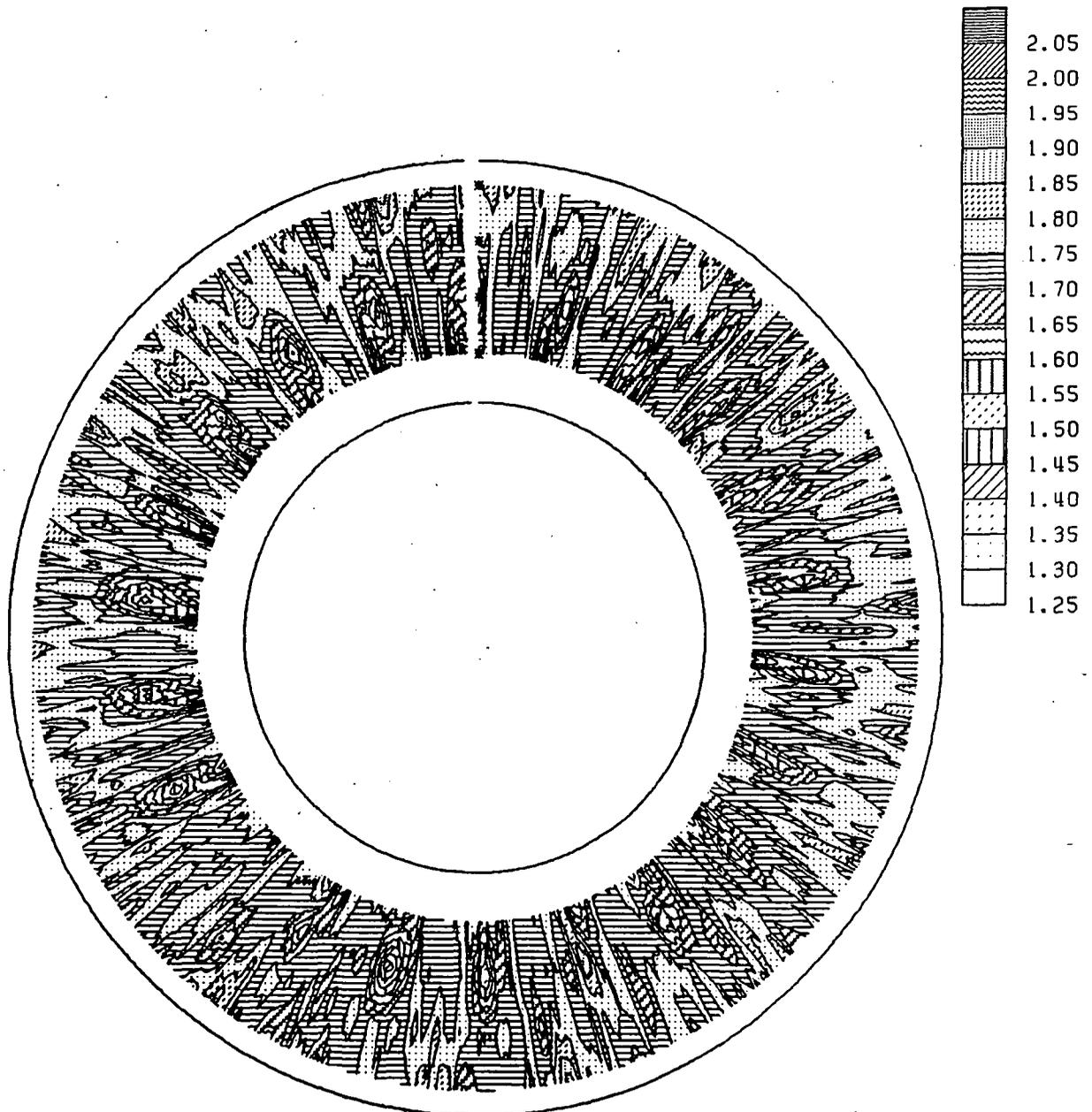
Figure 5.11   Contours of the instantaneous rotor exit total
pressure ratio for the rotor revolution which
immediately succeeds the revolution shown in
figure 5.1Ø

ROTOR EXIT TOTAL PRESSURE RATIO
(ENSEMBLE AVERAGED)
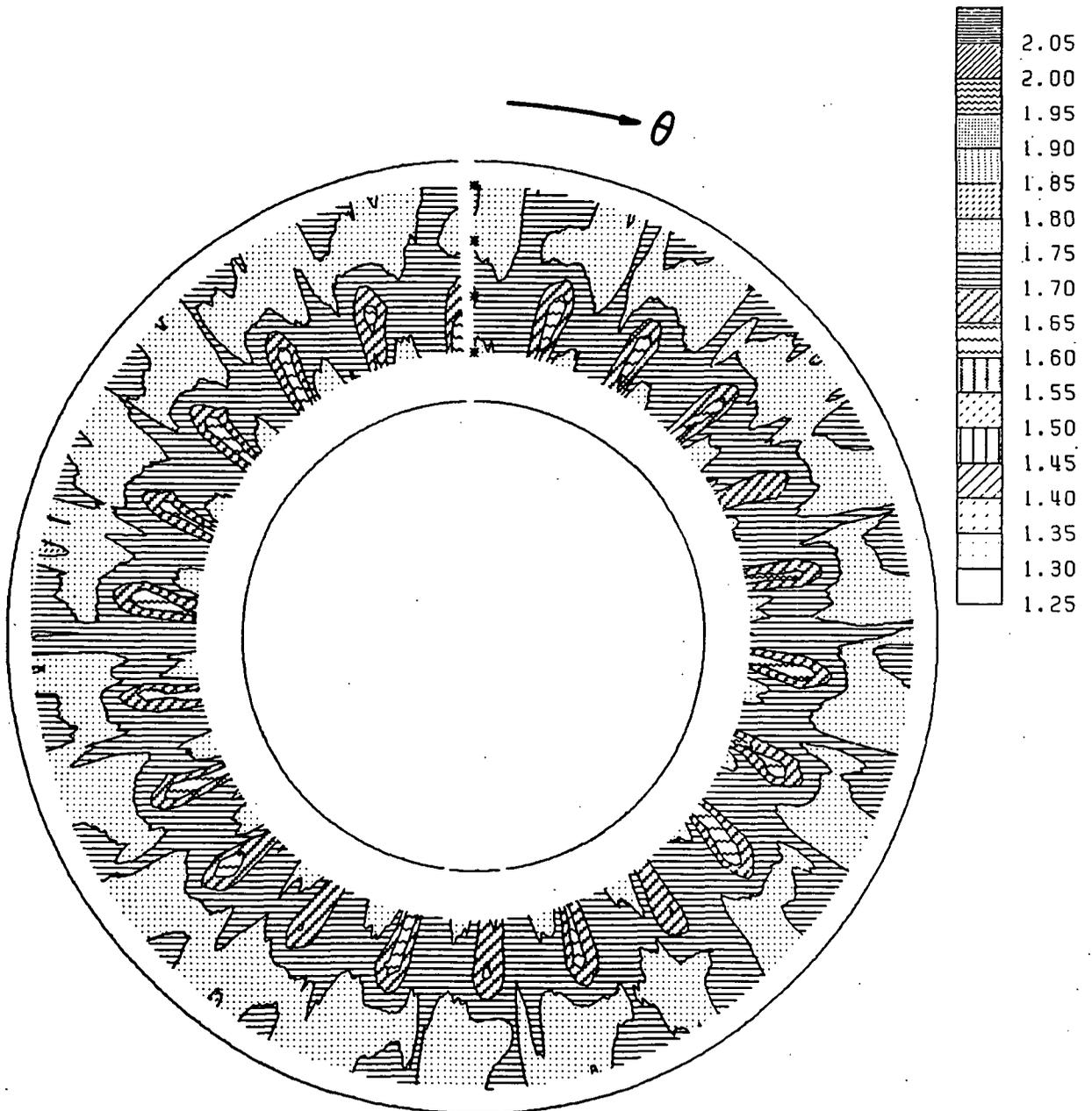
Figure 5.12   Contours of the blade by blade 30 revolution
ensemble-averaged rotor exit total pressure
ratio from measurements obtained with the
total pressure rake

ROTOR EXIT STATIC PRESSURE (MIT BLOWDOWN)
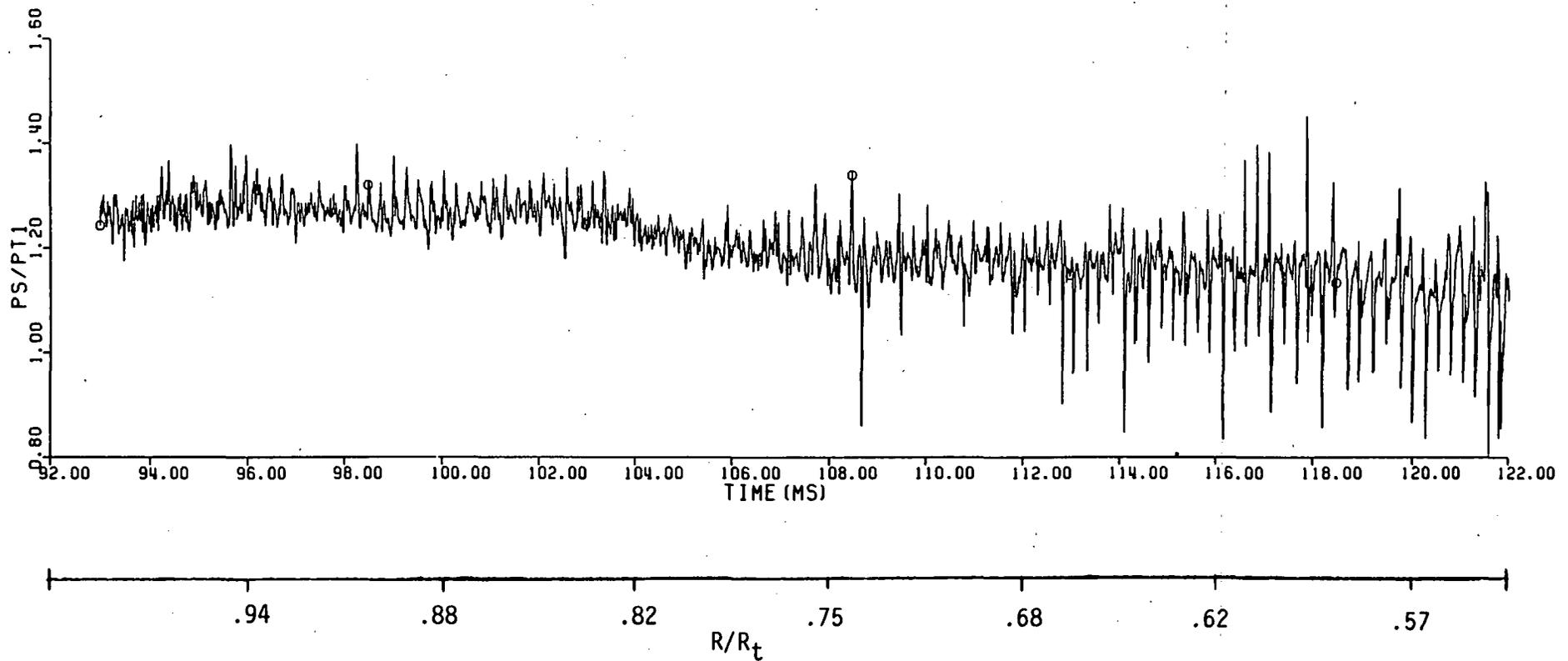
Figure 5.13   Ratio of rotor exit static pressure to upstream total pressure
measured during a traverse of the 5-Way sphere probe in an
MIT Blowdown Test

ROTOR EXIT STATIC PRESSURE

MIT BLOWDOWN: 6 BLADE PASSINGS

NASA STEADY STATE: 6 BLADE PASSINGS

NASA STEADY STATE: 68 BLADE PASSINGS
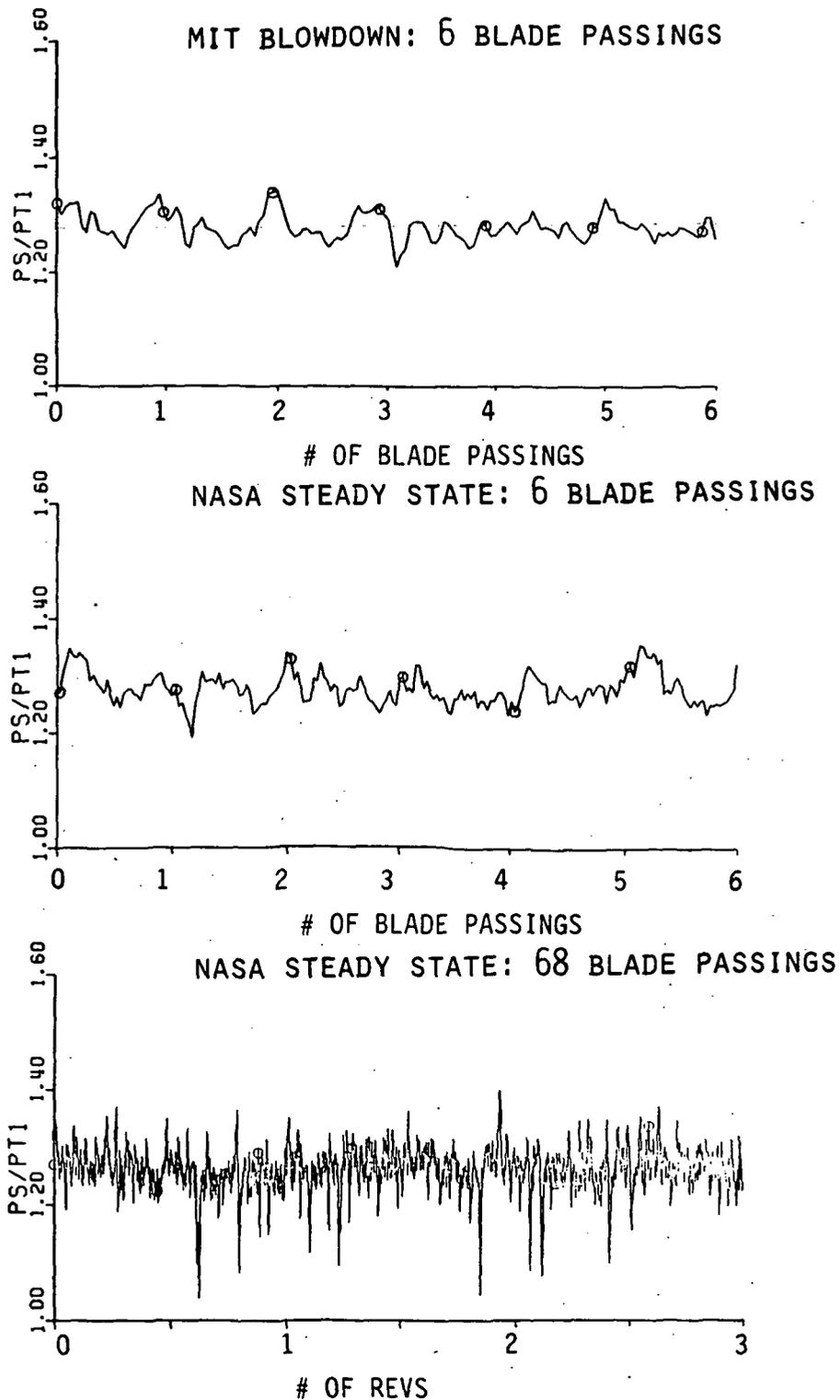
Figure 5.14   Comparison of the ratio of rotor exit static
pressure to upstream total pressure at R/Rt=.93
in the MIT Blowdown Facility with the 5-Way sphere
probe and the NASA Lewis Steady State Facility
with the 4-Way cylinder probe

ROTOR EXIT STATIC PRESSURE
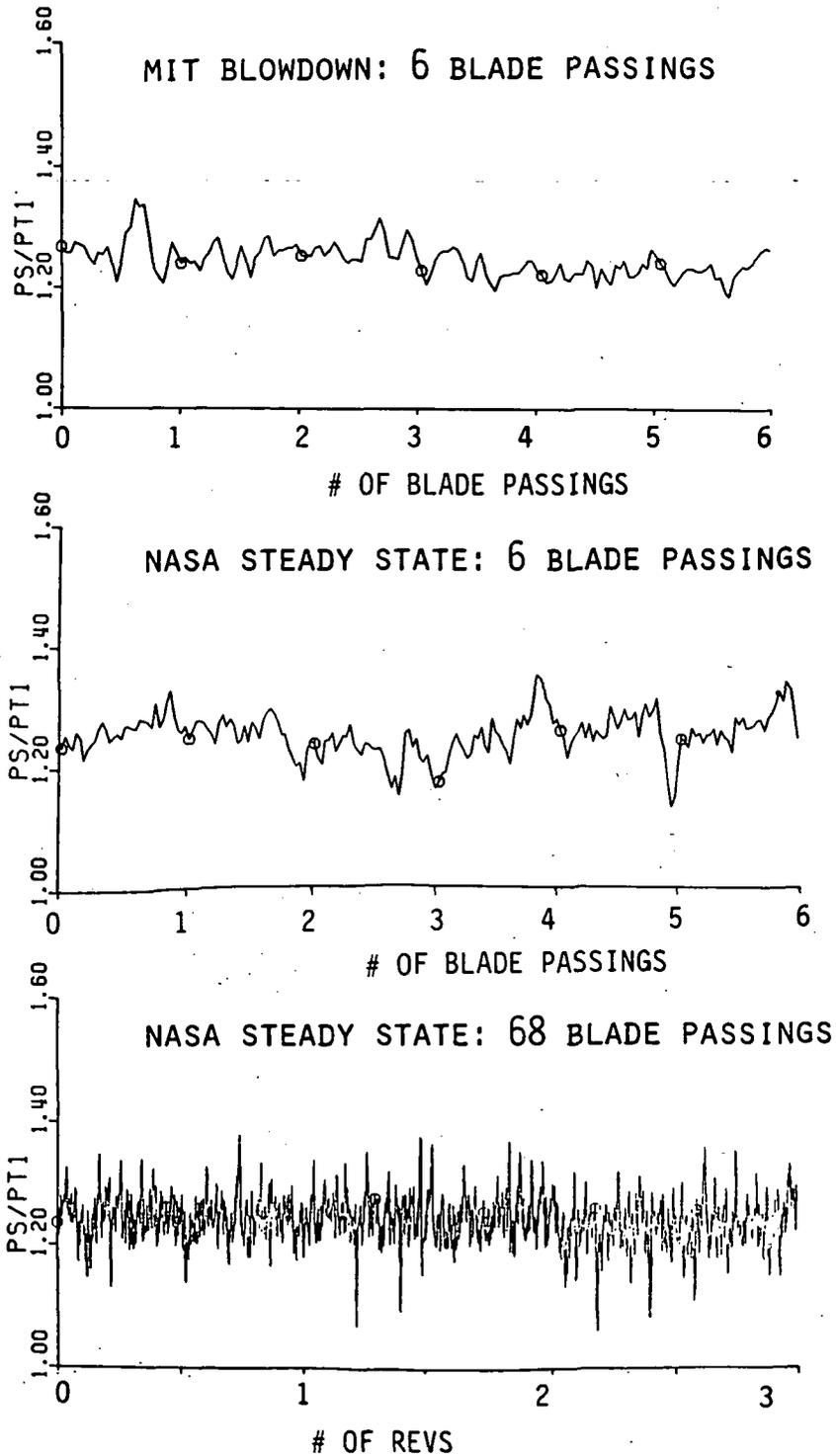
Figure 5.15   Comparison of the ratio of rotor exit static
               pressure to upstream total pressure at R/Rt=.82
               in the MIT Blowdown Facility with the 5-Way sphere
               probe and the NASA Lewis Steady State Facility
               with the 4-Way cylinder probe

ROTOR EXIT STATIC PRESSURE
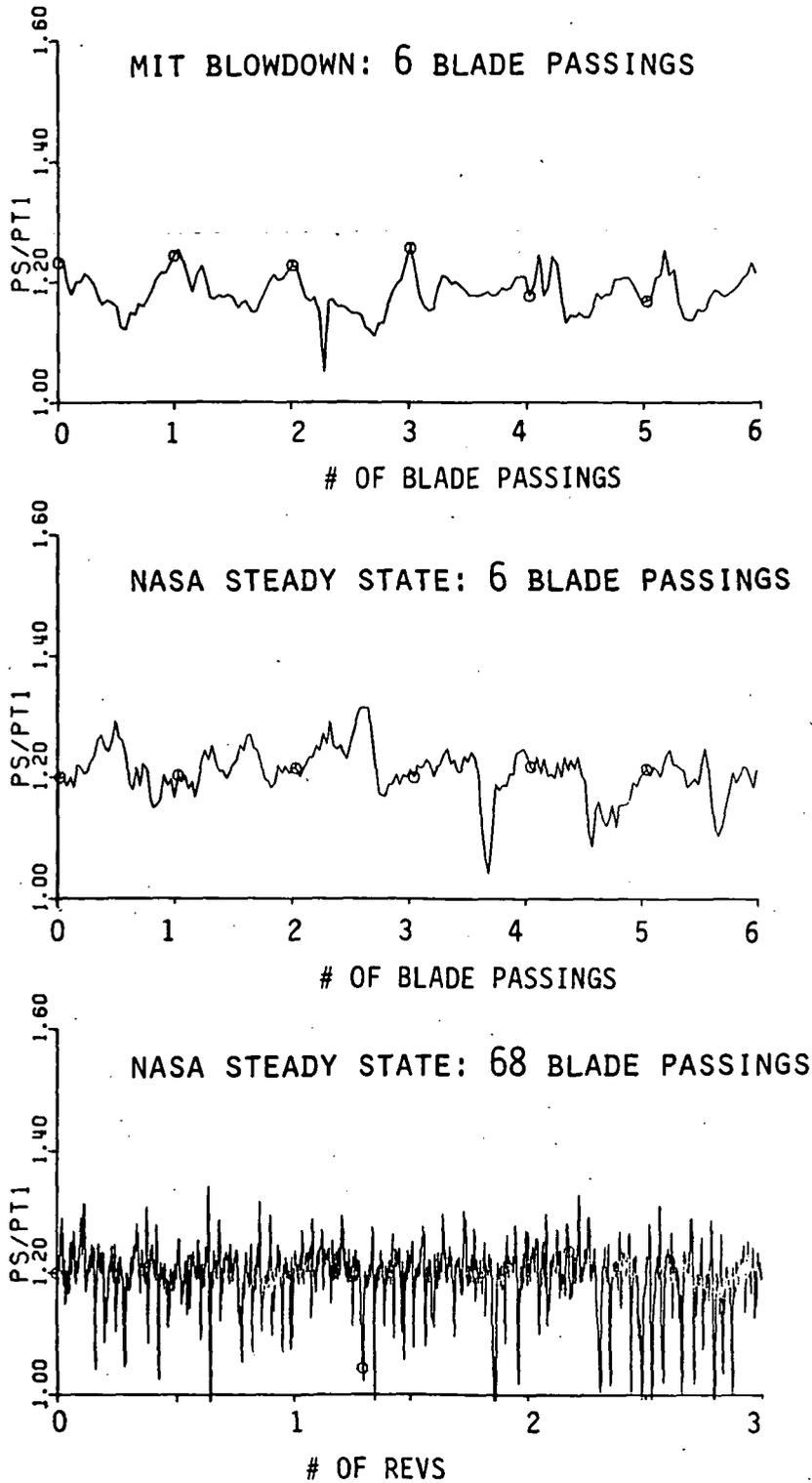
Figure 5.16   Comparison of the ratio of rotor exit static
pressure to upstream total pressure at R/Rt=.70
in the MIT Blowdown Facility with the 5-Way sphere
probe and the NASA Lewis Steady State Facility
with the 4-Way cylinder probe
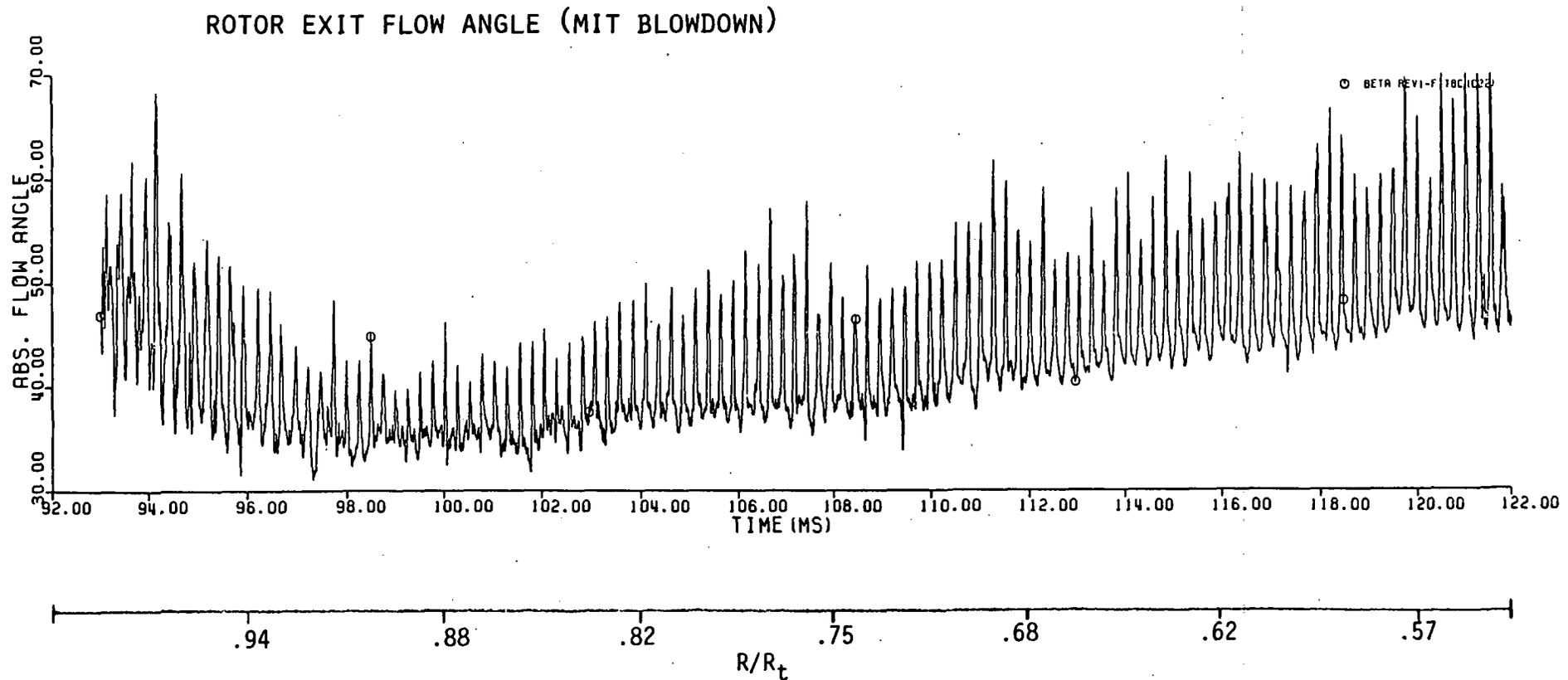
Figure 5.17   Rotor exit absolute tangential flow angle measured during a
                traverse of the 5-Way sphere probe in a MIT Blowdown Test

ROTOR EXIT FLOW ANGLE
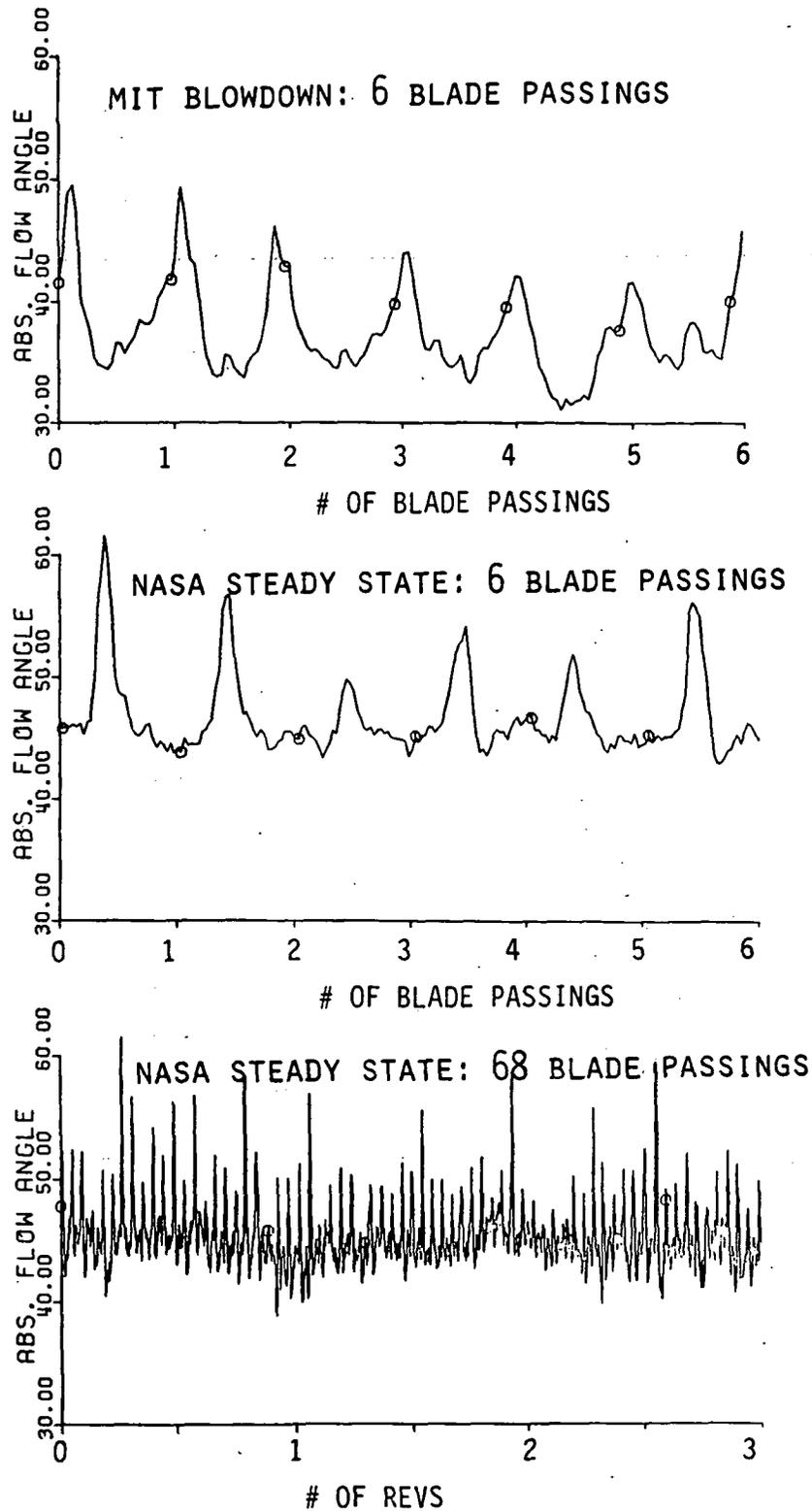
Figure 5.18   Comparison of the rotor exit tangential flow
angle at R/Rt=.93 in the MIT Blowdown Facilit
with the 5-Way sphere probe and the NASA Lew:
Facility with the 4-Way cylinder probe

ROTOR EXIT FLOW ANGLE

MIT BLOWDOWN: 6 BLADE PASSINGS

NASA STEADY STATE: 6 BLADE PASSINGS

NASA STEADY STATE: 68 BLADE PASSINGS
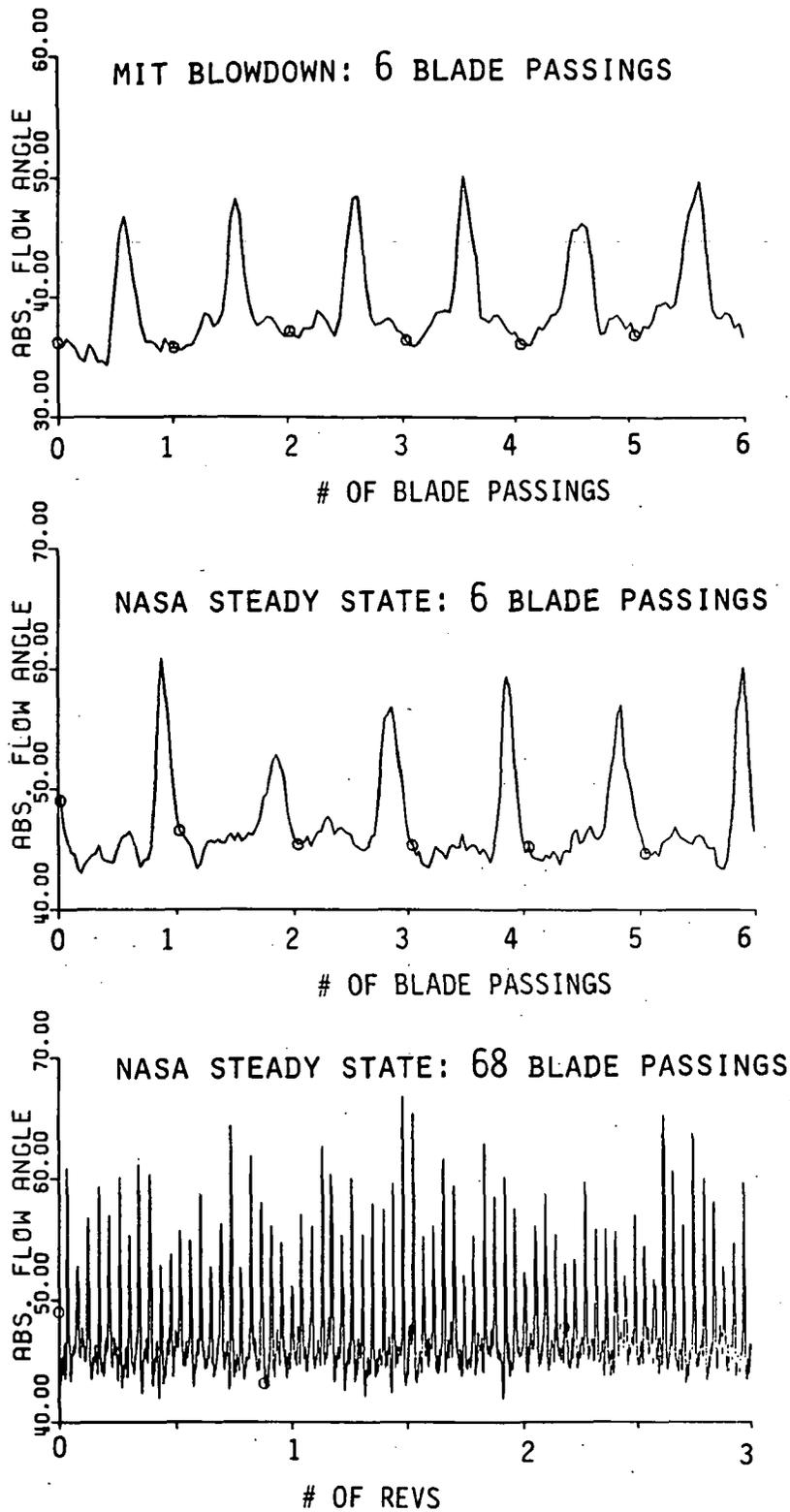
Figure 5.19   Comparison of the rotor exit tangential flow
angle at R/Rt=.82 in the MIT Blowdown Facility
with the 5-Way sphere probe and the NASA Lewis
Facility with the 4-Way cylinder probe

ROTOR EXIT FLOW ANGLE
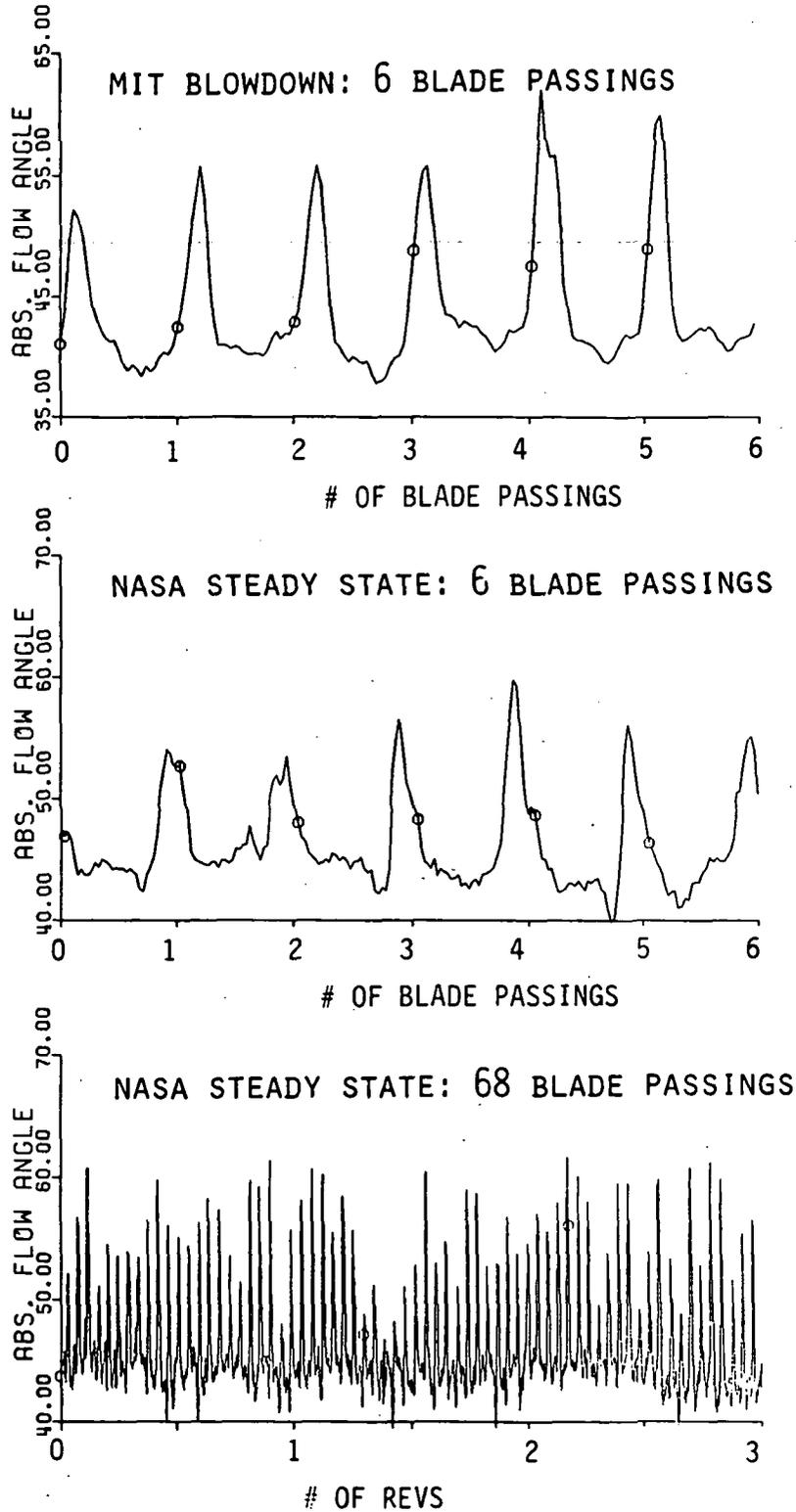
Figure 5.20   Comparison of the rotor exit tangential flow
angle at R/Rt=.70 in the MIT Blowdown Facility
with the 5-Way sphere probe and the NASA Lewis
Facility with the 4-Way cylinder probe
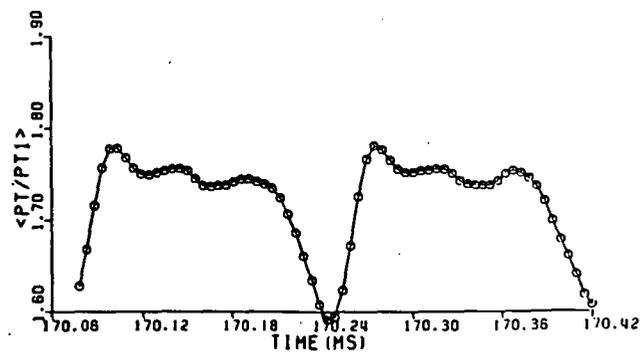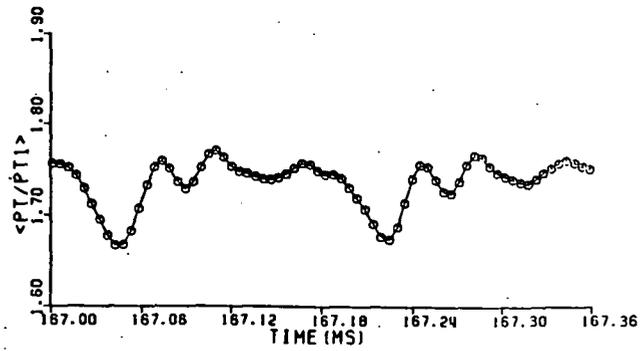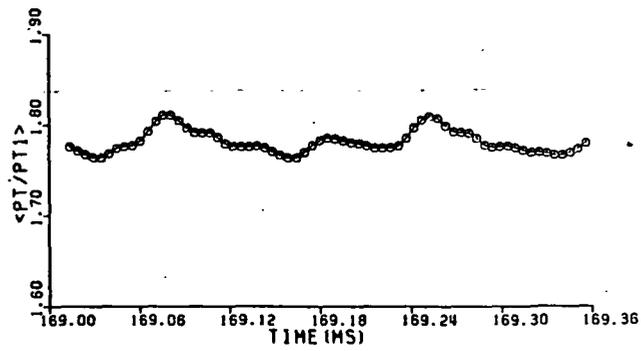
$R/R_T = .93$

$R/R_T = .82$

$R/R_T = .70$

Figure 5.21   Rotor-averaged total pressure ratio for blade
passage #1 at three radii for three fixed immersion
tests at NASA Lewis
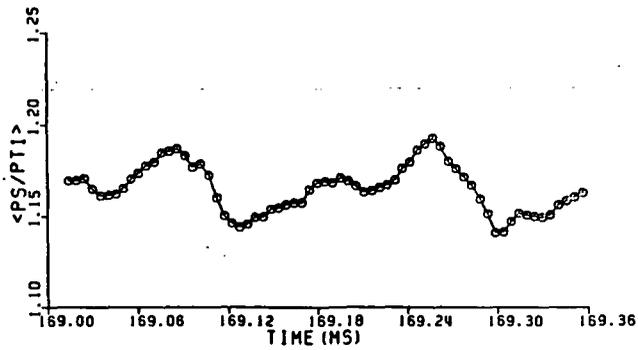
R/R$_T$=.93
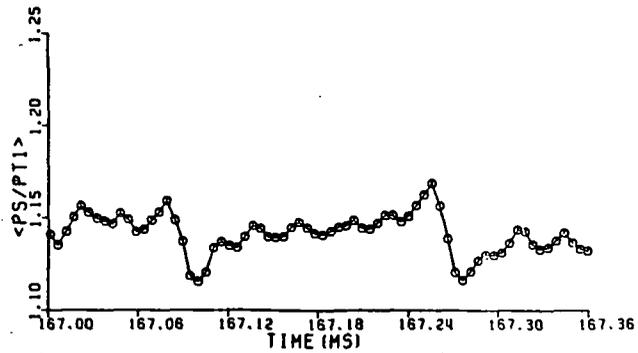
R/R$_T$=.82
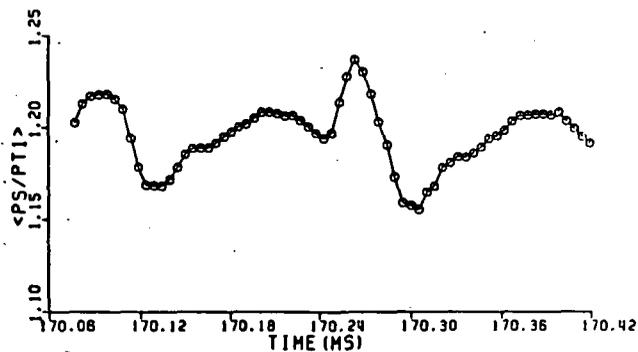
R/R$_T$=.70

Figure 5.22   Rotor-averaged ratio of rotor exit static pressure
to upstream total pressure for blade passage #1
at three radii for three fixed immersion tests at
NASA Lewis.
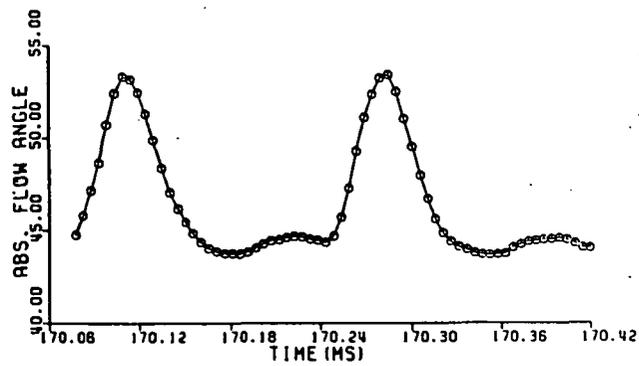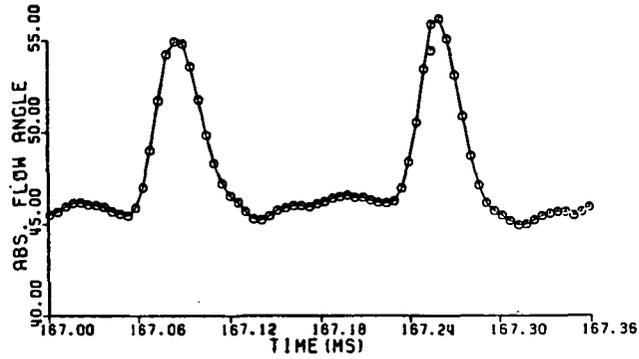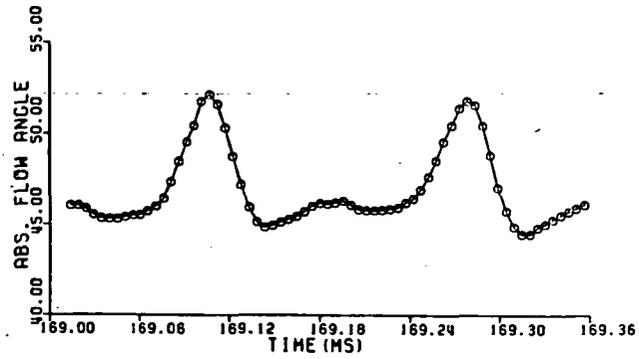
Figure 5.23   Rotor-averaged rotor exit absolute tangential
flow angle for blade passage #1 at three radii
for three fixed immersion tests at NASA Lewis

ROTOR EXIT TOTAL PRESSURE
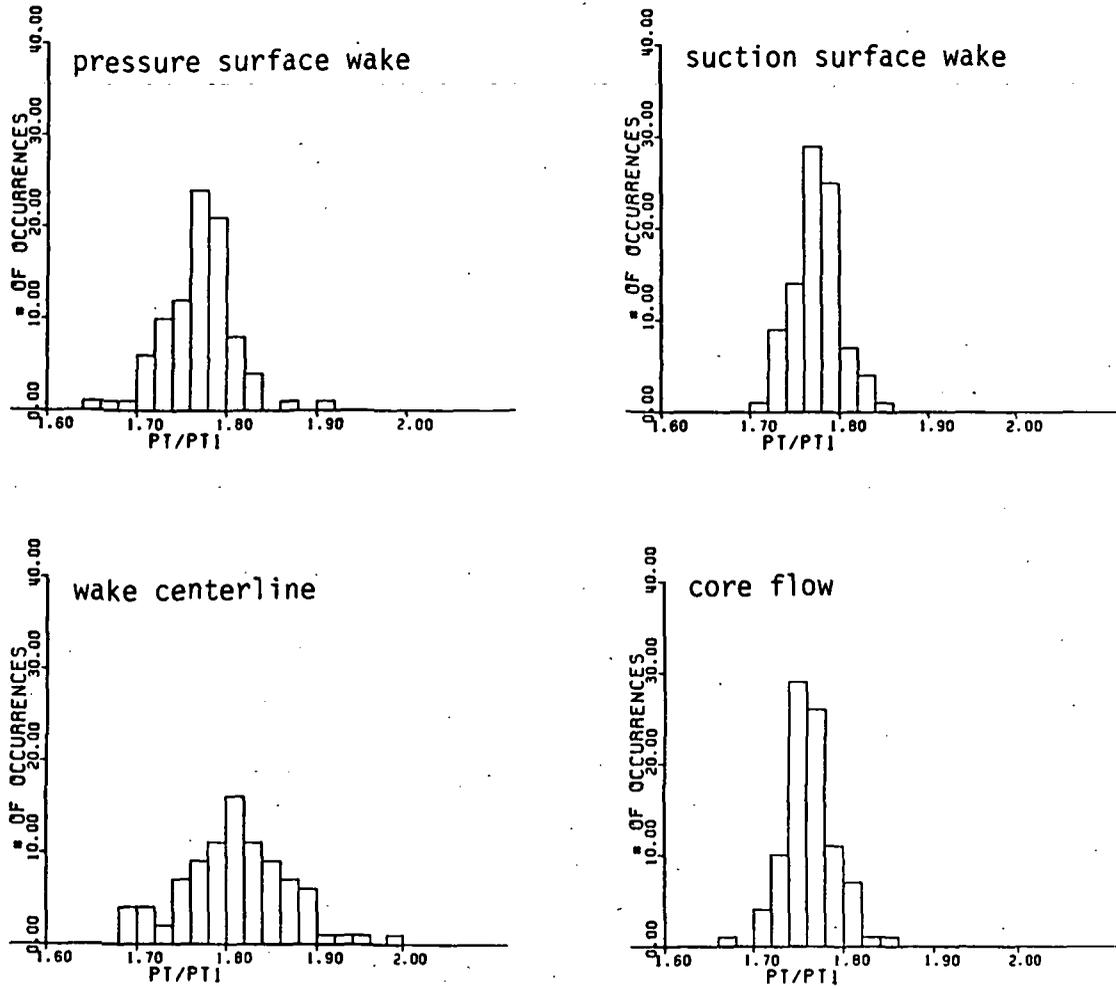
Figure 5.24   Probability density distributions of total pressure
                ratio in blade passage #1 at R/Rt=.93

ROTOR EXIT TOTAL PRESSURE
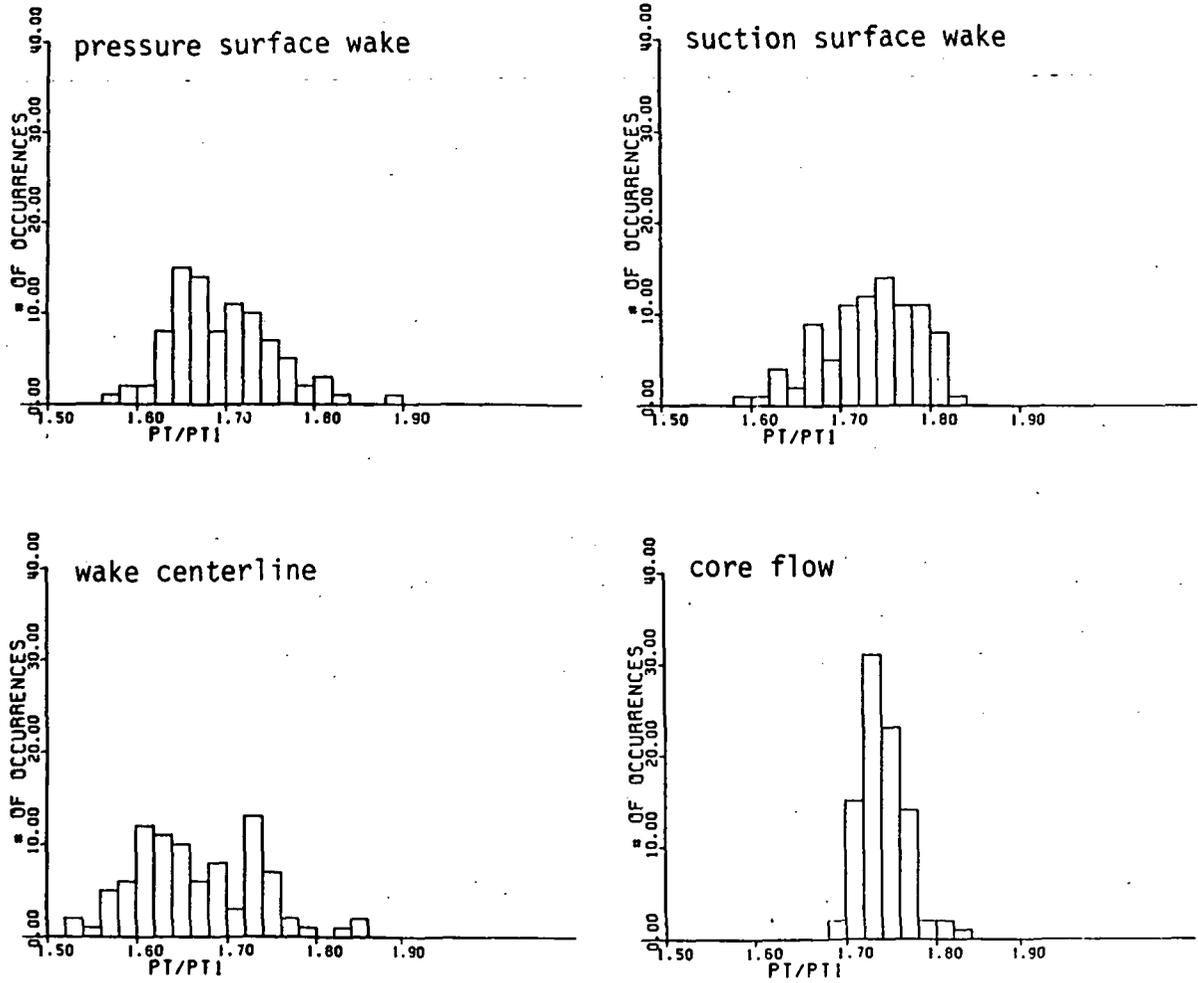
Figure 5.25   Probability density distributions of total pressure
                ratio in blade passage #1 at R/Rt=.82

ROTOR EXIT TOTAL PRESSURE
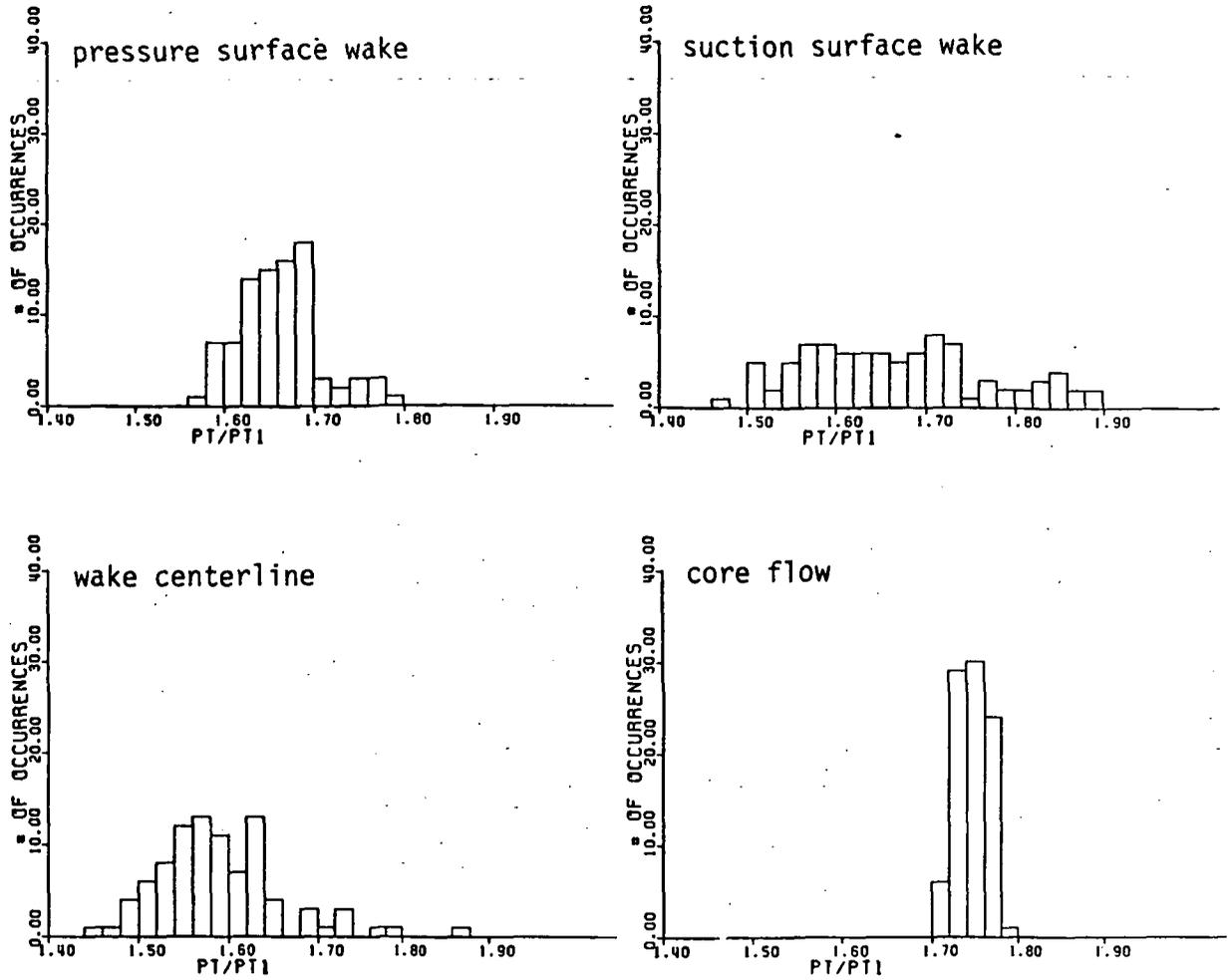
Figure 5.26   Probability density distributions of total pressure
ratio in blade passage #1 at R/Rt=.70

ROTOR EXIT STATIC PRESSURE
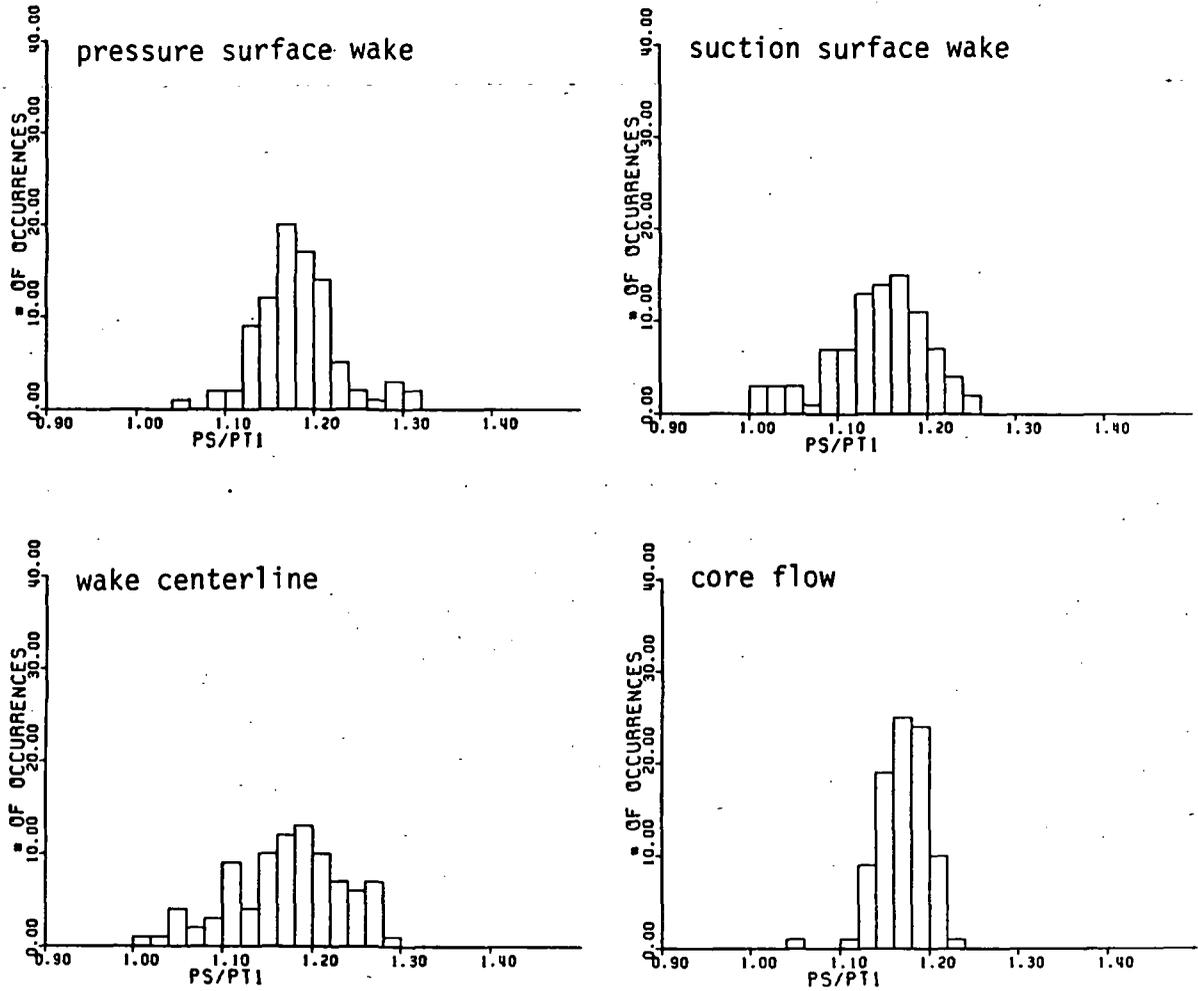
Figure 5.27   Probability density distributions of the ratio of
the rotor exit static pressure to the upstream
total pressure in blade passage #1 at R/Rt=.93

Figure 5.28   Probability density distributions of the ratio of
               the rotor exit static pressure to the upstream
               total pressure in blade passage #1 at R/Rt=.82

ROTOR EXIT STATIC PRESSURE
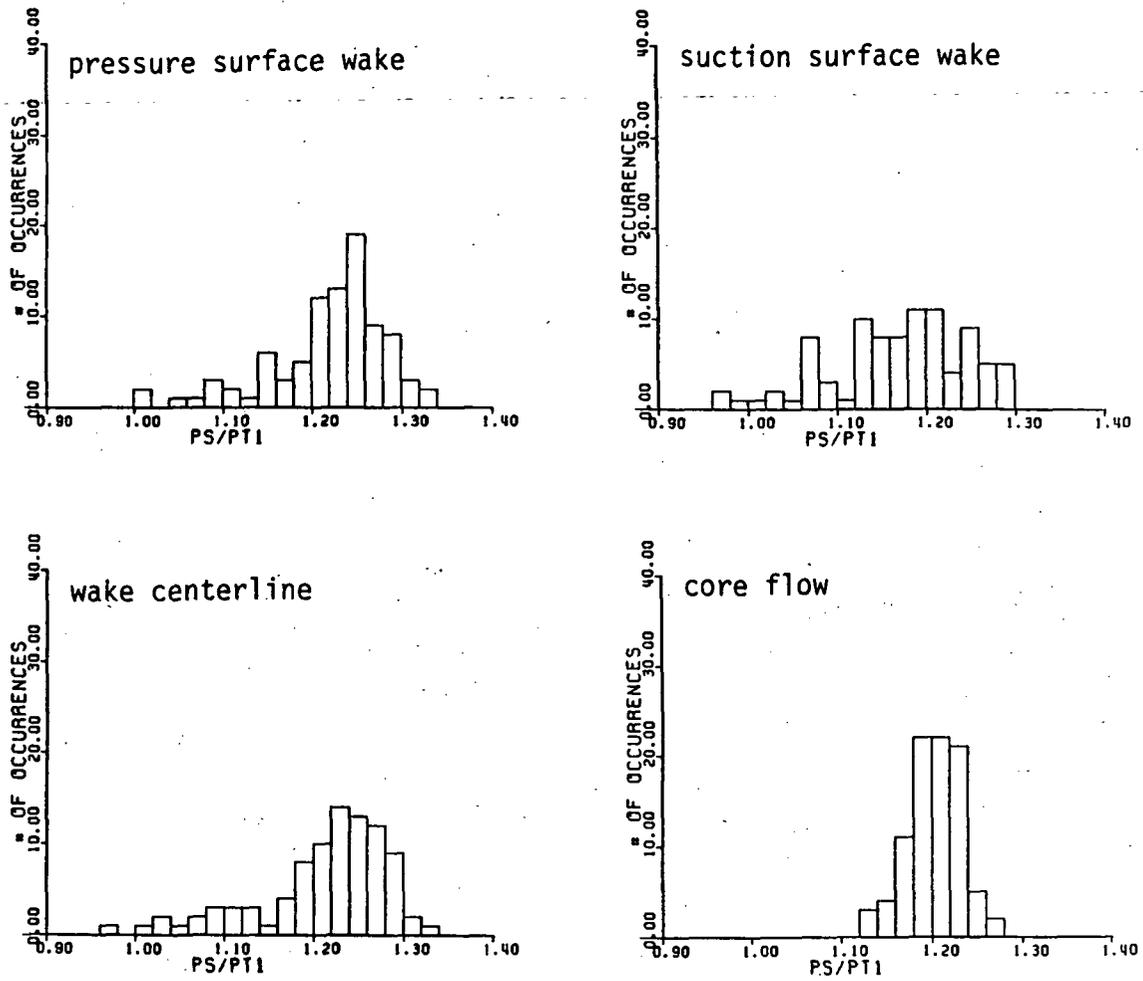
Figure 5.29   Probability density distributions of the ratio of
               the rotor exit static pressure to the upstream
               total pressure in blade passage #1 at R/Rt=.70

ROTOR EXIT FLOW ANGLE
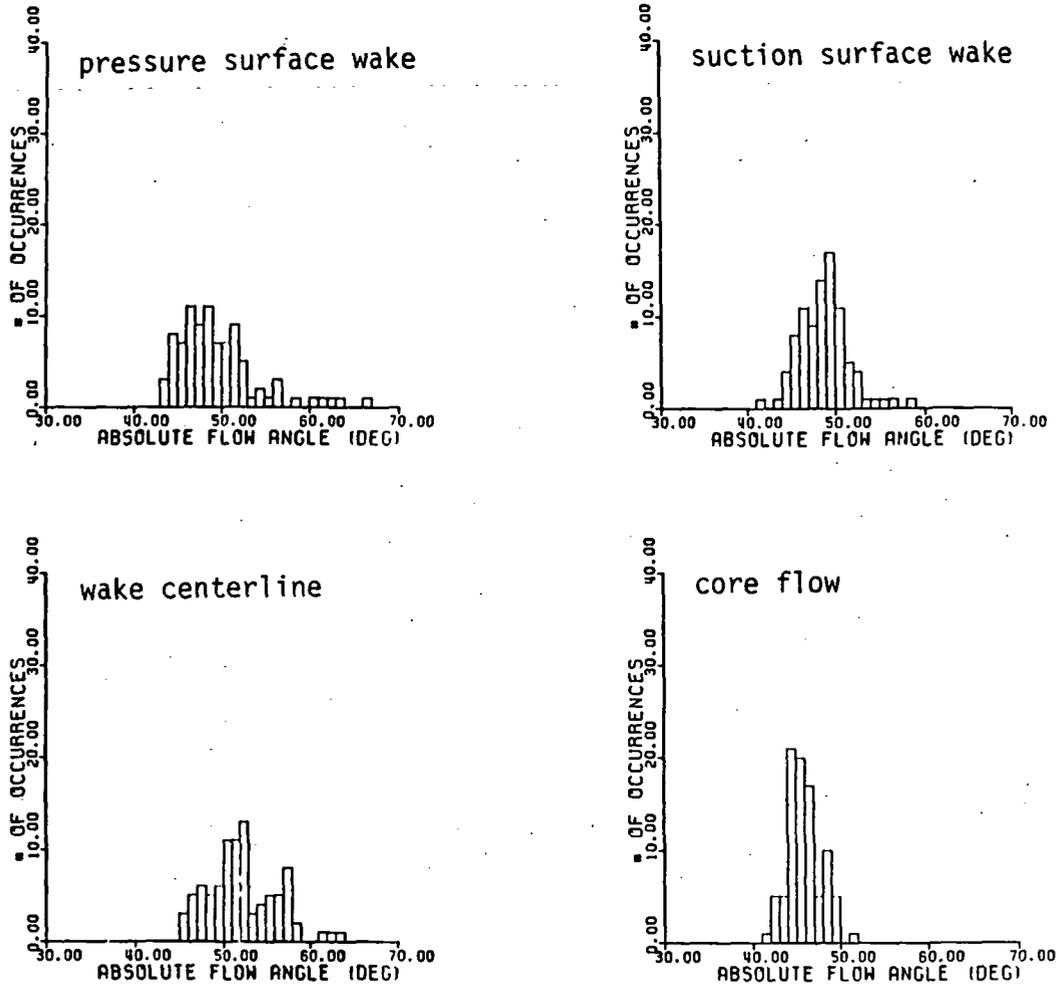
Figure 5.30   Probability density distributions of rotor exit
              absolute tangential flow angle in blade passage
              #1 at R/Rt=.93

Figure 5.31   Probability density distributions of rotor exit
absolute tangential flow angle in blade passage
#1 at R/Rt=.82

ROTOR EXIT FLOW ANGLE
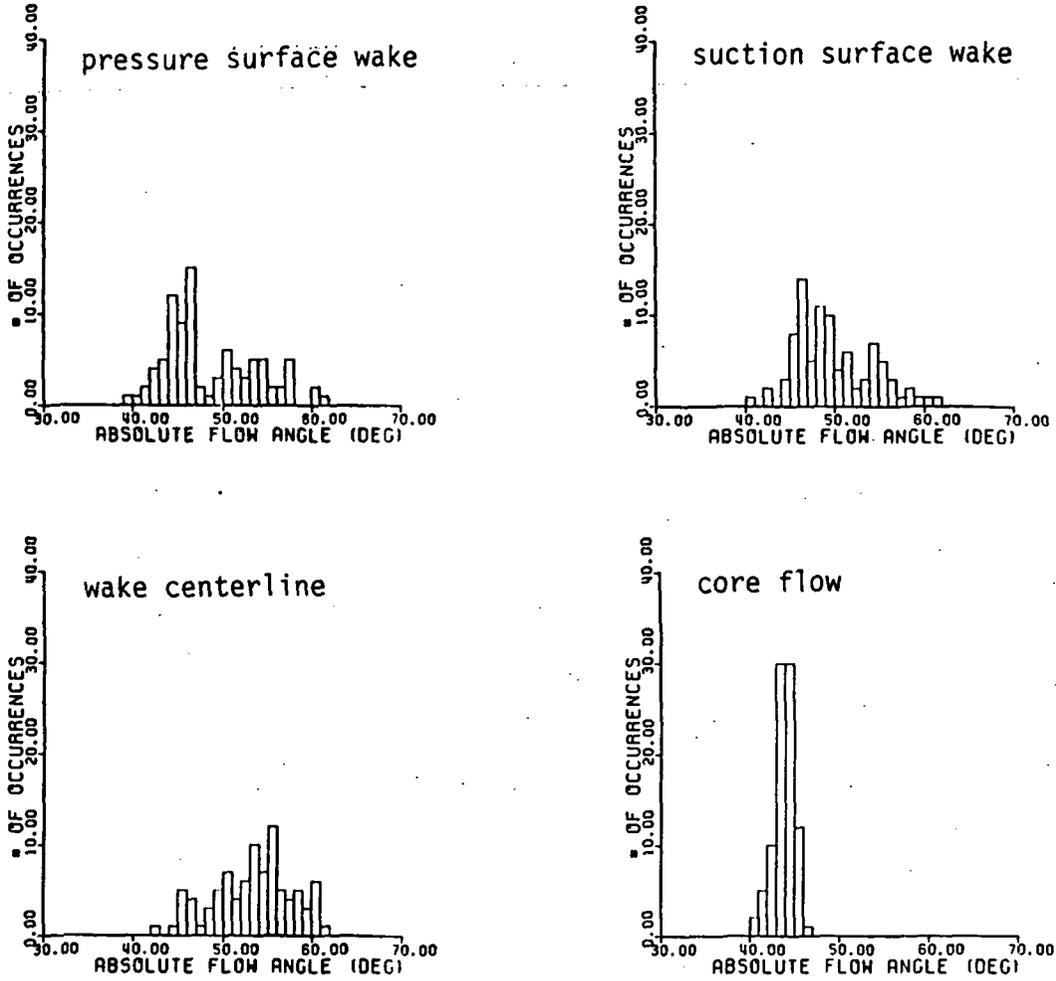
Figure 5.32 Probability density distributions of rotor exit absolute tangential flow angle in blade passage #1 at R/Rt=.70
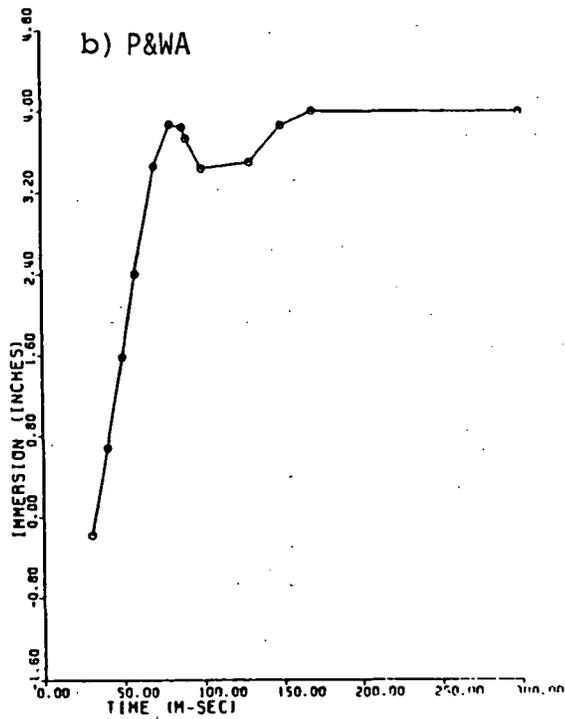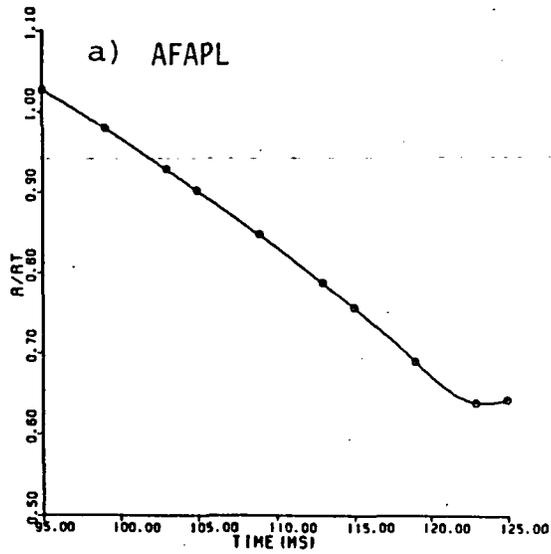
Figure 6.1   Total pressure probe position during traverses in the a) AFAPL rotor at the MIT Blowdown facility b) PW rotor at the Wilgoos test facility

ROTOR EXIT TOTAL PRESSURE RATIO
INLET RELATIVE MACH NUMBER = 1.34
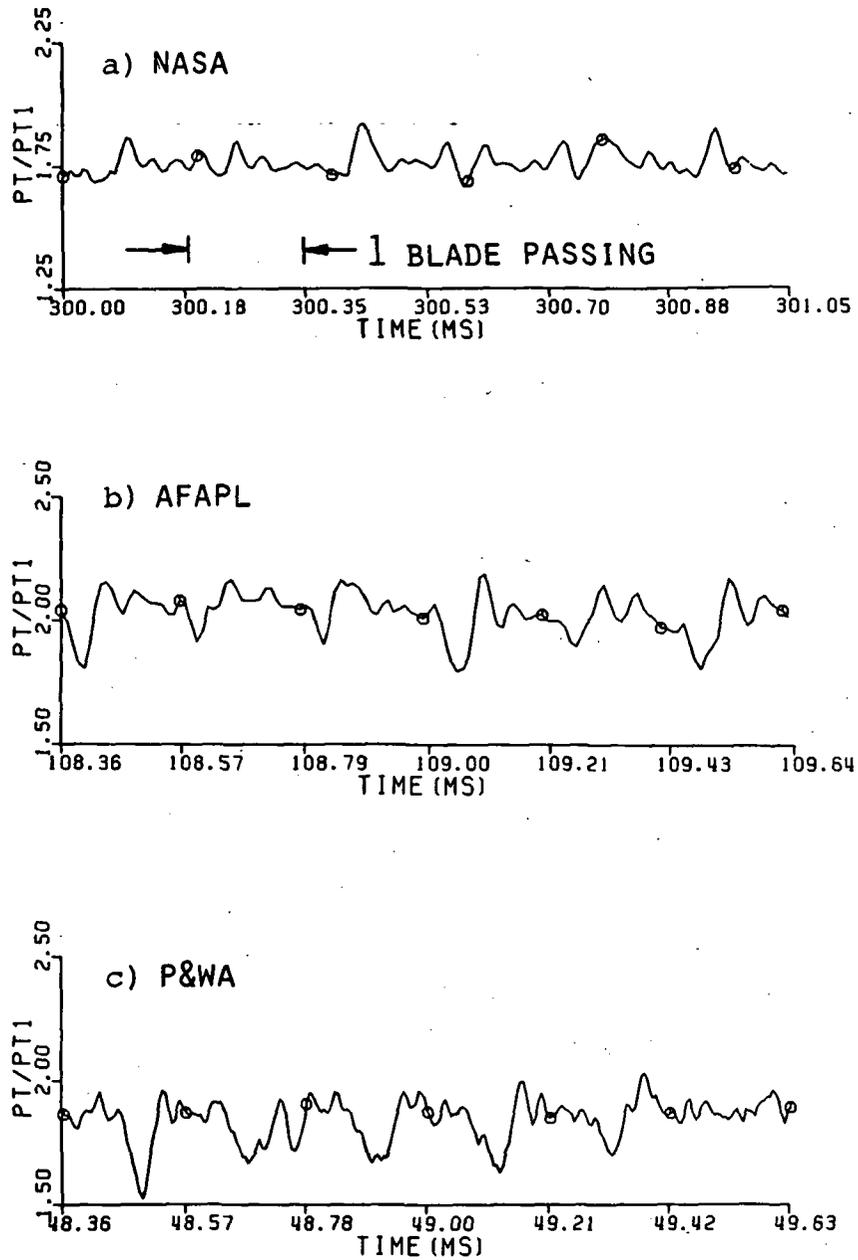
Figure 6.2   Instantaneous total pressure ratio for a time
period of approximately six blade passings
corresponding to an inlet relative Mach number
of 1.34   a) NASA Lewis Fan b) AFAPL High Through
Flow Compressor   c) P&WA Split-Flow Fan

ROTOR EXIT TOTAL PRESSURE RATIO
INLET RELATIVE MACH NUMBER = 1.25
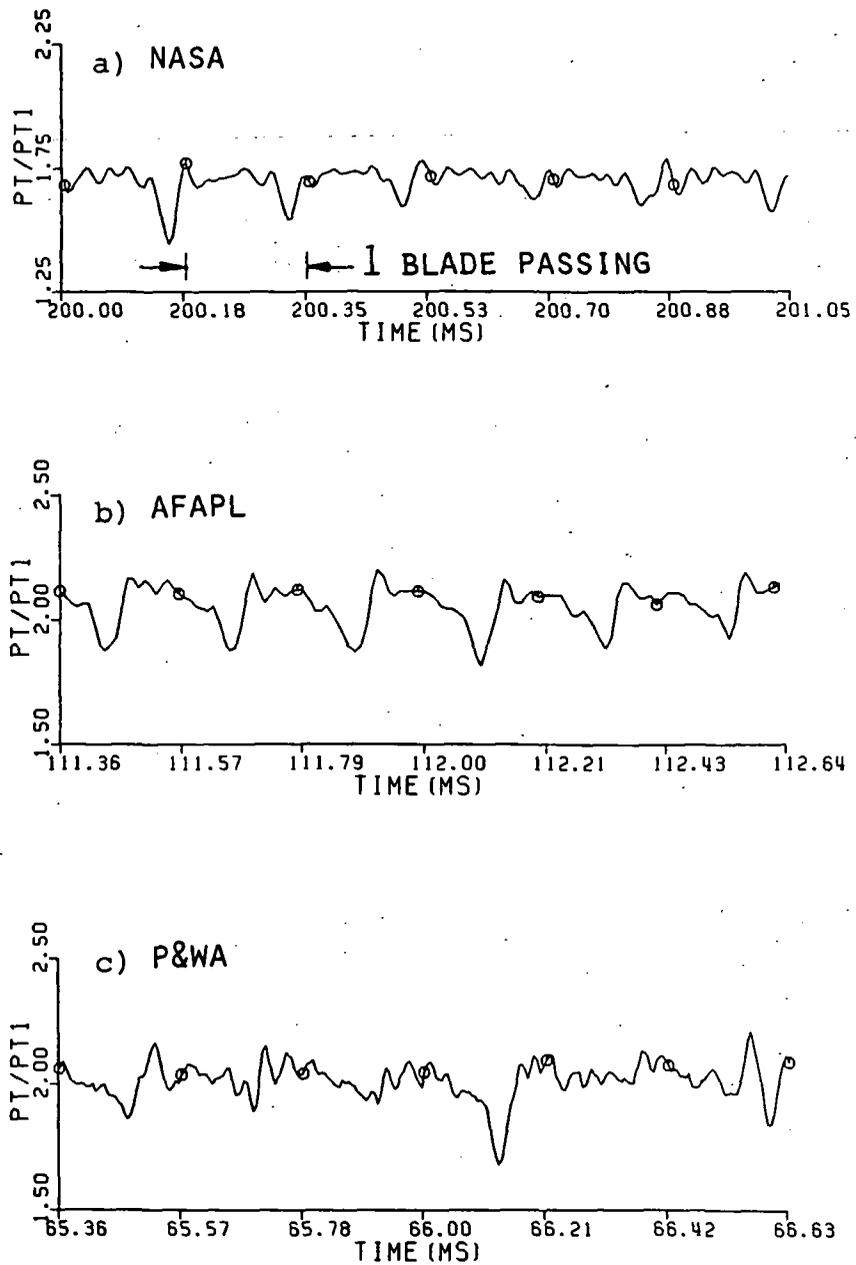
Figure 6.3   Instantaneous total pressure ratio for a time
period of approximately six blade passings
corresponding to an inlet relative Mach number
of 1.25   a) NASA Lewis Fan   b) AFAPL High Through
Flow Compressor   c) P&WA Split-Flow Fan

ROTOR EXIT TOTAL PRESSURE RATIO

INLET RELATIVE MACH NUMBER = 1.14
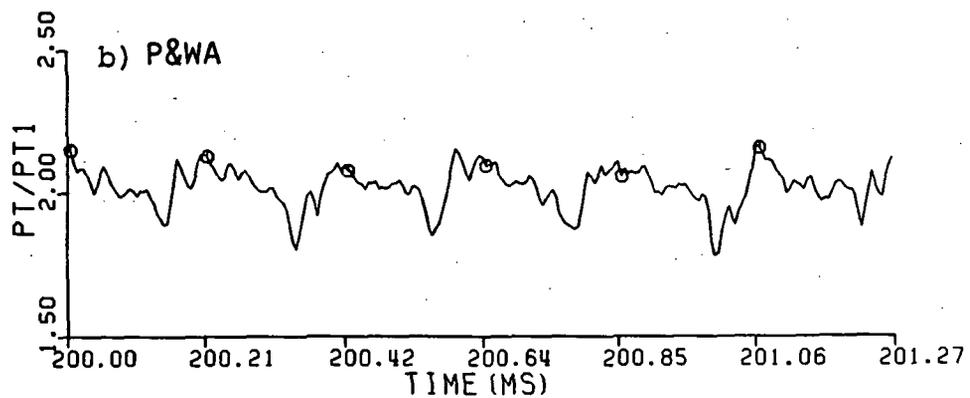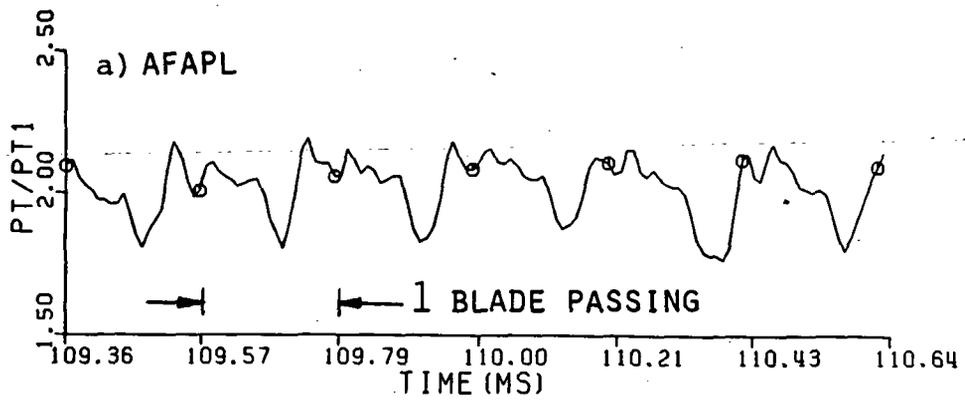
Figure 6.4   Instantaneous total pressure ratio for a time period of approximately six blade passings corresponding to an inlet relative Mach number of 1.14   a) AFAPL High Through Flow Compressor b) P&WA Split-Flow Fan

ROTOR EXIT TOTAL PRESSURE RATIO
INLET RELATIVE MACH NUMBER = 1.03
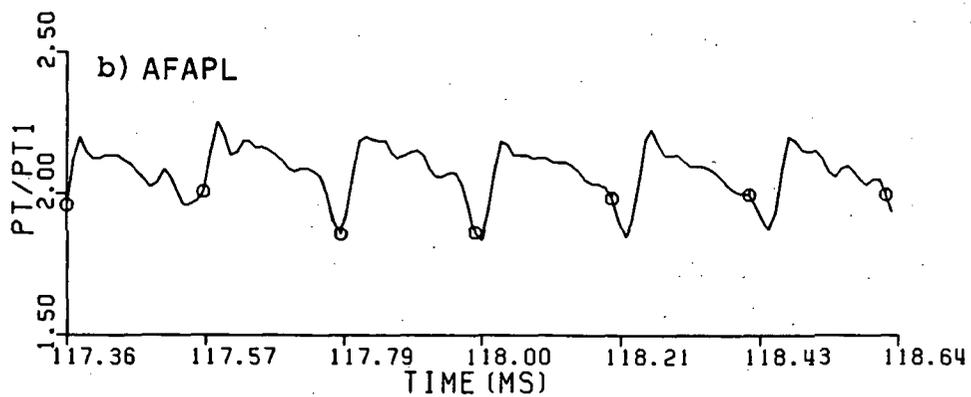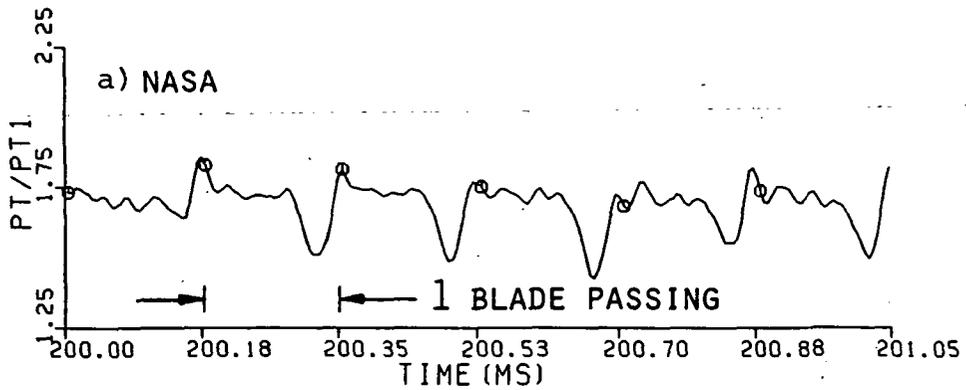
Figure 6.5   Instantaneous total pressure ratio for a time
              period of approximately six blade passings
              corresponding to an inlet relative Mach number
              of 1.03 a) NASA Lewis Fan b) AFAPL High Through
              Flow Compressor

ROTOR EXIT TOTAL PRESSURE RATIO
INLET RELATIVE MACH NUMBER = .89

a) NASA

|←——1 BLADE PASSING
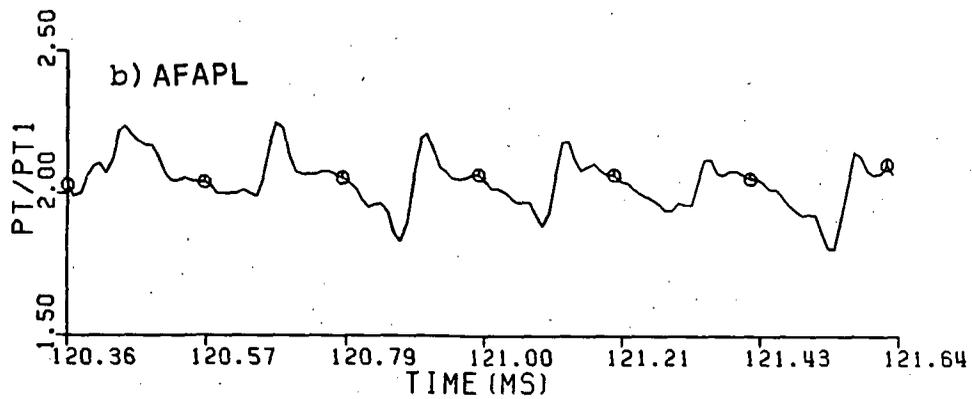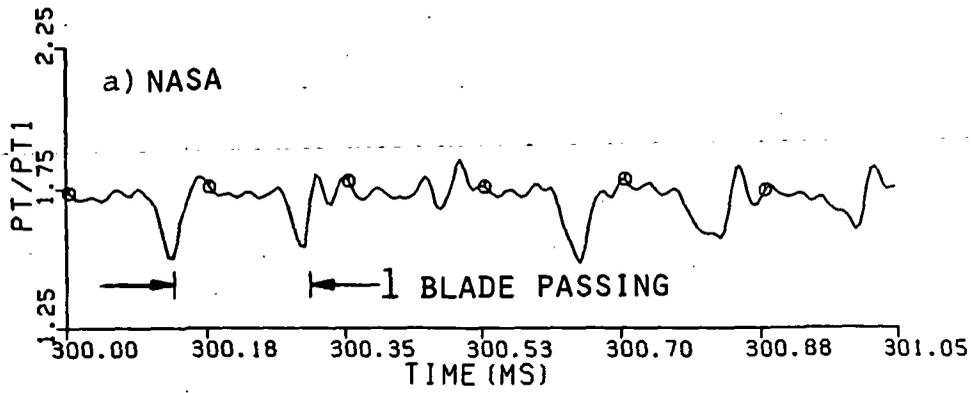
b) AFAPL

Figure 6.6   Instantaneous total pressure ratio for a time
period of approximately six blade passings
corresponding to an inlet relative Mach number
of 0.89   a) NASA Lewis Fan   b) AFAPL High Through
Flow Compressor

TEST N263

POWER SPECTRAL DENSITY OF PT(ASP) MREL=1.34

TO=300.00 MS TF=302.94 MS 512 PTS
FREQUENCY RANGE 0.07 KHZ TO 30.0 KHZ
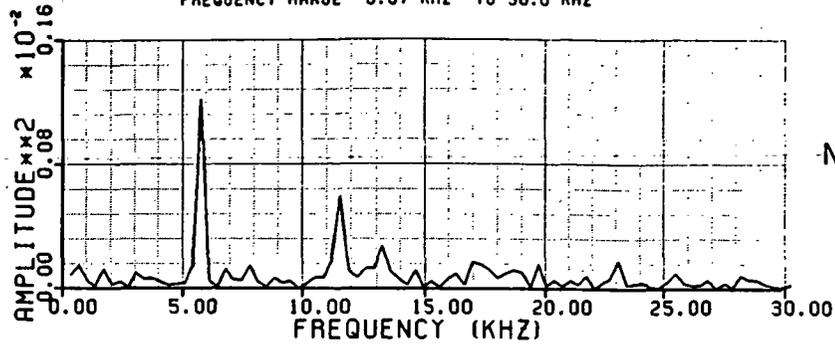
NASA

TEST AF51

POWER SPECTRAL DENSITY OF PT(ASP) MREL=1.34

TO=107.00 MS TF=112.12 MS 512 PTS
FREQUENCY RANGE 0.07 KHZ TO 30.0 KHZ
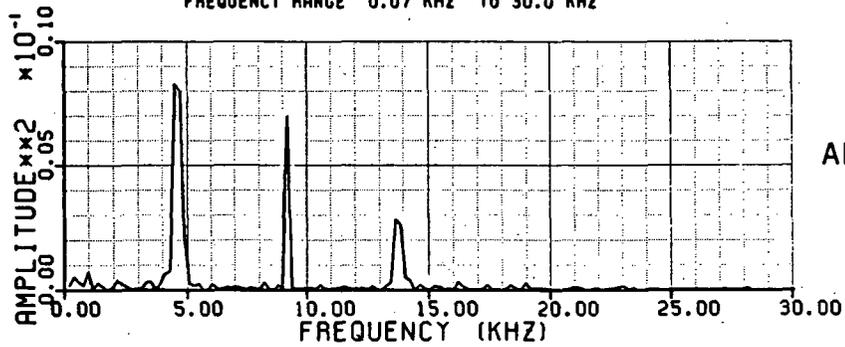
AFAPL

TEST P515

POWER SPECTRAL DENSITY OF PT(ASP) MREL=1.34

TO=48.00 MS TF=50.66 MS 512 PTS
FREQUENCY RANGE 0.07 KHZ TO 30.0 KHZ
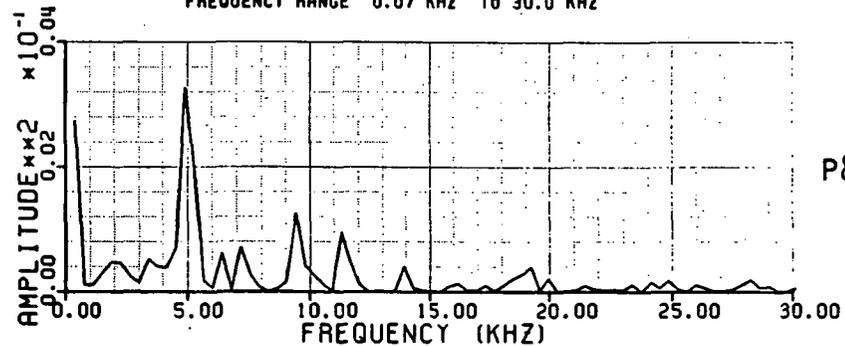
P&WA

Figure 6.7   Power spectral densities of total pressure ratio
corresponding to an inlet relative Mach number of
1.34   a) NASA Lewis Fan b) AFAPL High Through Flow
Compressor c) P&WA Split-Flow Fan

TEST N266

POWER SPECTRAL DENSITY OF PT(ASP) MREL=1.25

TO=200.00 MS TF=202.66 MS 512 PTS
FREQUENCY RANGE 0.07 KHZ TO 30.0 KHZ
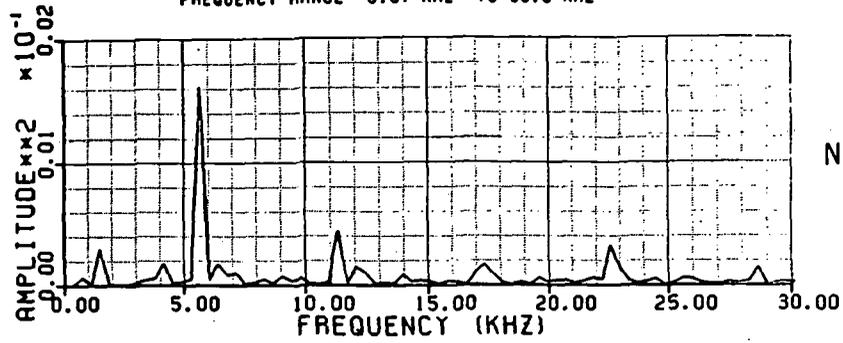
NASA

TEST AFS1

POWER SPECTRAL DENSITY OF PT(ASP) MREL=1.25

TO=110.00 MS TF=115.12 MS 512 PTS
FREQUENCY RANGE 0.07 KHZ TO 30.0 KHZ
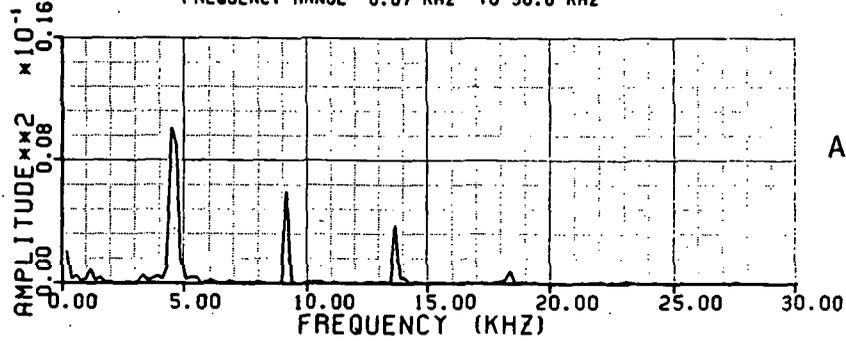
AFAPL

TEST P515

POWER SPECTRAL DENSITY OF PT(ASP) MREL=1.25

TO=65.00 MS TF=67.66 MS 512 PTS
FREQUENCY RANGE 0.07 KHZ TO 30.0 KHZ
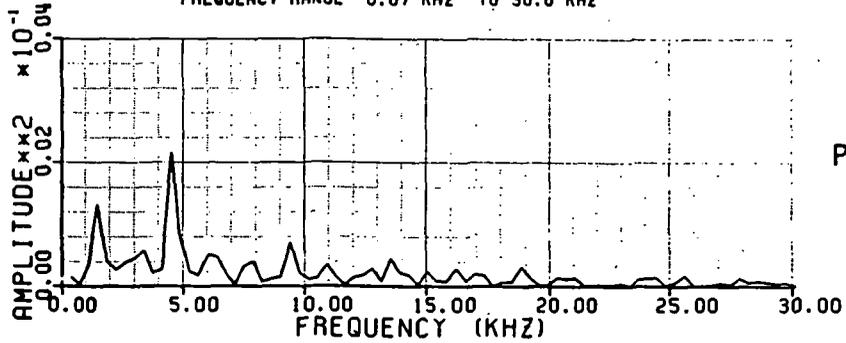
P&WA

Figure 6.8   Power spectral densities of total pressure ratio
corresponding to an inlet relative Mach number of
1.25   a) NASA Lewis Fan b) AFAPL High Through Flow
Compressor c) P&WA Split-Flow Fan

TEST AF51

POWER SPECTRAL DENSITY OF PT(ASP) MREL=1.14

TO=108.00 MS TF=113.12 MS 512 PTS
FREQUENCY RANGE 0.07 KHZ TO 30.0 KHZ
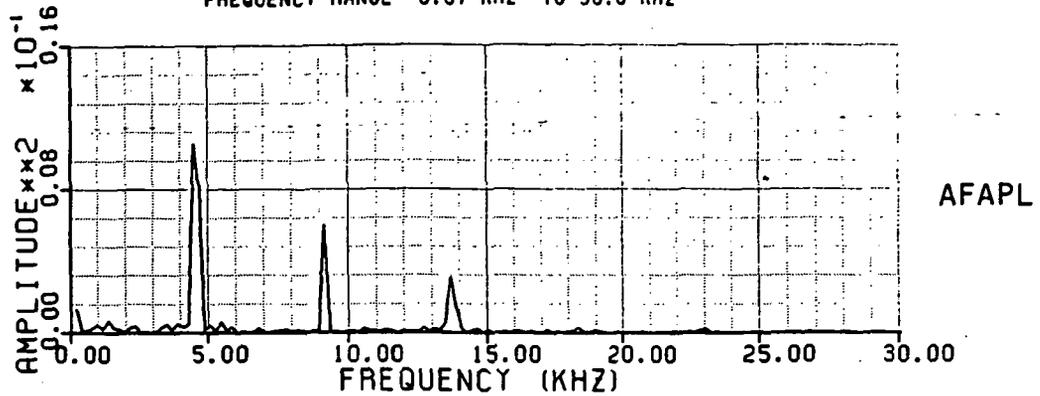
AFAPL

TEST P515

POWER SPECTRAL DENSITY OF PT(ASP) MREL=1.14

TO=200.00 MS TF=202.66 MS 512 PTS
FREQUENCY RANGE 0.07 KHZ TO 30.0 KHZ

P&WA
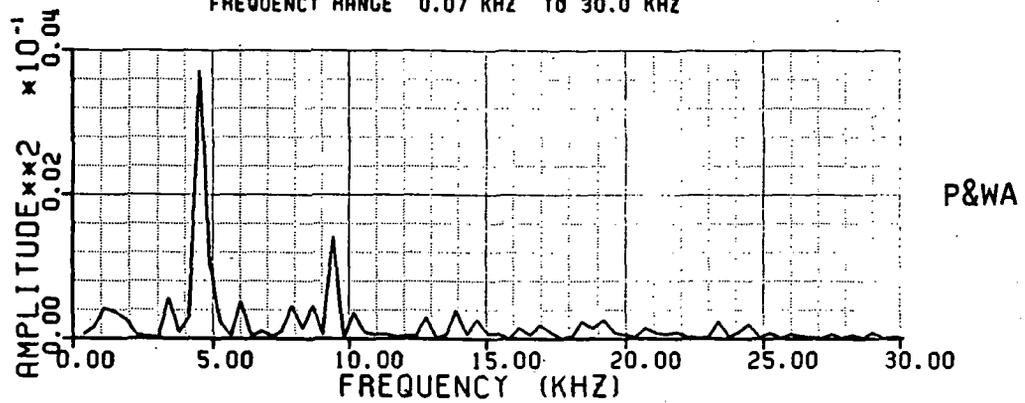
Figure 6.9   Power spectral densities of total pressure ratio
corresponding to an inlet relative Mach number of
1.14   a) AFAPL High Through Flow Compressor
b) P&WA Split-Flow Fan

TEST N269

POWER SPECTRAL DENSITY OF PT(ASP) MREL=1.03

TO=200.00 MS TF=202.66 MS 512 PTS
FREQUENCY RANGE 0.07 KHZ TO 30.0 KHZ
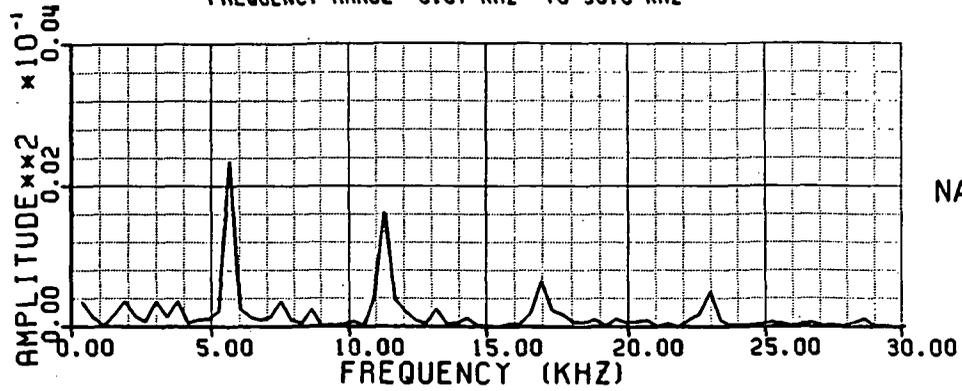
NASA

TEST AF51

POWER SPECTRAL DENSITY OF PT(ASP) MREL=1.03

TO=116.00 MS TF=121.12 MS 512 PTS
FREQUENCY RANGE 0.07 KHZ TO 30.0 KHZ
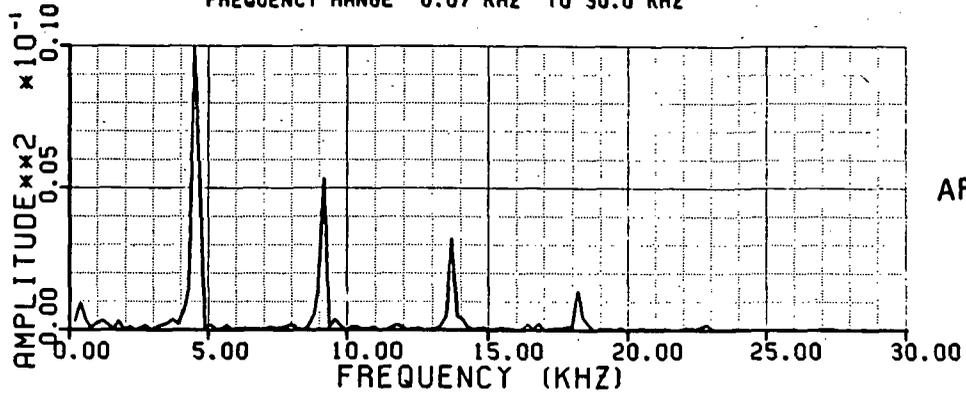
AFAPL

Figure 6.1Ø Power spectral densities of total pressure ratio
corresponding to an inlet relative Mach number of
1.Ø3   a) NASA Lewis Fan   b) AFAPL High Through Flow
Compressor

TEST N272

POWER SPECTRAL DENSITY OF PT (ASP) MREL=.89

TO=300.00 MS TF=302.66 MS 512 PTS
FREQUENCY RANGE 0.07 KHZ TO 30.0 KHZ
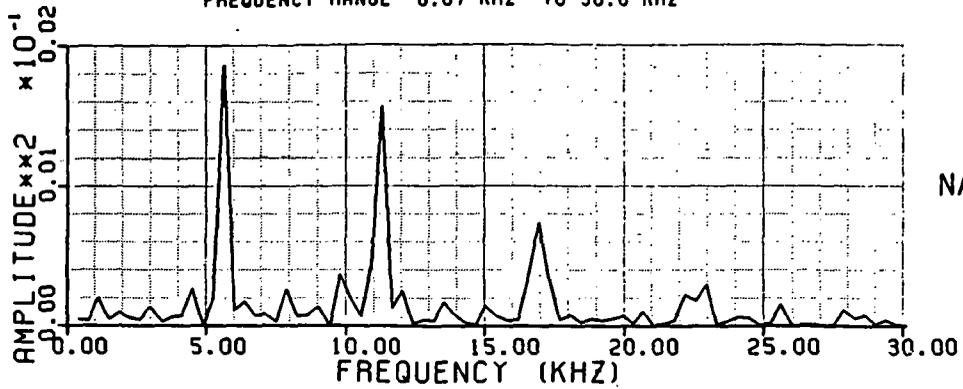
NASA

TEST AF51

POWER SPECTRAL DENSITY OF PT (ASP) MREL=.89

TO=119.00 MS TF=124.12 MS 512 PTS
FREQUENCY RANGE 0.07 KHZ TO 30.0 KHZ
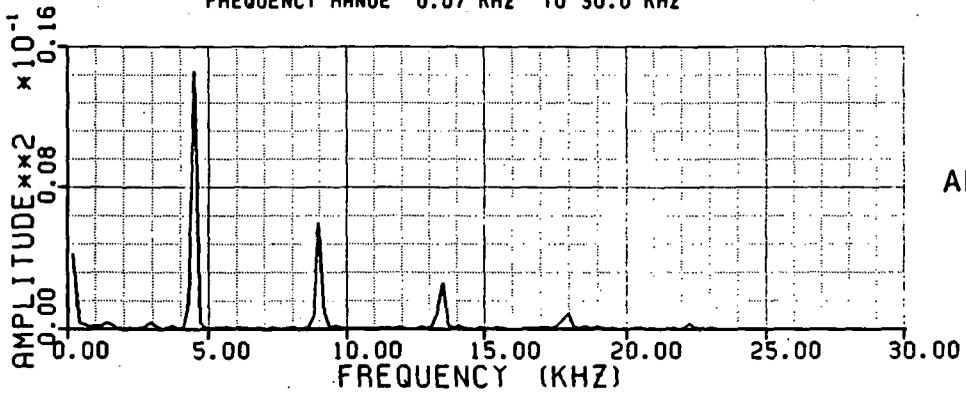
AFAPL

Figure 6.11   Power spectral densities of total pressure ratio
corresponding to an inlet relative Mach number of
0.89   a) NASA Lewis b) AFAPL High Through Flow
Compressor

ROTOR EXIT TOTAL PRESSURE RATIO
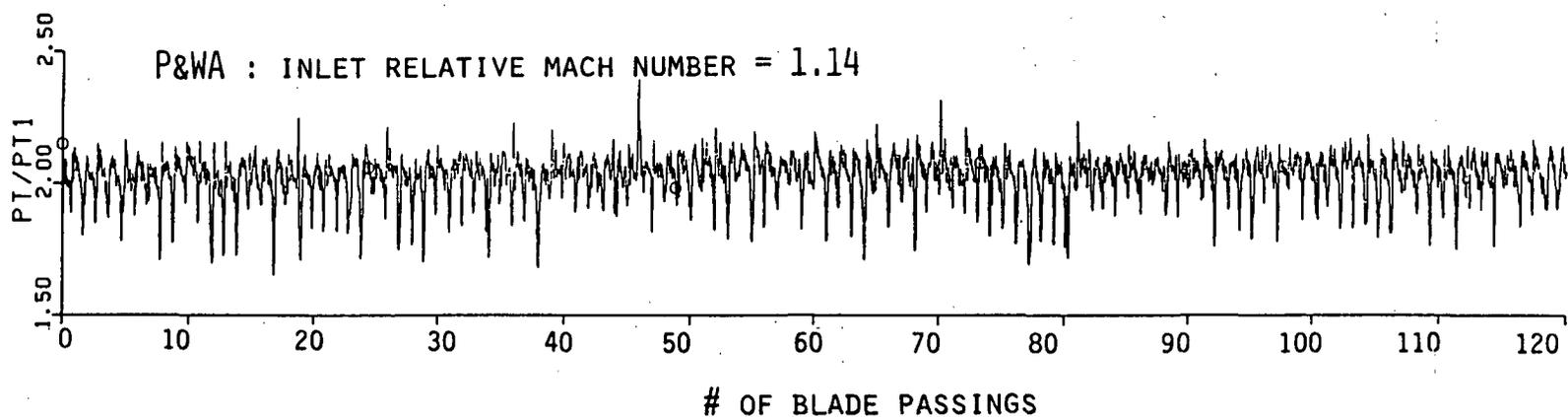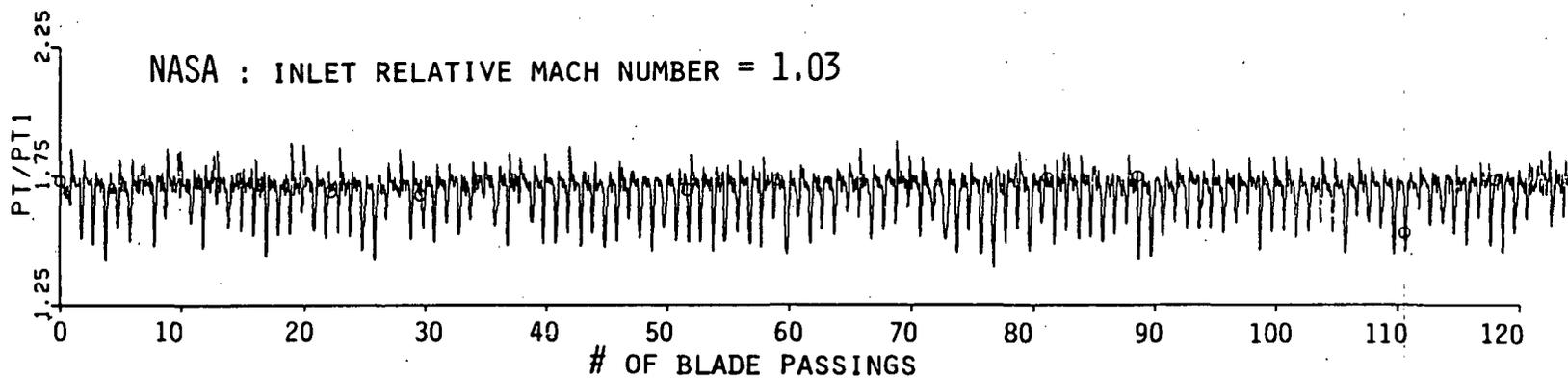
Figure 6.12   Instantaneous total pressure ratio for a time period of
approximately five rotor rotations a) NASA Lewis Fan
(Mrel)inlet=1.03   b) P&WA Split-Flow Fan   (Mrel)inlet=1.14

MEAN ABSOLUTE VELOCITY DISTRIBUTION
MEASURED BY THE LASER ANEMOMETER

(NASA LEWIS)
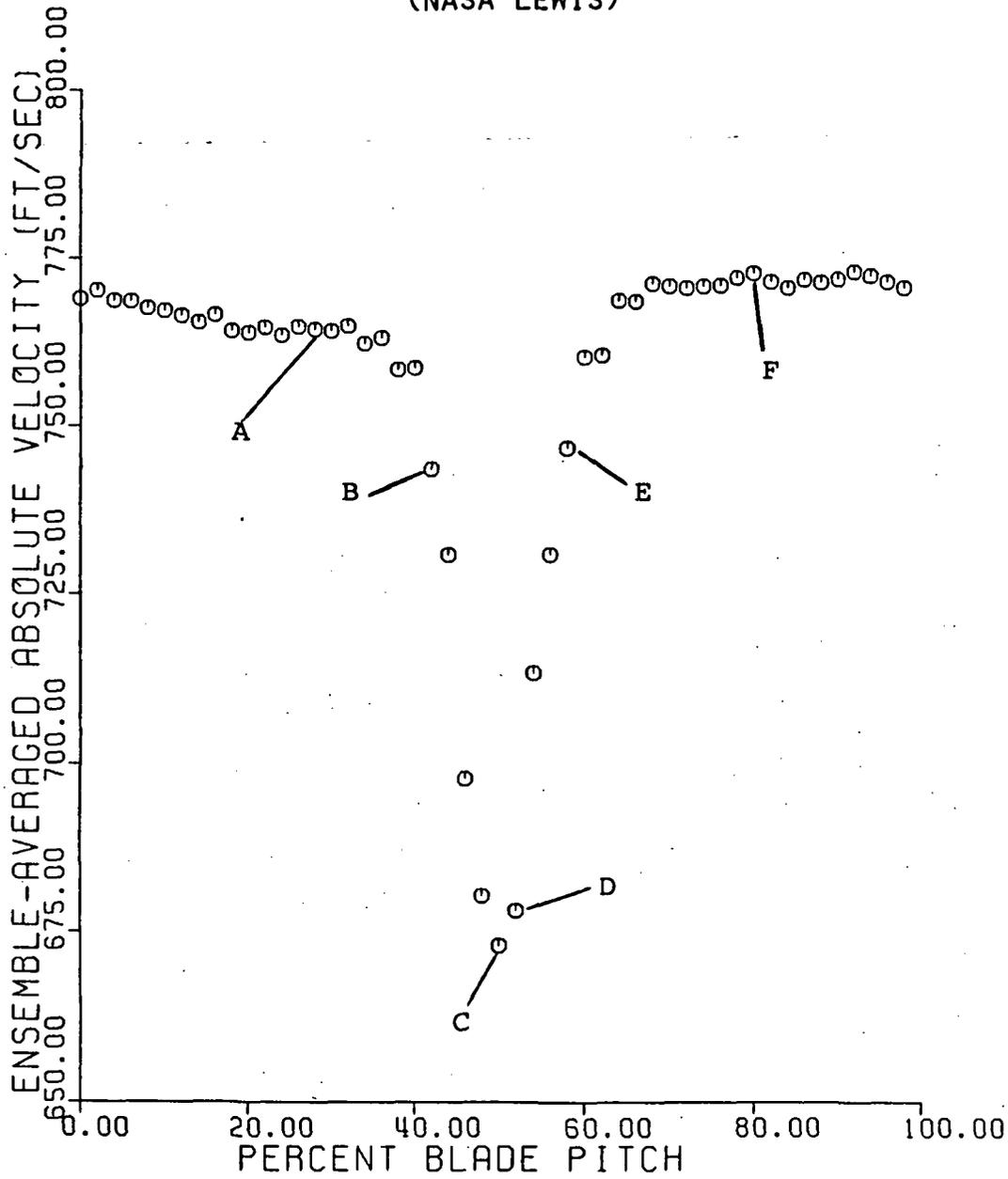
Figure 7.1   Mean rotor exit absolute velocity distribution for
NASA Lewis rotor measured by the laser anemometer
at 6Ø% span, 14Ø% chord in a plane 42 degrees from
the axial direction
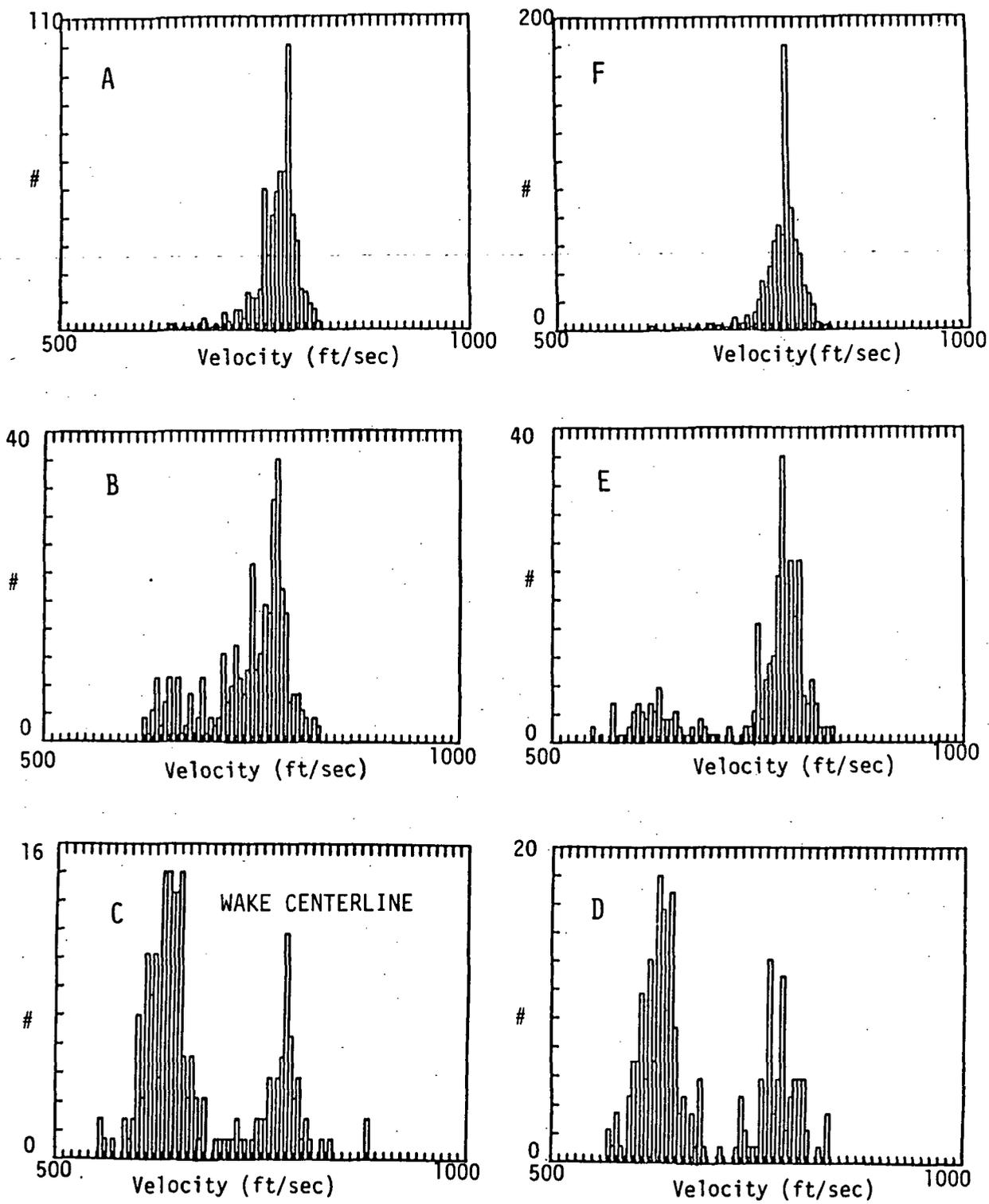
Figure 7.2   Probability density distributions of velocity measured
by the LA at points A-F in figure 7.1
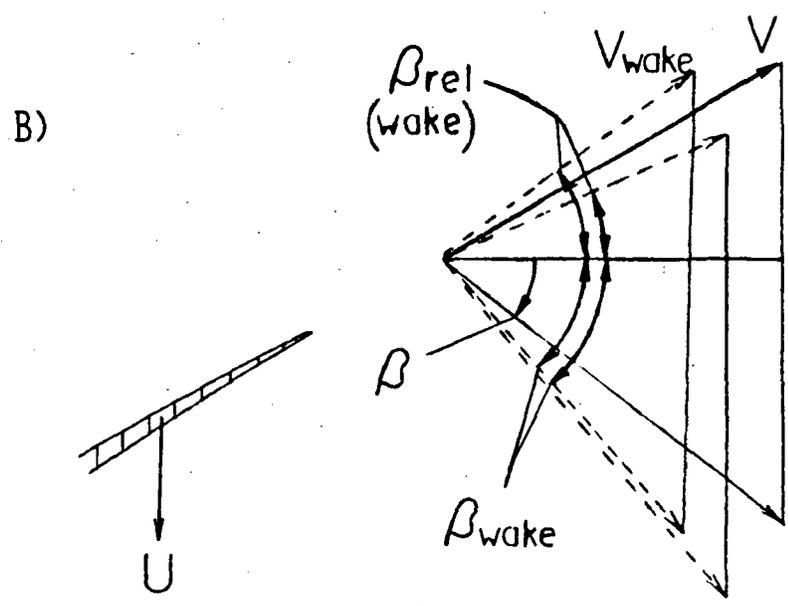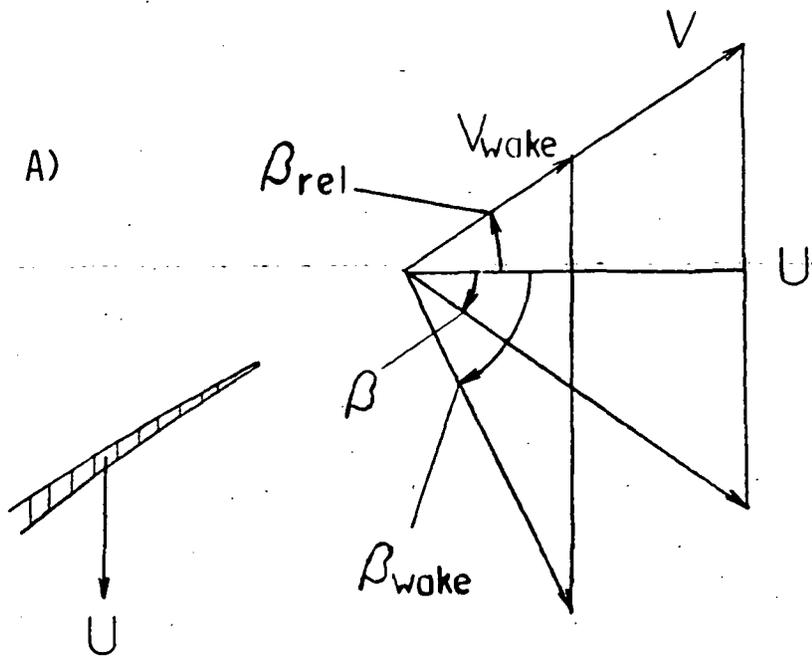
Figure 7.3   Rotor exit velocity triangles showing the effect of
wake in the absolute frame a) uniform relative flow
angle b) variable relative flow angle in the rotor
wake

ROTOR EXIT ABSOLUTE VELOCITY
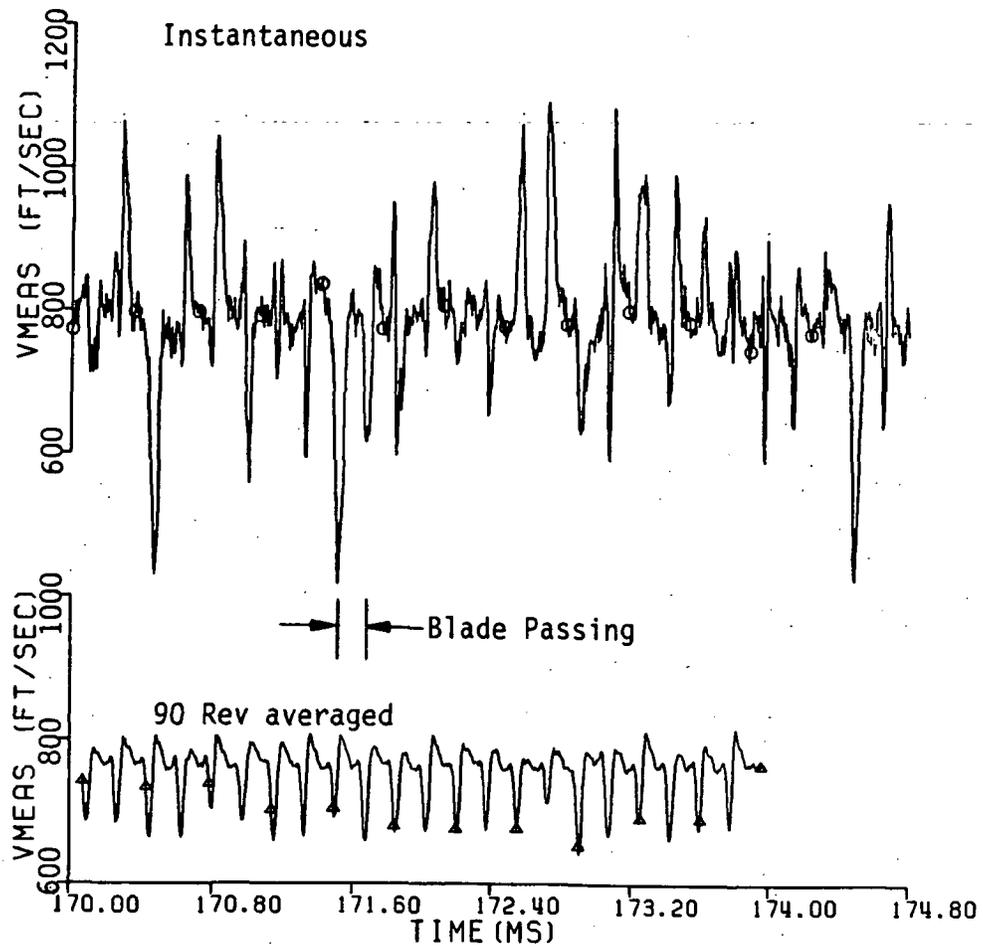
Figure 7.4   Comparison of the instantaneous velocity component
measured by the 4-Way probe corresponding to the LA
measurement and a blade by blade ensemble average over
90 rotor revolutions

ROTOR EXIT RELATIVE FLOW ANGLE
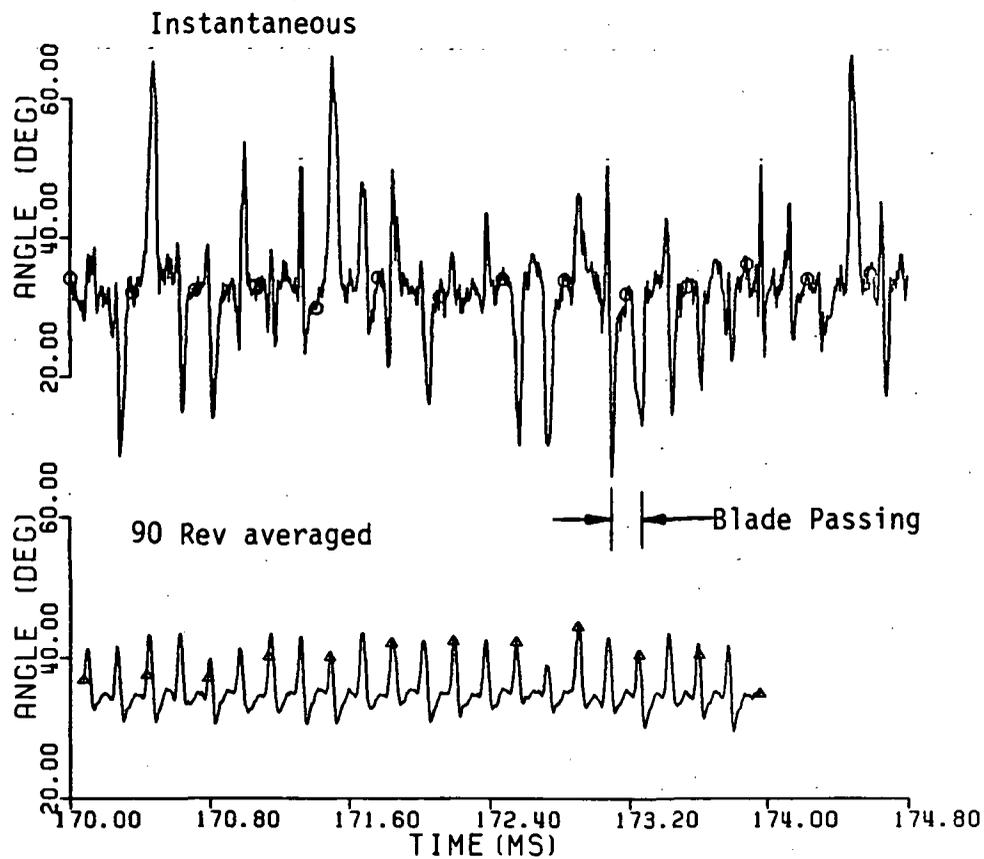
Figure 7.5   Comparison of the instantaneous relative flow angle
             measured by the 4-Way probe and a blade by blade
             ensemble average over 90 rotor revolutions

ROTOR EXIT STATIC PRESSURE
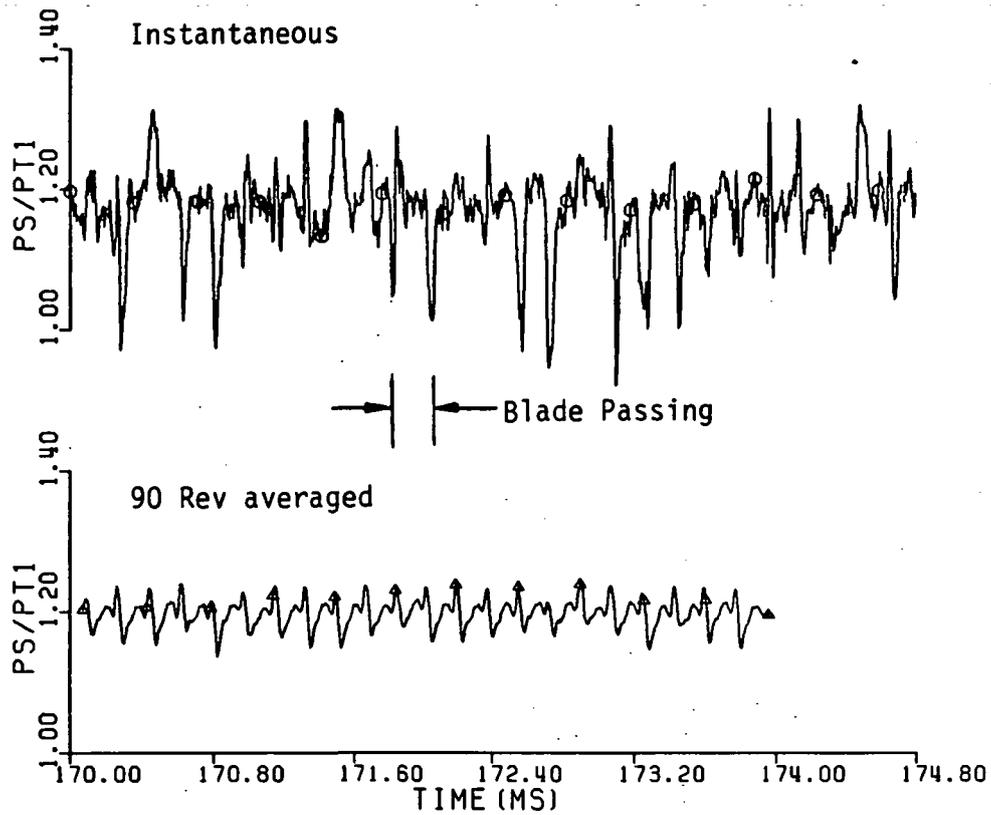
Figure 7.6   Comparison of the instantaneous ratio of the static
pressure measured by the 4-Way probe to the upstream
total pressure and a blade by blade ensemble
average over 90 rotor revolutions
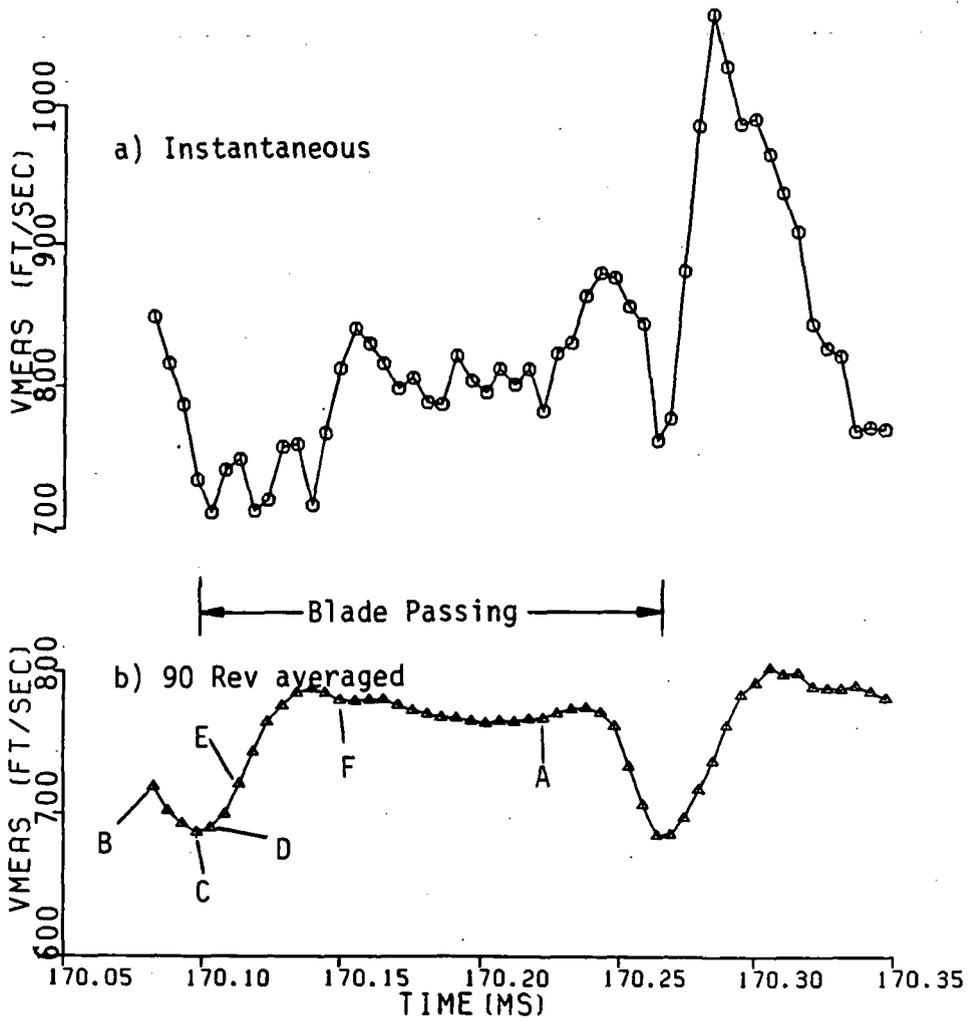
Figure 7.7 Time-trace of the component of velocity measured by the
4-way probe corresponding to the LA measurement
for slightly more than one blade passing
a) instantaneous velocity(blade passage #1)
b) blade by blade ensemble average over 90 consecutive
revolutions
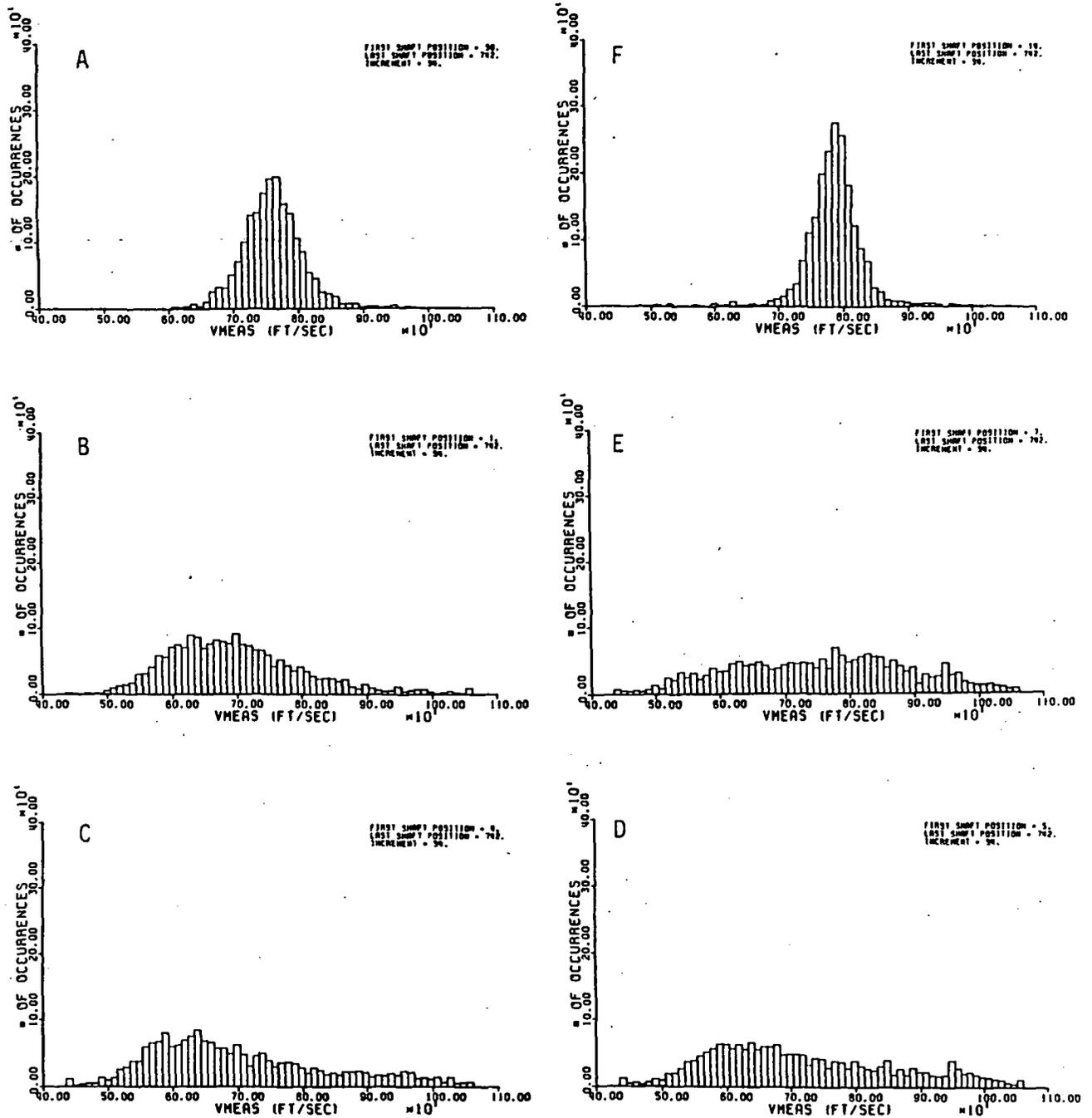
Figure 7.8   Probability density distribution of the velocity
measured by 4-way probe at points A-F in figure
7.7 for all 22 blade passages
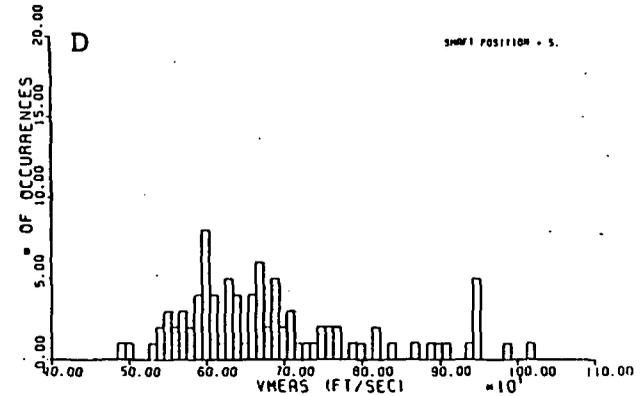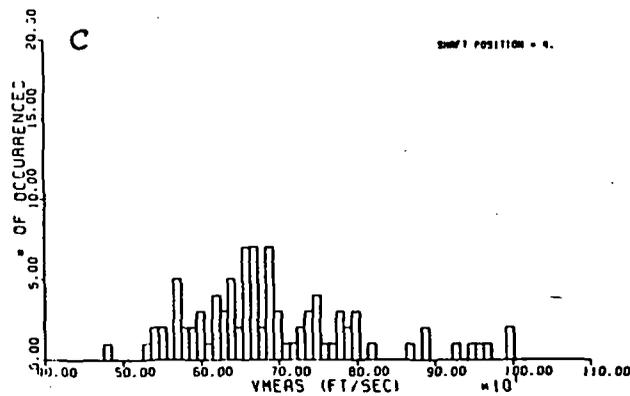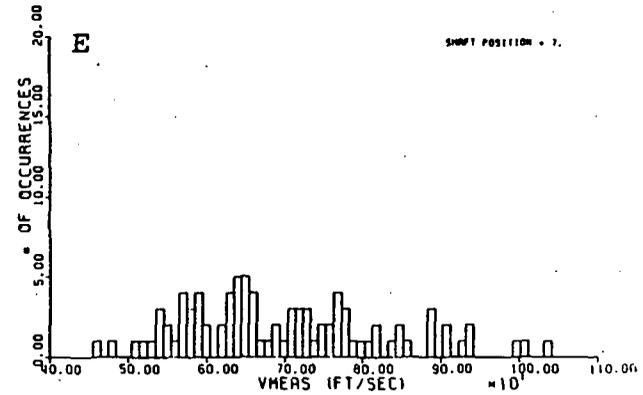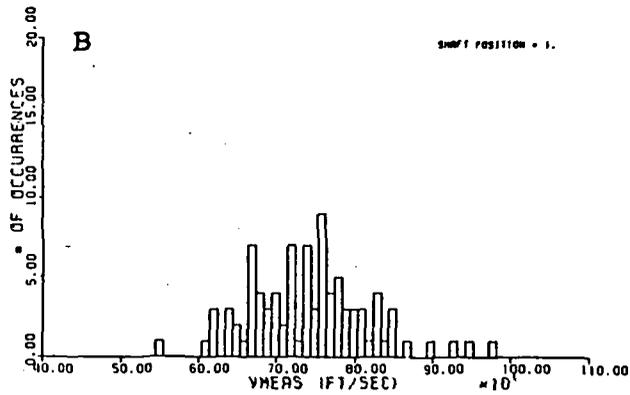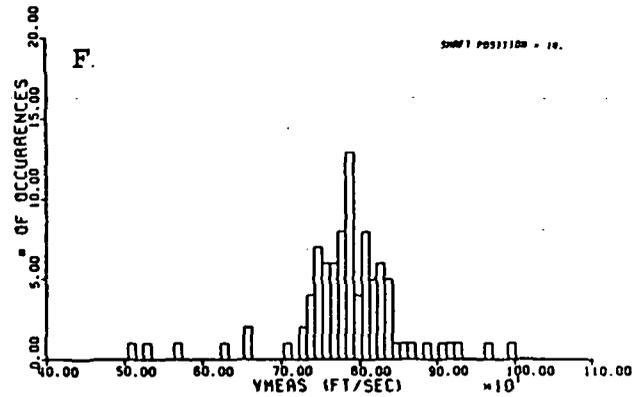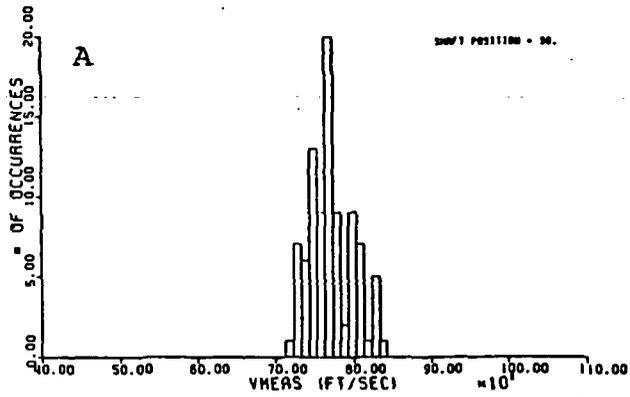
Figure 7.9   Probability density distribution of the velocity
measured by the 4-way probe at points A-F in figure
7.7 for blade passage #1
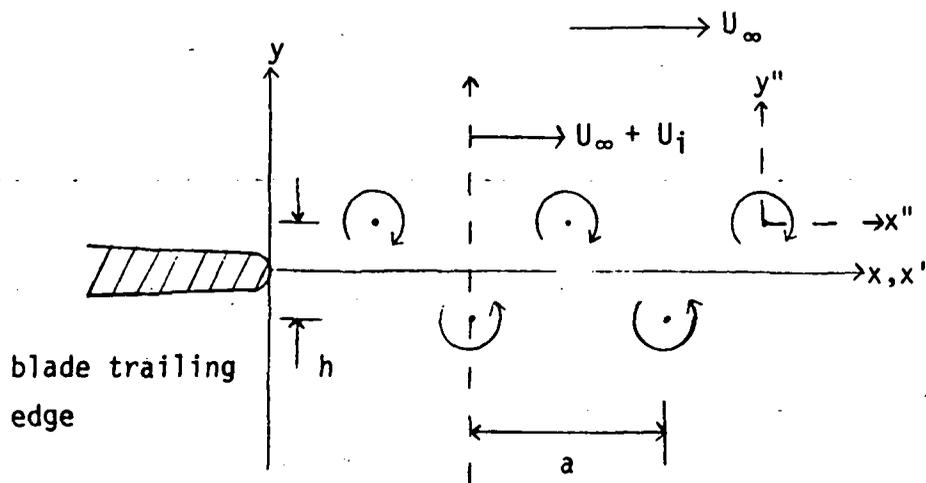
Figure 7.10   Geometry of rotor blade vortex street
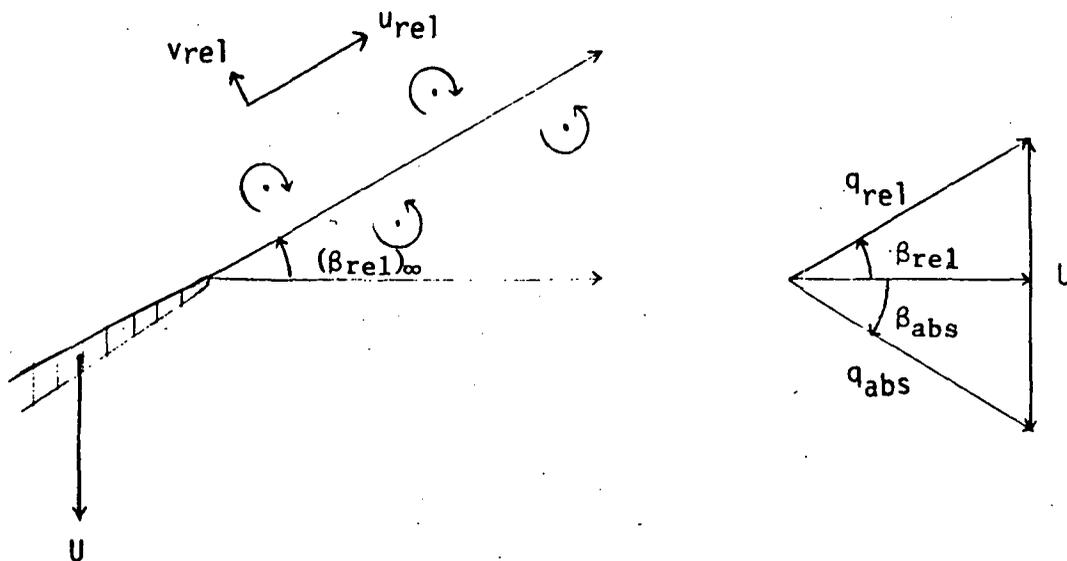
Figure 7.11   Rotor blade velocity triangle

BLADE WAKE VORTEX STREET
CORE RADIUS PARAMETER (RO/H) = 0.2500
H/A = 0.281

BLADE WAKE VORTEX STREET
CORE RADIUS PARAMETER (RO/H) = 0.5000
H/A = 0.281

a)

b)
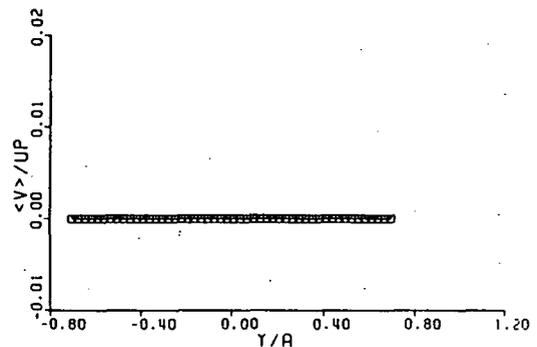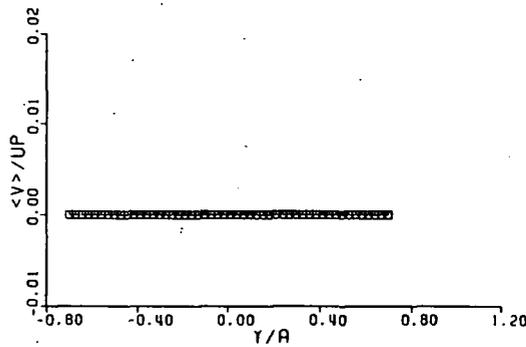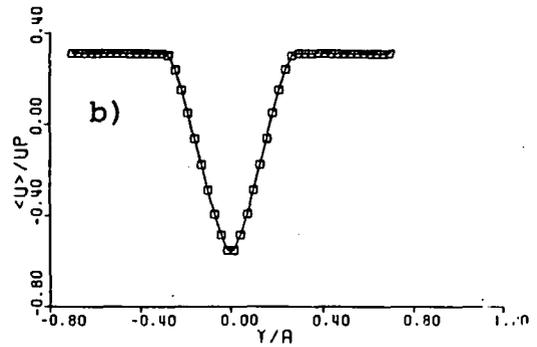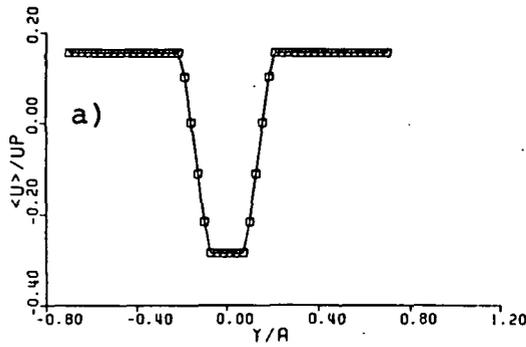
Figure 7.12   Von-Karman vortex street velocity profiles
            a) rØ/h = Ø.25   b) rØ/h = Ø.5Ø
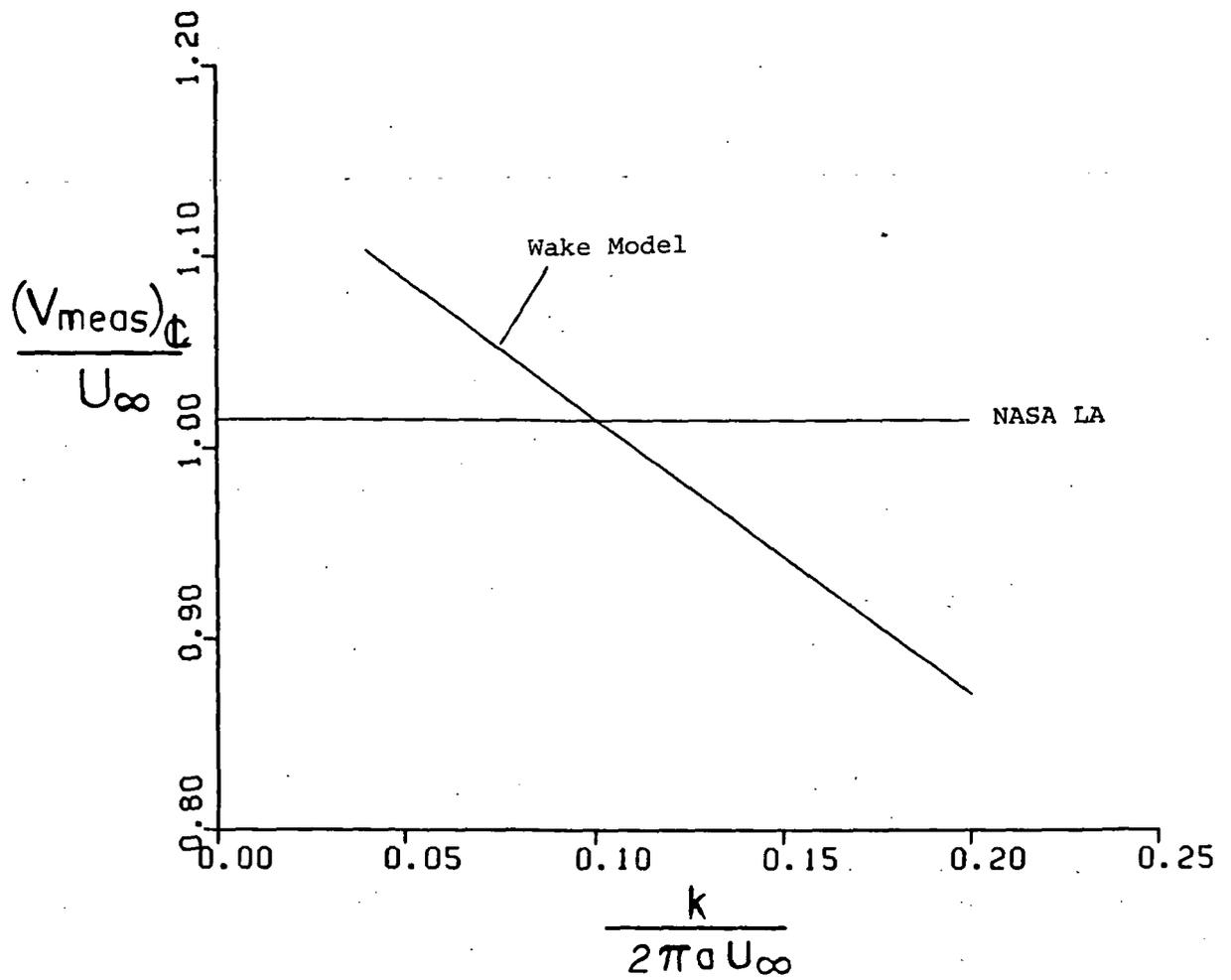
Figure 7.13 Absolute measured component of velocity at the vortex street centerline vs. vortex strength for $r\emptyset/h = \emptyset.5$
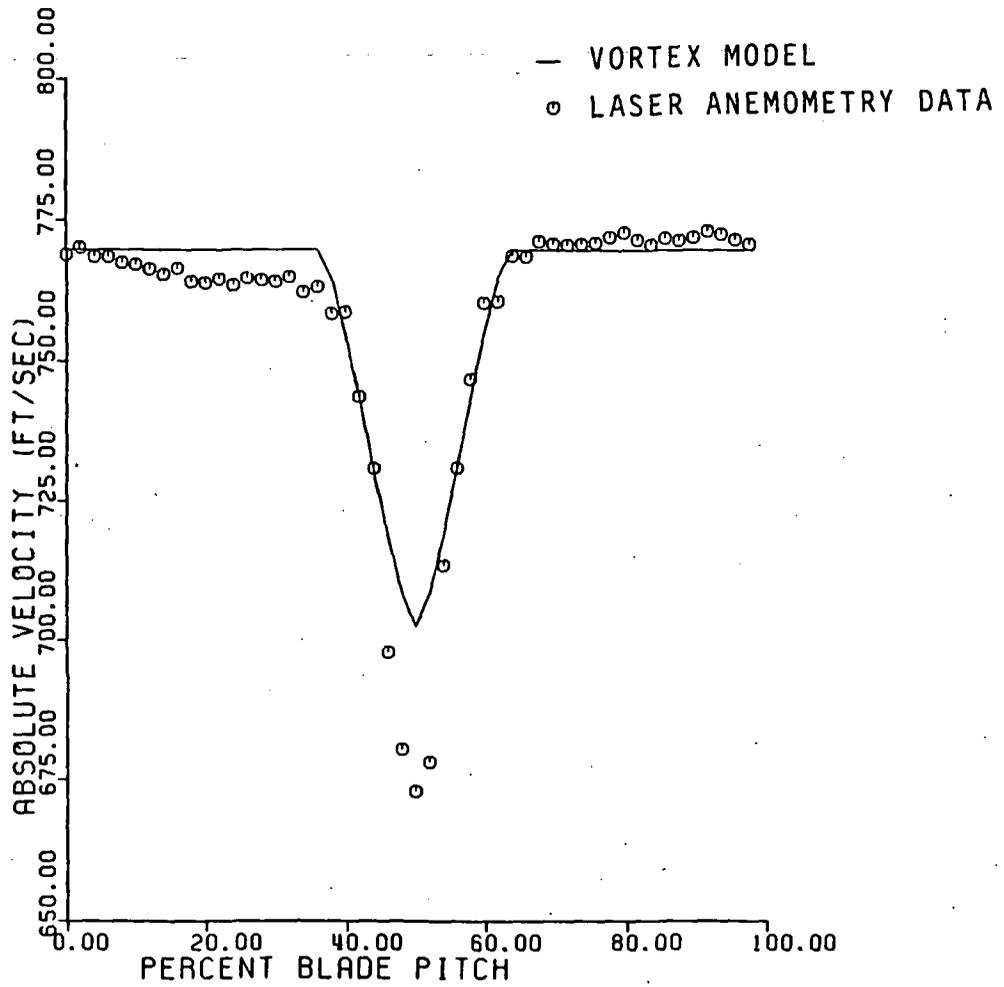
Figure 7.14   Comparison of the mean absolute velocity as measured
              by the LA to the "measured" component calculated
              from the vortex model
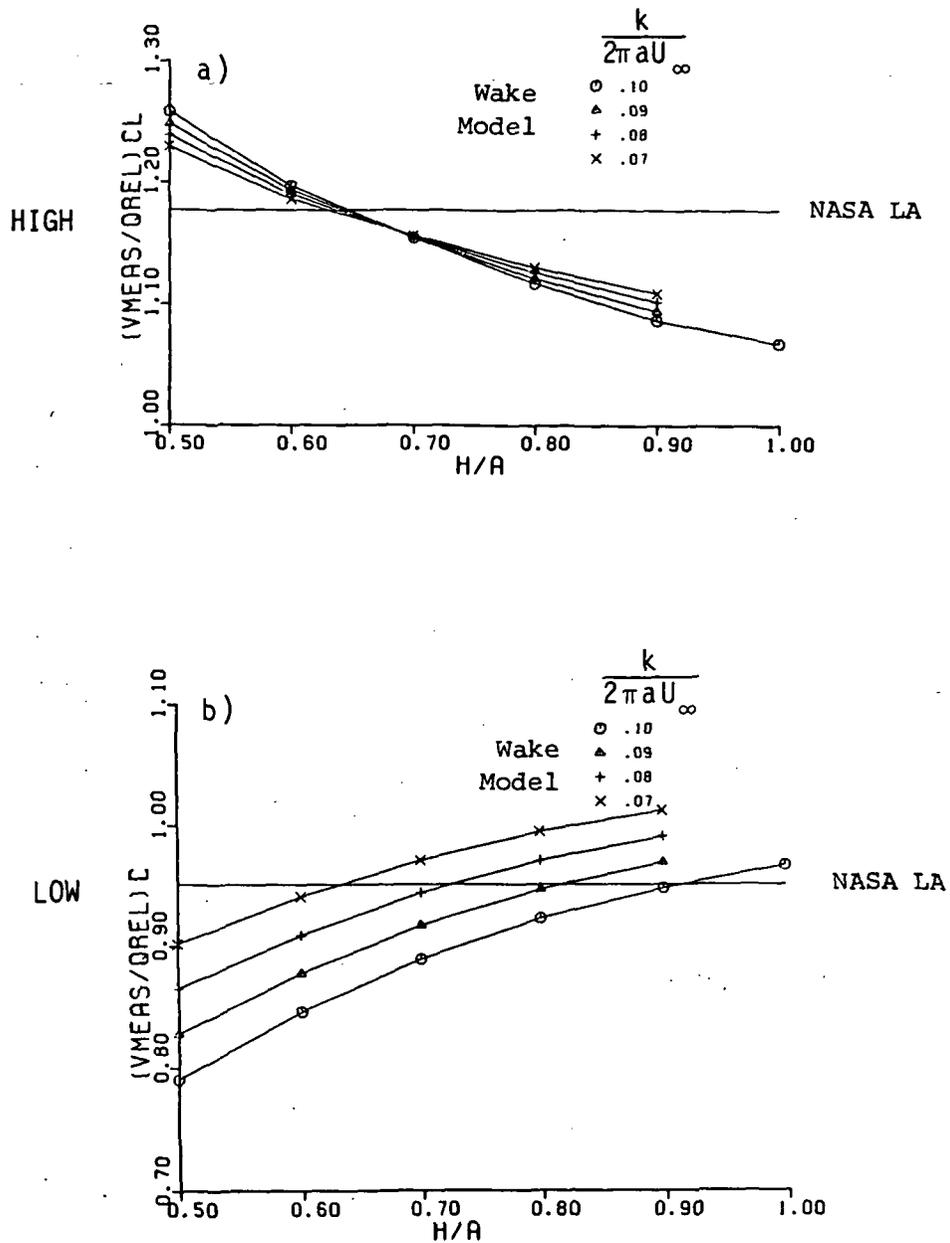
Figure 7.15   Most-probable velocities in bi-modal velocity
distributions of a blade wake vortex street
vs. h/a for rØ/h = Ø.5   a) upper most probable
velocity   b) lower most probable velocity

a)

□ Y/A=0.0000
⊙ Y/A=0.3175
△ Y/A=0.6350
+ Y/A=0.9525

VX/UP

X/A

b)

□ Y/A=0.0000
⊙ Y/A=0.3175
△ Y/A=0.6350
+ Y/A=0.9525

VY/UP

X/A
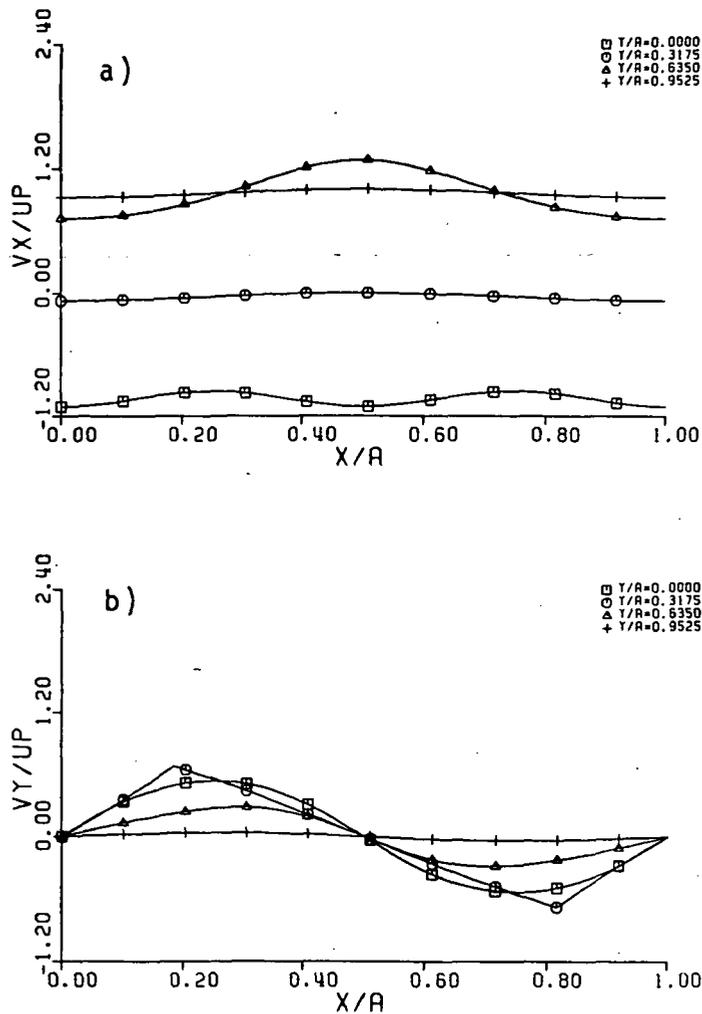
Figure 7.16 Velocity components of rotor blade vortex street
in frame of reference moving with the vortex street
a) parallel component b) perpendicular component
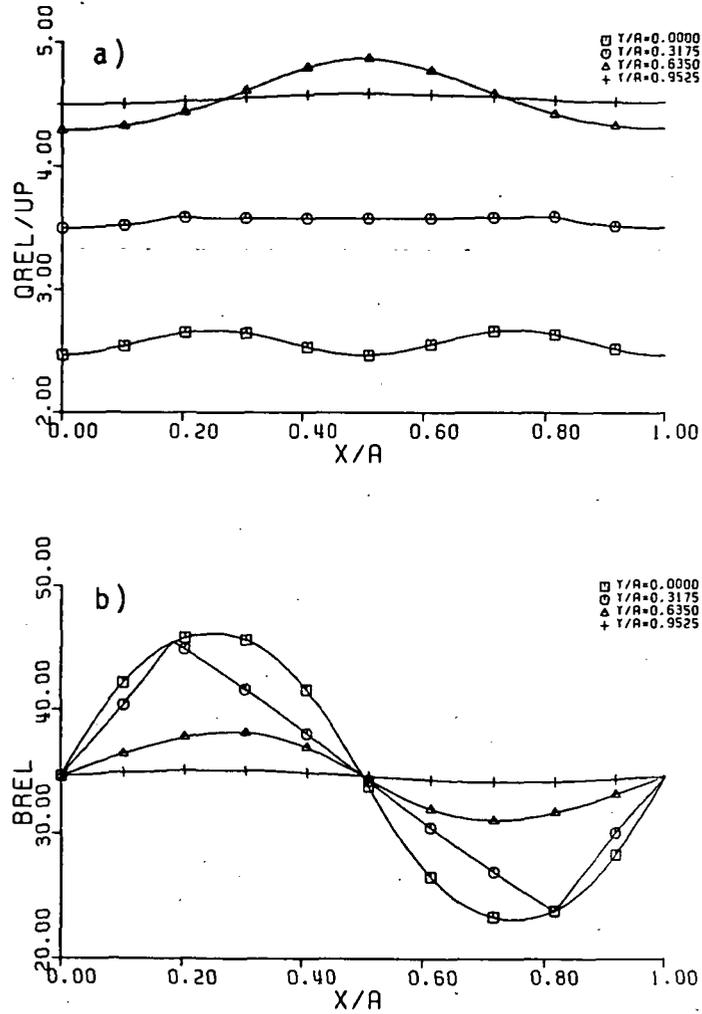
Figure 7.17   a) Relative velocity and b) relative flow angle
             in blade wake vortex street

BLADE WAKE VORTEX STREET
CORE RADIUS PARAMETER (RO/H) = 0.5000
VORTEX SPACING RATIO (H/A) = 0.635
PRESSURE VELOCITY (UP/UF) = 0.2205
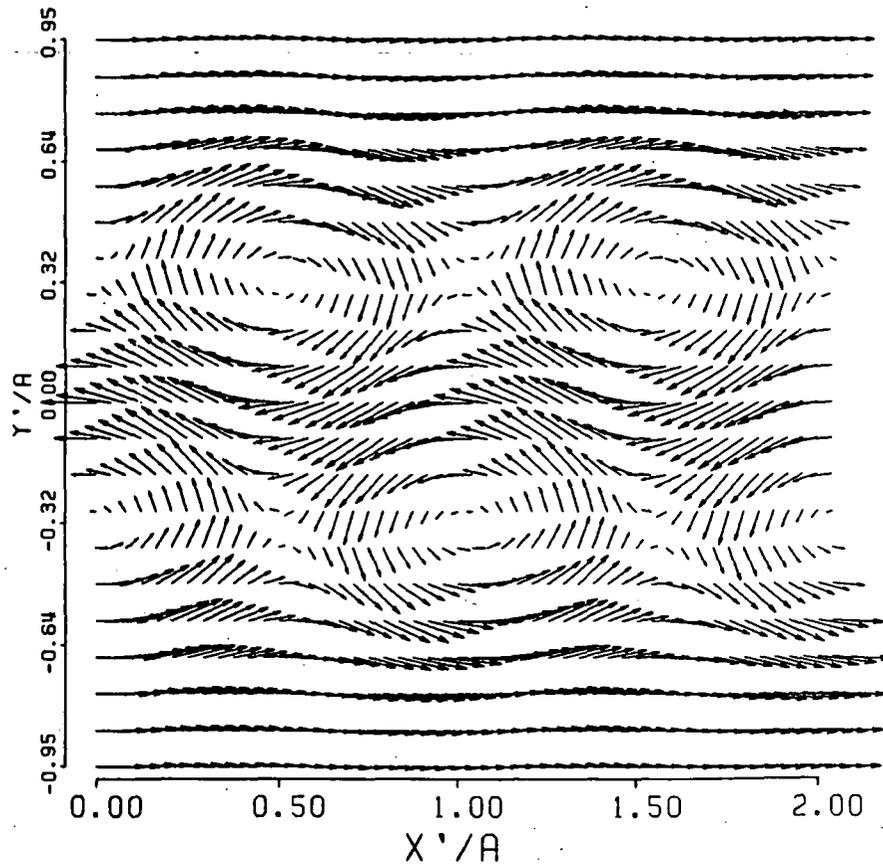
Figure 7.18   Velocity field of blade wake vortex street in the
frame of reference moving with the street

BLADE WAKE VORTEX STREET
CORE RADIUS PARAMETER (RO/H) = 0.5000
VORTEX SPACING RATIO (H/A) = 0.635
PRESSURE VELOCITY (UP/UF) = 0.2205
MEAN RELATIVE FLOW ANGLE = 34.7
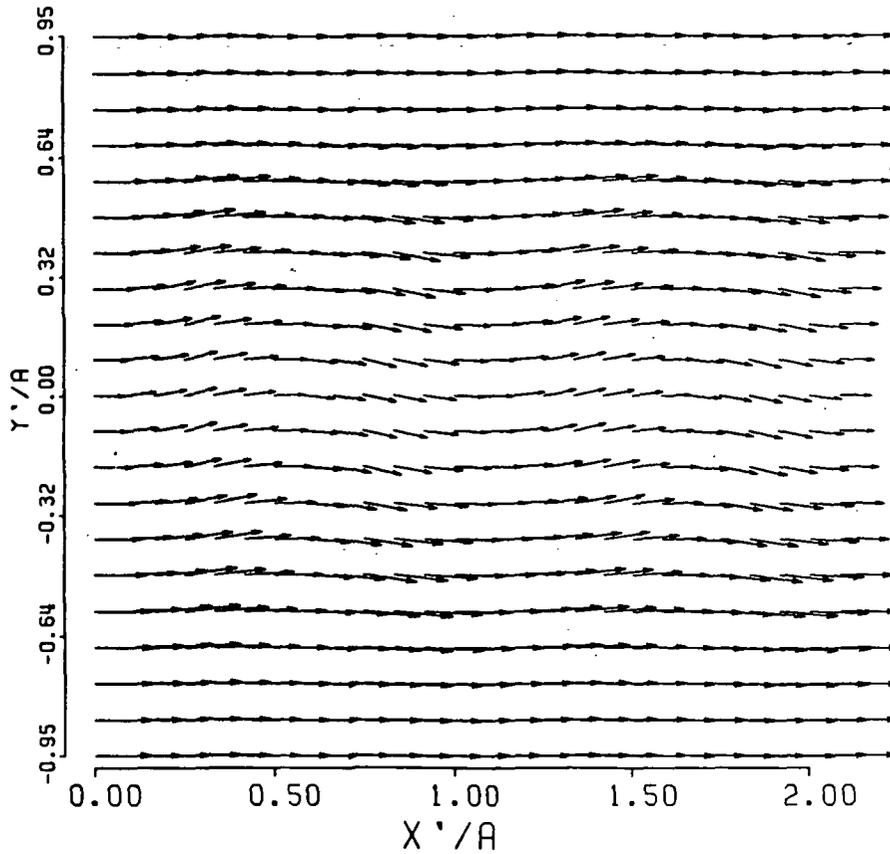
Figure 7.19   Velocity field of blade wake vortex street in the
frame of reference fixed to the blade trailing edge
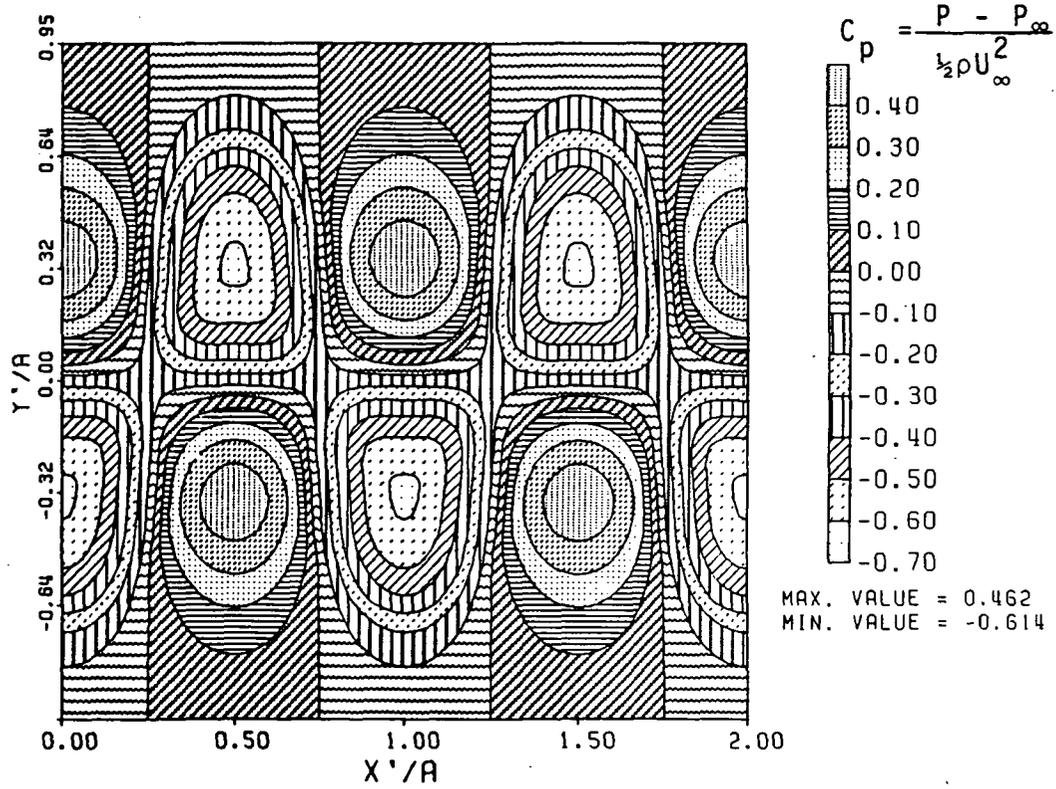
Figure 7.20 Static pressure contours from wake model

BLADE WAKE VORTEX STREET
CORE RADIUS PARAMETER (RO/H) = 0.5000
VORTEX SPACING RATIO (H/A) = 0.635
PRESSURE VELOCITY (UP/UF) = 0.2205
MEAN RELATIVE FLOW ANGLE = 34.7
WHEEL SPEED (WR/UF) = 1.3910
LFA ANGLE = 42.00
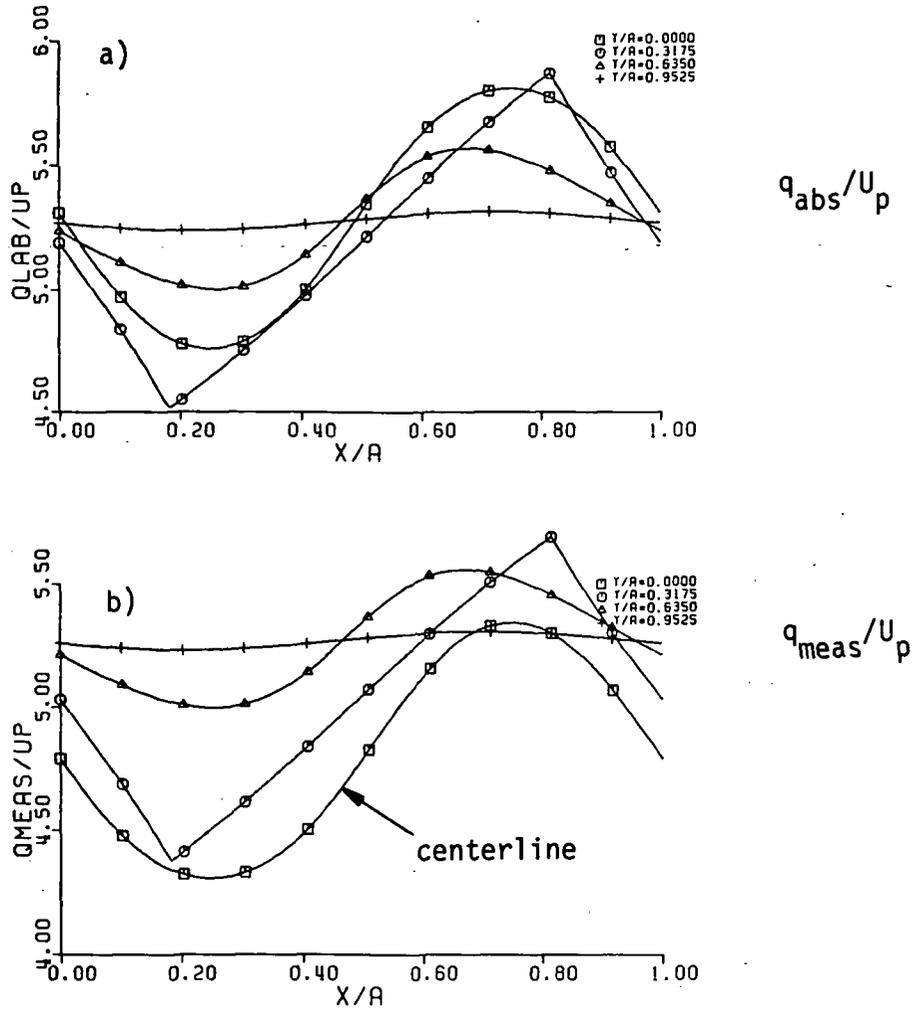
Figure 7.21   Velocity distributions from wake model
a) absolute velocity b) component of
absolute velocity corresponding to
the LA measurements
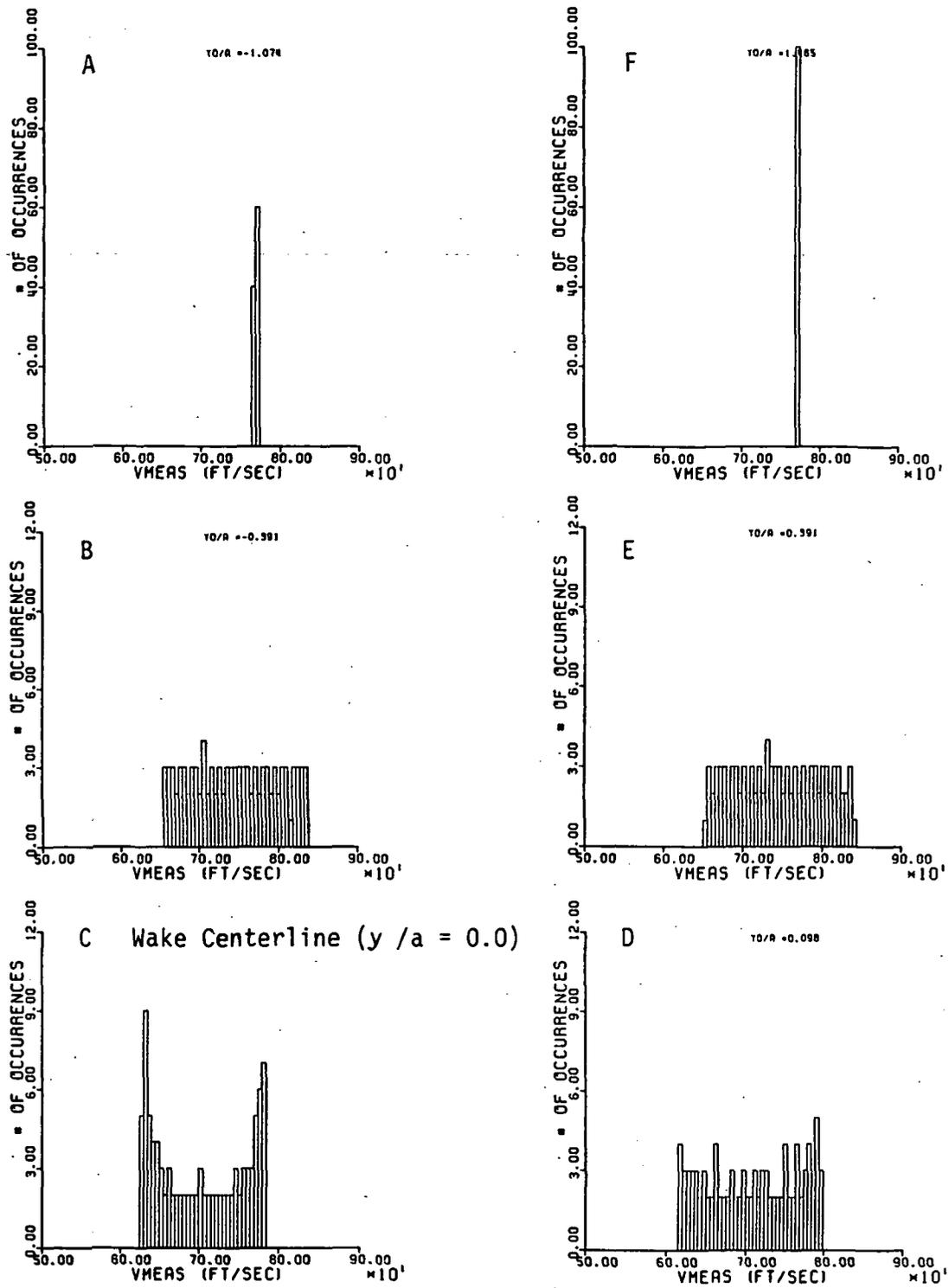
Figure 7.22 Probability density distributions of "measured"
velocities computed from wake model at points
A-F shown in figure 7.7
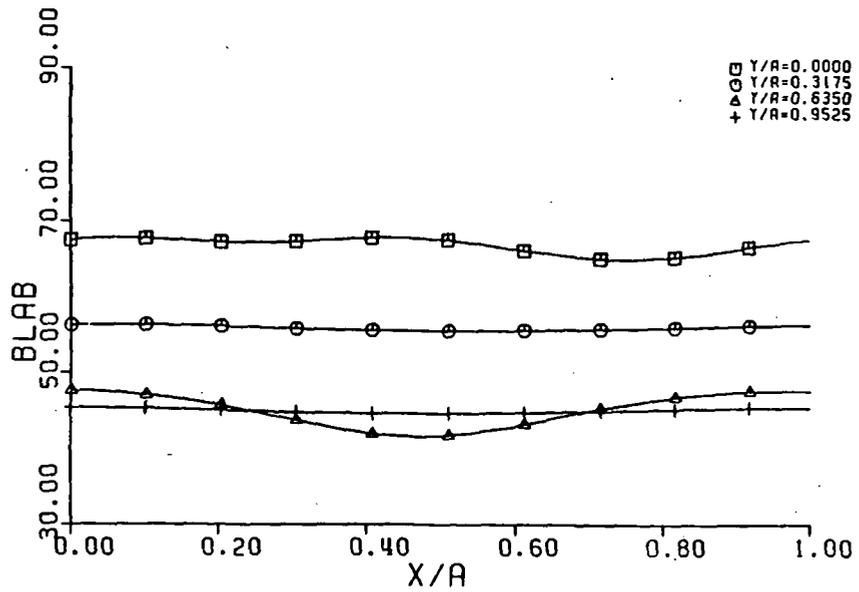
Figure 7.23   Distribtution of absolute tangential flow angle
              calculated from wake model

BLADE WAKE VORTEX STREET
CORE RADIUS PARAMETER (RO/H) = 0.5000
VORTEX SPACING RATIO (H/A) = 0.635
PRESSURE VELOCITY (UP/UF) = 0.2205
MEAN RELATIVE FLOW ANGLE = 34.7
WHEEL SPEED (WA/UF) = 1.3910
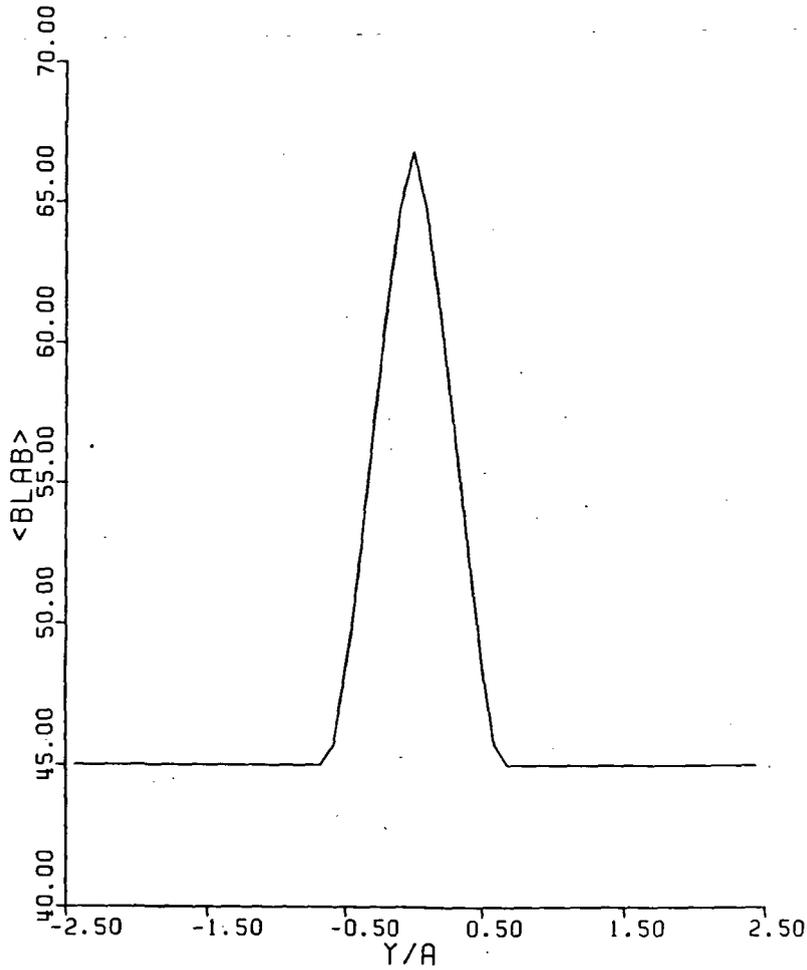
Figure 7.24   Average absolute tangential flow angle calculated from wake model

BLADE WAKE VORTEX STREET
CORE RADIUS PARAMETER (RO/H) = 0.5000
VORTEX SPACING RATIO (H/A) = 0.635
PRESSURE VELOCITY (UP/UF) = 0.2205
MEAN RELATIVE FLOW ANGLE = 34.7
WHEEL SPEED (WR/UF) = 1.3910
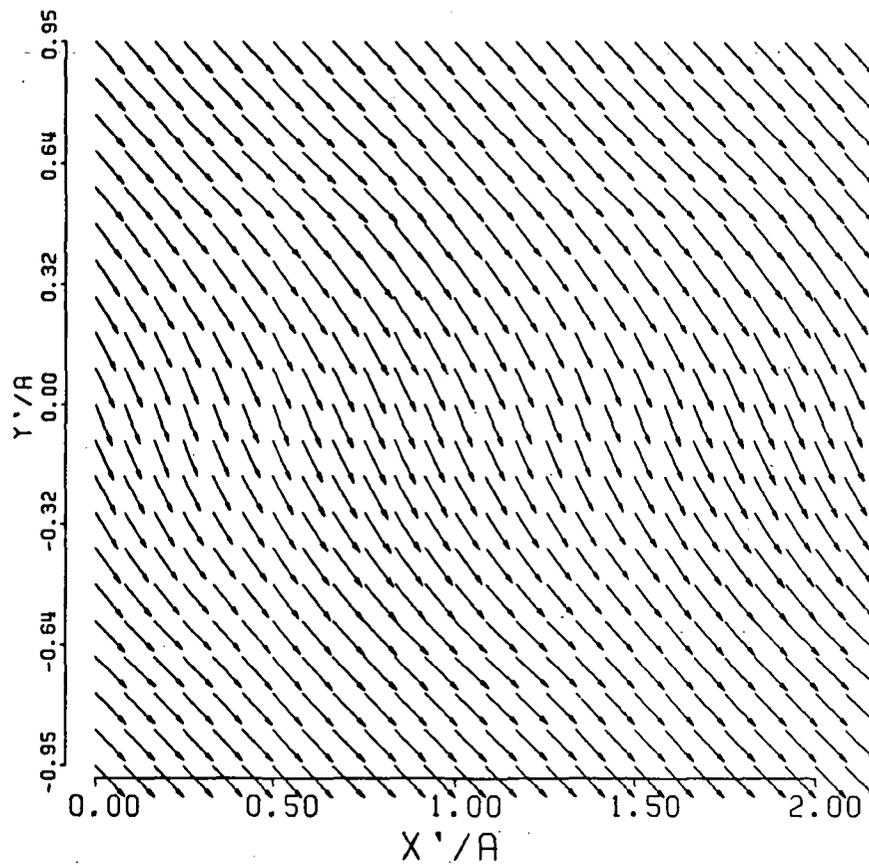
Figure 7.25   Absolute(laboratory) velocity field calculated from wake model
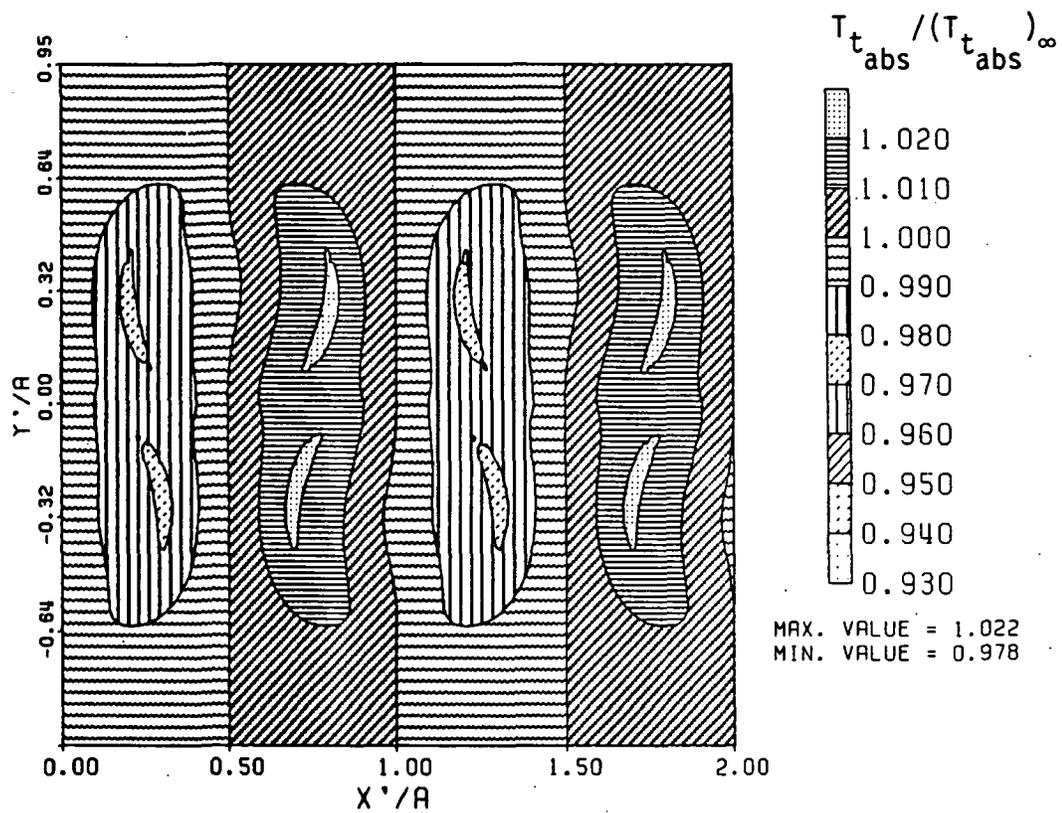
Figure 7.26   Absolute total temperature contours from wake model
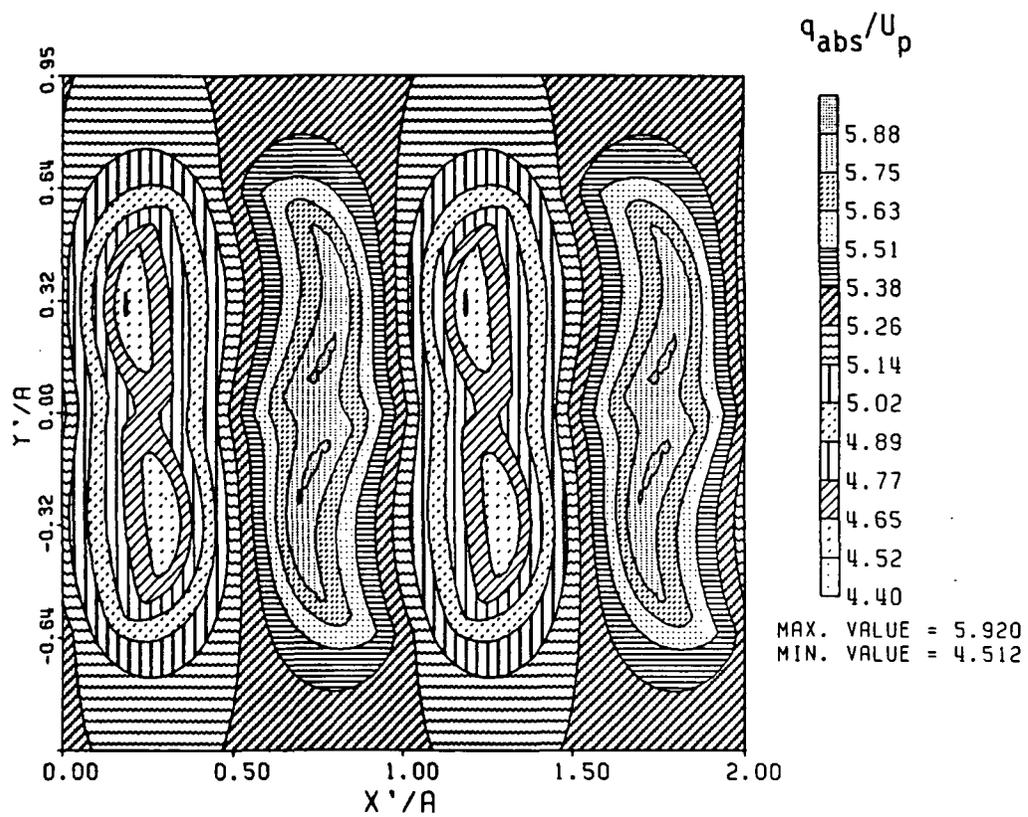
Figure 7.27   Absolute velocity contours from wake model
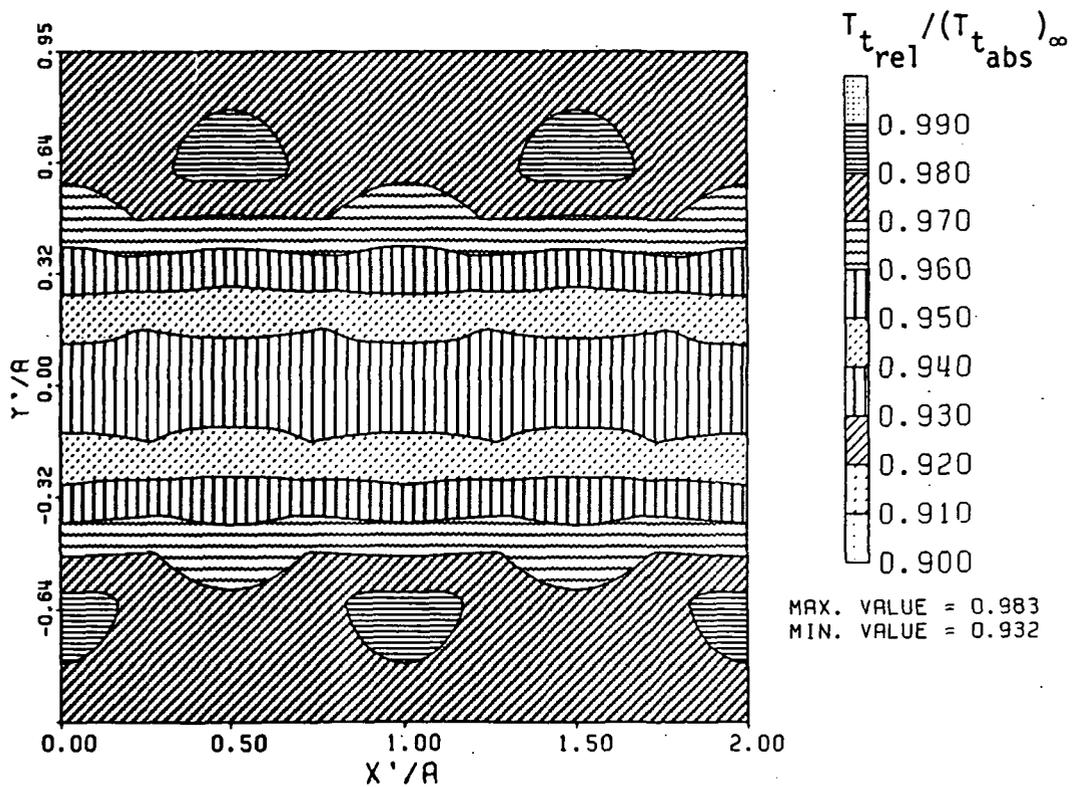
Figure 7.28 Relative total temperature contours from wake model
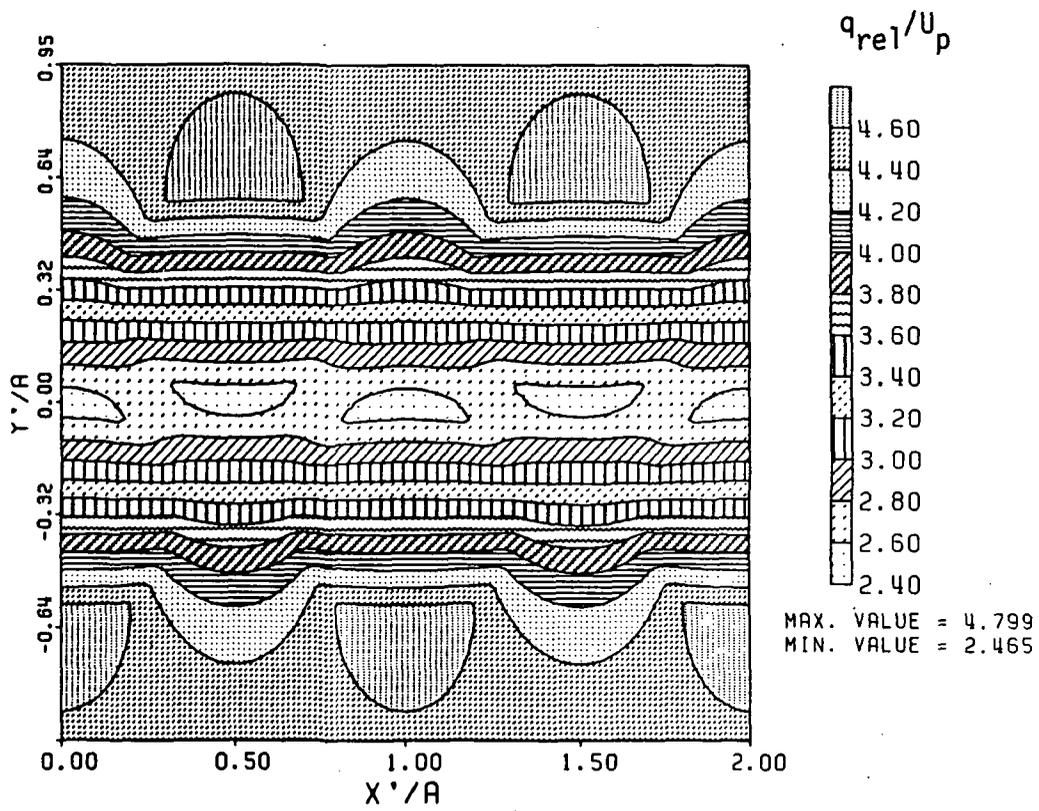
Figure 7.29   Relative velocity contours from wake model
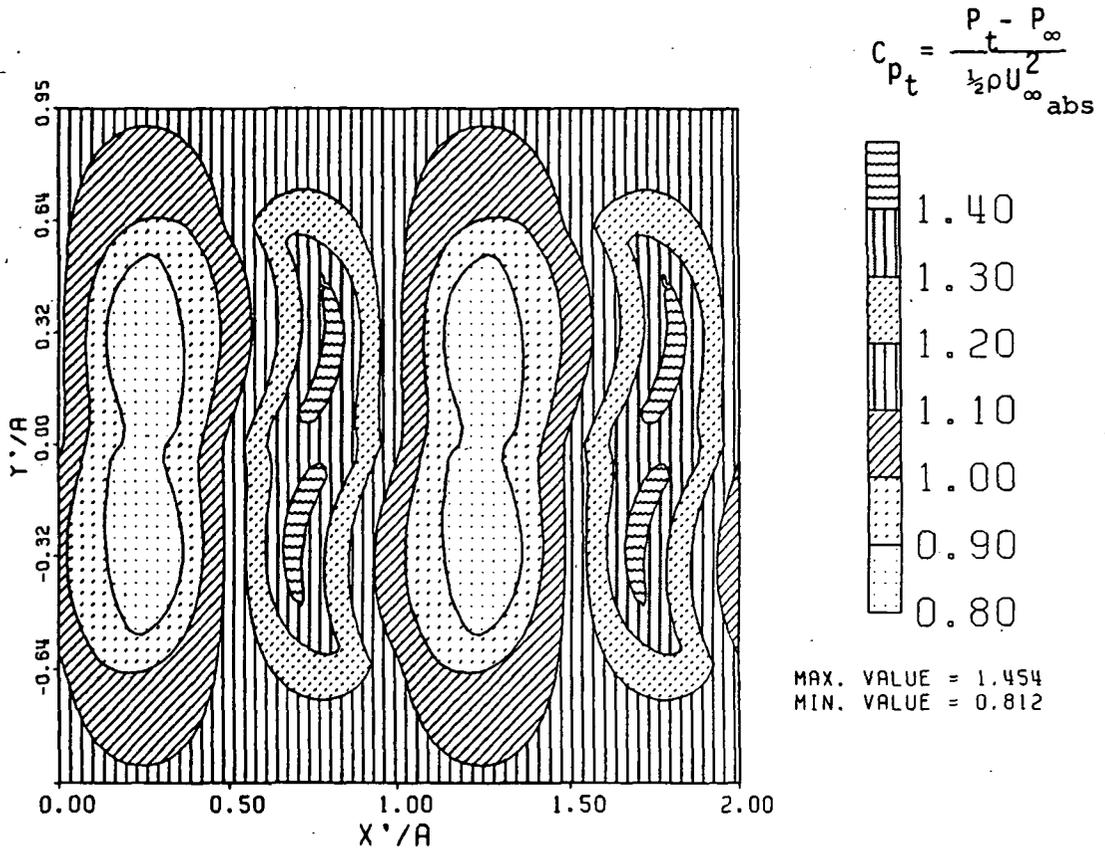
Figure 7.30   Absolute total pressure contours from wake model

ROTOR EXIT STATIC PRESSURE
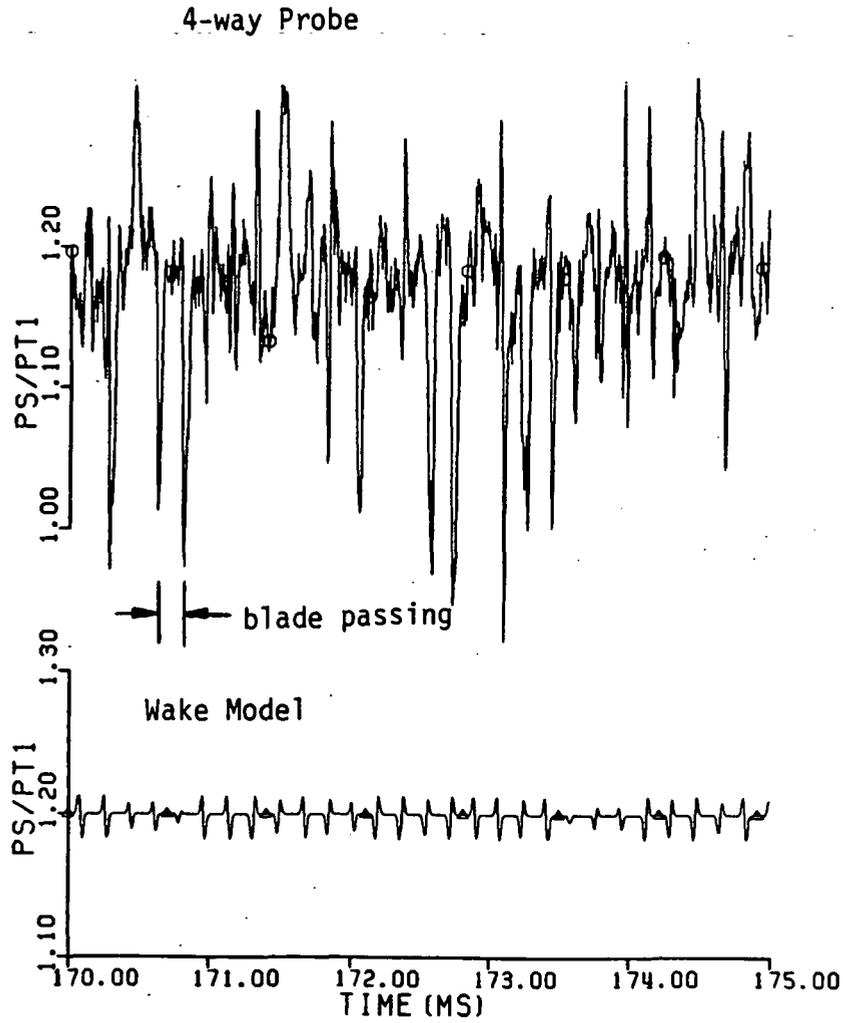
Figure 7.31 Comparison of the ratio of the rotor exit static
pressure to the upstream total pressure measured
by the 4-way probe to the wake model
prediction

ROTOR EXIT RELATIVE TOTAL PRESSURE RATIO
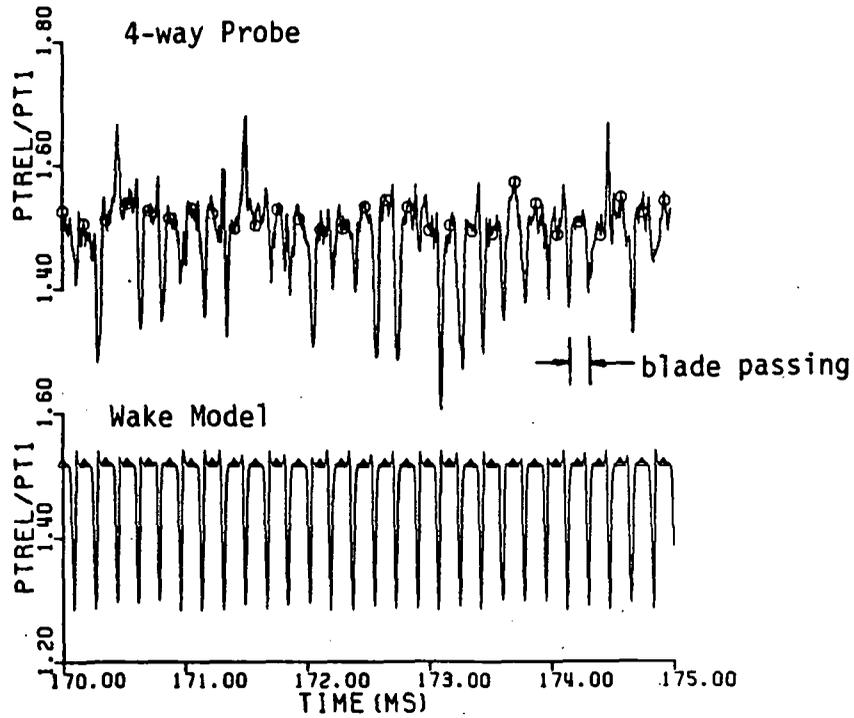
Figure 7.32   Comparison of the rotor exit relative total
pressure ratio measured by the 4-way probe
to the wake model prediction

ROTOR EXIT ABSOLUTE TOTAL PRESSURE RATIO
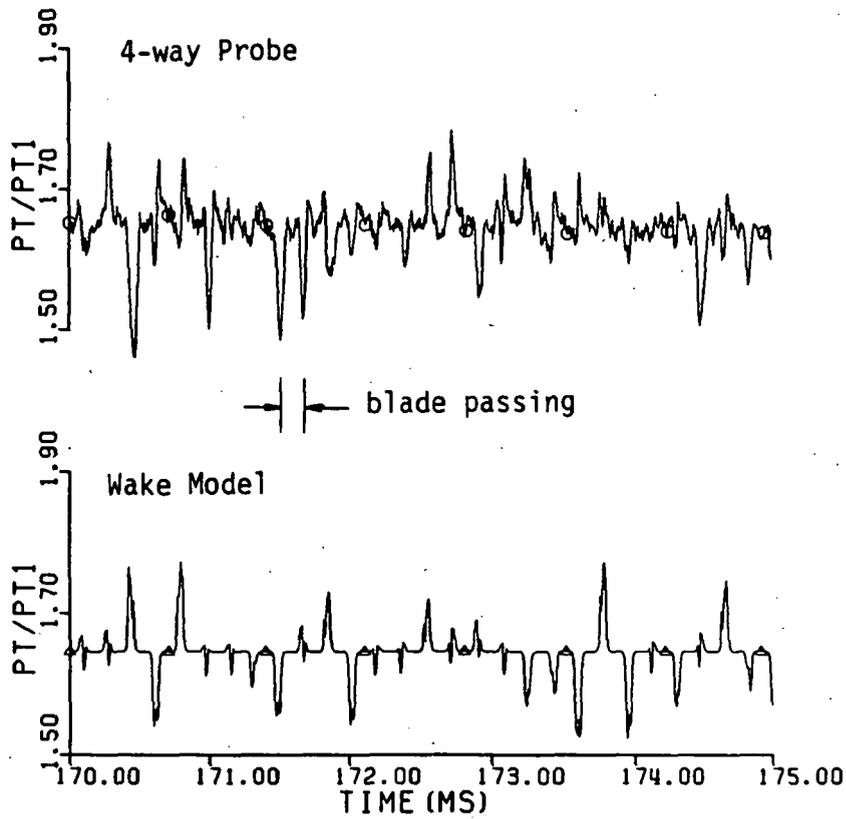
Figure 7.33 Comparison of the rotor exit absolute total
pressure ratio measured by the 4-way probe
to the wake model prediction

ROTOR EXIT RELATIVE FLOW ANGLE
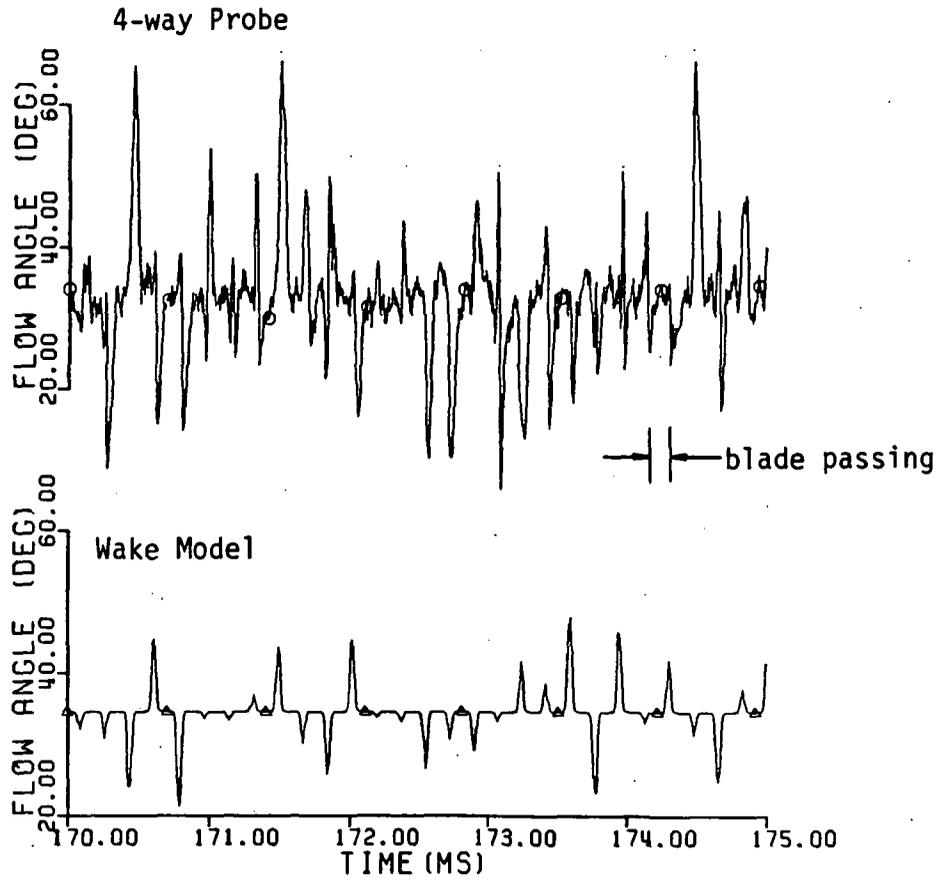
Figure 7.34 Comparison of the rotor exit relative flow angle
measured by the 4-way probe to the wake model
prediction

ROTOR EXIT ABSOLUTE FLOW ANGLE
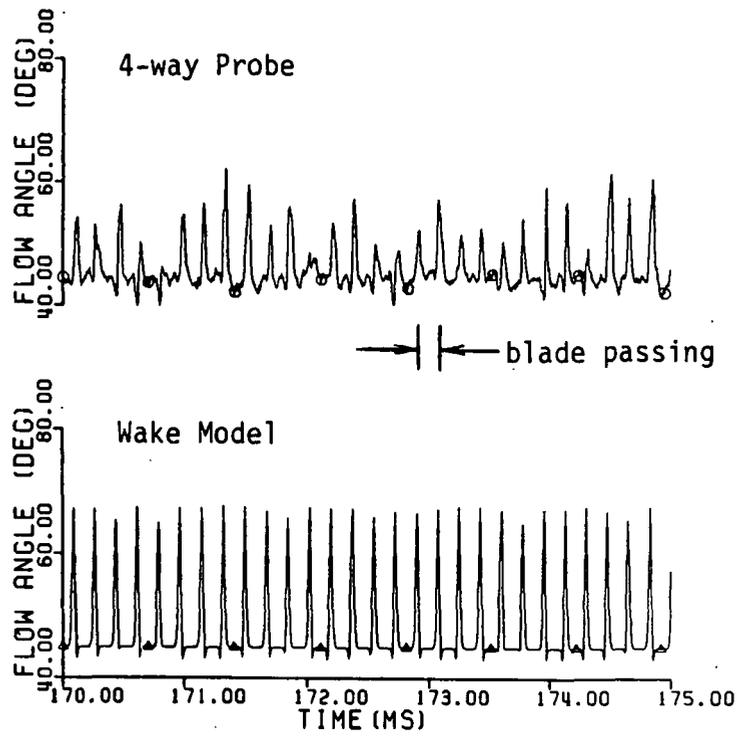
Figure 7.35 Comparison of the rotor exit absolute flow an~
measured by the 4-way probe to the wake model
prediction

ROTOR EXIT ABSOLUTE TOTAL TEMPERATURE RATIO
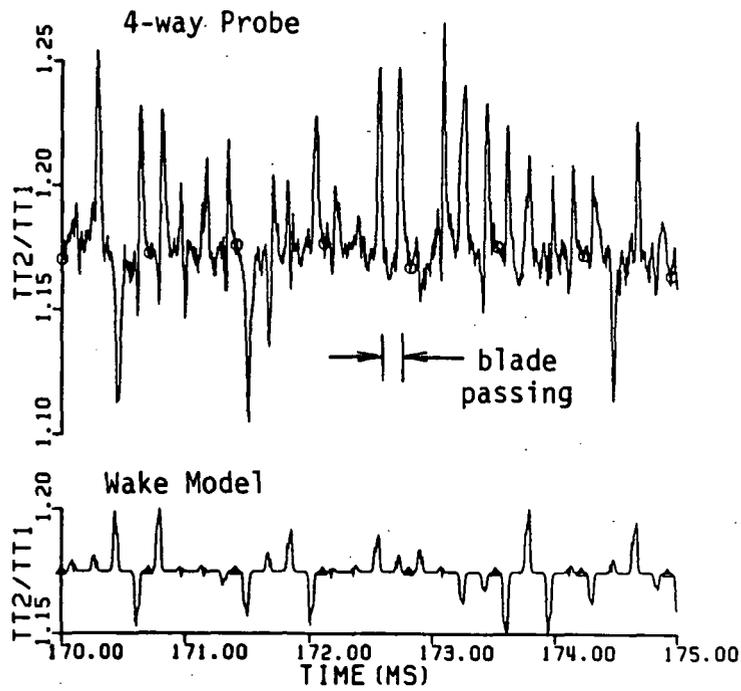
Figure 7.36   Comparison of the rotor exit absolute total
temperature ratio measured by the 4-way probe
to the wake model prediction
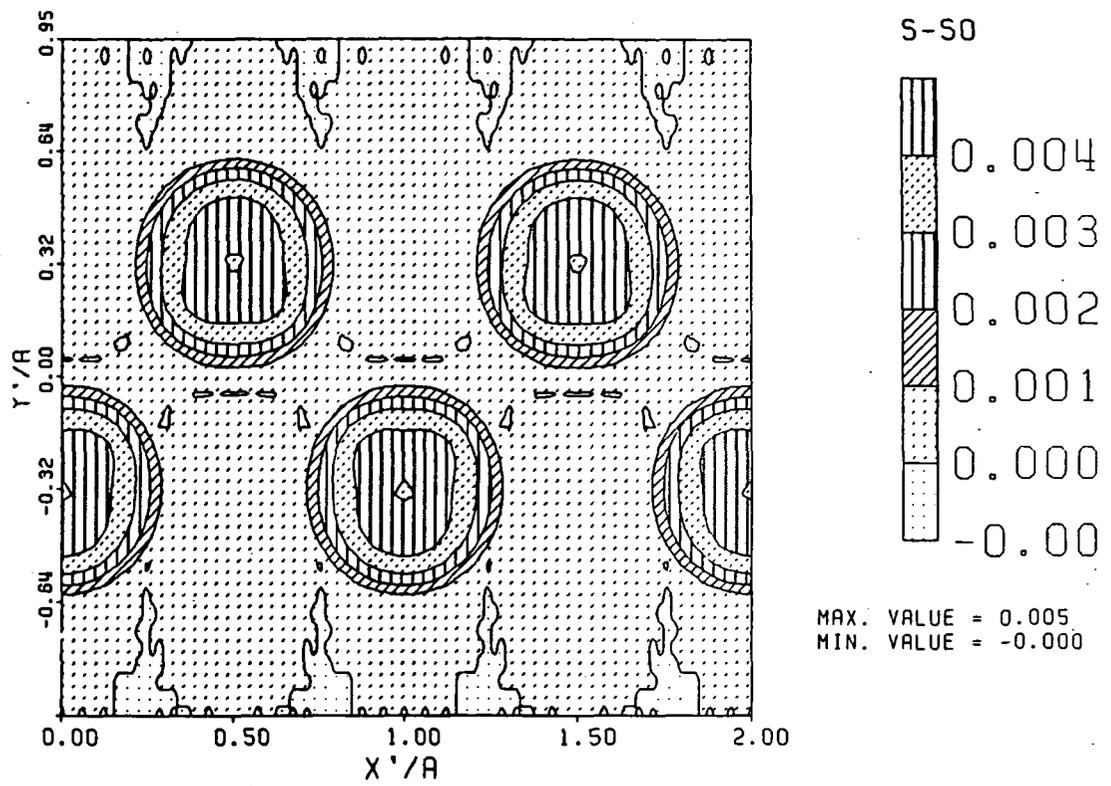
Figure 7.37   Contours of entropy rise from wake model
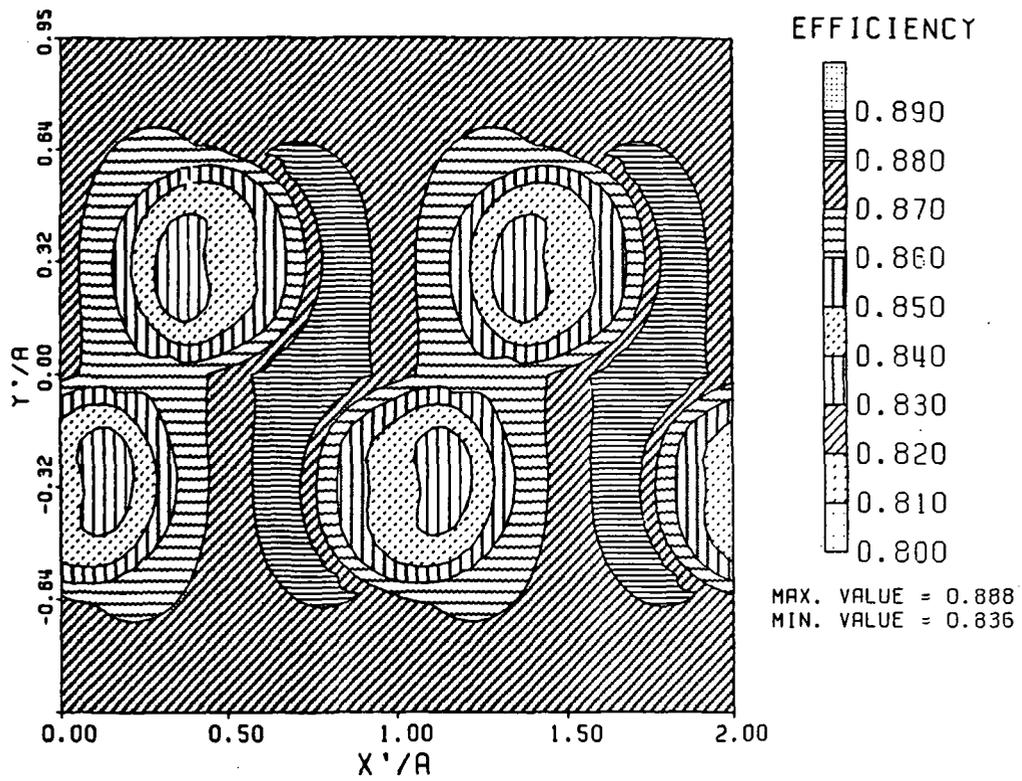
Figure 7.38   Contours of adiabatic efficiency from wake model

ROTOR EXIT ADIABATIC EFFICIENCY
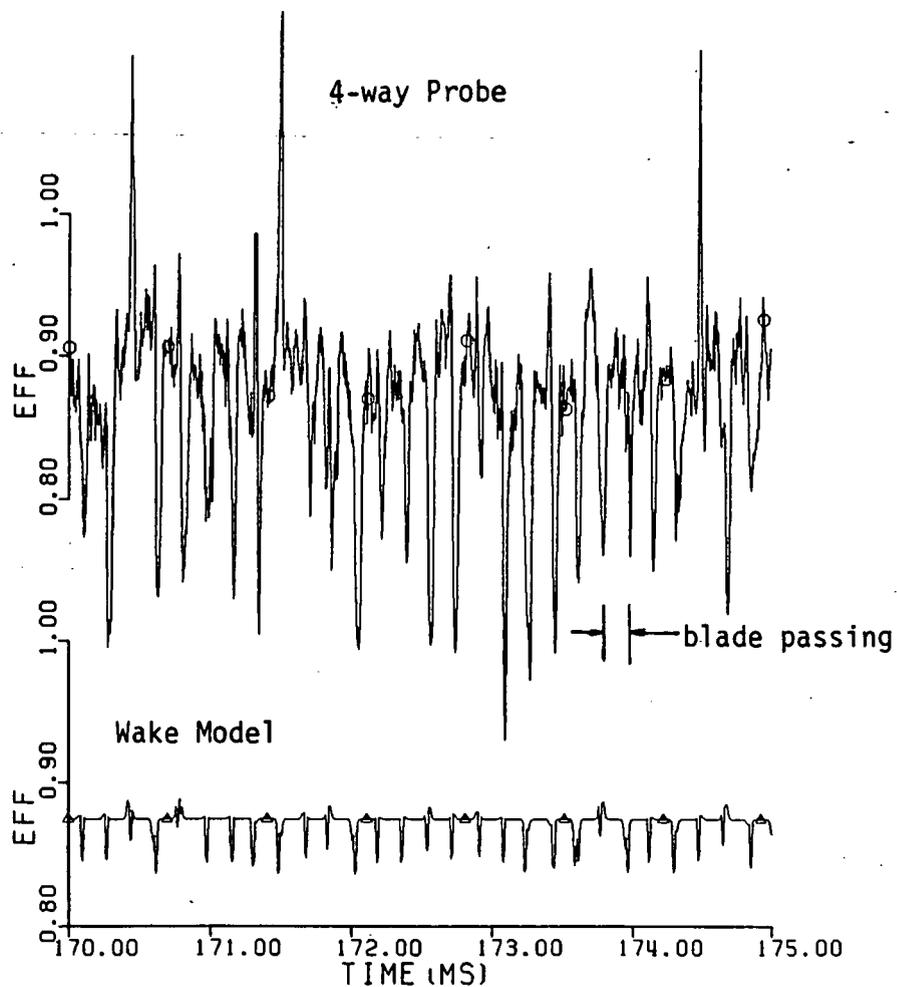
Figure 7.39   Comparison of the rotor exit adiabatic efficiency
   measured by the 4-way probe to the wake model
             prediction

$$u = u_o \left(1 + \frac{\omega_o}{u_o} y \right)$$
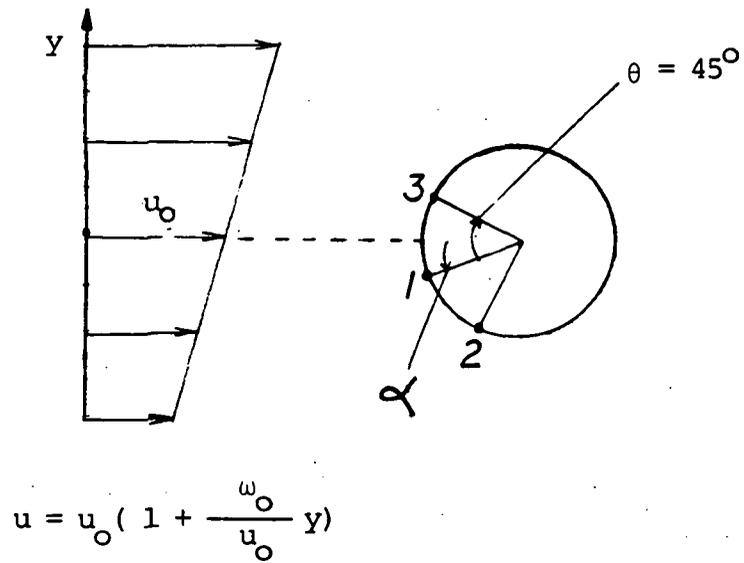
Figure A.1   Idealized Cylindrical Pressure Probe
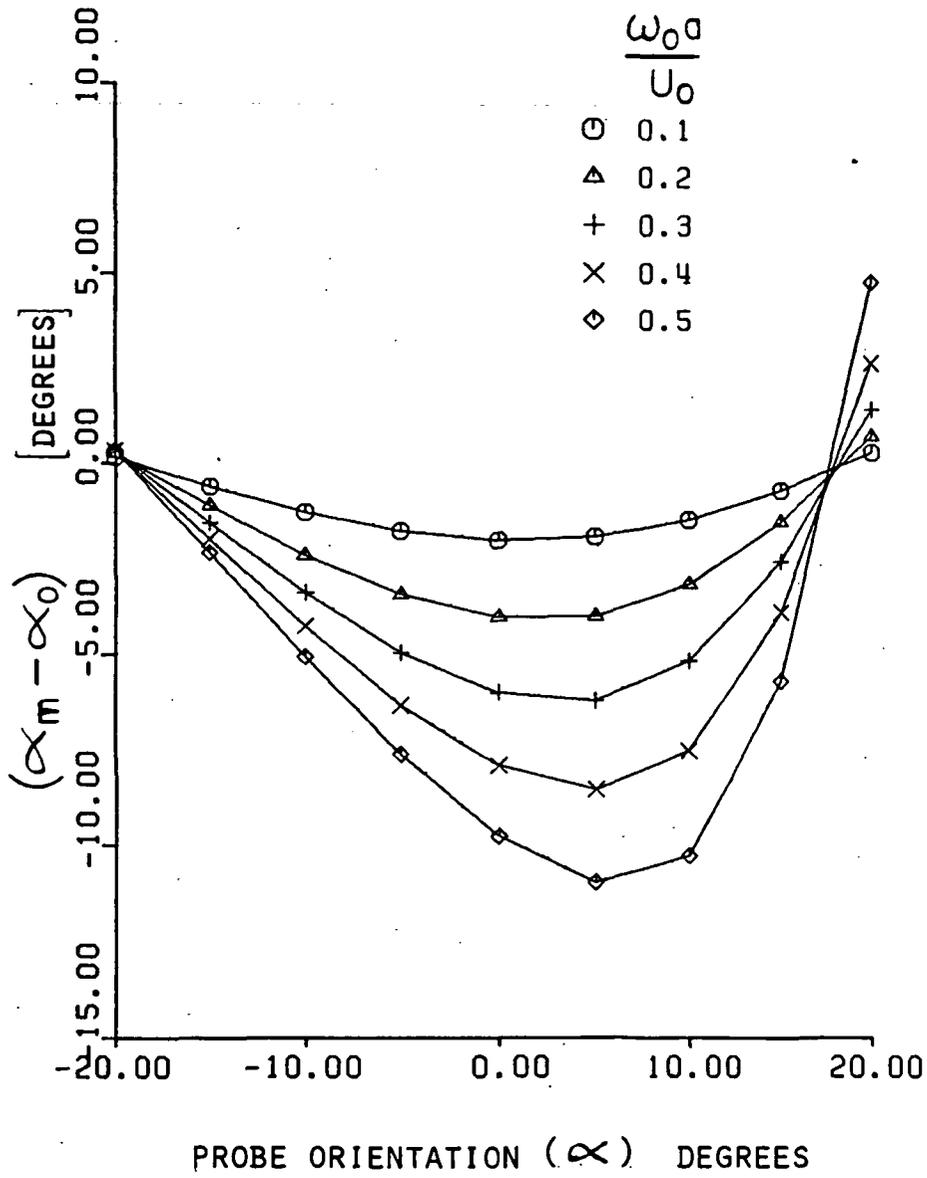
Figure A.2 Flow Angle Error for Cylindrical Probe
in Shear Flow
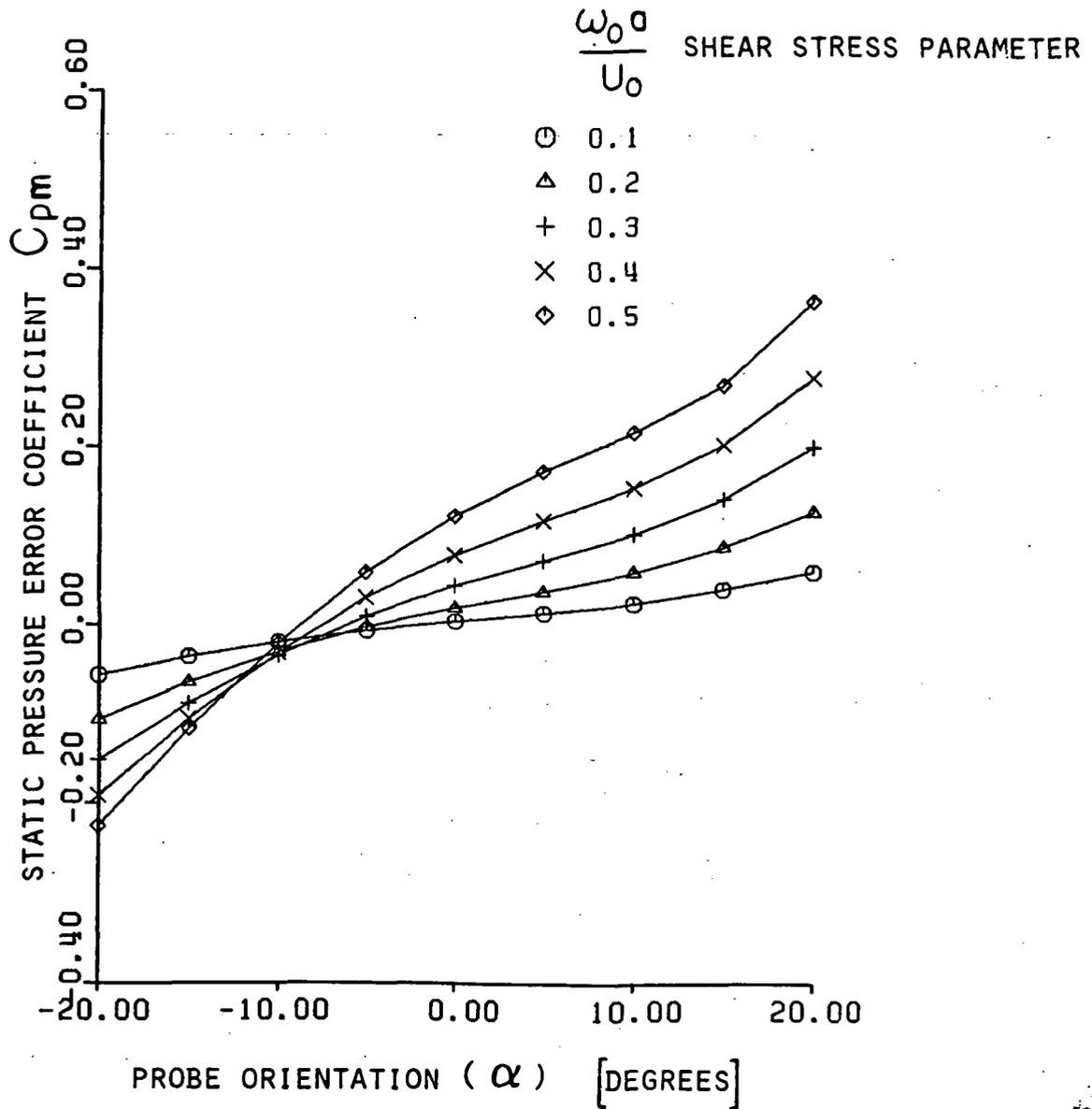
Figure A.3   Static Pressure Error Coefficient for
Cylinder Probe in Shear Flow
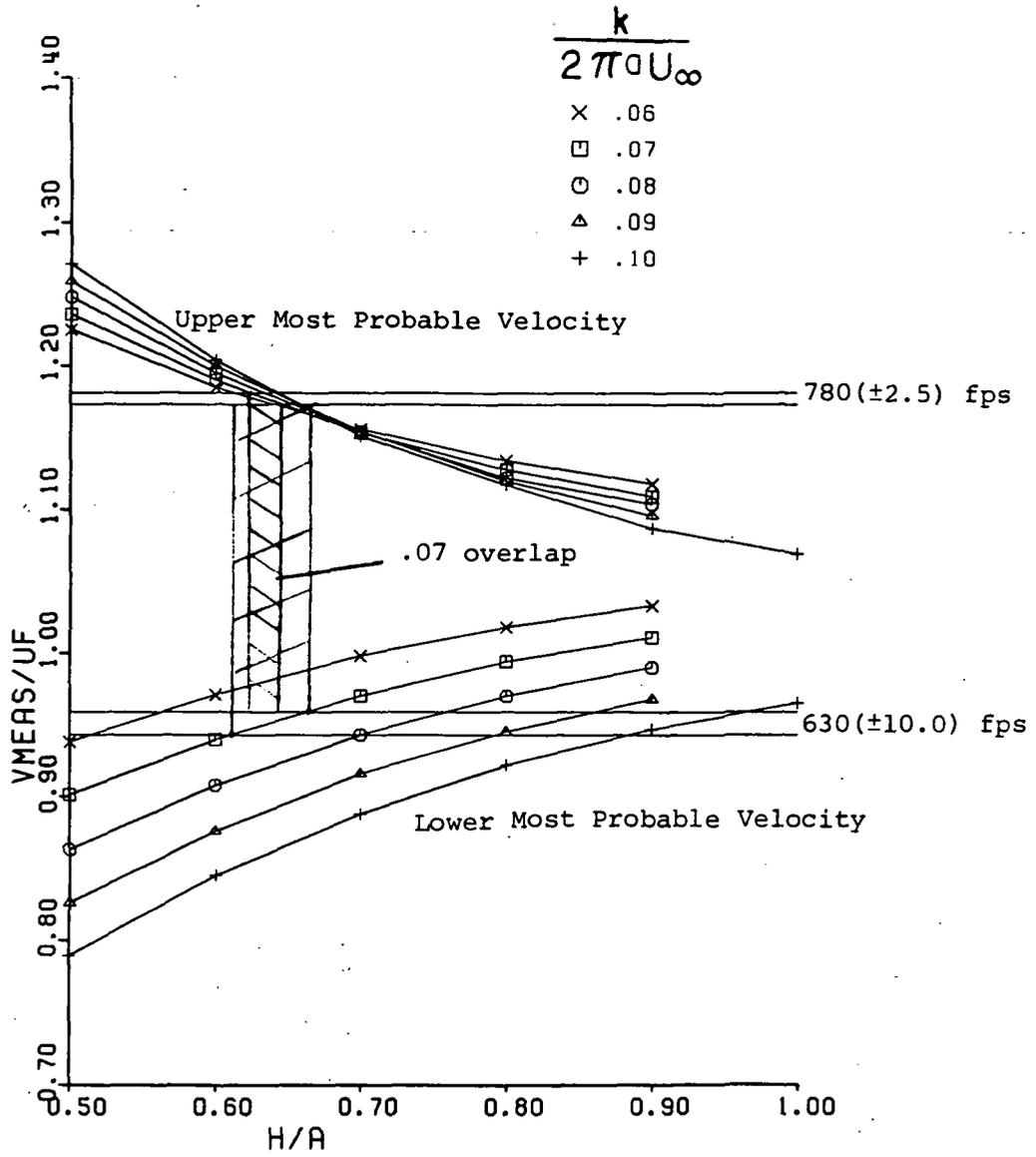
Figure B.1   Effect of Uncertainty in Most-Probable Velocities
On Vortex Model Fit